Bulletin de la Société Royale des Sciences de Liège, Vol. 71, 5-6, 2002, pp. 249-445

Non-radial non-adiabatic oscillations of near main sequence variable stars

Marc-Antoine DUPRET

Prefatory note

The present PhD thesis is a shortened version compared to the original text. More precisely, the chapter which details the numerical method of solution as well as the different appendices are not given here. Moreover, the number of applications to Slowly Pulsating B stars has been reduced to 3 stars (instead of 11). If the reader wishes to have the complete version, he can contact the author who will send it with pleasure.

Address of the author:

Marc-Antoine Dupret
Rue de Morimont, 9
1340 Ottignies, Belgium
email: madupret@ulg.ac.be

MERCI !!

Merci d'abord à toi, Richard Scuflaire mon promoteur, ta porte a toujours été ouverte quand j'avais des questions. Tu m'as aidé, épaulé, guidé et tant appris tout au long de ces années de recherche. Ce fut une très grande chance pour moi d'avoir le plaisir de travailler sous ta tutelle. Au-delà de tes très hautes qualités scientifiques et de la passion que nous partageons pour les problèmes numériques, je retiendrai surtout la chaleur humaine et générosité collées pour ainsi dire à ta personne.

Merci à toi Arlette Noels, co-promotrice et présidente de mon jury de thèse. Merci de m'avoir accueilli dans l'équipe que tu diriges si bien, ce fut un immense plaisir pour moi d'y travailler durant toutes ces années. Tu m'as toujours soutenu, aidé et appuyé et je t'en suis très reconnaissant.

Merci à toi, François mon père, c'est de toi que je tiens (au delà de notre si grande amitié) l'éveil et l'enrichissement de ma curiosité et de ma passion pour les sciences et la découverte des secrets de notre univers. Je compte sur toi pour lire ma thèse et j'espère bien que nous trouverons un jour le temps de faire des recherches scientifiques ensembles.

Merci à toi, Madeleine ma mère, c'est de ton amour que je tiens ma confiance en moi, toi qui as toujours cru en tes enfants et m'as encouragé dans tout ce que j'entreprenais. Sans vous deux, papa et maman, rien de tout cela n'aurait commencé après tout ...

Thank you, Joris, I have been so lucky and happy to work and collaborate with you during my thesis, you who are always curious and full of questions. With your search for perfection, you taught me to be more precise and clear in my explanations, which is so important.

Thank you, Conny Aerts, you encouraged me and taught me so much. I am very grateful to you who helped and pushed me to communicate and publish my researchs in the scientific world, which is so important.

Merci à tous les membres de mon jury de thèse: MarieJo Goupil, Rafael Garrido, Conny Aerts, Richard Scuflaire, Arlette Noels et Anne Thoul, pour avoir pris le temps de lire ma thèse.

Merci à tous les chercheurs de l'Institut d'Astrophysique et Géophysique de l'Université de Liège, vous qui m'avez aidé à différents degrés dans mes recherches et m'avez soutenu par votre sympathie. Merci particulièrement à Maurice Gabriel pour les discussions scientifiques très intéressantes que nous avons pu avoir, elles m'ont beaucoup appris.

Thank you to all the astronomers of the Instituut voor Sterrenkunde of the Katholieke Universiteit Leuven, it has been a great pleasure to collaborate with you.

Thank you to all the astronomers of the Instituto de Astrofisica de Andalucia, Granada, Spain: Rafa, Andy, Antonio, ... for your welcome and all what I learned from you, it will be a great pleasure for me to work with you in the next years.

Thank you to Paul Bradley, Joyce Guzik and Art. Cox for all what I learned from you during my research stay at the Los Alamos National Laboratory (USA).

Merci à vous mes amis: Pino, Patrick, Benoît ... avec qui j'ai pu partager lors de soirées bien sympatiques ma passion pour l'astrophysique et plein d'autres chose.

Merci à vous mes frères et soeurs: Gabriel, Juliette, Annabelle et Adèle. Je vous aime tellement, rameaux de la même branche, à la vie à la mort !

Contents

Summary

Asteroseismology is a new domain of astrophysics whose the goal is to improve our knowledge of stellar interiors by studying very precisely their oscillations or pulsations. In the frame of our thesis, we have implemented a precise computation tool for asteroseismology: a code which computes the non-radial non-adiabatic oscillations of stars. This code takes as data a stellar model at equilibrium computed by the new Code Liégeois d'Évolution Stellaire (CLÉS), and determines precisely the oscillation modes of this model around its equilibrium: oscillation frequencies, growth rates, phase-lags, ... The main characteristics of our code are the followings:

1. It is able to study the *radial* as well as the *non-radial* oscillations of stars.
2. The transfers of heat occuring during the thermodynamical pulsation cycles are taken into account in a full consistent way. In the usual terminology of thermodynamics, such cycles are called *non-adiabatic* by opposition to *adiabatic* cycles without heat exchanges.
3. In our code, special care is given to the treatment of the oscillations in the superficial layers of the star and in its atmosphere (see Section 2.3).

The main advantages of a non-adiabatic pulsation code, in comparison with an adiabatic code, are the followings. On one hand, only a non-adiabatic code permits to describe in a consistent way the damping or driving mechanisms at the origin of the stability or instability of a star. On the other hand, the oscillations of a star are always totally non-adiabatic in the superficial layers and, in particular, in the visible part of a star. Therefore, the pulsation observables linked directly to the photosphere such as the photometric amplitudes and the phase-lags can be reliably compared to the theoretical predictions, only by using a non-adiabatic code.

The numerical method we have adopted in order to solve the problem is a finite differences method, together with a generalized inverse iteration algorithm. Moreover, our discrete scheme of equations is such that it is intrinsically compatible with the integral expressions for the pulsation frequencies, which makes it very stable and precise from a numerical point of view.

Finally, we have applied our non-adiabatic code to the study of 4 types of near main sequence variable stars: the β Cephei, the Slowly Pulsating B (SPB), the δ Scuti and

the γ Doradus stars. We recall that the main sequence corresponds to stars in the phase of core Hydrogen burning.

The application of our non-adiabatic code to the study of β Cephei stars shows very precisely the mechanism at the origin of their instability. It is a κ-mechanism associated to the opacity bump in the partial ionization zone of Iron. Moreover, in collaboration with the Katholieke Universiteit of Leuven (Dupret et al. 2002, De Ridder et al. 2002), we have shown that the influence of surface temperature variations on the line-profile variations of Si^{2+} (456.784 nm) is very small compared to the influence of the velocity field (Doppler effect) for a typical β Cephei model. Finally, we have applied our non-adiabatic code to the study of the photometric variations (Johnson filters) of the star 16 Lacertae. In the frame of this study, we were able to identify the degree ℓ of the 3 pulsation frequencies. Moreover, by searching for the model giving the best fit between theory and observations, we showed that the metallicity of this star ($Z \simeq 0.015$) is slightly smaller than the solar metallicity (Dupret et al. 2003a).

Concerning the Slowly Pulsating B stars, our study shows precisely the mechanism at the origin of their instability. As for the β Cephei stars, it is a κ-mechanism associated to the opacity bump in the partial ionization zone of Iron. Secondly, we showed in collaboration with Leuven that the influence of surface temperature variations on the line-profile variations of Si^{+} (412.8054 nm) is very small compared to the influence of the velocity field for a typical SPB model. Finally, we have applied our non-adiabatic code to the study of the photometric variations (Geneva filters) of 11 SPBs observed by Dr. De Cat (2001), and we could identify the degree ℓ of their dominant modes.

Concerning the δ Scuti stars, our study shows firstly the driving mechanism of these stars, which is associated to the opacity bump in the second partial ionization zone of Helium. On the other hand, we have applied our non-adiabatic code to the study of the photometric variations (Strömgren filters) of δ Scuti stars. Our results (amplitude ratios and phase-lags) are very sensitive to the characteristics of the very thin convective zone situated in the partial ionization zone of Hydrogen; precise informations on the characteristics of this zone can thus be obtained by confronting the theoretical predictions to the observations.

And finally, we have studied the γ Doradus stars. On one hand we showed that, under the frozen convection approximation, the excitation of these stars can be explained by a blocking of the flux at the base of the thin convective envelope. However, this mechanism is not unanimously accepted by the scientific community. On the other hand, we have shown that the photometric amplitudes and phase-lags predicted by our non-adiabatic code are extremely sensitive to the characteristics of the convective envelope. However, in all the cases, these theoretical predictions were not in agreement with observations. We can thus conclude that the variability of the γ Doradus stars remains a mystery for the theoreticians.

Introduction

Simple introduction

The study of variable stars has been since a very long time one of the key of our understanding of the universe. The reason is that they give direct informations on intrinsic characteristics of the stars. And precisely, the main challenge in astrophysics is to get information about the intrinsic characteristics of these things so far away that we observe. This is really a difficult challenge, since the time when we will travel from stars to stars in order to see *in situ* what they really are does not seem to be close ...

Why and how the variable stars give such intrinsic informations about themselves ? Let's consider the case of a periodic variable star, and admit that the observed frequencies are due to its vibrations (like the sound of a music instrument). On one hand theses frequencies are not affected by the distance between the observer and the star (if we neglect the relativistic effects, which is perfectly admissible in the local universe). On the other hand, these frequencies give direct information about the star itself (similarly to the sound of a music instrument which gives direct information about the instrument itself). Therefore, by determining with high precision these frequencies, we can get direct information about the stars themselves. A great progress in our understanding of our universe was for example the determination of the distance scales. This progress came precisely from the study of variable stars called the "Cepheids". Astrophysicists of the beginning of this century were able to relate the periods of these stars to their absolute luminosity and by comparing it to the quantity of light received on earth, they were able to determine their distance, which was (and remains) one of the bases of our determination of the distances in the universe.

Closer to the present times and thanks to future space missions (COROT, MOST, Eddington) that will be launched in the following years, we will be able to observe the stellar oscillations (or vibrations) with an extremely high precision. And since these oscillations are directly linked to the internal characteristics of stars, we will be able to improve significantly our knowledge of stellar interiors. I recall that stars are opaque so that all what we see of them is their surface (called the stellar atmosphere). This procedure is called *asteroseismology* in the case of stars and *helioseismology* for our Sun, because of its similarity with the "classical" seismology where the earth's seismic waves (due to earthquakes) are studied in order to improve our knowledge of the earth's interior. For our Sun, helioseismology was really a great success. Thanks to the observations from space with SOHO and from the ground with GONG, BiSON, IRIS, ... astrophysicists were able to determine with very high precision the periods (around 5 minutes) of the extremely numerous oscillation modes of our Sun, and therefore they were able to determine very precisely its physical characteristics, from its center to its surface, typically: the sound speed, the density, the rotational velocity (solar rotation is not rigid), the chemical mixing processes, the exact depth of the envelope convection zone, ...

The present study is exactly situated in this field. We have developed during our thesis a computer program able to compute the oscillations of stars. Taking as data an equilibrium stellar model, this program is able to determine very precisely, how the star will oscillate around its equilibrium. The particularities of our program are as follows:

1. Our program is able to study the *radial* oscillations (periodical spherical symmetrical expansions and contractions of the star) as well as the *non-radial* oscillations (more complex oscillations without spherical symmetry, where the periodical movements of the matter, the variations of the radiative flux, ... depend on the 3 spatial coordinates inside the star).
2. Our program takes the periodical transfers of heat into account in the simulation of the oscillations. In the thermodynamics terminology, these processes are called *non-adiabatic* by opposition to adiabatic processes without heat transfers.
3. A special care is given to the simulation of the oscillations in the very superficial layers of the stars (a region called the atmosphere).

Our program is very useful for improving the knowledge of stellar interiors and atmospheres. More precisely, its theoretical predictions (pulsation frequencies, excitation mechanisms, photometric amplitudes and phase-lags, ...) can directly be confronted with the observations. By adjusting the stellar parameters (mass, chemical composition and mixing processes, convection parameters, age, ... of the stellar model), we can then determine the model giving the best agreement between theory and observations.

In Figure 1, we give an illustration of the well known Hertzsprung-Russel (HR) diagram. All the stars can be situated in this diagram. The abscissa corresponds to the logarithm of the effective temperature (see the definition in Section 1.3.2, Eq. (1.16)), which is directly linked to the colour of the star (the left part of the diagram corresponds to hot blue stars and the right part to cold red stars); and the ordinate corresponds to the logarithm of the absolute luminosity of the star (quantity of light emitted by the star) in units of solar luminosity. In Figure 1, we give the position of different classes of pulsating variable stars in the HR diagram. As a quick recall about stellar evolution, during the longest part of their life, the stars are burning hydrogen in their core and transform it into helium. The position of these stars in the HR diagram has the remarkable property of being situated along a line called the *main sequence* going from the top left (high masses) to the bottom right (low masses) of this diagram (dashed line in Figure 1).

All the stars that we will study in the present work are close to the main sequence and thus in, or close to, the phase of core hydrogen burning. They are also of population I, which corresponds to the second generation of metal rich stars situated in the disk of our galaxy, by opposition to the population II stars, which are the very old first generation of metal poor stars situated in the halo of our galaxy and in the globular clusters gravitating around the galaxy. More precisely, the different kinds of stars that we will study are:

1. **The β Cephei stars** (β Cep). These are massive blue stars with masses from 7 $M_\odot$ to 20 $M_\odot$ ($M_\odot$ is the mass of our Sun) and typical pulsation periods from 3 to 8 hours, corresponding to low order p-modes (as defined in Section 1.10). They are situated in the upper left part of the HR diagram (see Figure 1). Our study of these stars is presented in Section 4.1.
2. **The Slowly Pulsating B stars** (SPB). These are blue stars (colder and less luminous than the β Cephei), with masses from 3 $M_\odot$ to 8 $M_\odot$ and with long pulsation periods from 1 to 4 days, corresponding to high order g-modes (as defined in Section 1.10). This a new class of pulsating stars discovered 10 years ago by astronomers of Leuven (Waelkens 1991). Our study of these stars is presented in Section 4.2.
3. **The δ Scuti stars** (δ Sct). These are colder stars situated at the intersection between the "classical" instability strip and the main sequence, with masses from 1.5 $M_\odot$ to 2.5 $M_\odot$ and typical pulsation periods from 0.5 to 6 hours. Some δ Scuti stars are highly multi-periodic. Our study of these stars is presented in Section 4.3.
4. **The γ Doradus stars** (γ Dor). This is a new class of pulsating stars very recently discovered. They are a little colder than the δ Scuti stars and have long periods from 8 hours to 3 days. They remain a mystery for the astrophysicists. Our study of these stars is presented in Section 4.4.

Besides the above stars, other well known classes of pulsating stars can be seen in Figure 1: the classical Cepheids (Ceph) situated in the "classical" instability strip (see above their use for the determination of the distances), the Mira stars which are red giants called from their prototype Mira (the Wonderfull) discovered as a variable star in 1596, ...

Asteroseismology

The goal of asteroseismology is to measure with very high precisions the periodical variations of pulsating stars and to use these informations in order to improve our knowledge of stellar interiors. Asteroseismology is thus a tool to test stellar evolution theory and in particular the basics of stellar hydrodynamics. Its name comes from

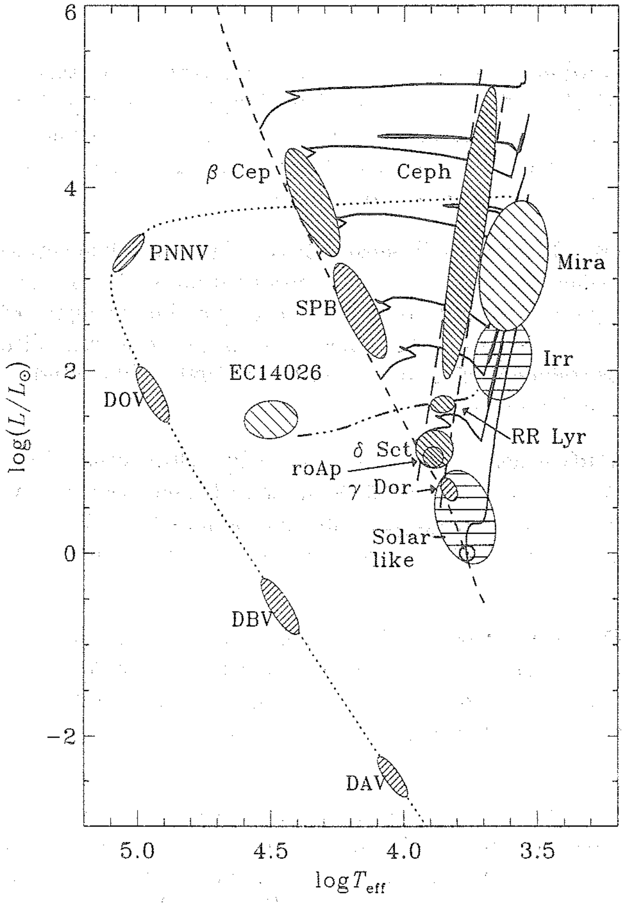

Figure 1: A Hertzsprung-Russell diagram showing the zero-age main sequence (dashed) and the position of several classes of pulsating stars. The continuous curves are evolution tracks for stars with masses 1,2,3,4,7,12 and 20 $M_{\odot}$. Figure taken from Christensen-Dalsgaard & Dziembowski (1998).

its similitude with the "classical" seismology whose the goal is to study the seismic waves (due to earthquakes) in order to improve our knowledge of the Earth's interior. More precisely, the study of stellar pulsations offers an unique opportunity to probe the stellar interiors, because the pulsation frequencies of a star are directly linked to its internal characteristics (IAU Colloquium 185, *Radial and nonradial pulsations as probes of stellar physics*, 2001, Leuven; Porto Conference, *Asteroseismology Across the HR Diagram*, 2002, Porto). This procedure has already been applied with a great success for the Sun by helioseismology (*SOHO 10/GONG 2000 Workshop, Helio- and Asteroseismology at the Dawn of the Millenium*, Tenerife, Spain), permitting to determine with high precision the differential rotation, the sound speed and the density from the center to the surface of the Sun, the position and the characteristics of the frontier between the radiative and the convective zone (the tachocline), the influence of the magnetism, the mixing and diffusion processes, ... In close future, we expect to be able to fulfil the goals of asteroseismology with a success comparable to the one obtained for the Sun, for the following reasons.

On one hand, precise periods for different kinds of multiperiodically pulsating stars have been recently detected from the ground, on the base of photometric data, for example for δ Scuti stars (e.g. Breger et al. 1998, 1999, 2002), or on the base of spectroscopic data, for example for the solar-like oscillations of α Centauri A (Bouchy & Carrier 2001, 2002). The observation and analysis of line-profile variations for variable stars is also in great development. In those observations, a precise trace of non-radial oscillations is now clearly admitted.

On the other hand, space missions dedicated to asteroseismology will be launched in the following years, which will give observational data of extremely high precision to the astrophysicists. The great advantages of these space missions compared to ground based observations are as follows.

1. The oscillations in stars similar the Sun produce very small fluctuations in brightness. The Earth's atmosphere interferes with light, a phenomenon called *scintillation*. This source of variations can easily drown out the signal that we are looking for. From space, there is no longer atmosphere between the instruments and the stars, which gives observations of incomparably better quality.

2. Another problem from the ground is of course that we can only observe the night, when the weather is good ... This is a great handicap when we want to study stellar oscillations, particularly for stars with pulsation periods of the order of 1 day. From space on the contrary, it is possible to observe during very long runs and without interruption, leading to a very low noise level compared to the signal (see below the specifications of the COROT space mission).

These two advantages are so significant that even with a very small 30 cm space telescope, one can do easily what is almost impossible with a 8 meter telescope on Earth. These different future space missions are, in order of launch:

- MOST (Microvariability and Oscillations in STars). MOST, sometimes called the "humble space telescope" is a Canadian space mission. With a collecting mirror only 15 cm across and a total size of 65 × 65 × 30 cm, MOST is a very small space telescope. However, it will be able to observe stellar oscillations with much better precision than from the ground. The three main goals of MOST are the detection and characterisation of

  1. the oscillations of solar-like stars, including very old stars (metal-poor subdwarfs) and magnetic stars (roAp), in order to probe their structures;
  2. the reflected light from giant exoplanets closely orbiting solar-like stars;
  3. the turbulent variations in massive evolved (Wolf-Rayet) stars.

  The launch of MOST is expected for April 2003 with a life time estimated to 3 years.

- COROT (COnvection ROtation and planetary Transits). COROT is a french-european space mission. With a 27 cm telescope and 4 CCDs separated in 2 fields of view: the SISMO field and the EXO field, COROT will be able to fulfil at the same time its two main goals:

  1. In the SISMO field, the detection and study of stellar oscillations with very high precision. For the central program, at least 5 runs of observations of 150 days with a duty cycle of 80 % are planned during which one bright star (the main target) and several fainter ones in the surrounding field of view will be followed. COROT will be able to observe stellar oscillations with a noise level down to 2.5 ppm for A anf F type stars (δ Scuti) and 0.6 ppm for G type stars (solar-like). With these specifications, the observations of COROT will be incomparably more precise than all what is possible from the ground.
  2. In the EXO field, the search for extrasolar planets and in particular telluric ones. Because of its very high precision photometry, COROT will be able to detect the small occultation due to the transit of planets before the observed stars, which will allows to precisely determine their orbital periods and sizes.

  COROT will be launched in 2005 and is expected to be operative for at least 2.5 years

- And last but not least Eddington. Eddington is a very recently accepted space mission of ESA. Its project is globally the same as the previous missions, but much more ambitious. The satellite will travel beyond the Moon to the second Lagrangian point, where it will perform its five-years mission. During the first two years, it will measure the oscillations of approximately 50 000 stars, with such a high precision that it could perform for the first time a seismic study of solar-like stars in open clusters. During the next three years, Eddington will be looking at one single star-rich field, searching for planetary transits in a survey of approximately 500 000 stars, with a precision permitting to detect planets down to the size of Mars (i.e. about one-third the size of the Earth !).

Non-adiabatic oscillations

In order to fulfil the goal of asteroseismology, a precise confrontation between theory and observation has to be performed. The works presented in this thesis concern the theoretical part of this aim. More precisely, we have written a linear non-radial non-adiabatic code and applied it to the study of different kinds of pulsating stars. This code takes as data a stellar model at thermal and hydrostatic equilibrium and determines precisely the characteristics of the proper modes of oscillation with respect to the equilibrium configuration. "Non-adiabatic" means that, in our modelling, the periodic transfers of heat due to the pulsation are taken into account in a full consistent way. The main advantages of a non-adiabatic code, compared to an adiabatic code, are as follows:

1. It is able to determine accurately the stability or instability of the different modes of a stellar model. Our code computes in a consistent way the growth rates of the different modes (positive for the unstable modes and negative for the stable modes). Moreover, it is able to localize precisely in the star the regions which have a driving effect on the oscillations and the regions which have a damping effect, which is very useful for the analysis of the mechanisms at the origin of the instability of pulsating stars.
2. It computes very precisely the amplitudes of variation (for a given normalization since we work in the linear approximation) and the phases of the different physical quantities (temperature, pressure, luminosity, displacement field, ...), from the center to the surface of the star. In particular, our code computes the amplitudes (for a given normalization) and phases of the local effective temperature variations at the photosphere. On one hand, from a spectroscopic point of view, this permits to determine the influence of temperature variations on line profile variations. On the other hand, from a photometric point of view, this permits to determine the theoretical photometric amplitude ratios and phase-lags and, by confronting them to the observations, to identify the modes and constrain the models. We emphasize that the oscillations are always highly non-adiabatic in the superficial layers, so that the adiabatic approximation is totally inappropriate for the determination of the amplitudes and phase-lags at the photosphere.

The main specificity of our non-adiabatic code, compared to the one of other authors (Dziembowski 1977a, Pesnell 1990), is that it includes a detailed treatment of the pulsation in the outer atmosphere (see Section 2.3 and Dupret et al. 2002).

By confronting the theoretical predictions of our non-adiabatic code obtained for differents models and for different modes of oscillation to the observations, it is possible to determine the modes and models which best fit the observations and by the way to improve our knowledge of stellar interiors and our understanding of stellar pulsations. In this sence, our code is a direct tool for asteroseismology.

Mode identification

In a non-radially pulsating star, and when the pulsation-rotation interaction is small, the dependence with respect to the spherical coordinates θ and ϕ of the amplitudes of variation of the different physical quantities are, for a given mode, represented by a spherical harmonic $Y_\ell^m(\theta,\phi)$. We denote here by mode identification, the problem of determining from the observations the spherical degree ℓ and the azimuthal order m of the different pulsation modes. This is a crucial problem in Asteroseismology for the following reasons. Firstly, from a theoretical point of view, despite the linear non-adiabatic predictions, the mode selection mechanisms are not well understood for many kinds of pulsating stars (δ Scuti, β Cephei, Slowly Pulsating B stars, γ Doradus, roAp stars, ...). Secondly, from an observational point of view, the mode identification is far from trivial, simply because we do not resolve the disks of stars (except for the Sun or by interferometry). Thirdly, the rotational splittings and the "avoided crossing" effect produce such a mess in the power spectrum that a mode identification based on the pulsation frequencies alone is generally impossible (except for solar-like oscillations in the asymptotic regime). At the present, two kinds of mode identification methods have been developed. These two methods are based on photospheric observables, where the pulsation is totally non-adiabatic, so that our non-adiabatic code is very useful in this frame.

Line-profile variations

The first kind of methods is based on the study of line-profile variations (see e.g. Aerts 1996, Telting & Schrijvers 1997, Townsend 1997). The principle is to make spectroscopic observations of the line-profile variations of one or several spectral lines of a pulsating star and compare them to the theoretical predictions. These line-profile variations come mainly from the velocity field associated to the pulsation. At a given time, some parts of the disk are going towards the observer and the Doppler effect implies a blue shift of the line and at the same time, other parts of the disk are going outwards from the observer with a red shift of the line, and the total resultant is a line-profile variation. Since the (θ, ϕ) dependence of the velocity field is given by the spherical harmonics $Y_\ell^m(\theta,\phi)$, the confrontation between theory and observations permits to determine ℓ and m. A part of the work presented in this thesis is to study the influence of non-adiabatic temperature variations on line-profile variations of β Cephei and Slowly Pulsating B stars (SPBs). This work has been done in collaboration with Dr. De Ridder and Prof. Aerts of the Katholieke Universiteit Leuven.

Multi-colour photometry and non-adiabatic asteroseismology

The second kind of methods is based on multi-colour photometry. The principle is to observe the photometric variations due to stellar oscillations in different colour filters and compare them to the theoretical predictions (Dziembowski 1977b, Stamford &

Watson 1981, Watson 1988, Garrido et al. 1990, Garrido 2000). The theoretical amplitude ratios and phase differences between different filters depend explicitly on the degree ℓ (but not on the azimuthal order m), so that ℓ can be determined by searching for the best fit with the observations. In these methods, the theoretical predictions are very sensitive to the non-adiabatic temperature variations at the photosphere so that, by using our non-adiabatic code, their discriminant power is significantly improved. The non-adiabatic predictions (amplitudes and phases) are very sensitive to some dominant parameters of the theoretical models. Therefore, once the modes are identified, we can search by an iterative process for the model which best fits the observations; we call this method *non-adiabatic asteroseismology.* On one hand, with this method, we can derive strong constraints on the metallicity of β Cephei and SPB stars, as will be shown in Section 4.1.6 for the β Cephei star 16 Lacertae. On the other hand, the characteristics of the thin superficial convection zone can be constrained for δ Scuti and γ Doradus stars.

Chapter 1

Some theoretical aspects of stellar pulsations

The goal of this chapter is to give an overview of the theoretical background at the basis of the works presented in this thesis. As a simple introduction to the physics inside the stars, we present in Section 1.1 the typical time scales associated to them. In Section 1.2, we present the general equations of hydrodynamic with the usual hypotheses made for stars (ideal fluid, Newton theory of gravitation, magnetic field neglected, ...). In Section 1.3, we give the main differential equations of equilibrium spherically symmetric stellar models (rotation neglected). Next, in Section 1.4, we introduce the method of small perturbations and the linear approximation, widely used to model stellar oscillations of small amplitudes. This method is used in Section 1.5 to derive the general equations of linear non-radial non-adiabatic stellar oscillations. In Section 1.5.2, it is explained how this system of equations can be separated, each general solution being decomposed as an infinite linear combination of propre modes of oscillation proportional to spherical harmonics. The perturbed equations of state used to close the problem are presented in Section 1.6. An overview of the usual boundary conditions is presented in Section 1.7. We note however that some of these boundary conditions are very approximate and significant improvements are proposed by us in chapter 2. In Section 1.8, we derive the integral expressions for the eigenvalues. These integral expressions are very important in asteroseismology: they are at the basis of the inversion methods and of the interpretation of the exciting and damping mechanisms in pulsating stars. In Section 1.9, some widely adopted approximations are presented: the adiabatic approximation, the quasi-adiabatic approximation and the Cowling approximation. And finally, the well known two kinds of pulsation modes: the pressure modes (p-modes) and the gravity modes (g-modes) are presented in Section 1.10.

1.1 Time scales

The physical phenomena affecting stars happen at very different time scales. Examining and comparing them is a good introduction for understanding the physics inside stars and the main approximations adequate to model them.

The dynamical time of a star is the time scale associated to the dynamical phenomena happening inside it. It is of the order of the star's free fall time and is defined by:

$$\tau_{\mathrm{dyn}} = \sqrt{\frac{R^3}{GM}} \approx \frac{1}{\sqrt{G\,\overline{\rho}}} \tag{1.1}$$

where R, M and $\overline{\rho}$ are the radius, the mass and the mean density of the star and G is the constant of gravitation. Stellar pulsation is a typical dynamical phenomenon. For the simple case of the fundamental radial mode of oscillation, the stellar gas periodically expands and compress itself with a period of the order of the dynamical time. Being directly linked to the mean density (Eq. (1.1)), the dynamical time takes very different values for different kinds of stars. For example, $\tau_{\mathrm{dyn}} \simeq 0.12$ ms for a neutron star, $\tau_{\mathrm{dyn}} \simeq 3.9$ s for a white dwarf, $\tau_{\mathrm{dyn}} = 54$ min for the Sun and $\tau_{\mathrm{dyn}} \simeq 3.9$ years for a red super giant. Because of this wide range of times, the constant of pulsation Q in days has been introduced. For a pulsating star with period P, Q is defined as:

$$Q = P\,\frac{\tau_{\mathrm{dyn},\odot}}{\tau_{\mathrm{dyn}}} = P\,\sqrt{\frac{\overline{\rho}}{\overline{\rho}_{\odot}}} = P\,\sqrt{\frac{M}{M_{\odot}}\left(\frac{R_{\odot}}{R}\right)^{3}}\,, \tag{1.2}$$

where the subscript $\odot$ denotes solar values. The advantage of Q is that it is approximately the same for the fundamental radial mode of different kinds of pulsating stars. For example, $Q \simeq 0.033$ days and $Q \simeq 0.034$ days for the fundamental radial modes of δ Scuti and β Cephei stars, respectively.

The Kelvin-Helmoltz time and the thermal relaxation time are time scales associated to the transfer of energy throughout the star.

The Kelvin-Helmoltz time is defined as:

$$\tau_{\mathrm{HK}} = \frac{GM^2}{LR}, \tag{1.3}$$

where L is the luminosity of the star. It is of the order of the global cooling time of the star if the nuclear energy source was cut off. For the Sun, $\tau_{\mathrm{HK}} \simeq 3.1 \times 10^7$ years.

The thermal relaxation time is a time scale defined at each layer of the star:

$$\tau_{\mathrm{th},i} = \int_{\Delta m_i} T\,c_v\,\mathrm{d}m \;/\; L\,, \tag{1.4}$$

where Δm_i is the mass between the layer i and the surface of the star, T is the temperature and c_v is the specific heat at constant volume. It is also of the order of the stellar cooling time, but as function of the depth. We note that some authors (Unno et al. 1989, Pamyatnykh 1999) define it with c_p instead of c_v. In Figures 4.4, 4.23 and 4.41, we give at the bottom the logarithm of the thermal relaxation time (in seconds) as function of the logarithm of temperature, from the center (left) to the surface (right) of a β Cephei model, a Slowly Pulsating B model and a δ Scuti model. By comparison, the dynamical time of these stars is of the order of some hours. We see that in the internal layers, the thermal relaxation time is much larger than the dynamical time. But it is the contrary in the superficial layers. The region where these two times are of the same order is called the *transition region.* The impact of this large variation of $\tau_{\rm th}/\tau_{\rm dyn}$ on the physics of stellar pulsations is very important, as it will be discussed in detail in the following sections and chapters.

The nuclear time is associated to the nuclear reactions inside the star. During their life on the main sequence, stars are burning the hydrogen of their central regions. The nuclear time is defined as the time necessary for the star to burn 10 % of its hydrogen, with a given luminosity. The nuclear time of the Sun is of the order of 9.8×10^9 years. We see that the nuclear time is much larger than the dynamical time and the Kelvin-Helmoltz time.

1.2 General equations of hydrodynamic

Stars can be considered as continuous media and except extreme cases such as neutron stars, the classical Newton theory of gravitation is applying. There are two kinds of description of the hydrodynamic of a continuous medium: the Lagrangian description and the Eulerian description.

In the Lagrangian description, a continuous label $\vec{a}$ is assigned to each infinitesimal mass element of the medium, and the local physical characteristics are described as function of $\vec{a}$ and of the time t: the position $\vec{r}(\vec{a},t)$, the density $\rho(\vec{a},t)$, the temperature $T(\vec{a},t)$ ... In all this thesis, the partial derivative with respect to time of a quantity X in a Lagrangian description will be denoted by dX/dt. It is the time derivative of X, following the movement of a given mass element.

In the Eulerian description, the local physical characteristics are described as function of the position $\vec{r}$ and the time t: $\vec{v}(\vec{r},t)$, $\rho(\vec{r},t)$ ... The partial derivative with respect to time of a quantity X in an Eulerian description will be denoted by $\partial X/\partial t$. It is the time derivative of X, at a given fixed position in the space.

We give now the different equations of stellar hydrodynamic.

The equation of mass conservation reads:

$$\frac{d\rho}{dt} + \rho\nabla\cdot\vec{v} = \frac{\partial\rho}{\partial t} + \nabla\cdot(\rho\vec{v}) = 0\,, \tag{1.5}$$

where $\vec{v}$ and ρ are the local velocity and density.

In stellar pulsations, the Reynolds number is very high, so that the viscosity can be neglected. We neglect also the Lorentz force due to the magnetic field.

The equation of momentum conservation reads then:

$$\frac{d\vec{v}}{dt} = \frac{\partial\vec{v}}{\partial t} + \vec{v}\cdot\nabla\vec{v} = -\nabla\psi - \frac{\nabla P}{\rho}\,, \tag{1.6}$$

where P is the total pressure (gas pressure + radiative pressure + turbulent pressure) and ψ is the gravitational potential.

The Poisson equation reads:

$$\Delta\psi = 4\pi G\rho\,. \tag{1.7}$$

The equation of energy conservation reads:

$$T\frac{dS}{dt} = \epsilon - \frac{\nabla\cdot\vec{F}}{\rho}\,, \tag{1.8}$$

where T is the temperature, S is the entropy, ϵ is the rate of energy generation (mainly by nuclear reactions) and $\vec{F}$ is the flux of energy.

In stellar interiors, there are mainly two mecanisms of energy transfer: by radiation and by convection, so whe have $\vec{F} = \vec{F}_{\mathrm{R}} + \vec{F}_{\mathrm{C}}$, where $\vec{F}_{\mathrm{R}}$ is the radiative flux and $\vec{F}_{\mathrm{C}}$ is the convective flux. From the center of a star to the base of its atmosphere, the mean free path of a photon is very small and the the radiative transfer is described in very good approximation by

the diffusion equation:

$$\vec{F}_{\mathrm{R}} = -\frac{4\,a\,c\,T^3}{3\,\kappa\,\rho}\,\nabla T\,, \tag{1.9}$$

where κ is Rosseland mean opacity. We do not detail here the equations of transfer by convection. The treatment of the convection zones is one of the main source of uncertainties in the theory of stellar evolution and stellar pulsation. The mixing length theory is generally applied since it introduces a small number of unknown parameters. For the massive stars studied in the frame of this thesis, only central convection zones are present. In a central convection zone, the temperature gradient is given in very good approximation by the adiabatic gradient:

$$\frac{\mathrm{d}\ln T}{\mathrm{d}\ln P} = \left.\frac{\partial\ln T}{\partial\ln P}\right|_S\,. \tag{1.10}$$

Different algebraic equations have to be added to close the problem. The equations of state relate the different thermodynamic variables. Choosing ρ and T as independent variables,

the equations of state needed in the present study are:

$$P = P(\rho, T, \chi_i)\,, \quad S = S(\rho, T, \chi_i) \quad \text{and} \quad \kappa = \kappa(\rho, T, \chi_i)\,, \tag{1.11}$$

where χ_i represents the chemical composition.
Nuclear physics permits to determine $\epsilon(\rho, T, \chi_i)$.

Finally, different boundary conditions have to be imposed. For stars, boundaries conditions are imposed at the surface. The rigorous determination of these boundary conditions is far from trivial. The way to proceed is generally to split the stellar model into two parts:

The interior where the medium is optically thick and the diffusion approximation is valid. This part corresponds to the quasi-totality of the star in term of mass.

The atmosphere where the medium is optically thin and the diffusion approximation is not valid. This is the visible part of the star.

In stellar evolution codes, the equations are generally solved in the interior model alone and the surface boundary conditions impose a good linking with precomputed atmosphere models.

Besides the surface boundary conditions, central boundary conditions have to be imposed in order to have regularity of the different physical quantities at the center.

1.3 Equilibrium models

1.3.1 Interior

During the main part of its life, the characteristic time of stellar evolution is the nuclear time. We have seen in Section 1.1 that the nuclear time of a star is much larger than its dynamical time and its Kelvin-Helmoltz time. Therefore, *in the study of stellar evolution*, it can be assumed in a very good approximation that, at each given time, it is in hydrostatic equilibrium. And, except at some specific evolution stages during which the gravitational contraction is significant, it can be assumed in good approximation that, at each time, it is in energy balance. For slowly rotating stars (like the Sun), the influence of rotation on the equilibrium models is very small; therefore it can be assumed that these models have a *spherical symmetry* and the centrifugal and Coriolis forces are neglected. Under these hypotheses the equations are much simplified.

The equation of hydrostatic equilibrium:

$$\frac{dP}{dr} = -\frac{Gm\rho}{r^2} . \tag{1.12}$$

The mass of a shell:

$$\frac{dm}{dr} = 4\pi r^2 \rho . \tag{1.13}$$

The equation of energy conservation:

$$\frac{dL}{dr} = 4\pi r^2 \rho\epsilon . \tag{1.14}$$

The diffusion equation (in a radiative zone):

$$\frac{dT}{dr} = -\frac{3\kappa\rho L_{\rm R}}{16\pi r^2 acT^3} . \tag{1.15}$$

The central boundary conditions are simply $L(0) = 0$ and $m(0) = 0$, and the surface boundary conditions come from adequate linking with atmosphere models. In all what follows, we call an *equilibrium model* or an *equilibrium configuration*, a model which is solution of these equations in the interior of the star.

1.3.2 Atmosphere

The particularity of our treatment is that our equilibrium models include the stellar atmosphere also. More precisely, the domain of integration is $[0, R_s]$ where 0 corresponds to the center and R_s is the radius of the last layer of the stellar model. We emphasize that R_s is not what is usually denoted as the radius R of the star. The usual definition of the stellar radius R is the radius of the layer where $L = 4\pi\, R^2\, \sigma\, T^4$ (L is the total luminosity of the star and T is the local temperature at this layer). This layer is called the **photosphere**, and the value of the temperature at this specific layer is called the **effective temperature** (T_{eff}), so that:

$$L = 4\pi\, R^2\, \sigma\, {T_{\text{eff}}}^4\,. \tag{1.16}$$

From the Stefan's law, we see that the effective temperature is the temperature of a spherical black body having the same radius R and luminosity L as the star. In good approximation, the medium is optically thick beneath the photosphere and optically thin above it, so that the radius R is in very good approximation the visual radius of the star. The problem is that stars have not one intrinsic surface boundary. There is not a "last layer" after which the density is exactly zero, but at the outermost layers of the atmosphere, a wind is appearing progressively. The models used in our computations include the atmosphere up to very small optical depths, so that the last layer is at a distance R_s from the center larger than R.

We note that in the atmosphere, the diffusion equation is no longer valid, and the rigorous way to proceed is to solve the radiative transfer equation which depends on the wavelength. Some approximations are frequently made in the computation of atmosphere models:

1. **The hypothesis of Local Thermodynamic Equilibrium (LTE).** It is assumed that the collision processes still dominate the state of the material, which can be calculated from the equations of statistical mechanics evaluated at local values of the temperature and density: Maxwellian velocity distribution, Source function given by the Planck law ($S_\nu = B_\nu(T)$), equilibrium between ionization stages given by the Saha-Boltzmann formula …).
2. **The plane parallel approximation.** For most of the stars such as near main sequence stars, the thickness of the atmosphere is very small compared to the radius of the star. In the plane parallel approximation, the atmosphere is approximated as a stratification of parallel planes and the radiative flux and the gravity are assumed to be constant and perpendicular to the planes.

For more details about the computation and the study of stellar atmospheres, we propose the following references (Kurucz 1970, Mihalas 1978, Gray 1992, Mihalas & Weibel-Mihalas 1999).

1.4 The method of small perturbations

In a pulsating star, the positions and the physical characteristics (density, temperature ...) of each mass elements are periodically varying with time scales "of the order" of the dynamical time (Eq. 1.1). Therefore, at each given time, the star is not at equilibrium and most of the equations presented in Section 1.3 are not valid. In fact, the star is oscillating around its equilibrium configuration. Formally, there are two ways for describing this oscillation: by use of Lagrangian perturbations and/or by use of Eulerian perturbations. Let's X be a given physical quantity, X_0 its equilibrium value, $\vec{a}$ a label associated to a given mass element and $\vec{r}$ a given position in the space.

The Lagrangian perturbation of X is defined by:

$$\delta X(\vec{a},t) \equiv X(\vec{a},t) - X_0(\vec{a})\,. \tag{1.17}$$

It represents the variation of X, following the movement of the mass element labeled by $\vec{a}$. In all our study, we are going to use the notation ' δ ' for the Lagrangian perturbation.

The Eulerian perturbation of X is defined by:

$$X'(\vec{r},t) \equiv X(\vec{r},t) - X_0(\vec{r})\,. \tag{1.18}$$

It represents the variation of X, at a given fixed position $\vec{r}$ in the space. In all our study, we are going to use the notation ' $'$ ' for the Eulerian perturbation.

In most of the cases, the amplitudes of variation of each physical quantities are small compared to their equilibrium values, and Taylor developments limited to the first order around the equilibrium configuration can be made in good approximation. This is the linear approximation.

The linear approximation consists in neglecting, in all the equations modelling the oscillation, the second order terms and the higher order terms in the perturbed variables. In the linear approximation, the Lagrangian perturbation and the Eulerian perturbation of a scalar X are related by the following law:

$$\delta X = X' + \nabla X_0 \cdot \overrightarrow{\delta r}\,. \tag{1.19}$$

Throughout all the study presented here we are going to work in the linear approximation.

"Perturbing" an equation means taking the Lagrangian or Eulerian perturbation of both sides of an equation. In order to simplify the notations, we will omit the subscript 0 for equilibrium quantities in what follows.

1.5 Equations of linear non-radial non-adiabatic oscillations

1.5.1 General linear equations

Under the linear approximation, the equations presented in sect. 1.2 are simplified.

Perturbing Eq. (1.5) and integrating with respect to time gives the linear equation of mass conservation:

$$\rho' + \nabla \cdot (\rho\, \overrightarrow{\delta r}\,) = \delta\rho + \rho \nabla \cdot \overrightarrow{\delta r} = 0\,. \tag{1.20}$$

In this study, we neglect the influence of rotation on the equilibrium model and on the oscillations, more precisely the centrifugal force and the Coriolis forces are neglected and the equilibrium value of the velocity is assumed to be zero. Under these hypotheses, perturbing Eq. (1.6) gives the linear equation of momentum conservation:

$$\frac{\partial^2 \overrightarrow{\delta r}}{\partial t^2} = -\nabla\psi' + \frac{\rho'}{\rho^2}\nabla P - \frac{\nabla P'}{\rho}\,. \tag{1.21}$$

Perturbing Eq. (1.7) gives the linear perturbed Poisson equation:

$$\Delta\psi' = 4\pi G\rho'\,. \tag{1.22}$$

Perturbing Eq. (1.8) gives the linear equation of energy conservation:

$$T\,\frac{d\,\delta S}{dt} = T\left(\frac{\partial S'}{\partial t} + \vec{v}\cdot\nabla S\right) = \epsilon' + \frac{\rho'}{\rho^2}\nabla\cdot\vec{F} - \frac{\nabla\cdot\vec{F}'}{\rho}\,. \tag{1.23}$$

And finally, perturbing Eq. (1.9) gives the perturbed diffusion equation:

$$\vec{F}_{\mathrm{R}}' = \left(3\,\frac{T'}{T} - \frac{\kappa'}{\kappa} - \frac{\rho'}{\rho}\right)\vec{F}_{\mathrm{R}} - \frac{4\,a\,c\,T^3}{3\,\kappa\,\rho}\,\nabla T'\,. \tag{1.24}$$

All the partial differential equations we have obtained are linear with coefficients independent of the time. A solution of these equations can be expressed as an infinite linear combination of solutions with a time dependence of the form $\exp(i\,\sigma_k t)$:

$$\vec{X}(\vec{r},t) = \Re\left\{\sum_{k=0}^{+\infty} A_k\,\vec{X}_k(\vec{r})\,e^{i\,\sigma_k t}\right\}\,, \tag{1.25}$$

where A_k, $\vec{X}_k(\vec{r})$ and σ_k are complex and $\Re\{Y\}$ denotes the real part of Y.

For a given solution with a time dependance proportional to $\exp(i\,\sigma\,t)$, the equations of momentum and energy conservation are simplified.
The equation of momentum conservation (Eq. (1.21)) becomes:

$$\sigma^2\overrightarrow{\delta r} = \nabla\psi' - \frac{\rho'}{\rho^2}\nabla P + \frac{\nabla P'}{\rho}\,. \tag{1.26}$$

And the equation of energy conservation (Eq. (1.23)) becomes:

$$i\,\sigma\,T\,\delta S = \epsilon' + \frac{\rho'}{\rho^2}\nabla\cdot\overrightarrow{F} - \frac{\nabla\cdot\overrightarrow{F}'}{\rho}\,. \tag{1.27}$$

Together with boundary conditions that we are going to detail later, the system of equations has now the form of an eigenvalue problem whose the different perturbed quantitities are the eigenfunctions and σ is the eigenvalue (both are complex).

We are going now to do some manipulations of the equations which simplify the problem even more. We work in a spherical coordinate system (r,θ,ϕ) with a canonical orthogonal base $(\overrightarrow{e_r},\overrightarrow{e_\theta},\overrightarrow{e_\phi})$ defined at each point. We use the following notation for the coordinates of the displacement vector $\overrightarrow{\delta r}$:

$$\overrightarrow{\delta r} = \xi_r\,\overrightarrow{e_r} + \xi_\theta\,\overrightarrow{e_\theta} + \xi_\phi\,\overrightarrow{e_\phi}\,, \tag{1.28}$$

$\nabla_h\cdot\overrightarrow{V}$ is the angular part of the divergence of $\overrightarrow{V}$:

$$\nabla_h\cdot\overrightarrow{V} = \frac{1}{r\sin\theta}\frac{\partial}{\partial\theta}(\sin\theta\,V_\theta) + \frac{1}{r\sin\theta}\frac{\partial V_\phi}{\partial\phi}\,, \tag{1.29}$$

and $\mathcal{L}^2$ is the Legendre operator:

$$\mathcal{L}^2 = -\frac{1}{\sin\theta}\frac{\partial}{\partial\theta}\left(\sin\theta\frac{\partial}{\partial\theta}\right) - \frac{1}{\sin^2\theta}\frac{\partial^2}{\partial\phi^2}\,. \tag{1.30}$$

Since the equilibrium configuration has a spherical symmetry, the 3 components of the equation of momentum conservation are, from Eq. (1.26):

$$\sigma^2\,\xi_r = \frac{\partial\psi'}{\partial r} + \frac{\rho'}{\rho}\frac{Gm}{r^2} + \frac{1}{\rho}\frac{\partial P'}{\partial r}\,, \tag{1.31}$$

$$\sigma^2\,\xi_\theta = \frac{1}{r}\frac{\partial}{\partial\theta}\left(\psi' + \frac{P'}{\rho}\right)\,, \tag{1.32}$$

$$\sigma^2\,\xi_\phi = \frac{1}{r\sin\theta}\frac{\partial}{\partial\phi}\left(\psi' + \frac{P'}{\rho}\right)\,. \tag{1.33}$$

From Eq. (1.20), we obtain for the equation of mass conservation:

$$\delta\rho + \rho\left[\frac{1}{r^2}\frac{\partial}{\partial r}\left(r^2\xi_r\right) + \frac{1}{r\,\sin\theta}\frac{\partial}{\partial\theta}\left(\sin\theta\;\xi_\theta\right) + \frac{1}{r\,\sin\theta}\frac{\partial\xi_\phi}{\partial\phi}\right] = 0\,, \tag{1.34}$$

which gives, using the values of ξ_θ and ξ_ϕ given by Eqs. (1.32) and (1.33) and the definition of $\mathcal{L}^2$ (Eq. (1.30)):

$$\frac{\delta\rho}{\rho} + \frac{1}{r^2}\frac{\partial}{\partial r}\left(r^2\xi_r\right) - \frac{1}{\sigma^2 r^2}\,\mathcal{L}^2\left(\psi' + \frac{P'}{\rho}\right) = 0\,. \tag{1.35}$$

From Eq. (1.22), we find for the perturbed Poisson equation:

$$\frac{1}{r^2}\frac{\partial}{\partial r}\left(r^2\frac{\partial\psi'}{\partial r}\right)-\frac{1}{r^2}\,\mathcal{L}^2\,\psi'=4\pi G\,\rho'\,. \tag{1.36}$$

And finally, we make some manipulations of the equation of energy conservation and the transfer equation. We introduce the following notations:

$$\delta L\equiv\delta(4\pi r^2F_r)\ ,\quad \delta L_{\rm R}\equiv\delta(4\pi r^2F_{Rr})\quad\text{and}\quad \delta L_{\rm C}\equiv\delta(4\pi r^2F_{Cr})$$

where F_r, F_{Rr} and F_{Cr} are the radial components of the total flux, the radiative flux and the convective flux respectively. δL is not the Lagrangian variation of the total luminosity, which is a quantity integrated over a sphere. δL is a local quantity related to the local flux by the above definition. For the sake of simplicity, we make here a frozen convection approximation.

We ignore the Lagrangian variation of the convective luminosity: $\delta L_{\rm C}=0$ and we ignore the Lagrangian variation of the transversal components of the convective flux.

We note that there are different other ways to freeze the convection: ignore the Lagrangian variation of the convective flux, ignore the variations of the divergence of the convective flux ...

From Eq. (1.27), we have:

$$i\,\sigma\,T\,\delta S\ =\ \left(\frac{\delta\epsilon}{\epsilon}+\frac{\delta\rho}{\rho}\right)\epsilon\ -\ \left(\frac{d\,\epsilon}{d\,r}+\epsilon\,\frac{d\,\ln\rho}{d\,r}\right)\xi_r\ -\ \frac{1}{4\pi r^2\rho}\,\frac{\partial(4\pi r^2F_r{}')}{\partial r}\ -\ \frac{\nabla_h\cdot\vec{F}'}{\rho}\,. \tag{1.37}$$

After some algebra, we find on one hand:

$$-\frac{1}{4\pi r^2\rho}\,\frac{\partial(4\pi r^2F_r{}')}{\partial r}\ =\ -\frac{1}{4\pi r^2\rho}\,\frac{\partial\,\delta L}{\partial r}\ +\ \left(\frac{d\,\epsilon}{d\,r}+\epsilon\,\frac{d\,\ln\rho}{d\,r}\right)\xi_r\ +\ \frac{\epsilon}{r^2}\,\frac{\partial\,(r^2\xi_r)}{\partial r}\,, \tag{1.38}$$

and on the other hand, neglecting the Lagrangian variation of the transversal components of the convective flux, we have :

$$\begin{aligned}-\frac{\nabla_h\cdot\vec{F}'}{\rho}\ &=\ -\frac{\nabla_h\cdot\vec{F_{\rm R}}'}{\rho}\ -\ \frac{\nabla_h\cdot\vec{F_{\rm C}}'}{\rho}\\ &=\ -\frac{\nabla_h\cdot\vec{F_{\rm R}}'}{\rho}\ +\ \frac{F_{\rm C}}{\rho\,r}\,\nabla_h\cdot(\xi_\theta\,\vec{e_\theta}+\xi_\phi\,\vec{e_\phi})\ ,\end{aligned} \tag{1.39}$$

which gives, using Eqs. (1.24), (1.32), (1.33) and (1.15):

$$\begin{aligned}-\frac{\nabla_h\cdot\vec{F}'}{\rho}\ &=\ -\frac{4\,a\,c\,T^3}{3\,\kappa\,\rho^2r^2}\,\mathcal{L}^2\,T'\ -\ \frac{F_{\rm C}}{\rho\,r^3\sigma^2}\,\mathcal{L}^2\left(\psi'+\frac{P'}{\rho}\right)\\ &=\ \frac{1}{4\pi\rho\,r^3}\left(\frac{L_{\rm R}}{r\,(dT/dr)}\,\mathcal{L}^2\,T'\ -\ \frac{L_{\rm C}}{r^2\sigma^2}\,\mathcal{L}^2\left(\psi'+\frac{P'}{\rho}\right)\right)\,.\end{aligned} \tag{1.40}$$

And finally, we find for the equation of energy conservation:

$$\begin{aligned} \mathrm{i}\sigma T\,\delta S \;&=\; -\frac{1}{4\pi r^2\rho}\frac{\partial\,\delta L}{\partial r} + \epsilon\left(\frac{\delta\epsilon}{\epsilon}+\frac{\delta\rho}{\rho}+\frac{1}{r^2}\frac{\partial\left(r^2\xi_r\right)}{\partial r}\right) \\ &+\; \frac{1}{4\pi\rho\, r^3}\,\mathcal{L}^2\left(L_{\mathrm{R}}\left(\frac{\delta T}{r\,(dT/dr)}-\frac{\xi_r}{r}\right) - \frac{L_{\mathrm{C}}}{r^2\sigma^2}\left(\psi'+\frac{P'}{\rho}\right)\right). \end{aligned} \tag{1.41}$$

From Eq. (1.24) and neglecting the Lagrangian variation of the convective luminosity, we find for the radial component of the perturbed transfer equation in a Lagrangian formalism:

$$\frac{\delta L}{L}=\frac{L_{\mathrm{R}}}{L}\frac{\delta L_{\mathrm{R}}}{L_{\mathrm{R}}}=\frac{L_{\mathrm{R}}}{L}\left(2\,\frac{\xi_r}{r}+3\,\frac{\delta T}{T}-\frac{\delta\kappa}{\kappa}-\frac{\delta\rho}{\rho}+\frac{\partial\delta T/\partial r}{\mathrm{d}T/\mathrm{d}r}-\frac{\partial\,\xi_r}{\partial r}\right). \tag{1.42}$$

1.5.2 Splitting in spheroidal modes

We can now introduce the notion of **spherical harmonic**:
The spherical harmonics ($Y_\ell^m(\theta,\phi)$, $\ell=0\rightarrow+\infty$, $m=-\ell\rightarrow\ell$) are a well known infinite family of functions defined on the sphere. Two important properties of the spherical harmonics are that they form a complete set of orthogonal functions on the sphere and that they are eigenfunctions of the Legendre operator $\mathcal{L}^2$:

$$\mathcal{L}^2\,Y_\ell^m(\theta,\phi)=\ell(\ell+1)Y_\ell^m(\theta,\phi)\,. \tag{1.43}$$

After the transformations we did on the equations, we can see that in all the equations where there are partial derivatives with respect to the angular coordinates (θ, ϕ) (Eqs. (1.35), (1.36) and (1.41)), these derivatives appear under the Legendre operator $\mathcal{L}^2$. This together with the two properties of the spherical harmonics we have seen implies that any general solution of the equations can be written as an infinite linear combination of solutions proportional to $Y_\ell^m(\theta,\phi)$ and the system of partial differential equations can be separated:

$$\overrightarrow{X}(r,\theta,\phi,t)=\Re\left\{\sum_{\ell=0}^{+\infty}\sum_{m=-\ell}^{+\ell}\sum_{k=0}^{+\infty}A_{\ell,m,k}\,\overrightarrow{X}_{\ell,m,k}(r)\,Y_\ell^m(\theta,\phi)\,e^{i\sigma_{\ell,m,k}t}\right\}. \tag{1.44}$$

A solution of the form $\overrightarrow{X}(r,\theta,\phi,t)=\overrightarrow{X}(r)\,Y_\ell^m(\theta,\phi)\,e^{i\sigma t}$ is called a spheroidal mode of oscillation or simply a mode with spherical degree ℓ and azimuthal order m. And the study of stellar pulsation is reduced to the study of the different proper modes of oscillation of a star. We did not consider here the toroidal modes which are of no interest when the rotation is neglected.

The real part of σ is the **angular frequency** of the spheroidal mode and the opposite of the imaginary part ($-\Im(\sigma)$) is its **growth rate**.

If the imaginary part of σ is positive, then the mode is vibrationally **stable**, the oscillations are damped and the amplitudes of variations of the different physical quantities decrease exponentially with time.

If the imaginary part of σ is negative, then the mode is vibrationally **unstable**, the oscillations are excited and the amplitudes of variations of the different physical quantities increase exponentially with time.

From Eqs. (1.32) and (1.33), we see that for a given spheroidal mode of degree and order $(\ell,\, m)$, the displacement vector is written:

$$\overrightarrow{\delta r} = \Re\left\{\left[\xi_r(r)Y_\ell^m(\theta,\phi)\,\vec{e}_r + \xi_h(r)\left(\frac{\partial Y_\ell^m}{\partial\theta}(\theta,\phi)\,\vec{e}_\theta + \frac{1}{\sin\theta}\frac{\partial Y_\ell^m}{\partial\phi}(\theta,\phi)\,\vec{e}_\phi\right)\right]e^{i\,\sigma t}\right\}, \tag{1.45}$$

where ξ_h is given by:

$$\sigma^2\xi_h = \frac{1}{r}\left(\psi' + \frac{P'}{\rho}\right) = \frac{1}{r}\left(\delta\psi + \frac{\delta P}{\rho}\right). \tag{1.46}$$

For a given spheroidal mode of spherical degree ℓ, the system of partial differential equations is separated and reduces to a more simple system of ordinary differential equations.

From Eqs. (1.35) and (1.43), the equation of mass conservation becomes in a Lagrangian formalism:

$$\frac{\delta\rho}{\rho} + \frac{1}{r^2}\frac{d}{dr}\left(r^2\xi_r\right) - \frac{\ell(\ell+1)}{\sigma^2 r^2}\left(\delta\psi + \frac{\delta P}{\rho}\right) = 0\,. \tag{1.47}$$

From Eqs. (1.36) and (1.43), we find for the perturbed Poisson equation:

$$\frac{1}{r^2}\frac{d}{dr}\left(r^2\frac{d\psi'}{dr}\right) - \frac{\ell(\ell+1)}{r^2}\psi' = 4\pi G\,\rho'\,. \tag{1.48}$$

And from Eqs. (1.41), (1.43) and (1.46), we find for the equation of energy conservation:

$$\begin{aligned} \mathrm{i}\,\sigma T\,\delta S \;&=\; -\frac{1}{4\pi r^2\rho}\frac{d\,\delta L}{dr} + \epsilon\left(\frac{\delta\epsilon}{\epsilon} + \frac{\delta\rho}{\rho} + \frac{1}{r^2}\frac{d\,(r^2\xi_r)}{dr}\right) \\ &+\; \frac{\ell(\ell+1)}{4\pi\rho\, r^3}\left(L_{\mathrm{R}}\left(\frac{\delta T}{r\,(dT/dr)} - \frac{\xi_r}{r}\right) - L_{\mathrm{C}}\frac{\xi_h}{r}\right). \end{aligned} \tag{1.49}$$

These equations as well as the boundary conditions do not depend on m. Therefore, for each fixed value of ℓ, the solutions (eigenfunctions and eigenvalues) are the same for the $2\ell+1$ values of m: there is a $(2\ell+1)$-fold degeneracy. This degeneracy is well known in quantum physics and comes from the spherical symmetry. In the presence of a magnetic field or rotation, the degeneracy is lifted and there is a splitting of $(2\ell+1)$ frequencies for each value of ℓ (this phenomenon is analogous to the Zeeman effect in quantum physics).

With these simplifications, the initial 3-dimensional domain is reduced to 1 dimension. More precisely, the domain is $[0, R_{\mathrm{s}}]$ where 0 corresponds to the center and R_{s} is the radius of the last layer of the stellar model, we recall that $R_{\mathrm{s}} > R$ (see Section 1.3.2).

1.6 Perturbed equations of state

The total number of perturbed variables defined in Section 1.5 is higher than the total number of differential equations. But these perturbed variables are not independent, the equations of state impose algebraic relations between them. More precisely, it is quite usual to make the hypothesis of Local Thermodynamic Equilibrium (LTE) in stellar interiors and atmospheres. Under this hypothesis, if the chemical composition (χ_i) and the values of two independent thermodynamic quantities are given (for example the density ρ and the temperature T), all the other thermodynamic quantities can be determined from the equations of states (Eq. (1.11)).

In an oscillating star, it is usual to neglect the Lagrangian variation of the chemical composition. This approximation is perfectly valid in the main part of the star, because the time scales of the diffusion and rotational mixing processes are much higher than the periods of pulsations. However, in the central layers, some nuclear reactions have small time scales and the abundance of some elements of these reactions cannot be assumed to remain constant. The variation of the abundance of these elements plays a significant role only for the determination of the nuclear energy generation rate variation ($\delta\epsilon$). For the other thermodynamic quantities, we can neglect this phenomenon.

We recall the definitions of some quantities obtained as derivatives of the equations of state:

$$\begin{aligned}
\Gamma_1 &= \left.\frac{\partial \ln P}{\partial \ln \rho}\right|_S , \; \Gamma_3 - 1 = \left.\frac{\partial \ln T}{\partial \ln \rho}\right|_S , \; \nabla_{\mathrm{ad}} = \frac{\Gamma_2 - 1}{\Gamma_2} = \frac{\Gamma_3 - 1}{\Gamma_1} = \left.\frac{\partial \ln T}{\partial \ln P}\right|_S , \\
P_T &= \left.\frac{\partial \ln P}{\partial \ln T}\right|_\rho , \; P_\rho = \left.\frac{\partial \ln P}{\partial \ln \rho}\right|_T , \; c_v = \left.\frac{\partial U}{\partial T}\right|_\rho , \; c_p = \left.\frac{\partial H}{\partial T}\right|_P , \\
\kappa_T &= \left.\frac{\partial \ln \kappa}{\partial \ln T}\right|_\rho , \; \kappa_\rho = \left.\frac{\partial \ln \kappa}{\partial \ln \rho}\right|_T , \; \kappa_{\rho S} = \left.\frac{\partial \ln \kappa}{\partial \ln \rho}\right|_S , \qquad (1.50)
\end{aligned}$$

where U and H are the internal energy and the enthalpy. All the previous quantities are not independent and we have:

$$\begin{aligned}
P_\rho &= \Gamma_1 - (\Gamma_3 - 1)^2 c_v \rho T / P , &(1.51)\\
P_T &= (\Gamma_3 - 1) c_v \rho T / P , &(1.52)\\
\kappa_{\rho S} &= \kappa_\rho + (\Gamma_3 - 1) \kappa_T , &(1.53)\\
c_p &= c_v \left[1 - (\Gamma_3 - 1)^2 c_v \rho T / (\Gamma_1 P)\right]^{-1} . &(1.54)
\end{aligned}$$

By perturbing the equations of states and neglecting the Lagrangian variation of the chemical composition, we obtain then:

$$\frac{\delta T}{T} = \frac{\delta S}{c_v} + (\Gamma_3 - 1)\frac{\delta\rho}{\rho} = \frac{\delta S}{c_p} + \nabla_{\mathrm{ad}}\frac{\delta P}{P} , \qquad (1.55)$$

$$\frac{\delta P}{P} = P_T \frac{\delta T}{T} + P_\rho \frac{\delta\rho}{\rho} = P_T \frac{\delta S}{c_v} + \Gamma_1 \frac{\delta\rho}{\rho} , \qquad (1.56)$$

$$\frac{\delta\kappa}{\kappa} = \kappa_T \frac{\delta T}{T} + \kappa_\rho \frac{\delta\rho}{\rho} = \kappa_T \frac{\delta S}{c_v} + \kappa_{\rho S} \frac{\delta\rho}{\rho} . \qquad (1.57)$$

Concerning the Lagrangian variation of the rate of nuclear energy generation ($\delta\epsilon$), we have to be more carefull for the reasons said above. The rigorous derivation of $\delta\epsilon$ is given in Ledoux & Walraven (1958, §66) and we do not detail it here. As a quick summary, by perturbing the different reaction rates of the p-p chain and the CNO cycle, we obtain a linear system of equations whose solution gives the variations of the abundances of the elements. Then, we can derive the variations of the nuclear energy generation rates for each reactions, and the sum gives finally $\delta\epsilon$. In a synthetic form, we can write:

$$\frac{\delta\epsilon}{\epsilon} = \epsilon_T(\sigma)\,\frac{\delta T}{T} + \epsilon_\rho(\sigma)\,\frac{\delta\rho}{\rho} = \epsilon_T(\sigma)\,\frac{\delta S}{c_v} + \epsilon_{\rho S}(\sigma)\,\frac{\delta\rho}{\rho}\,, \tag{1.58}$$

where we note that the coefficients ϵ_T and $\epsilon_{\rho S}$ depend strongly on the angular pulsation frequency σ.

1.7 Boundary conditions

By substituting the perturbed equations of state of Section 1.6 into the equations of linear non-radial non-adiabatic oscillations derived in Section 1.5, we obtain a system of 6 first order differential equations with 6 unknowns. In order to close this problem, we have to add some boundary conditions.

On one hand, the central boundary conditions are obtained by imposing the regularity of the solutions at the center (finite values for the perturbed variables and their derivatives). The derivation of these conditions is detailed in Unno et al. (1989, §18.1 p. 162). An usual way to derive them is to keep only the terms of lowest order in the Taylor developments of the differential equations close to the center. The system of differential equations obtained by this procedure can then be solved analytically. Finally, the condition of regularity imposes the following asymptotic behaviour of the perturbed variables for non-radial modes ($\ell \geq 1$) and for $x \to 0$: the radial displacement is proportional to $r^{\ell-1}$ ($\xi_r \propto r^{\ell-1}$) and for the other perturbed variables, we have $\psi' \propto r^\ell$, $\delta P/P \propto r^\ell$, $\delta S/c_v \propto r^\ell$, $\delta L/L \propto r^\ell$, ... In Section 2.2, we will propose a dimensionless formalism appropriate for the description of the perturbed variables close to the center and we will derive in details the central boundary conditions used in our method.

On the other hand, 3 boundary conditions have to be imposed at the surface of the star. The main particularity of our non-adiabatic method is the special care given to the treatment of the pulsation in the atmosphere and to the derivation of appropriate surface boundary conditions. We will give the details of this improved treatment in Section 2.3. Other authors (Dziembowski 1977a, Saio & Cox 1980, Pesnell 1990) did not include the entire atmosphere in their non-adiabatic treatment, so that they had to impose less accurate surface boundary conditions at the base of the atmosphere. In order to help for the comparison, we give here the surface boundary conditions used most frequently in the litterature.

The surface boundary condition for the gravitational potential is obtained by imposing a first order continuous match (i.e. continuity of ψ' and its first derivatives) between the inner solution of the Poisson equation and the outer solution of the Laplace equation (Ledoux & Walraven 1958). We find after some algebra:

$$\frac{\mathrm{d}\psi'}{\mathrm{d}r} + \frac{\ell+1}{r}\,\psi' = -\,4\pi\,G\,\rho\,\xi_r\,. \tag{1.59}$$

We adopt the same boundary condition in our treatment. We note that we found very often in the litterature (Unno et al. 1989, ...) a slightly different boundary condition for the potential, where the right-hand side of Eq. (1.59) is neglected. This approximation is admissible because the surface density is much smaller than the mean density of the star.

The mechanical boundary condition is generally obtained by imposing a complete reflection of the pressure waves at the surface. In order to obtain this condition, it is appropriate to rewrite the radial component of the equation of momentum conservation (Eq. (1.31)) in the following form:

$$\sigma^2\xi_r = \frac{\mathrm{d}\psi'}{\mathrm{d}r} + \frac{\mathrm{d}(g\,\xi_r)}{\mathrm{d}r} + \frac{P}{\rho}\frac{\mathrm{d}(\delta P/P)}{\mathrm{d}r} + g\left(\frac{\delta\rho}{\rho} - \frac{\delta P}{P}\right). \tag{1.60}$$

By assuming that $P/(\rho\,g\,r) \to 0$ at the surface (Cox 1980, §17.6b) or $\mathrm{d}(\delta P/P)/\mathrm{d}r = 0$ at the surface (Pesnell 1990), we obtain the following mechanical boundary condition:

$$\sigma^2\xi_r = \frac{\mathrm{d}\psi'}{\mathrm{d}r} + \frac{\mathrm{d}(g\,\xi_r)}{\mathrm{d}r} + g\left(\frac{\delta\rho}{\rho} - \frac{\delta P}{P}\right). \tag{1.61}$$

By eliminating in this equation $\mathrm{d}\psi'/\mathrm{d}r$, from Eq. (1.59), and $\mathrm{d}\xi_r/\mathrm{d}r$, from Eq. (1.47), we obtain an homogeneous equation without derivatives, as usually expected for a boundary condition. Proceeding so, it is easy to see that Eq. (1.61) is equivalent to the mechanical boundary condition of Unno et al. (1989, Eq. (24.19)). It can be shown that Eq. (1.61) is valid to the first order in $V^{-1} = P/(\rho\,g\,r)$. However, it is not valid to assume $V^{-1} \to 0$ at the surface of massive stars such as β Cephei stars and SPBs, because the radiation pressure is not negligible. We will propose in Section 2.3 (Eq. (2.46)) an improved mechanical boundary condition where the contribution of the gas pressure is neglected at the surface, but not the contribution of the radiation pressure. We note that for modes with very high or very low frequencies, we have no longer a complete reflection at the surface, and energy leakage occurs throughout the atmosphere. There are two critical frequencies σ_{c_1} and σ_{c_2} called cut-off frequencies such as for $\sigma > \sigma_{c_2}$ (resp. $\sigma < \sigma_{c_1}$) the pressure waves (resp. the gravity waves) are propagating throughout the atmosphere without reflection at all; we refer to Unno et al. (1989, §18.1) for the description of this phenomenon in an isothermal atmosphere.

Finally, a thermal boundary condition has to be imposed. Dziembowski (1977a) and Pesnell (1990) proposed the following condition at the photosphere:

$$\frac{\delta L}{L} = 2\,\frac{\xi_r}{r} + 4\,\frac{\delta T}{T}\,. \tag{1.62}$$

The main default of this boundary condition is that it assumes implicitly that the Lagrangian temperature variation at the photosphere is equal to the effective temperature variation. We will show in Section 2.3 that this assumption is not valid and we will propose better boundary conditions: Eqs. (2.42) and (2.48). Gabriel (1989) proposed an accurate thermal boundary condition valid in the outermost stellar layers where matter and radiation no longer interact but did not propose a treatment of the pulsation between the photosphere and these very superficial layers. We will propose such a treatment in Section 2.3.

1.8 Integral expressions for the eigenvalues

Integral expressions are associated to the eigenvalue problem of stellar oscillations and they play a crucial role in asteroseismology. These expressions can be derived on the basis of the general partial differential equations of the problem (see Unno et al. 1989 or Cox 1980) but it is easier to derive them for a given spheroidal mode, as we do here.

Rewriting the radial component of the equation of momentum conservation (Eq. (1.31)) in a Lagrangian formalism gives:

$$\sigma^2 \xi_r = \frac{d\delta\psi}{dr} + \frac{1}{\rho}\frac{d\,\delta P}{dr} + \frac{\delta\rho}{\rho}\,g\,. \tag{1.63}$$

Multiplying by $4\pi r^2 \rho \overline{\xi_r}$ and integrating over the radius r, from the center to the surface, we find:

$$\sigma^2 \int_0^R |\xi_r|^2 4\pi r^2 \rho\, dr = \int_0^R \overline{\xi_r} \left(\frac{d\,\delta\psi}{d\,r} + \frac{1}{\rho}\frac{d\,\delta P}{d\,r} + \frac{\delta\rho}{\rho}\,g \right) 4\pi r^2 \rho\, dr\,. \tag{1.64}$$

Integrating by part the first term of Eq. (1.64), we find:

$$\int_0^R \overline{\xi_r}\, \frac{d\,\delta\psi}{d\,r}\, 4\pi r^2 \rho\, dr \;=\; \left[\overline{\xi_r}\, \delta\psi\, 4\pi r^2 \rho\right]_0^R - \int_0^R \frac{d\left(r^2 \rho\, \overline{\xi_r}\right)}{d\,r}\, \delta\psi\, 4\pi\, dr\,. \tag{1.65}$$

The term in brackets is equal to zero if we assume that the density goes to zero at the surface of the star, and we have:

$$\int_0^R \overline{\xi_r}\, \frac{d\,\delta\psi}{d\,r}\, 4\pi r^2 \rho\, dr \;=\; -\int_0^R \frac{d\left(r^2\, \overline{\xi_r}\right)}{d\,r}\, \delta\psi\, 4\pi \rho\, dr - \int_0^R \overline{\xi_r}\, \delta\psi\, \frac{d\,\rho}{d\,r}\, 4\pi r^2\, dr\,. \tag{1.66}$$

Eliminating $d\,(r^2\, \overline{\xi_r}\,)/dr$ by use of Eq. (1.47), we find then:

$$\begin{aligned} \int_0^R \overline{\xi_r}\, \frac{d\,\delta\psi}{d\,r}\, 4\pi r^2 \rho\, dr \;&=\; \int_0^R \frac{\overline{\delta\rho}}{\rho}\, \delta\psi\, 4\pi r^2 \rho\, dr \;-\; \frac{\ell(\ell+1)}{\overline{\sigma}^2} \int_0^R \left(\overline{\delta\psi} + \frac{\overline{\delta P}}{\rho} \right) \delta\psi\, 4\pi \rho\, dr \\ &\quad - \int_0^R \overline{\xi_r}\, \delta\psi\, \frac{d\,\rho}{d\,r}\, 4\pi r^2\, dr\,. \end{aligned} \tag{1.67}$$

Integrating by part the second term of Eq. (1.64), we find:

$$\int_0^R \overline{\xi_r}\,\frac{d\,\delta P}{d\,r}\,4\pi r^2\,dr \;=\; \left[\overline{\xi_r}\,\delta P\,4\pi r^2\right]_0^R - \int_0^R \frac{d\left(r^2\,\overline{\xi_r}\right)}{d\,r}\,\delta P\,4\pi\,dr\,. \tag{1.68}$$

The term in brackets is equal to zero if we assume that the Lagrangian variation of the total pressure goes to zero at the surface of the star. Eliminating $d\,(r^2\,\overline{\xi_r})/dr$ by use of Eq. (1.47), we find then:

$$\int_0^R \overline{\xi_r}\,\frac{d\,\delta P}{d\,r}\,4\pi r^2\,dr \;=\; \int_0^R \frac{\overline{\delta\rho}}{\rho}\,\delta P\,4\pi r^2\,dr \;-\; \frac{\ell(\ell+1)}{\overline{\sigma}^2}\int_0^R \left(\overline{\delta\psi}+\frac{\overline{\delta P}}{\rho}\right)\delta P\,4\pi\,dr\,. \tag{1.69}$$

Substituting Eqs. (1.67) and (1.69) in Eq. (1.64), and using Eq. (1.46), we have:

$$\begin{aligned}
&\sigma^2\int_0^R \left(|\xi_r|^2+\ell(\ell+1)\,|\xi_h|^2\right)4\pi r^2\rho\,dr \\
&= \sigma^2\left(\int_0^R |\xi_r|^2 4\pi r^2\rho\,dr \;+\; \frac{\ell(\ell+1)}{|\sigma|^4}\int_0^R \left|\delta\psi+\frac{\delta P}{\rho}\right|^2 4\pi\rho\,dr\right) \\
&= \int_0^R \frac{\overline{\delta\rho}}{\rho}\left(\delta\psi+\frac{\delta P}{\rho}\right)4\pi r^2\rho\,dr \;-\; \int_0^R \overline{\xi_r}\,\delta\psi\,\frac{d\,\rho}{d\,r}\,4\pi r^2\,dr \\
&\quad + \int_0^R \frac{\delta\rho}{\rho}\,g\,\overline{\xi_r}\,4\pi r^2\rho\,dr \\
&= \int_0^R \frac{\overline{\delta\rho}}{\rho}\,\frac{\delta P}{\rho}\,4\pi r^2\rho\,dr \;+\; \int_0^R \frac{\overline{\delta\rho}}{\rho}\,\psi'\,4\pi r^2\rho\,dr \\
&\quad + 2\,\Re\left\{\int_0^R \frac{\delta\rho}{\rho}\,g\,\overline{\xi_r}\,4\pi r^2\rho\,dr\right\} \;-\; \int_0^R \overline{\xi_r}\,\delta\psi\,\frac{d\,\rho}{d\,r}\,4\pi r^2\,dr\,.
\end{aligned} \tag{1.70}$$

And finally we find the following integral expression for the eigenvalue:

$$\sigma^2 \;=\; \frac{\begin{aligned}&\left[\int_0^R \frac{\overline{\delta\rho}}{\rho}\,\frac{\delta P}{\rho}\,4\pi r^2\rho\,dr \;+\; 2\,\Re\left\{\int_0^R \frac{\delta\rho}{\rho}\,g\,\overline{\xi_r}\,4\pi r^2\rho\,dr\right\}\right.\\ &\left.\quad+\int_0^R \frac{\overline{\rho'}}{\rho}\,\psi'\,4\pi r^2\rho\,dr \;-\; \int_0^R |\xi_r|^2\,g\,\frac{d\,\rho}{d\,r}\,4\pi r^2\,dr\;\right]\end{aligned}}{\displaystyle\int_0^R \left(|\xi_r|^2+\ell(\ell+1)\,|\xi_h|^2\right)4\pi r^2\rho\,dr}\,. \tag{1.71}$$

In Eq. (1.71), the term $\int_0^R (\overline{\rho'}/\rho)\,\psi'\,4\pi r^2\rho\,dr$ is real if we assume that the density goes to zero at the surface of the star. To show it, we use Eq. (1.48) and integrate by part:

$$\begin{aligned}
\int_0^R \overline{\rho'}\,\psi'\,4\pi r^2\,dr \;&=\; \int_0^R \frac{d}{d\,r}\left(r^2\frac{d\,\overline{\psi'}}{d\,r}\right)\frac{\psi'}{G}\,dr \;-\; \frac{\ell(\ell+1)}{G}\int_0^R |\psi'|^2\,dr \\
&= \left[\frac{r^2}{G}\,\frac{d\,\overline{\psi'}}{d\,r}\,\psi'\right]_0^R \;-\; \int_0^R \frac{r^2}{G}\left|\frac{d\,\psi'}{d\,r}\right|^2 dr \;-\; \frac{\ell(\ell+1)}{G}\int_0^R |\psi'|^2\,dr\,.
\end{aligned} \tag{1.72}$$

From the boundary condition on the gravitational potential (Eq. (1.59)) and neglecting the density at the surface of the star, the first term of the right hand side of Eq. (1.72) is real.

Therefore, all the terms of Eq. (1.71) are real except the term: $\int_0^R (\overline{\delta\rho}/\rho)\, \delta P\, 4\pi r^2\, dr$. And the imaginary part of Eq. (1.71) reads:

$$2\,\Re\{\sigma\}\,\Im\{\sigma\} \;=\; \frac{\displaystyle\int_0^R \Im\left\{\frac{\overline{\delta\rho}}{\rho}\,\frac{\delta P}{\rho}\right\} 4\pi r^2 \rho\, dr}{\displaystyle\int_0^R \left(|\xi_r|^2 + \ell(\ell+1)\,|\xi_h|^2\right) 4\pi r^2 \rho\, dr}\,. \tag{1.73}$$

From Eqs. (1.52) and (1.56), we find then:

$$\Im\{\sigma\} \;=\; \frac{1}{2\,\Re\{\sigma\}}\,\frac{\displaystyle\int_0^R \Im\left\{\frac{\overline{\delta\rho}}{\rho}\,T\delta S\right\} (\Gamma_3 - 1)\, 4\pi r^2 \rho\, dr}{\displaystyle\int_0^R \left(|\xi_r|^2 + \ell(\ell+1)\,|\xi_h|^2\right) 4\pi r^2 \rho\, dr}\,. \tag{1.74}$$

1.9 The adiabatic, quasi-adiabatic and Cowling approximations

1.9.1 The adiabatic approximation

Throughout most of the star (in term of mass), the thermal relaxation time is much larger than the observed pulsation periods. From a physical point of view, the heat capacity is so high that, during one pulsation cycle, the entropy of the matter has not the time to vary significantly: $\delta S/c_v \simeq 0$. This leads to the adiabatic approximation.

In the **adiabatic approximation**, it is assumed that, throughout the entire star, the Lagrangian variation of the entropy is zero during the oscillations:

$$\delta S = 0\,. \tag{1.75}$$

Under the adiabatic approximation, the dynamical equations (equations of momentum and mass conservation, Poisson equation) and the thermal equations (equation of energy conservation and transfer equation) are uncoupled. The dynamical equations can be solved alone and the problem is reduced to solving the 3 differential equations: Eqs. (1.47), (1.48) and (1.63) with for example the 3 unknowns: ξ_r, $\delta P/P$ and ψ' (this system of equations is of the fourth order since Eqs. (1.47) and (1.63) are of the first order and Eq. (1.48) is of the second order). From Eqs. (1.56) and (1.55), the Lagrangian variations of the pressure, temperature and density are related by the following laws in the adiabatic approximation:

$$\frac{\delta P}{P} = \Gamma_1\,\frac{\delta\rho}{\rho} \qquad \text{and} \qquad \frac{\delta T}{T} = (\Gamma_3 - 1)\,\frac{\delta\rho}{\rho}\,. \tag{1.76}$$

Under the adiabatic approximation, the problem to solve is an hermitian eigenvalue problem. Therefore, the eigenfunctions solutions of the adiabatic problem are pure real, and the eigenvalues (σ) are either pure real or pure imaginary.

If the adiabatic eigenvalue of a given mode is pure real then the mode is **dynamically stable** and the time dependence of the oscillations is sinusoidal.

If the adiabatic eigenvalue of a given mode is pure imaginary then the mode is **dynamically unstable**, there is no longer oscillation at all and the distance to the equilibrium configuration increases exponentially with time. It is typically the case at the dramatic last step of the life of a massive star, leading to a supernova explosion. In our study we are going to consider only dynamically stable modes.

1.9.2 The quasi-adiabatic approximation

Under the adiabatic approximation, it is not possible to determine if a mode is vibrationally stable or unstable (the eigenvalues are pure real). This can only be done rigorously by full non-adiabatic computations, solving together the dynamical and thermal equations presented in Section 1.5. The quasi-adiabatic approximation is a method whose the goal is to estimate if a mode is vibrationally stable or unstable without doing non-adiabatic computations. The procedure is the following:

1. Adiabatic computations are performed giving the adiabatic eigenfunctions and eigenvalue of a given mode.

2. The Lagrangian variation of the luminosity is determined from Eq. (1.42) and using the adiabatic eigenfunctions computed at step 1, $\delta\epsilon$ is computed similarly.

3. The imaginary part of the eigenvalue is estimated by using the integral expression given by Eq. (1.74). More precisely, for a radial mode (the generalization for a non-radial mode is easy), the equation of energy conservation Eq. ((1.49)) gives:

$$T\,\delta S = \frac{i}{\sigma}\left(\frac{d\,\delta L}{d\,m} - \delta\epsilon\right)\,. \tag{1.77}$$

We are now at the delicate part of the method. In the quasi-adiabatic approximation, the right hand side of Eq. (1.77) is computed using the "adiabatic" values of δL and $\delta\epsilon$ obtained at step 2. Non zero values of $T\delta S$ are then obtained from Eq. (1.77), and these values are used to compute the imaginary part of σ by Eq. (1.74), we have thus for a radial mode:

$$\Im\{\sigma\} \;=\; \frac{1}{2\,\sigma_0{}^2}\,\frac{\displaystyle\int_0^M (\Gamma_3-1)\,\frac{\delta\rho}{\rho}\left(\frac{d\,\delta L}{d\,m} - \delta\epsilon\right)\,dm}{\displaystyle\int_0^M \xi_r{}^2\,dm}\,, \tag{1.78}$$

where σ_0 is the adiabatic eigenvalue.

This procedure is inconsistent since the adiabatic approximation made at the first two steps is no longer made at the last step, where non zero values of $T\delta S$ are obtained ! As said before, the rigorous way to obtain the imaginary part of σ is to perform full non-adiabatic computations. Generally, the quasi-adiabatic procedure can be used in reasonably good approximation from the center to the bottom of the external driving region of a star, where the degree of non-adiabaticity is small ($|\delta S/c_p| \ll |\delta P/P|$). But on the contrary, in the superficial layers, the oscillations are always highly non-adiabatic and the quasi-adiabatic procedure leads to wrong values of δL. More precisely, the quasi-adiabatic approximation gives rapidly increasing values of $|\delta L|$ towards the surface, contrary to full non-adiabatic computations which predict, as it will be shown and explained in the next chapters, a flat behaviour of δL in the superficial layers. This problem is generally avoided in the quasi-adiabatic procedure by truncating the integration in Eq. (1.78) before the highly non-adiabatic layers.

1.9.3 The Cowling + adiabatic approximation

In the Cowling approximation (Cowling 1941), the Eulerian perturbation of the gravitational potential is neglected:

$$\psi' = 0 \,. \tag{1.79}$$

This approximation is generally admissible for modes with a large number of nodes and in the superficial layers, where the local density is much smaller than the mean density of the star: $\rho \ll 3M/(4\pi R^3)$. Under the adiabatic and Cowling approximations, the modelling of stellar oscillations is much simplified: the equations of linear stellar oscillations reduce to one single second order differential equation, as we are going to show.

From Eqs. (1.31), (1.76) and (1.79), we have on one hand:

$$\frac{\mathrm{d}P'}{\mathrm{d}r} + \frac{g}{c^2}\, P' = (\sigma^2 - N^2)\, \rho\, \xi_r \,, \tag{1.80}$$

where N and c are the Brunt-Väisälä frequency and the sound speed respectively:

$$N^2 = \frac{Gm}{r^2} \left(\frac{1}{\Gamma_1} \frac{\mathrm{d}\ln P}{\mathrm{d}r} - \frac{\mathrm{d}\ln \rho}{\mathrm{d}r} \right) \qquad \text{and} \qquad c^2 = \frac{P\,\Gamma_1}{\rho} \,. \tag{1.81}$$

On the other hand, from Eqs. (1.47), (1.76) and (1.79), we have:

$$\frac{P'}{\rho\, c^2} \left(1 - \frac{{L_\ell}^2}{\sigma^2} \right) - \frac{g}{c^2}\, \xi_r + \frac{1}{r^2} \frac{\mathrm{d}}{\mathrm{d}r} \left(r^2 \xi_r \right) = 0 \,, \tag{1.82}$$

where L_ℓ is the Lamb frequency:

$$L_\ell^2 = \frac{\ell(\ell+1)\, c^2}{r^2} \,. \tag{1.83}$$

The following change of variables has been proposed by Gabriel & Scuflaire (1979) and permits to simplify the problem even more:

$$\begin{aligned} v &= f_1 r^2 \xi_r \,, & w = f_2 \frac{P'}{\rho} \quad \text{with} \qquad (1.84) \\ f_1 &= \exp\left(\int_0^r \frac{1}{\Gamma_1} \frac{\mathrm{d}\ln P}{\mathrm{d}r} \mathrm{d}r\right) & \text{and} \quad f_2 = \exp\left(-\int_0^r \frac{N^2}{g} \mathrm{d}r\right) . \end{aligned}$$

With this change of variables, Eqs. (1.80) and (1.82) take the following form:

$$\frac{\mathrm{d}w}{\mathrm{d}r} = (\sigma^2 - N^2) \frac{f_2}{r^2 f_1} v \,, \qquad (1.85)$$

$$\frac{\mathrm{d}v}{\mathrm{d}r} = \left(\frac{{L_\ell}^2}{\sigma^2} - 1\right) \frac{r^2 f_1}{c^2 f_2} w \,. \qquad (1.86)$$

This system of two differential equations is easily simplified into one second order differential equation, either by eliminating w, which gives:

$$\frac{\mathrm{d}}{\mathrm{d}r}\left(\frac{1}{1 - {L_\ell}^2/\sigma^2} \frac{c^2 f_2}{r^2 f_1} \frac{\mathrm{d}v}{\mathrm{d}r}\right) + (\sigma^2 - N^2) \frac{f_2}{r^2 f_1} v = 0 \,, \qquad (1.87)$$

or by eliminating v, which gives:

$$\frac{\mathrm{d}}{\mathrm{d}r}\left(\frac{1}{N^2 - \sigma^2} \frac{r^2 f_1}{f_2} \frac{\mathrm{d}w}{\mathrm{d}r}\right) + \left(\frac{{L_\ell}^2}{\sigma^2} - 1\right) \frac{r^2 f_1}{c^2 f_2} w = 0 \,. \qquad (1.88)$$

1.10 p-modes and g-modes

In stellar oscillations, we can distinguish two infinite families of modes for each $\ell > 0$: the p-modes (p for pressure) and the g-modes (g for gravity). The presence of these two families was firstly proposed by Cowling (1941), and is easily predicted in the frame of the Cowling approximation.

On one hand, let's consider modes with high frequencies σ. For these modes, ${L_\ell}^2/\sigma^2$ can be neglected in Eq. (1.87). With this simplification, and because f_1 and f_2 are $>$ 0 in all the domain, Eq. (1.87) together with the appropriate boundary conditions has the classical form of a Sturm-Liouville problem and it is mathematically demonstrated that this problem has an infinite countable familly of solutions, with $\sigma^2 \longrightarrow +\infty$. These dynamically stable modes ($\sigma^2 > 0$) are called pressure modes (p-modes), because the pressure plays a dominant role in their dynamic. They have the same nature as the acoustic waves, so that we can say that studying the stellar oscillations is, in some ways, studying the music of the stars …

On the other hand, let's consider modes with low frequencies σ. For these modes, $N^2 - \sigma^2 \simeq N^2$ in Eq. (1.88). With this simplification, Eq. (1.88) together with the appropriate boundary conditions has again the classical form of a Sturm-Liouville problem, with an infinite countable familly of solutions, but now with an accumulation point of σ^2 at zero ($\sigma^2 \longrightarrow 0$). These modes are called gravity modes (g-modes), because the buoyancy force (directly linked to the gravity) plays a significant role in their dynamic. When the stellar model is purely radiative in some regions ($N^2 > 0$) and convective in other regions ($N^2 < 0$), the g-modes are subdivided into two families: the g^+ modes which are dynamically stable ($\sigma^2 > 0$) and the g^- modes which are dynamically unstable ($\sigma^2 < 0$). The latter describe the instability of the model with respect to the convection. We note that $L_\ell = 0$ for the radial modes, so that they have only p-modes.

Finally, for $\ell > 1$, there is one additional mode with frequency intermediate between the ones of p-modes and g-modes. This mode is called f-mode (f for fundamental) and has the particularity to be the alone mode which subsists in the incompressible homogeneous sphere.

An important characteristic of the eigenfunctions of p-modes and g-modes is that they have an oscillatory behaviour in some regions called "cavities". The localization of these cavities depends directly on the angular frequency σ and is thus different for each modes. Firstly, concerning the p-modes, we see from Eq. (1.87) that they have an oscillatory behaviour in the regions where $\sigma^2 > N^2$ and $\sigma^2 > {L_\ell}^2$; these regions are called p-mode cavities. Secondly, concerning the g^+-modes, we see from Eq. (1.88) that they have an oscillatory behaviour in the regions where $0 < \sigma^2 < N^2$ and $\sigma^2 < {L_\ell}^2$; these regions are called g-mode cavities and are localized deeper than the p-mode cavities. Thirdly, concerning the g^--modes, we see from Eq. (1.88) that they have an oscillatory behaviour in the regions where $N^2 < \sigma^2 < 0$, and thus only in the convection zones. These spacial oscillations properties are explained and justified in more details in the Oscillations Theorems by Scuflaire (1974a). We note that in very condensed models, some modes can have a mixed character, with an oscillatory behaviour in an inner g-mode cavity and at the same time an oscillatory behaviour in an outer p-mode cavity.

In what follows, we will no longer consider g^--modes and will omit the "+" in the designation of the g^+-modes. For a given spherical degree ℓ, the g-modes, f-mode and p-modes are classified by assigning to each mode a radial order n. $n > 0$ for the p-modes denoted $p_{|n|}$, $n = 0$ for the f-mode denoted f, $n < 0$ for the g-modes denoted $g_{|n|}$ and we have:

$$0 < \ldots < \sigma(g_i) < \ldots < \sigma(g_2) < \sigma(g_1) < \sigma(f) < \sigma(p_1) < \sigma(p_2) < \ldots < \sigma(p_i) < \ldots$$

An algorithm for the determination of the radial order n of a given mode was firstly proposed by Scuflaire (1974b), where n is determined as the difference between the number of nodes in the p-mode cavities and the number of nodes in the g-mode cavities. This algorithm is perfectly valid under the Cowling approximation and thus accurate for high values of $|n|$, but must be used with care for small values of $|n|$.

Chapter 2

Our treatment of the stellar interior and atmosphere

This chapter is based on the article we have written in collaboration with Dr. J. De Ridder and the team of Professor C. Aerts of the Katholieke Universiteit Leuven: Dupret, De Ridder et al. (2002). Pulsating stars offer us a unique opportunity to probe their internal structure and, in turn, refine our knowledge of stellar evolution and test the physics used in the models. Although precise periods can now currently be detected in multi-periodic non-radial pulsators, the identification of the observed modes remains a problem, while it is critical in providing key ingredients for asteroseismic inferences. Different methods of mode identification in pulsating stars have been developed, based on multi-colour photometry as will be explained in Section 3.2 (Watson 1988, Garrido et al. 1990, Cugier et al. 1994, Heynderickx et al. 1994, Garrido 2000), or on spectroscopic observations of line-profile variations as explained in Section 3.3.3 (Buta & Smith 1979, Aerts 1996, Telting & Schrijvers 1997). Up to now, in all the methods based on line-profile variations, the non-adiabatic character of the pulsation was entirely neglected or treated with an *ad hoc* parameter (Lee et al. 1992, Cugier 1993, Townsend 1997). The pulsation is always highly non-adiabatic in the superficial layers of a star, i.e. from the transition region (where the thermal relaxation time is of the same order as the pulsation period) to the surface. The use of the adiabatic approximation is thus inappropriate to obtain credible values for eigenfunctions such as $\delta T/T$ or $\delta\vec{F}$ in the atmosphere.

Different authors (Dziembowski 1977a; Saio & Cox 1980; Pesnell 1990) have already performed calculations of non-radial non-adiabatic stellar pulsations, but none of their studies includes a detailed treatment of the pulsation in the line forming region. The goal of this chapter is to derive such a treatment, and to show how the results obtained can be used to obtain more reliable theoretical line-profile variations. The treatment proposed here and in Dupret, De Ridder et al. (2002) is an improvement of the treatment proposed by Dupret (2001), by deriving better equations to model the temperature variations in the atmosphere (Section 2.3.1) and taking more appropriately the radiation into account in the dynamical equations (Section 2.3.2). Our treatment does not use the diffusion approximation in the atmosphere. It is based instead on the hypothesis that the atmosphere remains in radiative equilibrium during the pulsation.

Our approach can be summarized as follows. In order to obtain better eigenfunctions in the atmospheric layers, the stellar model is subdivided into two parts: the *interior* and the *atmosphere*. The equations used in the interior are briefly recalled in Section 2.1. As some of them are no longer valid in the atmosphere, we use a more adequate treatment to model the pulsation in that region, as explained in Section 2.3. The eigenfunctions are then computed globally (interior + atmosphere) using the two different sets of differential equations for the two parts of the star, and with the appropriate matching and boundary conditions. We will refer to the layer that connects the two regions as the *connecting layer*. The depth of the connecting layer depends on the kind of star. For massive stars without superficial convective layer, we choose typically the connecting layer at a Rosseland optical depth $\tau_{\rm ross} = 10$, for δ Scuti stars, we choose it at $\tau_{\rm ross} = 1$ (at the end of the thin convective layer) and for solar-like stars at the photosphere (where $T = T_{\rm eff}$), but our results are not affected by moderate changes in the choice of this layer. The outermost layer of the model corresponds to a very small optical depth ($\log \tau_{\rm ross} < -4.125$). Therefore, the whole line forming region is included in our modeling. For the sake of brevity, we use the notation τ (resp. κ) for the Rosseland mean optical depth (resp. opacity).

2.1 Treatment of the stellar interior

The formalism and numerical method we use to model and compute the non-radial non-adiabatic oscillations in the interior are almost the same as those detailed in Dupret (2001). We have chosen a Lagrangian formalism for all the perturbed variable except the perturbation of the gravitational potential.

We think that this choice of a Lagrangian formalism is the best from a numerical point of view. The surface boundary conditions and the perturbed equations of state are naturally obtained using a Lagrangian description. With a Lagrangian description, it is no longer necessary to compute derivative quantitities such as the Brunt-Väisälä frequency which are delicate to estimate from a numerical point of view. Because of the boundary conditions, the Lagrangian variations of the thermodynamical quantities: $\delta P/P$, $\delta\rho/\rho$ and $\delta T/T$, ... remain bounded in the superficial layers. But in the superficial layers of a star, dimensionless derivative quantities such as $\mathrm{d}\ln P/\mathrm{d}\ln r$, $\mathrm{d}\ln \rho/\mathrm{d}\ln r$ or $\mathrm{d}\ln T/\mathrm{d}\ln r$ are quite large, going up to values of the order of 10^3. We recall that for example $\delta P/P = P'/P + (\mathrm{d}\ln P/\mathrm{d}\ln r)\ \delta r$. Therefore, small values of $\delta P/P$ can lead to large values of P'/P. For all these reasons, from a numerical point of view, the use of Eulerian perturbations is very different from the use of Lagrangian perturbations. The only difference compared to Dupret (2001) is that we adopt here the Eulerian perturbation of the gravitational potential instead of the Lagrangian perturbation because it is better suited to the computation of high-order g-modes. Our use of Lagrangian perturbations (except for the gravitational potential) leads to a system of equations very stable from a numerical point of view.

We work in the linear approximation, we neglect the influence of rotation on the pulsation eigenfunctions, we assume a frozen convection, and finally, we use the diffusion approximation to compute the perturbed radiative flux. The equations of linear non-radial non-adiabatic oscillations have been derived in Section 1.5. For the sake of clarity, we recall below their expressions in the Lagrangian formalism we have adopted.

The radial component of the equation of momentum conservation reads:

$$\sigma^2 \xi_r = \frac{\mathrm{d}\psi'}{\mathrm{d}r} + \frac{\mathrm{d}(g\,\xi_r)}{\mathrm{d}r} + \frac{1}{\rho}\frac{\mathrm{d}(\delta P)}{\mathrm{d}r} + g\,\frac{\delta\rho}{\rho}\,. \tag{2.1}$$

The transversal component of the equation of momentum conservation reads:

$$\sigma^2 \xi_h = \frac{1}{r}\left(\psi' + g\,\xi_r + \frac{\delta P}{\rho}\right). \tag{2.2}$$

The equation of mass conservation together with Eq. (2.2) gives:

$$\frac{\delta\rho}{\rho} + \frac{1}{r^2}\frac{\mathrm{d}}{\mathrm{d}r}\left(r^2\xi_r\right) - \frac{\ell(\ell+1)}{\sigma^2 r^2}\left(\psi' + g\,\xi_r + \frac{\delta P}{\rho}\right) = 0\,. \tag{2.3}$$

The perturbed Poisson equation reads:

$$\frac{1}{r^2}\frac{\mathrm{d}}{\mathrm{d}r}\left(r^2\frac{\mathrm{d}\psi'}{\mathrm{d}r}\right) - \frac{\ell(\ell+1)}{r^2}\,\psi' = 4\pi G\left(\delta\rho - \frac{\mathrm{d}\rho}{\mathrm{d}r}\,\xi_r\right). \tag{2.4}$$

Freezing the transversal component of the Lagrangian variation of the convective flux, the equation of energy conservation reads:

$$\begin{aligned} \mathrm{i}\,\sigma T\,\delta S &= -\frac{1}{4\pi r^2\rho}\frac{\mathrm{d}\,\delta L}{\mathrm{d}r} + \epsilon\left(\frac{\delta\epsilon}{\epsilon} + \frac{\delta\rho}{\rho} + \frac{1}{r^2}\frac{\mathrm{d}\,(r^2\xi_r)}{\mathrm{d}r}\right) \\ &+ \frac{\ell(\ell+1)}{4\pi\rho\, r^3}\left(L_{\mathrm{R}}\left(\frac{\delta T}{r\,(\mathrm{d}T/\mathrm{d}r)} - \frac{\xi_r}{r}\right) - L_{\mathrm{C}}\,\frac{\xi_h}{r}\right). \end{aligned} \tag{2.5}$$

where $L = 4\pi r^2 F_r$. Under the diffusion approximation and freezing the radial component of the Lagrangian variation of the convective flux, $\delta L/L$ is given by:

$$\frac{\delta L}{L} = 2\,\frac{\xi_r}{r} + \frac{L_{\mathrm{R}}}{L}\left(3\,\frac{\delta T}{T} - \frac{\delta\kappa}{\kappa} - \frac{\delta\rho}{\rho} + \frac{\mathrm{d}\,\delta T/\mathrm{d}r}{\mathrm{d}T/\mathrm{d}r} - \frac{\mathrm{d}\,\xi_r}{\mathrm{d}r}\right). \tag{2.6}$$

On the other hand, freezing the Lagrangian variation of the convective luminosity gives:

$$\frac{\delta L}{L} = \frac{L_{\mathrm{R}}}{L}\left(2\,\frac{\xi_r}{r} + 3\,\frac{\delta T}{T} - \frac{\delta\kappa}{\kappa} - \frac{\delta\rho}{\rho} + \frac{\mathrm{d}\,\delta T/\mathrm{d}r}{\mathrm{d}T/\mathrm{d}r} - \frac{\mathrm{d}\,\xi_r}{\mathrm{d}r}\right). \tag{2.7}$$

2.2 Dimensionless formulation and central boundary conditions

The central boundary conditions are obtained by imposing the regularity of the solutions at the center (finite values for the perturbed variables and their derivatives). After some algebra, it can be shown that this condition of regularity implies that, close to the center, the radial displacement is proportional to $r^{\ell-1}$ and the other perturbed variables are proportional to r^{ℓ}. A justification of those results can be found, for example, in Unno et al. (1989, §18.1 p. 162).

When equations have to be solved numerically, it is appropriate as a preliminary step to express them in a dimensionless form. We define the following dimensionless symbols:

$$x = \frac{r}{R}\,, \quad q = \frac{m}{M}\,, \quad \omega^2 = \frac{R^3}{GM}\,\sigma^2 \quad \text{and} \quad \rho_{\mathrm{m}} = \frac{4\pi R^3}{M}\,\rho\,. \tag{2.8}$$

And we define the following dimensionless variables:

$$\zeta = \frac{1}{x^{\ell-1}}\frac{\xi_r}{R}\,, \quad \varphi = \frac{R}{GM\,x^{\ell}}\,\psi'\,, \quad \beta = \frac{4\pi R^4}{GM^2\,x^{\ell}}\,\delta P\,, \quad \gamma = \frac{1}{x^{\ell}}\frac{\delta\rho}{\rho}\,,$$

$$\eta = \frac{1}{x^{\ell}}\frac{\delta S}{c_v}\,, \quad \vartheta = \frac{1}{x^{\ell}}\frac{\delta T}{T}\,, \quad \zeta_h = \frac{1}{x^{\ell-1}}\frac{\xi_h}{R} \quad \text{and} \quad \delta\epsilon_x = \frac{1}{x^{\ell}}\frac{\delta\epsilon}{\epsilon}\,, \tag{2.9}$$

where ζ, φ, β, γ, η, ϑ, ζ_h and $\delta\epsilon_x$ are finite at the centre, because of the condition of regularity imposed at the center.

Eqs. (2.1), (2.3), (2.4), (2.5) and (2.6) can be rewritten in a dimensionless form. All the dimensionless variables and equilibrium functions have a derivative equal to zero at the centre, which gives for example for ζ:

$$\lim_{x\to 0}\frac{1}{x}\frac{\mathrm{d}\zeta}{\mathrm{d}x} = 2\,\frac{\mathrm{d}\zeta}{\mathrm{d}(x^2)}(0) = \frac{\mathrm{d}^2\zeta}{\mathrm{d}x^2}(0)\,. \tag{2.10}$$

The radial component of the equation of momentum conservation (Eq. (2.1)) becomes in a dimensionless formulation:

$$\omega^2\,x^{\ell-1}\,\zeta = \frac{\mathrm{d}\,(x^{\ell}\varphi)}{\mathrm{d}x} + \frac{\mathrm{d}\,(q\,x^{\ell-3}\,\zeta)}{\mathrm{d}x} + \frac{1}{\rho_{\mathrm{m}}}\frac{\mathrm{d}\,(x^{\ell}\,\beta)}{\mathrm{d}x} + q\,x^{\ell-2}\,\gamma\,. \tag{2.11}$$

Dividing by $x^{\ell-1}$, we find after some algebra:

$$\omega^2\zeta = \ell\left(\varphi + \frac{q}{x^3}\,\zeta + \frac{\beta}{\rho_{\mathrm{m}}}\right) + x\,\frac{\mathrm{d}}{\mathrm{d}x}\left(\varphi + \frac{q}{x^3}\,\zeta\right) + \frac{x}{\rho_{\mathrm{m}}}\frac{\mathrm{d}\beta}{\mathrm{d}x} + \frac{q}{x}\,\gamma\,. \tag{2.12}$$

It is easy to show that:

$$\lim_{x\to 0}\frac{q}{x^3} = \frac{\rho_{\mathrm{m}}}{3}\,. \tag{2.13}$$

Therefore, at the center ($x = 0$), Eq. (2.12) reduces simply to:

$$\omega^2\zeta = \ell\left(\varphi + \frac{\rho_{\mathrm{m}}}{3}\,\zeta + \frac{\beta}{\rho_{\mathrm{m}}}\right)\,. \tag{2.14}$$

The equation of mass conservation (Eq. (2.3)) gives in a dimensionless formulation:

$$\omega^2 \left(x^{\ell+2} \gamma + \frac{\mathrm{d}\,(x^{\ell+1}\,\zeta)}{\mathrm{d}x} \right) = \ell(\ell+1) \left(x^\ell\,\varphi + \frac{q}{x^3}\,x^\ell\,\zeta + \frac{x^\ell\,\beta}{\rho_\mathrm{m}} \right) = \omega^2\,\ell(\ell+1)\,x^\ell\,\zeta_h\,. \tag{2.15}$$

Dividing by x^ℓ, we obtain:

$$\omega^2 \left(x^2\,\gamma + x\,\frac{\mathrm{d}\zeta}{\mathrm{d}x} + (\ell+1)\,\zeta \right) = \ell(\ell{+}1) \left(\varphi + \frac{q}{x^3}\,\zeta + \frac{\beta}{\rho_\mathrm{m}} \right) = \omega^2\,\ell(\ell{+}1)\,\zeta_h\,. \tag{2.16}$$

Eqs. (2.12) and (2.16) degenerate to the same equation when $x \to 0$. In order to lift this degeneracy, we substitute the value of $\omega^2\zeta - \ell\,(\varphi + (q/x^3)\,\zeta + \beta/\rho_\mathrm{m})$ given by Eq. (2.12) in Eq. (2.16), we divide by x^2, and we take the limit for $x \to 0$. Using:

$$\lim_{x\to 0} \frac{\rho_\mathrm{m} - 3\,q/x^3}{x^2} = \frac{1}{5}\,\frac{\mathrm{d}^2\rho_\mathrm{m}}{\mathrm{d}x^2}\,(0)\,, \tag{2.17}$$

we obtain then the following equation at the center:

$$\omega^2 \left(\gamma + \frac{\mathrm{d}^2\zeta}{\mathrm{d}x^2} \right) + (\ell+1) \left(\frac{\mathrm{d}^2\varphi}{\mathrm{d}x^2} + \frac{\rho_\mathrm{m}}{3}\,\frac{\mathrm{d}^2\zeta}{\mathrm{d}x^2} + \frac{1}{5}\,\frac{\mathrm{d}^2\rho_\mathrm{m}}{\mathrm{d}x^2}\,\zeta + \frac{1}{\rho_\mathrm{m}}\,\frac{\mathrm{d}^2\beta}{\mathrm{d}x^2} + \frac{\rho_\mathrm{m}}{3}\,\gamma \right) = 0\,. \tag{2.18}$$

The perturbed Poisson equation (Eq. (2.4)) gives in a dimensionless formulation:

$$\frac{\mathrm{d}^2\varphi}{\mathrm{d}x^2} + \frac{2\ell+2}{x}\,\frac{\mathrm{d}\varphi}{\mathrm{d}x} = \rho_\mathrm{m} \left(\gamma - \frac{1}{x}\,\frac{\mathrm{d}\ln\rho_\mathrm{m}}{\mathrm{d}x}\,\zeta \right), \tag{2.19}$$

which is equivalent to:

$$\frac{\mathrm{d}}{\mathrm{d}x} \left(x^{2\ell+2}\,\frac{\mathrm{d}\varphi}{\mathrm{d}x} \right) = x^{2\ell+2}\,\rho_\mathrm{m} \left(\gamma - \frac{1}{x}\,\frac{\mathrm{d}\ln\rho_\mathrm{m}}{\mathrm{d}x}\,\zeta \right). \tag{2.20}$$

At the centre, Eq. (2.19) gives:

$$(2\ell+3)\,\frac{\mathrm{d}^2\varphi}{\mathrm{d}x^2} = \rho_\mathrm{m} \left(\gamma - \frac{\mathrm{d}^2\ln\rho_\mathrm{m}}{\mathrm{d}x^2}\,\zeta \right). \tag{2.21}$$

For the conservation of energy equation (Eq. (2.5)), we introduce the following dimensionless symbols:

$$k = \sqrt{\frac{R^3}{GM}}\,\frac{L(r)}{MTc_v\rho_\mathrm{m}x^3}\,, \qquad \epsilon_0 = \frac{Mx^3}{L(r)}\,\epsilon\,, \qquad \epsilon_1 = \frac{\epsilon_0\rho_\mathrm{m} - 3}{x^2}\,,$$

$$L_\mathrm{m} = L(r)/L(R)\,, \qquad LrL = \frac{L_\mathrm{R}(r)}{L(r)} \quad \text{and} \quad LcL = \frac{L_\mathrm{C}(r)}{L(r)}\,. \tag{2.22}$$

Eq. (2.5) gives then:

$$\begin{aligned} \frac{i\,\omega\,\eta}{k} = {} & \epsilon_0\,\rho_\mathrm{m} \left(\delta\epsilon_x + \gamma + \frac{1}{x^{\ell+2}}\,\frac{\mathrm{d}\,(x^{\ell+1}\,\zeta)}{\mathrm{d}x} \right) - \frac{1}{L_\mathrm{m}\,x^{\ell-1}}\,\frac{\mathrm{d}\,(L_\mathrm{m}\,(\delta L/L))}{\mathrm{d}x} \\ & + \ell(\ell+1)\,LrL \left(\frac{\vartheta}{x\,(\mathrm{d}\ln T/\mathrm{d}x)} - \frac{\zeta}{x^2} \right) - LcL \left(\gamma + \frac{1}{x^{\ell+2}}\,\frac{\mathrm{d}\,(x^{\ell+1}\,\zeta)}{\mathrm{d}x} \right) \end{aligned} \tag{2.23}$$

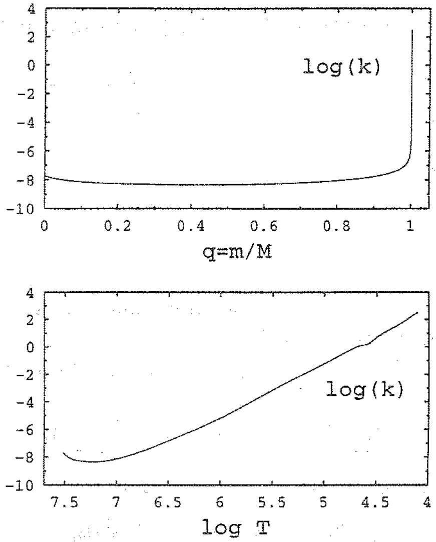

Figure 2.1: Logarithm of the dimensionless number k (defined in Eq. 2.22), as function of $q = m/M$ (top) and $\log T$ (bottom), for a 10 $M_\odot$ β Cephei model.

For the perturbed luminosity, we obtain from Eq. (2.6) (frozen convective flux):

$$\frac{\delta L}{L} = 2\,x^{\ell-2}\zeta + LrL\left[x^{\ell}\left((4-\kappa_T)\,\vartheta - (1+\kappa_\rho)\,\gamma\right) + \frac{1}{\mathrm{d}\ln T/\mathrm{d}x}\frac{\mathrm{d}(x^{\ell}\vartheta)}{\mathrm{d}x} - \frac{\mathrm{d}(x^{\ell-1}\zeta)}{\mathrm{d}x}\right]. \tag{2.24}$$

And on the other hand, with a frozen convective luminosity, Eq. (2.7) gives:

$$\frac{\delta L}{L} = LrL\left[x^{\ell}\left((4-\kappa_T)\,\vartheta - (1+\kappa_\rho)\,\gamma\right) + \frac{1}{\mathrm{d}\ln T/\mathrm{d}x}\frac{\mathrm{d}\,(x^{\ell}\,\vartheta)}{\mathrm{d}x} - x^2\,\frac{\mathrm{d}\,(x^{\ell-3}\,\zeta)}{\mathrm{d}x}\right]. \tag{2.25}$$

The three parts of a star

The dimensionless formulation of the equation of energy conservation (Eq. (2.23)) permits to see easily that a pulsating star can be divided into three parts. The important point is that the coefficient k appearing in Eq. (2.23) is of the order of the dynamical time divided by the thermal relaxation time (see Eqs. (1.1) and (1.4)) and has extremely different values in the central layers and in the superficial layers of a star. In Figure 2.1, we give the values of $\log(k)$ from the center (left) to the surface (right) of a 10 $M_\odot$ β Cephei model. The abscissa is the mass ratio $q = m/M$ in the top figure and the logarithm of temperature for the bottom figure.

We see that, in the internal layers of a star, k is extremely small, because the heat capacity is very high. Therefore, we deduce from Eq. (2.23) that the pulsation will be quasi-adiabatic ($\delta S/c_v \simeq 0$) in the main part of a star, in term of mass. We call this part of the star the **quasi-adiabatic region**. This part has a dominant weight in the integral expression for the pulsation frequencies (Eq. (1.71)). Therefore, the pulsation frequencies can be computed under the adiabatic approximation without significant loss of precision. We compared the frequencies computed by our non-adiabatic code to the ones computed with an adiabatic code and confirm this result, the difference is always negligible.

But k is increasing quickly in the superficial layers going up to significant values. Therefore, the pulsation is always highly **non-adiabatic** in the very superficial layers of a star. The reason is that, contrary to the internal layers, the heat capacity of the superficial layers is very low. In the very superficial layers, k is so high that the second term of the right hand side of Eq. (2.23) (derivative of δL) takes very low values. Therefore δL is approximately constant in the very superficial layers, so that these layers remain in very good approximation in **radiative equilibrium**. This hypothesis of radiative equilibrium is the main foundation of our non-adiabatic treatment in the stellar atmosphere, as will be explained in Section 2.3.

Between these two regions, there is a region where the thermal relaxation time is of the same order as the period of pulsation. We call this region: **the transition region**. This region is extremely important because it is there that the main driving and damping mechanisms are occuring, as will be discussed in Section 3.1.

We examine now the behaviour of these equations when $x \to 0$. With a frozen convective flux, we will see that the equation obtained by substituting Eq. (2.24) in Eq. (2.23) is regular at the center. But on the contrary, with a frozen convective luminosity, the equation obtained by substituting Eq. (2.25) in Eq. (2.23) has a singularity at $x = 0$. It is easy to show that k, ϵ_0 and ϵ_1 have finite values when $x \to 0$. Freezing the Lagrangian variation of the convective flux gives after some algebra the following equation at the center:

$$\begin{aligned}\frac{i\,\omega\,\eta}{k} \;&=\; 3(\delta\epsilon_x + \gamma) \,-\, LcL\,\gamma \,-\, LrL\,(\ell+3)\,\big((4 - \kappa_T)\,\vartheta \,-\, (1+\kappa_\rho)\,\gamma\big)\\ &-\; \ell\,\frac{x^3}{L_\mathrm{m}}\frac{\mathrm{d}^2}{\mathrm{d}x^2}\left[\frac{(LrL)\,L_\mathrm{m}}{x^2\,(\mathrm{d}\ln T/\mathrm{d}x)}\right]\vartheta \,-\, (2\ell+3)\,LrL\,\frac{x}{\mathrm{d}\ln T/\mathrm{d}x}\,\frac{\mathrm{d}^2\vartheta}{\mathrm{d}x^2}\\ &+\; (\ell-1)\left[\epsilon_1\,(1 + LrL) + \frac{\mathrm{d}^2(LrL)}{\mathrm{d}x^2}\right]\zeta \,+\, (2\ell+3)\,LrL\,\frac{\mathrm{d}^2\zeta}{\mathrm{d}x^2}\,.\end{aligned} \tag{2.26}$$

We note that all the terms of Eq. (2.26) are finite at the center.

For a frozen convective luminosity, we obtain a similar result, but with an additional term which is singular at the center. This singular term is:

$$2\,(\ell+1)\,LcL\,\frac{\zeta}{x^2}\,. \tag{2.27}$$

Therefore, freezing the Lagrangian variation of the convective luminosity is inappropriate in central convective zones.

2.3 Treatment of the atmosphere

The system of equations used in the interior is no longer valid in the atmosphere, for two reasons. Firstly, the diffusion equation relating the radiative flux to the local gradient of temperature is no longer valid, and secondly, the interior approximation of the radiative pressure

$$P_{\rm R} = \frac{1}{3}\, a\, T^4 \tag{2.28}$$

is also no longer valid in the atmosphere. In Section 2.3.1, we explain how Eqs. (2.5) and (2.6) can be replaced by a more appropriate one. Avoiding Eq. (2.28) will require a rewriting of the momentum equation, as explained in Section 2.3.2. In Section 2.3.3, we give the surface boundary conditions used to close the problem.

2.3.1 Radiative equilibrium in the local atmosphere

In a non-radially pulsating star, all the eigenfunctions have an angular dependence. It is therefore useful to define a "local atmosphere" as the gas column at a given angular position (θ, φ), and at a given time. In what follows we will always refer to this local atmosphere although we will often omit the word "local" for the sake of brevity.

An important property of the atmosphere of a pulsating star is that its heat capacity is very small. Defining the thermal relaxation time of the atmosphere as the time necessary for it to lose all its internal energy with a luminosity L:

$$\tau_{\rm th} \; = \; \int_{\rm atm.} T\, c_v\, {\rm d}m \;/\; L \tag{2.29}$$

(in this case, the bottom of the atmosphere is at an optical depth $\tau = 1$), we find that, for the atmosphere of near-main sequence variable stars, $\tau_{\rm th} \approx 1\, s$, which is much smaller than the typical pulsation periods. In a very good approximation, we can therefore assume that the local atmosphere remains in *radiative equilibrium* during the pulsation ($\nabla \cdot \overrightarrow{F} = 0$).

A hydrostatic equilibrium atmosphere model in the plane-parallel approximation is entirely determined by its effective temperature $T_{\rm eff}$, its gravity g and its chemical composition. Given the chemical composition, the local temperature can therefore be written as a function of the Rosseland mean optical depth τ, $T_{\rm eff}$ and g:

$$T = T(\tau, T_{\rm eff}, g). \tag{2.30}$$

Considering the radiative equilibrium property of the local atmosphere, our main approximation is to assume that, at each phase during the pulsation cycle, the $T(\tau)$ law in the local atmosphere is the same as the $T(\tau)$ law of an equilibrium atmosphere model. During the pulsation, the two parameters $T_{\rm eff}$ and g characterising the equilibrium atmosphere model, and thus the *local* atmosphere, are varying with time and are function of θ and φ. For a given time and a given (θ, φ), the temperature in the local atmosphere (equilibrium value + perturbation) is thus given by:

$$T_0 + \delta T = T(\tau_0 + \delta\tau\,,\ T_{\mathrm{eff}\,0} + \delta T_{\mathrm{eff}}\,,\ g_0 + \delta g_{\mathrm{e}}). \tag{2.31}$$

$\delta\tau$ is the Lagrangian perturbation of the Rosseland mean optical depth whereby we remark that layers of constant optical depth do not follow the motion of matter. δT_{eff} is the variation of the effective temperature of the local atmosphere. δg_{e} is the variation of the local gravity from the point of view of a comoving frame, i.e. the gravity corrected for the pulsational acceleration.

In the linear approximation, Eq. (2.31) gives:

$$\frac{\delta T}{T} = \frac{\partial \ln T}{\partial \ln T_{\mathrm{eff}}}\,\frac{\delta T_{\mathrm{eff}}}{T_{\mathrm{eff}}} + \frac{\partial \ln T}{\partial \ln g_{\mathrm{e}}}\,\frac{\delta g_{\mathrm{e}}}{g_{\mathrm{e}}} + \frac{\partial \ln T}{\partial \ln \tau}\,\frac{\delta\tau}{\tau}. \tag{2.32}$$

For a given mode, the different perturbed quantities appearing in this equation are proportional to the spherical harmonic $Y_\ell^m(\theta,\varphi)$. Perturbing the definition of the Rosseland mean optical depth leads to:

$$\frac{\partial\delta\tau}{\partial\tau} = \frac{\delta\kappa}{\kappa} + \frac{\delta\rho}{\rho} + \frac{\partial\,\xi_r}{\partial r}. \tag{2.33}$$

And finally, eliminating $\delta\tau$ between Eq. (2.32) and Eq. (2.33) gives:

$$\begin{aligned}
\frac{\partial(\delta T/T)}{\partial \ln\tau} &= \frac{\partial \ln T}{\partial \ln \tau}\left(\frac{\delta\kappa}{\kappa} + \frac{\delta\rho}{\rho} + \frac{\partial\,\xi_r}{\partial r}\right)\\
&- \left(1 - \frac{\partial^2 \ln T/\partial \ln\tau^2}{\partial \ln T/\partial\ln\tau}\right)\left(\frac{\delta T}{T} - \frac{\partial \ln T}{\partial \ln T_{\mathrm{eff}}}\,\frac{\delta T_{\mathrm{eff}}}{T_{\mathrm{eff}}} - \frac{\partial \ln T}{\partial \ln g_{\mathrm{e}}}\,\frac{\delta g_{\mathrm{e}}}{g_{\mathrm{e}}}\right)\\
&+ \frac{\partial^2 \ln T}{\partial\ln\tau\,\partial\ln T_{\mathrm{eff}}}\,\frac{\delta T_{\mathrm{eff}}}{T_{\mathrm{eff}}} + \frac{\partial^2 \ln T}{\partial\ln\tau\,\partial\ln g_{\mathrm{e}}}\,\frac{\delta g_{\mathrm{e}}}{g_{\mathrm{e}}}.
\end{aligned} \tag{2.34}$$

It is Eq. (2.34) that we use instead of Eqs. (2.5) and (2.6) in the atmosphere. The different derivatives appearing in this equation are numerically estimated using a family of hydrostatic equilibrium atmosphere models with different effective temperatures and gravities bracketing those of the reference equilibrium model around which the star is oscillating. In our applications, we use the atmosphere models by Kurucz (1993). How we compute $\delta T_{\mathrm{eff}}/T_{\mathrm{eff}}$ and $\delta g_{\mathrm{e}}/g_{\mathrm{e}}$ is explained in Section 2.3.3.

2.3.2 Acceleration due to the radiation

In the previous section, we argued that the temperature distribution of the local atmosphere can be obtained from an equilibrium atmosphere model. The pressure and density distributions as well as the displacement vector, however, must be computed by solving the equations of conservation of mass and momentum in the entire atmosphere. In what follows we explain how this is done.

In the outer atmosphere of a star, the radiation field is no longer isotropic. As a consequence, the radiation pressure tensor cannot be represented anymore by a diagonal matrix $P_{\rm R}\,\mathbb{I}$, where $P_{\rm R}$ is a scalar and $\mathbb{I}$ is the identity, and the law $P_{\rm R} = (1/3)\,a\,T^4$ is no longer valid (see e.g. Mihalas 1999, §66). We recall that the equilibrium quantities we use in the atmosphere are obtained from the models of Kurucz (1993). In these models, the total pressure gradient is split up into the gas pressure gradient and the acceleration due to the radiation (see Kurucz 1970, §2.11). In the perturbed model, we proceed in the same way, which permits to keep the consistency with the equilibrium model. The momentum equation reads then:

$$\frac{\partial \vec{v}}{\partial t} + \vec{v}\cdot\nabla\vec{v} = -\nabla\psi - \frac{\nabla P_{\rm g}}{\rho} + \vec{a_{\rm R}}\,, \tag{2.35}$$

where $\vec{v}$ is the velocity, $P_{\rm g}$ is the gas pressure and $\vec{a_{\rm R}}$ is the acceleration vector due to the radiation. In this case, the flux-weighted mean opacity $\kappa_{\rm F}$ is very useful since it can relate directly the acceleration due to the radiation to the flux:

$$\vec{a_{\rm R}} = \kappa_{\rm F}\,\vec{F}/c\,, \tag{2.36}$$

(see e.g. Mihalas 1999, §82). To obtain the perturbed momentum equation, we make the following assumptions:

a1) We assume that $\delta|\vec{F}|$ remains constant from the base of the atmosphere to the outermost layer.

a2) We assume that the flux vector $\vec{F}$ is parallel with $-\nabla T$ during the entire pulsation cycle.

a3) We approximate the relative variation of the flux-weighted mean opacity by the relative variation of the Rosseland opacity: $\delta\kappa_{\rm F}/\kappa_{\rm F} \simeq \delta\kappa/\kappa$.

To justify assumption (a1), we recall that the equilibrium atmosphere models we use (Kurucz models) are obtained assuming that the atmosphere is in radiative equilibrium and that it is so thin that a plane parallel approximation can be adopted. These two hypotheses imply that the equilibrium flux is assumed to be constant. As pointed out in Section 2.3.1, the very small thermal relaxation time of the atmosphere permits us to assume that the local atmosphere remains in radiative equilibrium during the pulsation. This leads us to assume, for the same reasons as in equilibrium, that $\delta|\vec{F}|$ remains constant in the atmosphere. Under the diffusion approximation, assumptions (a2) and (a3) are clearly valid (see e.g. Mihalas (1999, §82) for the equivalence between the two mean opacities). Assumptions (a2) and (a3) do not imply that the diffusion approximation is valid, because we adopt the equilibrium values of $\vec{a}_{\rm R}$ given by the atmosphere models of Kurucz, instead of obtaining them by computing the derivative of Eq.(2.28). It is not easy to examine to what extent assumptions (a2) and (a3) remain valid in the outermost layers of the atmosphere. We did different tests by changing artificially the coefficients of the equations associated to these assumptions and the conclusion is that the errors coming from them have a negligible impact on the final results of our study.

Assumption (a1) together with Stefan's law gives at first order:

$$\frac{\delta|\vec{F}|}{|\vec{F}|} = \frac{\delta F_r}{F_r} = 4\frac{\delta T_{\mathrm{eff}}}{T_{\mathrm{eff}}} \, . \tag{2.37}$$

Then, assumption (a3) together with Eq. (2.36) gives, for the radial component of $\delta\vec{a}_{\mathrm{R}}$:

$$(\delta\vec{a}_{\mathrm{R}})_{\mathrm{r}} = a_{\mathrm{R}}\left(\frac{\delta\kappa}{\kappa} + 4\frac{\delta T_{\mathrm{eff}}}{T_{\mathrm{eff}}}\right) . \tag{2.38}$$

In the following equations, a_{R} corresponds to the equilibrium value of the acceleration due to the radiation. This quantity is obtained at each layer directly from the Kurucz atmosphere models. From Eqs. (2.35) and (2.38) and after some algebra, we find the following expression for the radial component of the equation of momentum conservation:

$$\begin{aligned} \sigma^2\xi_r &= \frac{\partial(\delta P_{\mathrm{g}}/P_{\mathrm{g}})}{\partial r}\frac{P_{\mathrm{g}}}{\rho} \\ &+ \frac{\partial\psi'}{\partial r} + \frac{\partial(g\,\xi_r)}{\partial r} + \left(\frac{\delta\rho}{\rho} - \frac{\delta P_{\mathrm{g}}}{P_{\mathrm{g}}}\right)(g - a_{\mathrm{R}}) \\ &- a_{\mathrm{R}}\left(\frac{\delta\kappa}{\kappa} + 4\,\frac{\delta T_{\mathrm{eff}}}{T_{\mathrm{eff}}} + \frac{\partial\,\xi_r}{\partial r}\right) . \end{aligned} \tag{2.39}$$

Assumption (a2) is used to compute the transversal component of the momentum equation, and we find:

$$\sigma^2\xi_h = \frac{1}{r}\left(\frac{\delta P_{\mathrm{g}}}{\rho} + \psi' + g\,\xi_r - a_{\mathrm{R}}\,\frac{\delta T}{\partial T/\partial r}\right) . \tag{2.40}$$

Consequently, the continuity equation reads:

$$\frac{\delta\rho}{\rho} + \frac{1}{r^2}\frac{\partial}{\partial r}\left(r^2\xi_r\right) = \frac{\ell(\ell+1)}{\sigma^2 r^2}\left(\frac{\delta P_{\mathrm{g}}}{\rho} + \psi' + g\,\xi_r - \frac{a_{\mathrm{R}}\,\delta T}{\partial T/\partial r}\right) . \tag{2.41}$$

Eqs. (2.39) and (2.41) are used in the atmosphere instead of Eqs. (2.1) and (2.3). In the following subsection, we will show that these two sets of equations coincide at the connecting layer between interior and atmosphere.

2.3.3 Boundary and matching conditions

The matching conditions we impose are the continuity of the different perturbed variables at the connecting layer between the interior and the atmosphere. It is important to choose the connecting layer between interior and atmosphere at a place where the flux is purely radiative, or at least where the convective flux is negligible compared to the radiative flux. The reason will be given in the last paragraph of Section 2.4. The matching condition imposed on the perturbed flux allows us to compute $\delta T_{\rm eff}/T_{\rm eff}$. Indeed, from Eqs. (2.6) and (2.37), we find at the connecting layer:

$$3\,\frac{\delta T}{T} - \frac{\delta\kappa}{\kappa} - \frac{\delta\rho}{\rho} + \frac{{\rm d}\delta T/{\rm d}r}{{\rm d}T/{\rm d}r} - \frac{{\rm d}\,\xi_r}{{\rm d}r} = 4\frac{\delta T_{\rm eff}}{T_{\rm eff}}\,. \tag{2.42}$$

Also $\delta g_{\rm e}/g_{\rm e}$ is obtained at the connecting layer. The variation of the gravity from the point of view of a comoving frame reads:

$$\delta g_{\rm e} = -(\delta \vec{g_{\rm e}})_r = \delta(\partial\psi/\partial r) - \sigma^2\xi_r\,. \tag{2.43}$$

After some simple derivations, we find then:

$$\frac{\delta g_{\rm e}}{g_{\rm e}} = \frac{\partial\psi'/\partial r}{g} + \frac{4\pi\rho\, r^3}{m}\,\frac{\xi_r}{r} - \left(2+\frac{\sigma^2 r}{g}\right)\frac{\xi_r}{r}\,. \tag{2.44}$$

And we note that under the Cowling approximation and neglecting the surface density divided by the mean density of the star, this equation takes the very simple form:

$$\frac{\delta g_{\rm e}}{g_{\rm e}} = -\left(2+\frac{\sigma^2 r}{g}\right)\frac{\xi_r}{r}\,. \tag{2.45}$$

It is important to realize that Eqs. (2.39) and (2.41) mathematically coincide with Eqs. (2.1) and (2.3) at the connecting layer. This follows directly from Eqs. (2.28) and (2.42). As a consequence, the derivatives of ξ_r/R and $\delta P_{\rm g}/P_{\rm g}$ are continuous at the connecting layer. The continuity of the derivative of $\delta T/T$ at the connecting layer is not imposed by the equations. For all the modes we have computed, the smoothness of $\delta T/T$ at the connecting layer was found a posteriori (see Chapter 4, Figures 4.13 and 4.30 for β Cephei and SPB models with the connecting layer at $\log\tau = 1$ and Figure 4.50 for a δ Scuti model with the connecting layer at $\log\tau = 0$). This confirms the validity of our treatment.

Different boundary conditions have to be imposed at the outermost layer of the model. Firstly, we have the mechanical boundary condition. Usually, the mechanical boundary condition is obtained by assuming that the third term of the right hand side of Eq. (1.60) goes to zero at the surface, which gives the boundary condition Eq. (1.61). This condition is justified either by assuming that $\lim_{\tau\to 0} P/(\rho\, g\, R) = 0$ (Cox 1980, §17.6b) or by assuming that $\partial(\delta P/P)/\partial r = 0$ at the surface (Pesnell 1990). However, for massive stars such as β Cephei stars and SPBs, the acceleration due to the radiation ($\vec{a_{\rm R}}$) cannot be neglected in Eq. (2.35). Our mechanical boundary condition is obtained by neglecting the contribution due to the gas pressure alone. More precisely, we neglect the first term of Eq. (2.39) at the surface, and the mechanical boundary condition reads:

$$\begin{aligned}\sigma^2\xi_r \;&=\; \frac{\partial\psi'}{\partial r} + \frac{\partial(g\,\xi_r)}{\partial r} + \left(\frac{\delta\rho}{\rho} - \frac{\delta P_{\rm g}}{P_{\rm g}}\right)(g - a_{\rm R}) \\ &\quad - a_{\rm R}\left(\frac{\delta\kappa}{\kappa} + 4\,\frac{\delta T_{\rm eff}}{T_{\rm eff}} + \frac{\partial\,\xi_r}{\partial r}\right)\,. \end{aligned} \tag{2.46}$$

The potential boundary condition is, as usual, obtained by imposing a first order continuous match (i.e. continuity of ψ' and its first derivatives) between the inner solution of the Poisson equation and the outer solution of the Laplace equation (Ledoux & Walraven 1958):

$$\frac{\partial \psi'}{\partial r} + \frac{\ell+1}{r}\,\psi' = -4\pi G \rho\, \xi_r\,. \tag{2.47}$$

Finally, also Eq. (2.34) needs a boundary condition. It is obtained by evaluating Eq. (2.32) at the outermost layer. Using the rule of l'Hospital and Eq. (2.33) to evaluate $\lim_{\tau\to 0}\delta\tau/\tau$, we obtain the following boundary condition at the surface:

$$\frac{\delta T}{T} = \frac{\partial \ln T}{\partial \ln T_{\rm eff}}\frac{\delta T_{\rm eff}}{T_{\rm eff}} + \frac{\partial \ln T}{\partial \ln g_{\rm e}}\frac{\delta g_{\rm e}}{g_{\rm e}} + \frac{\partial \ln T}{\partial \ln \tau}\left(\frac{\delta\kappa}{\kappa} + \frac{\delta\rho}{\rho} + \frac{\partial\,\xi_r}{\partial r}\right). \tag{2.48}$$

2.4 Comparison with other approximations

To place our approximation in a broader context, we first recall the basic approximations made in three different equilibrium atmosphere models: the Eddington atmosphere, the grey atmosphere and the non-grey (e.g. Kurucz) atmosphere.

The Eddington atmosphere is a plane-parallel, grey atmosphere, in radiative equilibrium and in LTE, where it is assumed that $J = 3K$ (J is the mean intensity and K is the second angular moment of the radiation field). In a radiative zone, the temperature distribution of an Eddington atmosphere obeys the following well known law:

$$T^4(\tau) = \frac{3}{4}\,T_{\rm eff}^4\left(\tau + \frac{2}{3}\right). \tag{2.49}$$

For a more general grey atmosphere, it is not assumed that $J = 3K$, and the temperature distribution is given by

$$T^4(\tau) = \frac{3}{4}\,T_{\rm eff}^4\left(\tau + q(\tau)\right), \tag{2.50}$$

where $q(\tau)$ is the well known Hopf function, which can be determined analytically as well as numerically (see e.g. Mihalas 1978). We note that the Hopf function is unique, it does not depend on the effective temperature and gravity of the atmosphere.

Finally, if we consider much more precise non-grey atmospheres (such as the models of Kurucz), the temperature distribution takes a general form given by Eq. (2.30). We emphasize that non-grey Kurucz atmospheres differ significantly from Eddington and grey atmospheres. In Figure 2.2, we compare the temperature distribution of a Kurucz atmosphere to the one of an Eddington atmosphere for a 10 $M_\odot$ β Cephei model. We see that the two distributions are very different in most of the atmosphere. In particular, the steep temperature gradient found up to very small optical depths in the Kurucz atmosphere is not present in the Eddington atmosphere.

Our method is easily understood by following the same line of reasoning, going from Eddington atmospheres to non-grey atmospheres, in the case of pulsating stars. More

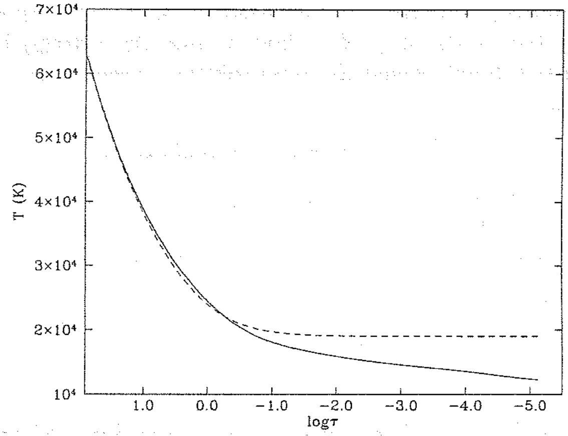

Figure 2.2: Temperature distribution of a Kurucz atmosphere model (solid line) compared to the one of an Eddington model (dashed line), in the atmosphere of a 10 $M_\odot$ β Cephei model. The abscissa corresponds to the logarithm of the Rosseland optical depth

precisely, in a pulsating star and in a radiative zone, the Eddington approximation leads to the following equations (Saio & Cox 1980; Balmforth 1992):

$$\vec{F} = -\frac{4\pi}{3\kappa\rho}\,\nabla J\,, \tag{2.51}$$

$$J = \frac{acT^4}{4\pi} + \frac{T}{4\pi\kappa}\,\frac{dS}{dt}\,. \tag{2.52}$$

In a plane-parallel atmosphere at radiative equilibrium, this system of equations reduces to Eq. (2.49) (see e.g. Mihalas 1999 §82). In particular, we note that the hypothesis of hydrostatic equilibrium need not be made in order to obtain Eqs. (2.49) and (2.50). In the beginning of Section 2.3.1, we argued that the hypothesis of radiative equilibrium can be applied to the perturbed atmosphere, and the plane-parallel hypothesis is certainly acceptable in our applications. Therefore, adopting the Eddington approximation in the atmosphere of a pulsating star reduces in very good approximation to perturbing Eq. (2.49). For the same physical reasons, making the grey approximation in the atmosphere of a pulsating star leads simply to perturbing Eq. (2.50), an approach which is adopted by Dupret (2001). In the treatment we propose in this section, we proceed in the same way, but now for the more realistic non-grey atmosphere models, which leads us to perturb Eq. (2.30).

We conclude that the Eddington approximation as well as the grey atmosphere approximation are particular cases of the more general approach presented in Section 2.3.1. As the Eddington and grey atmospheres do not lead to a good temperature distribution in the outer layers of the atmosphere (see Figure 2.2), the gain is significant when using more realistic non-grey atmosphere models as we do. It is important to note that, in the general method of small perturbations, the use of an approximation (e.g. the Eddington approximation) in the perturbed model makes sense if and only if it is made in the equilibrium model as well. Therefore, one of the main advantages of our method is simply that it *permits* to use better equilibrium models (the Kurucz atmosphere models).

It could be argued that consistency is somehow lost in our method, because the Kurucz atmosphere models make explicitly the hypothesis of hydrostatic equilibrium, which is not valid for pulsating stars. We argue however, that the gain with our method is significant. Firstly, the apparent loss of consistency is not important for the high order g-modes of Slowly Pulsating B stars and for the low order p-modes of β Cephei and δ Scuti stars. If we compare, for example, the values of $\delta P_g/P_g$ obtained by our method (solving the momentum equations throughout the entire atmosphere) to the ones consistent with the static Kurucz models, we find relative differences between 10 and 20%, depending on the mode order. Secondly, the coupling between the thermal structure of the atmosphere ($T(\tau)$ and T_{eff}) and its dynamical structure (linked in first approximation to its effective gravity) is generally small. The coefficient $\partial \ln T/\partial \ln g_{\text{e}}$ appears to be much smaller than $\partial \ln T/\partial \ln T_{\text{eff}}$, and even with the significant values of $\delta g_{\text{e}}/g_{\text{e}}$ found for the β Cephei p-modes, the corresponding term in Eq. (2.32) remains much smaller than the two other ones (see Figure 4.13 in Section 4.1.5). It is only for high order p-modes with frequencies close to the acoustic cut-off, that our use of hydrostatic Kurucz models becomes more questionable. For such modes, the only rigorous way would be to solve explicitly the perturbed equations of radiation hydrodynamics, which is beyond the scope of our current study.

We do not claim that the use of the Eddington and diffusion approximations are inappropriate in the study of non-adiabatic oscillations. For the study of the excitation and damping mechanisms in pulsating stars, these approximations remain appropriate when these mechanisms occur in layers much deeper than the atmosphere. Similarly, the adiabatic approximation remains suitable for the computation of the frequencies of g-modes and moderate order p-modes, as they are determined mostly by the internal layers.

We note that a better thermal boundary condition has been proposed by Gabriel (1989). The problem with Gabriel's treatment is that it applies only to the very superficial layers of a star, where matter and radiation no longer interact, but no treatment is proposed between the photosphere and these very superficial layers.

Finally, we remark that the natural path going from the Eddington approximation to our better treatment makes sence only when there is no convection in the atmosphere. In a convection zone, the Eddington approximation ($J = 3K, \dots$) no longer implies Eq. (2.49). More generally, there is no longer a simple link between the $T(\tau)$ distribution and the hypothesis of energy balance ($\nabla \cdot \overrightarrow{F} = 0$). We have thus no physical reasons to expect that the $T(\tau)$ distribution in the perturbed atmosphere is the same as the one of equilibrium atmosphere models in a convection zone. For stars with an envelope convection zone, it is thus important to choose the connecting layer sufficiently outside, so that the atmosphere is radiative.

Chapter 3

Utility of our non-radial non-adiabatic code

Our non-adiabatic code has different utilities. Firstly, it is a direct tool for the study of the driving mechanisms of pulsating stars, as will be detailed in Section 3.1. Secondly, it improves significantly the discriminant power of mode identification methods based on multi-colour photometry; and, by an appropriate confrontation between theory and observations, it can be used to constrain stellar models, as will be detailed in Section 3.2. And finally, it can be used to determine the influence of temperature variations on line-profile variations, as will be detailed in Section 3.3.

3.1 Driving mechanisms and stellar stability

One of the main utilities of a non-adiabatic code is that it is able to determine which modes of a pulsating star are vibrationally stable and which are vibrationally unstable. Moreover, the code permits to localize exactly the position of the driving and damping regions of a star and to interpret physically the driving origin and mechanism, when it occurs.

As explained in Section 1.5.2, the stability or instability of a mode (or more precisely its growth or damping rate) is directly deduced from the imaginary part of the angular frequency σ. We recall that, in our linear formalism, the time dependence of a pulsation mode is of the form $e^{i\sigma t}$, where σ is complex. We see therefore that, if $\Im(\sigma) > 0$ then the mode is stable and the damping rate is $\Im(\sigma)$, and if $\Im(\sigma) < 0$ then the mode is unstable and the growth rate is $-\Im(\sigma)$. The exact value of σ (real and imaginary part) is computed by our non-adiabatic code, so that we can determine directly which modes of a stellar model are vibrationally stable and which are vibrationally unstable. We note that in practical cases, the pulsation is quasi-adiabatic in the main part of the star. As a direct consequence, the imaginary part of σ is much smaller than the real part, typically $|\Im(\sigma)|/|\Re(\sigma)| \approx \tau_{\text{dyn}}/\tau_{\text{HK}} \approx 10^{-6}$ (see Eqs. (1.1) and (1.3) for the definition of $\tau_{\rm dyn}$ and $\tau_{\rm HK}$). Therefore, much care has to be given to the numerical algorithm of solution, in order to determine $\Im(\sigma)$ with high precision.

We have derived in Section 1.8 an integral expression for $\Im(\sigma)$. This equation is very useful for the physical interpretation of the driving mechanisms of pulsating stars and we recall it here for the sake of clarity:

$$\Im\{\sigma\} = \frac{1}{2\,\Re\{\sigma\}} \frac{\displaystyle\int_0^M \Im\left\{\frac{\overline{\delta\rho}}{\rho}T\delta S\right\}(\Gamma_3-1)\,\mathrm{d}m}{\displaystyle\int_0^M \left(|\xi_r|^2+\ell(\ell+1)\,|\xi_h|^2\right)\mathrm{d}m}\,. \tag{3.1}$$

On one hand, it is easily shown after some algebra, that the local work per unit of mass done by the system during one cycle of pulsation is:

$$\oint P\,\mathrm{d}v = -\pi\,\Im\left\{\frac{\overline{\delta\rho}}{\rho}\frac{\delta P}{\rho}\right\} = -\pi\,\Im\left\{\frac{\overline{\delta\rho}}{\rho}T\delta S\right\}(\Gamma_3-1)\,. \tag{3.2}$$

The average power of the thermodynamical cycle of pulsation of the entire star is obtained by integrating Eq. (3.2) over the entire mass of the star and dividing by the pulsation period:

$$\mathcal{P} = \frac{\mathrm{d}\mathcal{E}}{\mathrm{d}t} = -\frac{\Re\{\sigma\}}{2}\int_0^M \Im\left\{\frac{\overline{\delta\rho}}{\rho}T\delta S\right\}(\Gamma_3-1)\,\mathrm{d}m\,. \tag{3.3}$$

On the other hand, it can be shown that the total energy (kinetic energy + acoustic potential energy + gravitational potential energy) of a pulsation mode is:

$$\mathcal{E} = \frac{\Re\{\sigma\}^2}{2}\int_0^M \left(|\xi_r|^2+\ell(\ell+1)\,|\xi_h|^2\right)\mathrm{d}m\,. \tag{3.4}$$

By combining Eqs. (3.1), (3.3) and (3.4), we find thus:

$$\frac{\mathrm{d}\mathcal{E}/\mathrm{d}t}{\mathcal{E}} = -2\,\Im\{\sigma\}\,. \tag{3.5}$$

The physical interpretation of the above equations is immediate. If $\Im\{\sigma\} < 0$ then the total energy of the unstable mode increases with a growth rate $-2\,\Im\{\sigma\}$ (the factor 2 comes from the fact that the energy is proportional to the square of the velocity) and if $\Im\{\sigma\} > 0$ then the total energy of the stable mode decreases with a damping rate $2\,\Im\{\sigma\}$. The opposite of the numerator of Eq. (3.1) is proportional to the work done by the entire star during one thermodynamical cycle. By truncating this integral at a given layer, we get the work done by the part of the star beneath this layer during one cycle, which gives directly the effect of the different layers on the driving or damping of the star. The parts of the stars where $\Im\{(\overline{\delta\rho}/\rho)T\delta S\} < 0$ are driving the stellar pulsation and the parts of the star where $\Im\{(\overline{\delta\rho}/\rho)T\delta S\} > 0$ are damping the stellar pulsation. All the above quantities are computed by our non-adiabatic code, so that we can analyze and localize the driving mechanisms for a given stellar model.

We have shown in Section 2.2 that a star can be subdivided into three parts: the internal quasi-adiabatic region where $\delta S/c_v \simeq 0$, the transition region where the thermal relaxation time is of the same order as the period of pulsation and the very superficial region where the pulsation is highly non-adiabatic. It is easy to see that the region which will play the main role in the driving and damping mechanisms is the transition region. The quasi-adiabatic region does not play in general a significant role because $\delta S \simeq 0$ there (see Eq. (3.1)), and the very superficial region does not play a significant role because its heat capacity is very low, so that δL is approximately constant there (see Eq. (3.6)).

The main driving mechanism of the variable stars studied in the present work is usually named the κ-mechanism or κ-γ-mechanism. A qualitative explanation of this mechanism was firstly proposed by Cox (1967). In order to simplify the explanation, we will work now in the quasi-adiabatic approximation. Since the driving region (transition region) is generally situated close to the quasi-adiabatic region, this approximation is appropriate for the following discussion. Moreover, we consider radial modes. Under these assumptions, we showed in Section 1.9.2 that Eq. (3.1) reduces to Eq. (1.78), which gives, using Eq. (1.76):

$$\Im\{\sigma\} = \frac{1}{2\,\sigma_0{}^2} \frac{\displaystyle\int_0^M \frac{\delta T}{T}\left(\frac{d\,\delta L}{dm} - \delta\epsilon\right) dm}{\displaystyle\int_0^M \xi_r{}^2\, dm}\,, \tag{3.6}$$

And we see the two terms which can have a driving effect on the star: a term proportional to $\delta\epsilon$ (nuclear reactions term) and a term proportional to $\mathrm{d}\,\delta L/\mathrm{d}m$ (transport term). The nuclear reactions term gives the excitation due to the nuclear reactions. Except for very massive stars ($M > 20\,M_\odot$), this term does not play in a significant role in general, because the nuclear reactions occur in the very central layers were the pulsation is quasi-adiabatic. We will not discuss its influence here. The transport term is thus generally at the origin of the stability or instability of stars. From Eq. (3.6), we see that the regions where δL is decreasing outwards at the hot phase ($\delta T > 0$) have a driving effect on the star. From a thermodynamic point of view, this case corresponds to a motor cycle where energy is taken by the system at the hot phase and released at the cold phase. On the contrary, the regions where δL is increasing outwards at the hot phase have a damping effect. For a radial mode and a frozen convective luminosity, the perturbed luminosity is given by:

$$\frac{\delta L}{L} = \frac{L_\mathrm{R}}{L}\left(4\,\frac{\xi_r}{r} + 3\,\frac{\delta T}{T} - \frac{\delta\kappa}{\kappa} + \frac{\partial\delta T/\partial r}{\mathrm{d}T/\mathrm{d}r}\right). \tag{3.7}$$

We focus on the term $-\delta\kappa/\kappa$ which plays in general a dominant role on the variation of the luminosity. In the quasi adiabatic approximation, we can write:

$$\frac{\delta\kappa}{\kappa} = \kappa_\mathrm{PS}\,\frac{\delta P}{P} = \frac{(\Gamma_3 - 1)\kappa_T + \kappa_\rho}{\Gamma_1}\,\frac{\delta P}{P}\,. \tag{3.8}$$

The choice of $\delta P/P$ is appropriate because it is always a very smooth eigenfunction, not much affected by the opacity bumps, partial ionization zones and convection zones, contrary to other eigenfunctions ($\delta T/T$, $\delta\rho/\rho$, ...). This smooth behaviour of $\delta P/P$ is due to the control by the equation of momentum conservation.

In usual circumstances (e.g. Kramers opacity law, complete ionization) we have $\kappa_{\rm PS} \simeq -0.8$. Since $\delta P/P$ is generally increasing outwards at the hot phase, the contribution of $-\delta\kappa/\kappa$ in Eq. (3.7) implies that $\delta L/L$ is increasing outwards at the hot phase, which has a damping effect on the pulsation.

However, in the superficial layers of a star, large opacity bump(s) are present in the regions of partial ionization (see the graphs of κ in Figures 4.4, 4.23 and 4.41). These opacity bumps can have a significant driving effect on the star. More precisely, in parts of these regions, $\kappa_{\rm PS}$ is increasing very steeply outwards and can take positive values. Therefore, in these regions, the contribution of $-\delta\kappa/\kappa$ implies that $\delta L/L$ is decreasing outwards at the hot phase, which has a driving effect on the pulsation. This mechanism is called the κ-mechanism. The adiabatic exponents Γ_3 and Γ_1 are also significantly affected by the partial ionization zones, and play thus also an important role in this mechanism. For this reason, it is sometimes called the κ-γ-mechanism. It is efficient when it occurs in the transition region and thus when a partial ionization zone is situated exactly in the transition region. It can be shown that the "classical" instability strip where are situated the well known classical Cepheids, the RR Lyrae and the δ Scuti stars (see Figure 1) corresponds exactly to the region of the HR diagram for which the transition region and the HeII partial ionization zone coincide. The instability of the β Cephei and Slowly Pulsating B stars is also explained by a κ-mechanism. For these stars, it is the metal opacity bump which coincides with the transition region. We will illustrate and study in more details this mechanism in Sections 4.1.3, 4.2.3 and 4.3.3.

Finally, we mention another mechanism sometimes invoked for the explanation of the driving of some pulsating stars: the convective blocking. In some specific cases, the mean life time of the convective cells at the base of the envelope convection zone is much longer than the period of pulsation, so that a frozen convection approximation is admissible. By freezing the convective luminosity, we obtain Eq. (3.7) for a radial mode. In the convective blocking mechanism, the steep decrease of $L_{\rm R}/L$ at the base of the convection zone implies a decrease of $\delta L/L$ (see Eq. (3.7)) and thus the driving of the star. This mechanism has been proposed by Guzik et al. (2000) as an explanation of the driving of the gravity modes of γ Doradus stars. We will discuss in more detail this mechanism in Section 4.4.4.

3.2 Non-adiabatic observables in multi-colour photometry

The observation of the magnitude variations of a pulsating star in different colour filters and the confrontation with non-adiabatic theoretical predictions can be used in order to identify the degree ℓ of the pulsation modes, and to improve our knowledge of stellar interiors and atmospheres. Mode identification methods based on multi-colour photometry have been developed by different authors. Dziembowski (1977b) was the first to derive an expression for the bolometric magnitude variation of a non-radially pulsating star. He suggested also that a Wesselink technique could be formulated from these expressions. Balona & Stobie (1979) recast the suggestion of Dziembowski in an observationally feasible way. Stamford & Watson (1981) derived an expression for the monochromatic magnitude variations of a non-radially pulsating star. They proposed to compute the local emergent monochromatic flux variation on the basis of equilibrium atmosphere models (see Eq. (3.10) below) and they simplified the way to compute the influence of the stellar surface distortion. Watson (1988) improved the method by taking the variation of the limb darkening into account (see Eq. (3.11) below), and discussed the importance of the different terms in the equation giving the monochromatic magnitude variations of a non-radially pulsating star. Garrido et al. (1990) and Garrido (2000) derived a method of mode identification using Strömgren photometry, based on the formalism of Watson (1988), and applied it to δ Scuti and γ Doradus stars. Heynderickx et al. (1994) derived an expression for the surface distortion of a non-radially pulsating star in a Lagrangian formalism. He developed a method of mode identification based on photometric amplitude ratios and applied it to β Cephei stars.

In all the previously cited papers, the non-adiabatic character of the pulsation was neglected or treated with an *ad hoc* parameter. Cugier et al. (1994) was the first to use non-adiabatic computations for photometric mode identification, using the non-adiabatic pulsation code of Dziembowski (1977a). The same code was also used by Balona & Evers (1999) for mode identifications of δ Scuti stars. In comparison with other non-adiabatic codes, the special care that we give to the treatment of the pulsation in the atmosphere (see Section 2.3) improves the accuracy and thus the discriminant power of these methods.

3.2.1 The one-layer approximation

We mention firstly an approximation which has been always made until now in the photometric and in the spectroscopic mode identification methods: the *one-layer approximation*. Except from the pulsational frequencies, the only other observables when studying stellar pulsations are associated to the stellar surface, because stars are opaque mediums. Since the mode identification methods use such other observables, a natural hypothesis in this frame is to consider the star as a single surface deformed with time due to the stellar pulsation. In the next developments, we are going to call this surface: **the single photosphere**. The mean distance to the center of this single photosphere is the radius R of the star (see the definition of R in Section 1.3.2). In a linear approximation, the deformation and the velocity field of the single photosphere can be derived directly from the displacement vector $\vec{\xi}$ at a distance $r = R$, as will be explained later. We will discuss the validity of this approximation in Section 3.2.4. The problem is that, avoiding this approximation in a consistent way is very difficult and makes the computations much more complicated.

3.2.2 Monochromatic magnitude variations of a non-radially pulsating star

In this subsection, we derive a theoretical expression for the monochromatic magnitude variations of a non-radially pulsating star. Similar expressions have been derived by different authors (see above), but we remake here the entire developments, in order to see exactly the steps where the things can be improved.

Contrary to the equilibrium spherical symmetric case, for non-radial pulsations, the monochromatic amount of energy radiated by the entire star, as observed by a distant observer ($E(\lambda,t)$) and the monochromatic outgoing flux corresponding to a local surface element of the star ($\overrightarrow{F_\lambda}^+$) are no longer represented by the same quantity (we use here the same notations as in Heynderickx et al. (1994)). What we intend to determine here is the variation of $E(\lambda,t)$. To achieve this, we will have to integrate the monochromatic intensity variation over the perturbed stellar surface.

In what follows, we are going to work in two reference frames with origins at the center of the star: the $\mathcal{R}$ reference frame with spherical coordinates (r,θ,ϕ) is with a polar axis corresponding to the polar (rotation) axis of the star, and the $\mathcal{O}$ reference frame with spherical coordinates (r',θ',ϕ') is with a polar axis in the direction of the observer. The inclination angle between these two reference frames is denoted by i. We are also going to work with a new kind of perturbation, the **radial Lagrangian perturbation** denoted by δ_r. $\delta_r\,(X)$ is the variation of X, following the radial component of the movement of the matter. With this new notation, the next derivations will be simplified, because $\delta_r\theta = \delta_r\phi = 0$. In particular, this formalism is very well adapted to the determination of the geometrical distortion of the stellar surface, because at first order, this distorsion is not affected by the displacement field in the transversal direction. More precisely, the transversal motions change the stellar surface density, but do not affect the position and orientation of this surface (at first order).

We begin by giving all the assumptions we are going to make, in order to obtain a theoretical expression for the variation of $E(\lambda,t)$.

a1) We work in the linear approximation.

a2) We neglect the coupling of modes due to the interaction between rotation and pulsation. The angular dependence of a non-radial mode is thus described by a single spherical harmonic.

a3) We assume that the gas column of the atmosphere at a given angular position $(\theta,\ \phi)$ is well described by a plane parallel atmosphere, which we call the *local atmosphere.*

a4) For the geometrical distortion of the stellar surface, we work in the one-layer approximation. It is assumed that the visible part of the star, i.e. the photosphere, can be described by a single surface which is spherical at equilibrium. The radius R_0 of this sphere is the radius of the star, and in our method, we assume that it corresponds to the layer where the local temperature is equal to the effective temperature of the star. During the pulsation, it is assumed that the photosphere follows the movement of the matter. The surface distortion can therefore be deduced from the displacement field: $\vec{\xi}(R_0, \theta, \phi, t)$.

a5) We assume that during the pulsation cycle, the monochromatic outwards flux $\vec{F_\lambda}^+$ of the local atmosphere is, for each given time, the same as the monochromatic outwards flux of an equilibrium plane parallel atmosphere model.

a6) We assume that, during the pulsation cycle, $\vec{F_\lambda}^+$ remains perpendicular to the photosphere.

a7) We assume that $\vec{F_\lambda}^+$ does not depend on the optical depth in the local atmosphere.

a8) We assume that the local atmosphere depends only on two varying parameters: the local effective temperature and the local gravity. The chemical composition of the local atmosphere is assumed to remain constant.

a9) We assume that during the pulsation cycle, the limb darkening law h_λ of the local atmosphere is, for each given time, the same as the limb darkening law of an equilibrium plane parallel atmosphere model with the orientation given by assumption (a4) and (a6).

We will discuss in more details in Section 3.2.4 the validity of assumption (a4). The important point is that the relative difference between the displacement of constant optical depth layers and the "real" displacement of the matter ($\delta\tau/(\kappa\,\rho\,R_0)$) is very small for g-modes and moderate order p-modes (for these modes, the value of $|\xi_r|$ at the base of the atmosphere is close to the value of $|\xi_r|$ at the outermost layers). However, we showed in Section 2.3 that it is not appropriate to assume that the Lagrangian variation of the temperature is equal to the variation of the temperature at constant optical depth. We illustrate this clearly for a β Cephei model in Section 4.1.5, Figure 4.13, for a Slowly Pulsating B model in Section 4.2.5, Figure 4.30, and for a δ Scuti model in Section 4.3.5, Figure 4.50.

We note that assumption (a7) concerns only the flux. We do not make this hypothesis for the temperature which depends strongly on the optical depth in stellar atmospheres (see Section 2.3, Figure 2.2).

Assumptions (a5) and (a9) have the same physical justification as explained in Section 2.3.1. Because of the very small thermal relaxation time of the atmosphere, we assumed that, at each time of the pulsation cycle, the local atmosphere remains in radiative equilibrium. On the base of this approximation, we assumed in Section 2.3.1 that, during the pulsation cycle, the temperature distribution ($T(\tau)$ law) in the local atmosphere was, for each given time, the same as the temperature distribution of an equilibrium atmosphere model. For the same physical reasons, we make now the same assumption for the monochromatic flux $\overrightarrow{F_\lambda}^+$ and for the limb darkening coefficient h_λ.

From assumptions (a5), (a7) and (a8), the monochromatic flux variation in the local atmosphere (equilibrium value + perturbation) is given by:

$$\left(F_\lambda^+\right)_0 + \delta F_\lambda^+(\theta,\phi,t) \;=\; F_\lambda^+\left[\,(T_{\rm eff})_0 \,+\, \delta T_{\rm eff}(\theta,\phi,t)\,,\; g_0 \,+\, \delta g_{\rm e}(\theta,\phi,t)\,\right]\,, \tag{3.9}$$

where $F_\lambda^+ = \left|\overrightarrow{F_\lambda}^+\right|$. In the linear approximation, we have thus from Eq. (3.9):

$$\begin{aligned} \frac{\delta F_\lambda^+}{F_\lambda^+} &= \left(\frac{\partial \ln F_\lambda^+}{\partial \ln T_{\rm eff}}\right) \frac{\delta T_{\rm eff}}{T_{\rm eff}} + \left(\frac{\partial \ln F_\lambda^+}{\partial \ln g_{\rm e}}\right) \frac{\delta g_{\rm e}}{g_{\rm e}} \\ &= \alpha_{T\lambda}\, \frac{\delta T_{\rm eff}}{T_{\rm eff}} \,+\, \alpha_{g\lambda}\, \frac{\delta g_{\rm e}}{g_{\rm e}}\,. \end{aligned} \tag{3.10}$$

Eq. (3.9) was first proposed by Stamford & Watson (1981).

We proceed similarly for the variation of the limb darkening. From assumptions (a4), (a6), (a8) and (a9), we obtain in the linear approximation:

$$\frac{\delta_r h_\lambda}{h_\lambda} = \left(\frac{\partial \ln h_\lambda}{\partial \ln T_{\rm eff}}\right) \frac{\delta T_{\rm eff}}{T_{\rm eff}} + \left(\frac{\partial \ln h_\lambda}{\partial \ln g_{\rm e}}\right) \frac{\delta g_{\rm e}}{g_{\rm e}} + \left(\frac{\partial \ln h_\lambda}{\partial \mu'}\right) \delta_r \left(\overrightarrow{n} \cdot \overrightarrow{e_{z'}}\right)\,, \tag{3.11}$$

where $\overrightarrow{n}$ is the normal to the single photosphere. A similar equation was first proposed by Watson (1988).

We define a as the normalization constant such that the local radial displacement of the single photosphere is:

$$\xi_r(\theta,\phi,t) \;=\; R_0\, a\, P_\ell^m(\cos\theta)\, \cos(\sigma t \,+\, m\,\phi)\,, \tag{3.12}$$

where θ and ϕ are the usual spherical coordinates with respect to the polar (rotation) axis of the star, $P_\ell^m(x)$ is the Associated Legendre Function of degrees ℓ and m, and σ is the angular frequency of oscillation.

The quantities $\delta T_{\rm eff}/T_{\rm eff}$ and $\delta g_{\rm e}/g_{\rm e}$ can be computed very precisely by our non-adiabatic code (see Section 2.3). On the other hand, we have seen previously (see Eq. (2.45)), that in very good approximation, $\delta g_{\rm e}/g_{\rm e}$ is in antiphase with the radial displacement. These two quantities can be expressed in term of the associated Legendre functions:

$$\frac{\delta T_{\rm eff}}{T_{\rm eff}}(\theta,\phi,t) \;=\; f_T\, a\, P_\ell^m(\cos\theta)\, \cos(\sigma t \,+\, m\,\phi \,+\, \psi_T) \qquad \text{and} \tag{3.13}$$

$$\frac{\delta g_{\rm e}}{g_{\rm e}}(\theta,\phi,t) \;=\; -\,f_g\, a\, P_\ell^m(\cos\theta)\, \cos(\sigma t \,+\, m\,\phi)\,, \tag{3.14}$$

where f_T and f_g are the amplitudes of $\delta T_{\rm eff}/T_{\rm eff}$ and $\delta g_{\rm e}/g_{\rm e}$ corresponding to a normalized radial displacement at the photosphere.

After all these preliminaries, we can now compute the theoretical expression for the variation of $E(\lambda, t)$. At equilibrium, we have:

$$\begin{aligned} E(\lambda) &= (R_0^2/r_o^2) \int_0^1 \int_0^{2\pi} I_\lambda(\mu')\, \mu'\, {\rm d}\mu'\, {\rm d}\phi' \\ &= \frac{1}{2\pi\, r_o^2} \int_0^1 \int_0^{2\pi} F_\lambda^+\, h_\lambda(\mu')\, \mu'\, R_0^2\, {\rm d}\mu'\, {\rm d}\phi'\,, \end{aligned} \tag{3.15}$$

where r_o is the distance to the observer.

By perturbing Eq. (3.15) and defining S^+ as the visible stellar surface, we obtain:

$$\begin{aligned}
\delta E(\lambda,t) \;=\; \delta_r E(\lambda,t) \;&=\; \frac{1}{2\pi\, r_o^2}\int_{S^+}\delta_r\,\left[F^+_\lambda\, h_\lambda\,(\overrightarrow{n}\cdot\overrightarrow{e_{z'}})\;\overrightarrow{n}\cdot\overrightarrow{e_{z'}}\,\mathrm{d}S\right]\\
&=\; \frac{1}{2\pi\, r_o^2}\left[\int_0^1\int_0^{2\pi}(\delta F^+_\lambda)\;h_\lambda(\mu')\;\mu'\;R_0^2\,\mathrm{d}\mu'\,\mathrm{d}\phi'\right.\\
&\quad+\;F^+_\lambda\int_0^1\int_0^{2\pi}\delta_r\Big[h_\lambda\,(\overrightarrow{n}\cdot\overrightarrow{e_{z'}})\;\overrightarrow{n}\cdot\overrightarrow{e_{z'}}\Big]\;R_0^2\,\mathrm{d}\mu'\,\mathrm{d}\phi'\\
&\quad+\;\left.F^+_\lambda\int_{S^+}h_\lambda(\mu')\;\mu'\;\delta_r(\mathrm{d}S)\right]. \qquad (3.16)
\end{aligned}$$

For the first term of Eq. (3.16), we obtain, using Eq. (3.10), Eq. (3.13), Eq. (3.14) and $P_\ell^m(\cos\theta)\,e^{im\phi} = \sum_{k=-\ell}^{\ell} q_k\,P_\ell^k(\cos\theta')\,e^{ik\phi'}$:

$$\begin{aligned}
&\frac{1}{2\pi\, r_o^2}\int_0^1\int_0^{2\pi}(\delta F^+_\lambda)\;h_\lambda(\mu')\;\mu'\;R_0^2\,\mathrm{d}\mu'\,\mathrm{d}\phi'\\
&=\;\frac{a\,R_0^2\,F^+_\lambda}{2\pi\, r_o^2}\int_0^1\int_0^{2\pi}\Big[\alpha_{T\lambda}\,f_T\,P_\ell^m(\cos\theta)\;\cos(\sigma\,t\,+\,m\,\phi\,+\,\psi_T)\\
&\qquad\qquad -\,\alpha_{g\lambda}\,f_g\,P_\ell^m(\cos\theta)\;\cos(\sigma\,t\,+\,m\,\phi)\Big]\;h_\lambda(\mu')\;\mu'\;\mathrm{d}\mu'\,\mathrm{d}\phi'\\
&=\;\frac{a\,R_0^2\,F^+_\lambda}{2\pi\, r_o^2}\sum_{k=-\ell}^{\ell}\Big\{\;|q_k|\int_0^1\int_0^{2\pi}\Big[\alpha_{T\lambda}\,f_T\,P_\ell^k(\mu')\;\cos(\,\arg\{q_k\}+\sigma\,t+k\,\phi'+\psi_T)\\
&\qquad\qquad -\,\alpha_{g\lambda}\,f_g\,P_\ell^k(\mu')\;\cos(\,\arg\{q_k\}+\sigma\,t+k\,\phi')\Big]\;h_\lambda(\mu')\;\mu'\;\mathrm{d}\mu'\,\mathrm{d}\phi'\Big\}. \qquad (3.17)
\end{aligned}$$

Since $\int_0^{2\pi} cos(k\,\phi' + C) = 0$ for $|k| \geq 1$, only the term with $k = 0$ is not equal to zero in the right hand side of Eq. (3.17). We obtain therefore:

$$\begin{aligned}
\frac{1}{2\pi\, r_o^2}\int_0^1\int_0^{2\pi}(\delta F^+_\lambda)\;h_\lambda(\mu')\;\mu'\;R_0^2\,\mathrm{d}\mu'\,\mathrm{d}\phi' \;&=\; \frac{a\,R_0^2\,F^+_\lambda}{r_o^2}\;P_\ell^m(\cos i)\\
\Big[\alpha_{T\lambda}\,f_T\,\cos(\sigma t+\psi_T)-\alpha_{g\lambda}\,f_g\,\cos(\sigma t)\Big]&\int_0^1 P_\ell(\mu')\,h_\lambda(\mu')\,\mu'\,\mathrm{d}\mu'. \qquad (3.18)
\end{aligned}$$

We are going now to develop the second term of the right hand side of Eq. (3.16).

We compute now the variation of the normal: $\delta_r\overrightarrow{n}$. In Figure 3.1, we show how it can be related to the gradient of the radial displacement. We have thus:

$$\begin{aligned}
\delta_r\overrightarrow{n} \;&=\; -\,\nabla_{\mathrm{h}}\,\xi_r\\
&=\; -\,\frac{1}{R_0}\left(\frac{\partial\xi_r}{\partial\theta}\,\overrightarrow{e_\theta}\;+\;\frac{1}{\sin\theta}\,\frac{\partial\xi_r}{\partial\phi}\,\overrightarrow{e_\phi}\right)\\
&=\; -\,\frac{1}{R_0}\left(\frac{\partial\xi_r}{\partial\theta'}\,\overrightarrow{e_{\theta'}}\;+\;\frac{1}{\sin\theta'}\,\frac{\partial\xi_r}{\partial\phi'}\,\overrightarrow{e_{\phi'}}\right). \qquad (3.19)
\end{aligned}$$

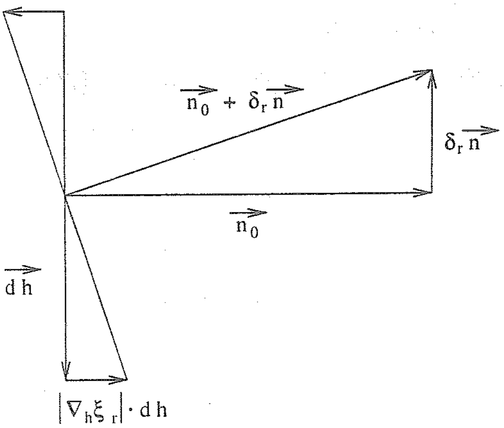

Figure 3.1: Variation of the normal to the single photosphere

And finally, using Eq. (3.12), we obtain in the $\mathcal{O}$ reference frame:

$$\begin{aligned}\delta_r\,(\vec{n}\cdot\vec{e_{z'}}) &= \delta_r\,(\vec{n})\cdot\vec{e_{z'}} = \frac{1}{R_0}\,\frac{\partial\xi_r}{\partial\theta'}\,\sin\theta' \\ &= -\,a\,\sin^2\theta'\,\sum_{k=-\ell}^{\ell}|q_k|\,\frac{\mathrm{d}P_\ell^k(\mu')}{\mathrm{d}\mu'}\,\cos(\,\arg\{q_k\}+\sigma\,t+k\,\phi')\,. \qquad (3.20)\end{aligned}$$

We can now compute the second term of the right hand side of Eq. (3.16). Using Eqs. (3.20) and (3.11), we find:

$$\begin{aligned}&\frac{F_\lambda^+}{2\pi\,r_o^2}\,\int_0^1\int_0^{2\pi}\delta_r\Big[h_\lambda\,(\vec{n}\cdot\vec{e_{z'}})\;\vec{n}\cdot\vec{e_{z'}}\Big]\,R_0^2\,\mathrm{d}\mu'\,\mathrm{d}\phi' \\ &= \frac{R_0^2\,F_\lambda^+}{2\pi\,r_o^2}\,\int_0^1\int_0^{2\pi}h_\lambda(\mu')\Bigg[\,\delta_r\,(\vec{n}\cdot\vec{e_{z'}}) \\ &+\;\mu'\Bigg(\left(\frac{\partial\ln h_\lambda}{\partial\ln T_{\mathrm{eff}}}\right)\frac{\delta T_{\mathrm{eff}}}{T_{\mathrm{eff}}}+\left(\frac{\partial\ln h_\lambda}{\partial\ln g_{\mathrm{e}}}\right)\frac{\delta g_{\mathrm{e}}}{g_{\mathrm{e}}}+\left(\frac{\partial\ln h_\lambda}{\partial\mu'}\right)\delta_r\,(\vec{n}\cdot\vec{e_{z'}})\Bigg)\Bigg]\,\mathrm{d}\mu'\,\mathrm{d}\phi' \\ &= \frac{aR_0^2F_\lambda^+}{2\pi\,r_o^2}\sum_{k=-\ell}^{\ell}\Bigg\{|q_k|\int_0^1\int_0^{2\pi}h_\lambda(\mu')\Bigg[-(1-\mu'^2)\frac{\mathrm{d}P_\ell^k(\mu')}{\mathrm{d}\mu'}\cos(\arg\{q_k\}+\sigma t+k\phi') \\ &+\;\Bigg(f_T\left(\frac{\partial\ln h_\lambda}{\partial\ln T_{\mathrm{eff}}}\right)\cos(\,\arg\{q_k\}+\sigma t+k\,\phi'+\psi_T) \\ &\quad-f_g\left(\frac{\partial\ln h_\lambda}{\partial\ln g_{\mathrm{e}}}\right)\cos(\,\arg\{q_k\}+\sigma t+k\,\phi')\Bigg)\,P_\ell^k(\mu')\,\mu' \\ &-\;\left(\frac{\partial\ln h_\lambda}{\partial\mu'}\right)\mu'\,(1-\mu'^2)\,\frac{\mathrm{d}P_\ell^k(\mu')}{\mathrm{d}\mu'}\,\cos(\,\arg\{q_k\}+\sigma\,t+k\,\phi')\Bigg]\,\mathrm{d}\mu'\,\mathrm{d}\phi'\Bigg\}\,. \qquad (3.21)\end{aligned}$$

Again, only the term with $k = 0$ is not equal to zero in the right hand side of this equation, and we have:

$$\begin{aligned} & \frac{F_\lambda^+}{2\pi\, r_o^2} \int_0^1 \int_0^{2\pi} \delta_r \Big[h_\lambda \, (\overrightarrow{n} \cdot \overrightarrow{e_{z'}}) \;\; \overrightarrow{n} \cdot \overrightarrow{e_{z'}} \Big] \; R_0^2 \, \mathrm{d}\mu' \, \mathrm{d}\phi' \\ = \;\; & \frac{a\, R_0^2 \, F_\lambda^+}{r_o^2} \, P_\ell^m(\cos i) \int_0^1 h_\lambda(\mu') \Bigg[- \; (1 - \mu'^2) \, \frac{\mathrm{d}P_\ell(\mu')}{\mathrm{d}\mu'} \; \cos(\sigma\, t) \\ + \;\; & \left(f_T \left(\frac{\partial \ln h_\lambda}{\partial \ln T_{\mathrm{eff}}} \right) \cos(\sigma t + \psi_T) \; - \; f_g \left(\frac{\partial \ln h_\lambda}{\partial \ln g_{\mathrm{e}}} \right) \cos(\sigma t) \right) P_\ell(\mu') \, \mu' \\ - \;\; & \left(\frac{\partial \ln h_\lambda}{\partial \mu'} \right) \mu' \, (1 - \mu'^2) \, \frac{\mathrm{d}P_\ell(\mu')}{\mathrm{d}\mu'} \; \cos(\sigma\, t) \Bigg] \, \mathrm{d}\mu' \, . \end{aligned} \tag{3.22}$$

And finally. we compute the last term of the right hand side of Eq. (3.16). $\delta_r(\mathrm{d}S)$ is easily computed in our formalism:

$$\delta_r(\mathrm{d}S) \; = \; \delta_r(\overrightarrow{\mathrm{d}S}) \cdot \overrightarrow{e_r} \; = \; 2 \, R_0 \, \xi_r \, \mathrm{d}\mu' \, \mathrm{d}\phi' \, . \tag{3.23}$$

Eq. (3.23) can be compared to what is obtained in a Lagrangian formalism. On the basis of Heynderickx et al. (1994), De Ridder (2001, PhD thesis) derived the following equation:

$$\delta(\mathrm{d}S) \; = \; \left(2 \, \frac{\xi_r}{R_0} \; + \; \nabla_h \cdot \overrightarrow{\xi_h} \right) \, R_0^2 \, \mathrm{d}\mu' \, \mathrm{d}\phi' \, , \tag{3.24}$$

where the definition of $\nabla_h \cdot$ is given in Eq. (1.29) and $\overrightarrow{\xi_h}$ is the transversal component of the displacement vector. The difference between Eqs. (3.23) and (3.24) comes from the fact that, on one hand in our formalism: $\delta_r \theta' = \delta_r \phi' = 0$; but on the other hand in a "classical" Lagrangian formalism: $\delta\theta'$ and $\delta\phi'$ are not equal to zero for non-radial modes. We checked that the final results obtained using one or another of these two formalisms are mathematically equivalent. The only difference is that the derivations are easier in our formalism.

We obtain therefore, for the last last term of the right hand side of Eq. (3.16):

$$\begin{aligned} & \frac{F_\lambda^+}{2\pi\, r_o^2} \int_{S+} h_\lambda(\mu') \, \mu' \, \delta_r(\mathrm{d}S) \\ = \;\; & \frac{R_0^2 \, F_\lambda^+}{2\pi\, r_o^2} \int_0^1 \int_0^{2\pi} h_\lambda(\mu') \, \mu' \, 2 \, \frac{\xi_r}{R_0} \, \mathrm{d}\mu' \, \mathrm{d}\phi' \\ = \;\; & 2 \, \frac{a\, R_0^2 \, F_\lambda^+}{2\pi\, r_o^2} \sum_{k=-\ell}^{\ell} \left\{ \; |q_k| \int_0^1 \int_0^{2\pi} h_\lambda(\mu') \, \mu' \, P_\ell^k(\mu') \; \cos(\, \arg\{q_k\} + \sigma\, t + k\, \phi') \, \mathrm{d}\mu' \, \mathrm{d}\phi' \right\} \\ = \;\; & 2 \, \frac{a\, R_0^2 \, F_\lambda^+}{r_o^2} \, P_\ell^m(\cos i) \; \cos(\sigma\, t) \int_0^1 h_\lambda(\mu') \, \mu' \, P_\ell(\mu') \, \mathrm{d}\mu' \, . \end{aligned} \tag{3.25}$$

From the property of the Legendre polynomials:

$$\int_0^1 (1 - x^2) \, \frac{\mathrm{d}P_\ell}{\mathrm{d}x} \left(f \; + \; x \, \frac{\mathrm{d}f}{\mathrm{d}x} \right) \, \mathrm{d}x \; = \; \ell(\ell + 1) \int_0^1 P_\ell(x) \, x \, f(x) \, \mathrm{d}x \, , \tag{3.26}$$

the sum of three terms of the previous equations can be simplified. These terms are: the first term and last term of the right hand side of Eq. (3.22) and the right hand side of Eq. (3.25). More precisely, we have:

$$\int_0^1 \left[2\, h_\lambda\, \mu'\, P_\ell \;-\; h_\lambda\, (1-\mu'^2)\, \frac{\mathrm{d}P_\ell}{\mathrm{d}\mu'} \;-\; \left(\frac{\partial h_\lambda}{\partial \mu'}\right)\, \mu'\, (1-\mu'^2)\, \frac{\mathrm{d}P_\ell}{\mathrm{d}\mu'} \right] \mathrm{d}\mu'$$

$$= \;-\, (\ell-1)(\ell+2) \int_0^1 h_\lambda\, \mu'\, P_\ell\, \mathrm{d}\mu' \,. \tag{3.27}$$

This simplification was first proposed by Stamford & Watson (1981). The final step of all these derivations is achieved by substituting Eqs. (3.18), (3.22), (3.25) and (3.27) into Eq. (3.16). We obtain then:

$$\delta m_\lambda \;=\; -\,\frac{2.5}{\ln 10}\,\frac{\delta E(\lambda,t)}{E(\lambda)} \;=\; -\,\frac{2.5}{\ln 10}\; a\; P_\ell^m(\cos i)\, b_{\ell\lambda}$$

$$\Big[-\, (\ell-1)(\ell+2)\, \cos(\sigma t) \;+\; f_T\, \cos(\sigma t + \psi_T)\, (\alpha_{T\lambda} + \beta_{T\lambda}) \;-\; f_g\, \cos(\sigma t)\, (\alpha_{g\lambda} + \beta_{g\lambda}) \Big] \,, \tag{3.28}$$

where δm_λ is the variation of the monochromatic visual magnitude at wavelenght λ and:

$$b_{\ell\lambda} \;=\; \int_0^1 h_\lambda\, \mu'\, P_\ell\, \mathrm{d}\,\mu' \,, \qquad \beta_{T\lambda} \;=\; \frac{\partial \ln b_{\ell\lambda}}{\partial \ln T_{\mathrm{eff}}} \qquad \text{and} \qquad \beta_{g\lambda} \;=\; \frac{\partial \ln b_{\ell\lambda}}{\partial \ln g} \,. \tag{3.29}$$

In Eq. (3.28), the term proportional to $(\ell-1)(\ell+2)$ corresponds to the influence of the stellar surface distortion, the term proportional to f_T corresponds to the influence of the local effective temperature variation and the term proportional to f_g corresponds to the influence of the effective gravity variation.

In practice, what is really observed in multi-colour photometry is the integral of the monochromatic magnitude variation over the response of the filter:

$$\delta m_i \;=\; \frac{\int_{\lambda_{\min}}^{\lambda_{\max}} \delta m_\lambda\, w_i(\lambda)\, \mathrm{d}\lambda}{\int_{\lambda_{\min}}^{\lambda_{\max}} w_i(\lambda)\, \mathrm{d}\lambda} \,, \tag{3.30}$$

where $w_i(\lambda)$ is the response curve of the filter i. Therefore, the different terms of Eq. (3.28) depending on λ have to be integrated, following Eq. (3.30).

3.2.3 Comparison with other methods

At this point, our way to proceed diverges significantly from the one proposed by Watson (1988), Heynderickx et al. (1994) and other authors. By using our non-adiabatic code, we can compute directly and very precisely the tree main unknown ingredients of Eq. (3.28): f_T, ψ_T and f_g. But on the other hand, the previous authors did not have such a non-adiabatic code and their way to estimate these parameters was very approximative. In order to clarify the improvement of our method, we present now the old method used by the previous authors, but we emphasize that, from this point, we do not follow them anymore.

Pressure variation

The first step of the procedure followed by the previous authors was to compute $\delta P/P$ at the photosphere. As initially proposed by Buta & Smith (1979), they used the following formula:

$$\frac{\delta P}{P} = \left(\ell(\ell+1)\,K \,-\, 4 \,-\, K^{-1}\right)\frac{\xi_r}{R_0}\,, \tag{3.31}$$

where K (also denoted by α_h, for example in Watson (1988)) is the K-value of the mode:

$$K \,=\, \alpha_h \,=\, \frac{G\,M}{\sigma^2\,R_0^3}\,. \tag{3.32}$$

Eq. (3.31) is deduced from the "classical" mechanical boundary condition (Eq. (1.61)), by doing furthermore the following assumptions at the photosphere: $\delta P/\rho = 0$ and $\psi' = 0$ (Cowling approximation). We recall that we proposed an improvement of the mechanical boundary condition in Section 2.3 (Eq. (2.46)). The advantage of Eq. (3.31) is that it gives $\delta P/P$, without having to compute numerically the adiabatic or non-adiabatic eigenfunctions troughout the entire star. If we assume that:

$$\frac{\delta P}{P}(\theta,\phi,t) \,=\, -\,C\,a\,P_\ell^m(\cos\theta)\,\cos(\sigma\,t\,+\,m\,\phi)\,, \tag{3.33}$$

we have therefore:

$$C \,=\, 4 \,+\, K^{-1} \,-\, \ell(\ell+1)\,K\,. \tag{3.34}$$

The computation of f_T

On one hand, in order to compute f_T, the previous authors propose to make a very crude approximation: the adiabatic approximation. But we emphasize that, in reality, the pulsation is always highly non-adiabatic in the superficial layers of a star, as will be shown in chapter 4. Under the adiabatic approximation, we have:

$$\frac{\delta T}{T} = \left.\frac{\partial \ln T}{\partial \ln P}\right|_S \frac{\delta P}{P} = \frac{\Gamma_2 - 1}{\Gamma_2}\,\frac{\delta P}{P}\,. \tag{3.35}$$

Another approximation made by these authors is to assume that, at the photosphere, the variation of the effective temperature is equal to the Lagrangian variation of the local temperature:

$$\frac{\delta T_{\text{eff}}}{T_{\text{eff}}} = \frac{\delta T}{T}\,. \tag{3.36}$$

We will show that this approximation is not appropriate and that these two quantities can be different for β Cephei stars (Section 4.1.5, Figure 4.13), Slowly Pulsating B stars (Section 4.2.5, Figure 4.30) and δ Scuti stars (Section 4.3.5, Figure 4.50), when a more rigorous treatment of the stellar atmosphere is adopted, as we did. From Eqs. (3.35) and (3.36), we obtain:

$$f_T = \frac{\Gamma_2 - 1}{\Gamma_2}\,|C| \quad \text{and} \quad \left\{ \begin{array}{lll} \psi_T = 180^\circ & \text{for } C > 0 & (\text{p} - \text{modes}) \\ \psi_T = 0^\circ & \text{for } C < 0 & (\text{high order g} - \text{modes}) \end{array} \right. \tag{3.37}$$

Watson (1988) introduced an ad-hoc parameter R to describe the departures from adiabatic conditions on the stellar surface:

$$R = \frac{f_T \, \Gamma_2}{|C| \, (\Gamma_2 - 1)} \,, \tag{3.38}$$

but he did not compute it and let it as a free parameter such that $0.25 \leq R \leq 1$. Some authors (Cugier et al. 1994, Balona & Evers 1999) performed non-adiabatic computations in order to determine R and thus f_T in a more rigorous way. However, they assumed Eq. (3.36) and their way to determine f_g was inappropriate, as we are going to show.

On the other hand, in comparison to all these derivations, we repeat that f_T can be computed in a more rigorous way, directly by our non-adiabatic code, with the treatment of the atmosphere presented in Section 2.3, and without need to introduce the free parameter R.

The computation of f_g

f_g also was not determined correctly until now. Stamford & Watson (1981), Heynderickx et al. (1994) and several other authors proposed to take:

$$f_g = p * C = \left(\frac{\partial \ln g}{\partial \ln P_g} \right)_{\tau=1} C \,, \tag{3.39}$$

where $p*$ is computed from equilibrium atmosphere models such as the models of Kurucz (1993). Even some authors (Cugier et al. 1994, Balona & Evers 1999) proposed to take: $p* = 1$!?

In Section 2.3.3, Eq. (2.44), we proposed a more accurate way to determine $\delta g_e / g_e$ and thus f_g. Under the Cowling approximation and neglecting the surface density divided by the mean density of the star, we showed that Eq. (2.44) reduces to Eq. (2.45). Eq. (2.45) gives simply:

$$f_g = 2 + K^{-1} \,. \tag{3.40}$$

We note that, indepentently from us, Cugier & Daszynska (2001) did also the correction and proposed to use exactly the same equation as Eq. (3.40). The difference between Eq. (3.40) and Eq. (3.39) with $p^* = 1$ is due to the fact that the Lagrangian variation of surface elements of the photosphere $(2 - \ell(\ell+1)K)$ affects the Lagrangian variation of the pressure described in Eq. (3.34), but does not affect the Lagrangian variation of the effective gravity.

By comparing Eqs. (3.34) and (3.40), we see that:

For p-modes : K is small so that the difference between C and f_g is approximately 2.

For g-modes : K is large, so that the difference between C and f_g becomes very important !

Therefore, our improved determination of f_g has the largest impact on the photometric mode identification of g-mode pulsators such as Slowly Pulsating B stars and γ Doradus stars.

As conclusion:

- In the old method, it was necessary to compute firstly C by use of Eq. (3.34), secondly f_T by use of Eq. (3.37) or (3.38) and finally f_g by use of Eq. (3.39).
- In our improved method, f_T, ψ_T and f_g are directly computed by our non-adiabatic code, with the treatment of the atmosphere presented in Section 2.3. It is no longer necessary to estimate the intermediate parameters C and R.

3.2.4 The perturbed stellar surface

In Section 3.2.2, we derived an expression for the monochromatic magnitude variation of a non-radially pulsating star. For obtaining it, one of the main approximation we did was the one-layer approximation. In the next paragraphs, we do not propose a better determination of the surface distorsion, but we make some physical considerations permitting to evaluate the validity of the one-layer approximation in the frame of multi-colour photometric studies.

The transparency effect

The question we are asking here is: what is the visible surface of a non-radially pulsating star ?

It is true that in sufficiently deep stellar layers, the medium is completely opaque; and for a completely opaque medium, the deformation of its visible surface is equal to the deformation of its material surface, as deduced from the displacement field. Therefore, for a completely opaque medium, the approximation we did for obtaining the perturbed stellar surface is perfectly valid.

But in reality, the visible part of a star (its photosphere) is the transition zone between the opaque interior and the optically thin atmosphere. Let $\Delta_\tau(X)$ be the variation of X, following layers of constant optical depth. The point here is that, around the photosphere, following constant optical depths or following the movement of the matter is not the same. The physical explanation of this phenomenon is easy. During the pulsation, the thermodynamical characteristics of the medium (temperature, density) are varying with time. Therefore, the opacity (which depends strongly on the temperature and density) is also varying with time, so that the Lagrangian variation of the optical depth is not negligible. In other words, as the star is pulsating, its transparency is varying with time so that the visible layers do not follow exactly the movement of the matter. We call this phenomenon: the transparency effect.

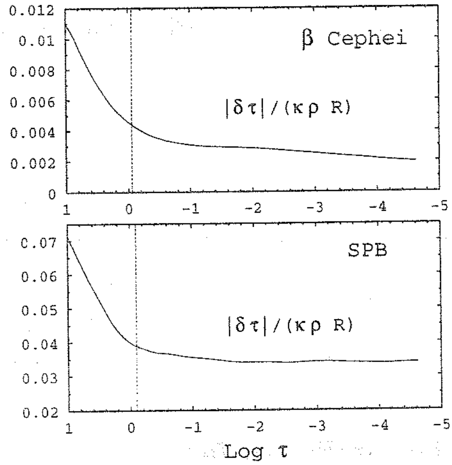

Figure 3.2: Relative displacement between layers of constant Rosseland optical depths and the Lagrangian movement of the matter, as function of the logarithm of the Rosseland optical depth, for the fundamental radial mode of a 9.5 $M_\odot$ β Cephei model (top) and for the mode $\ell = 1$, g_{22} of a 4 $M_\odot$ Slowly Pulsating B model (bottom). The vertical line corresponds to the "single" photosphere where $T = T_{\rm eff}$ (the radial displacement ξ_r/R is normalized to 1 at this layer).

The difference between the relative displacement of a constant Rosseland optical depth layer and the relative displacement of the matter is given by $\delta\tau/(\kappa\rho R)$. We show in Figure 3.2 the results obtained in the atmosphere of two different kinds of pulsating stars and for a normalized radial displacement at the photosphere ($\xi_r/R = 1$ at $r = R$). The top figure corresponds to the fundamental radial mode of a 9.5 $M_\odot$ β Cephei model and the bottom figure corresponds to the mode $\ell = 1$, g_{22} of a 4 $M_\odot$ Slowly Pulsating B (SPB) model. We see that, for both cases, $\delta\tau/(\kappa\rho R) \ll 1$ at the photosphere.

Therefore, we can conclude that, for these stars, the transparency effect is small and the "visible" stellar surface follows in good approximation the movement of the matter.

By comparing the results obtained for the two kinds of stars, we see that the transparency effect is more important for the SPB star than for the β Cephei star. This difference can be easily understood. For the high order g-modes of SPBs, the transversal compression and displacement are dominating, so that the temperature, opacity and optical depth variations are significant, for a given radial displacement. On the contrary, for the low order p-modes of β Cephei stars, the radial compression and displacement are dominating, so that the temperature, opacity and optical depth variations are smaller, for a given radial displacement.

The previous definitions and illustrations give an estimate of the importance of the transparency effect, but unfortunately, they do not permit to determine more precisely the real distorsion of the visible stellar surface, which would be much more complicated. When we are observing a stellar surface element in an oblique direction ($\vec{n} \cdot \vec{e_{z'}} = \mu'$), the optical depth $\tau_{\mu'}$ associated to the intensity field in the observer direction ($\vec{e_{z'}}$) is such that:

$$\frac{\mathrm{d}\tau_{\mu'}}{\mathrm{d}r} = \frac{1}{\mu'}\frac{\mathrm{d}\tau}{\mathrm{d}r} = -\frac{\kappa\,\rho}{\mu'} . \tag{3.41}$$

Assuming that the visible stellar surface corresponds to constant values of $\tau_{\mu'}$ (for example $\tau_{\mu'} = 1$), we deduce directly from Eq. (3.41) that the visible stellar surface is not spherical, even at equilibrium ! Therefore, if we want to proceed rigorously, we would have to determine the deformation of a surface which is not spherical at equilibrium. This very complex problem is out of the skope of our current study.

Surface orientation and limb darkening

Another point is to examine the validity of the expression we used for the variation of the normal to the stellar surface (Eq. (3.19)). We continue to assume here that the local atmosphere is well described by a plane parallel atmosphere. The physical observable directly linked to the orientation of the local plane parallel atmosphere is the limb darkening. It is natural to assume that, from the point of view of the radiation field, the planes parallel are perpendicular to the flux vector, so that the relevant angle for determining the limb darkening is the angle between the flux and the direction to the observer. But we know that, at least in the interior, the flux is parallel with $-\nabla T$. It is thus interesting to examine what would be the variation of a unit vector $\vec{n_F}$ parallel with $-\nabla T$. We have:

$$\delta_r(\vec{n_F}) = -\,\delta_r\left(\frac{\nabla T}{\|\nabla T\|}\right) = \frac{\nabla_h T'}{\mathrm{d}T/\mathrm{d}r} . \tag{3.42}$$

Assuming that:

$$\frac{\delta T(R,\theta,\phi,t)}{\mathrm{d}T/\mathrm{d}\ln r} = a\,E\,P_\ell^m(\cos\theta)\,\cos(\sigma\,t + m\,\phi + \psi) , \tag{3.43}$$

we obtain for the difference between Eq. (3.42) and Eq. (3.19):

$$\delta_r(\vec{n_F}) - \delta_r(\vec{n}) = -\,a\,E\,\left(\frac{\mathrm{d}P_\ell^m}{\mathrm{d}\mu}\sin\theta\,\cos(\sigma\,t + m\,\phi + \psi)\,\vec{e_\theta}\right.$$
$$\left. + \frac{m\,P_\ell^m}{\sin\theta}\,\sin(\sigma\,t + m\,\phi + \psi)\,\vec{e_\phi}\right) . \tag{3.44}$$

We show in Figure 3.3 the values of E obtained in the atmosphere of a 9.5 $M_\odot$ β Cephei model (top) and a 4 $M_\odot$ SPB model (bottom). We see that, for both cases, the values of E are much smaller than 1 at the photosphere.

We conclude that, for these stars, the variation of the normal is relatively well described by Eq. (3.19).

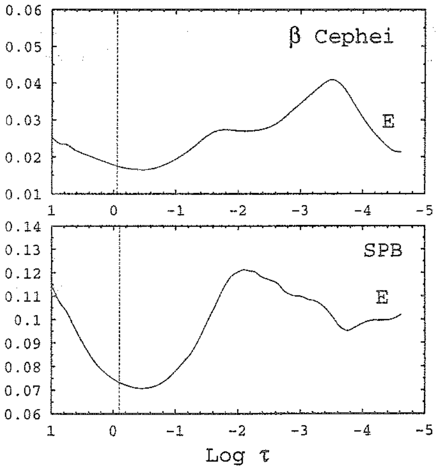

Figure 3.3: Amplitude E corresponding to the difference between the variation of a unit vector parallel with $-\nabla T$ and the variation of the normal to the "single" photosphere, as function of the logarithm of the Rosseland optical depth, for the fundamental radial mode of a 9.5 $M_\odot$ β Cephei model (top) and for the mode $\ell = 1$, g_{22} of a 4 $M_\odot$ Slowly Pulsating B model (bottom). The vertical line corresponds to the "single" photosphere where $T = T_{\rm eff}$.

The values of E are higher for the SPB model, because for high order g-modes the transversal compression is dominating, so that the temperature variations are higher, for a given radial displacement.

Again. the previous considerations give an estimate of the accuracy of our treatment but they do not permit to determine with more precision the real distorsion of the visible stellar surface. The problem here is that, assuming that the normal is parallel with $-\nabla T$ would imply that the deformed stellar surface is isothermal, but we have no physical reasons to expect that it is so. Even at equilibrium the visible surface is not isothermal, because we see at different depths corresponding to different temperatures, which is the origin of the limb darkening.

3.2.5 Mode identification and non-adiabatic asteroseismology

On the basis of Eq. (3.28), methods for the identification of the degree ℓ of pulsation modes can be derived. We have to consider two cases: the variable stars with phase-lags ψ_T close to the adiabatic 0° or 180° and the variable stars for which the phase-lag ψ_T is very different from the adiabatic values.

Variable stars with quasi-adiabatic phase-lags

In the adiabatic case, all the eigenfunctions are real so that the variations of the different physical quantities ξ_r, δT, $\delta \rho$, δL are either in phase or in antiphase. In particular, it is easy to show that the phase difference between the luminosity variation δL and the radial displacement ξ_r is 180° for p-mode pulsations and 0° for high order g-mode pulsations. From an observational point of view, the phase difference between the visual magnitude variation determined by photometry and the pulsational velocity variation determined by spectroscopy (Doppler effect) is thus $+90°$ for p-modes and $-90°$ for high order g-modes, in the adiabatic case.

Although the pulsation is always highly non-adiabatic in the superficial layers, some kinds of pulsating stars show phase differences close to the adiabatic values. This is typically the case for β Cephei and Slowly Pulsating B stars. A simple explanation is that the driving of these stars occurs in the relatively deep metal opacity bump close to the quasi-adiabatic region, and the heat capacity of the highly non-adiabatic superficial layers is too small to affect the phase of δL. For these stars, the observed phases of photometric magnitude variations are the same in the different filters and the only photometric observables are the amplitudes.

The linear theory does not permit to predict the amplitudes of the eigenfunctions. Therefore, it is appropriate to use amplitude ratios when comparing the theoretical predictions to the observations. Moreover, when using amplitude ratios, the coefficient $P_\ell^m(\cos i)$ appearing in Eq. (3.28) vanishes, which is a very positive point since the inclination angle i is extremely difficult to determine from observations.

A method of photometric mode identification based on amplitude ratios was first proposed by Heynderickx et al. (1994), but in their method, the degree of non-adiabaticity R (see Eq. (3.38)) was considered as a free ad-hoc parameter. We adopt here a similar method, but including more rigorous non-adiabatic computations. More precisely, Dr. J. De Ridder improved the initial code of Heynderickx, so that it can now take our non-adiabatic computations into account, throughout the parameters f_T and ψ_T (amplitude and phase of local effective temperature variation for a normalized radial displacement at the photosphere). The theoretical procedure of our mode identification method is the following:

1. We compute a stellar model with the appropriate effective temperature, luminosity and mass. In our applications, we use the new Code Liégeois d'Évolution Stellaire written by R. Scuflaire.

2. We perform non-adiabatic computations for different degrees ℓ and for pulsation frequencies close to the observed ones. In our applications, we use the non-adiabatic code written by us in the frame of the present work. These computations give the coefficients f_T, ψ_T and f_g for different degrees ℓ.

3. For each filter j and for each ℓ, we compute

$$A_{j,\mathrm{th}} = \frac{\int_{\lambda_{\min}}^{\lambda_{\max}} |b_{\ell\lambda}| \left| (1-\ell)(\ell+2) + f_T\, e^{i\psi_T}\, (\alpha_{T\lambda} + \beta_{T\lambda}) - f_g\, (\alpha_{g\lambda} + \beta_{g\lambda}) \right| w_j(\lambda) \mathrm{d}\lambda}{\int_{\lambda_{\min}}^{\lambda_{\max}} w_j(\lambda)\, \mathrm{d}\lambda}, \tag{3.45}$$

using the values of f_T, ψ_T and f_g computed at step 2. In our applications, we computed the coefficients $\alpha_{T\,\lambda}$ and $\alpha_{g\,\lambda}$ (derivatives of the monochromatic flux) from the models of Kurucz (1993). An analytical law for the limb darkening is needed for the computation of $b_{\ell\lambda}$ and its derivatives $\beta_{T\lambda}$ and $\beta_{g\lambda}$. In our applications, we used a quadratic limb darkening law (Wade & Rucinski 1985). We note that an improved non-linear limb darkening law has been proposed by Claret (2000), but his computations were only made for Strömgren filters, while our applications concern Geneva and Johnson filters.

4. We choose a reference filter (indicated with subindex 1). For B stars, this reference filter is the U filter giving the highest amplitudes and thus the highest S/N ratio. We compare the theoretical amplitude ratios ($A_{j,\mathrm{th}}/A_{1,\mathrm{th}}$) to the observed amplitude ratios ($A_{j,\mathrm{obs}}/A_{1,\mathrm{obs}}$). The identified degree ℓ is the value who minimizes the χ^2:

$$\sum_{j=2}^{k} \left[\frac{A_{j,\mathrm{th}}}{A_{1,\mathrm{th}}} - \frac{A_{j,\mathrm{obs}}}{A_{1,\mathrm{obs}}} \right]^2, \tag{3.46}$$

where k is the number of filters.
The application of this method to β Cephei, Slowly Pulsating B and γ Doradus stars will be presented in Sections 4.1.6, 4.2.6 and 4.4.5 respectively.

Variable stars with significant non-adiabatic phase-lags

Contrary to β Cephei and SPB stars, all the variable stars of the "classical" instability strip: δ Scuti, RR Lyrae and the classical Cepheids (see Figure 1 in the introduction) exhibit phase-lags totally different from the adiabatic values.

The amplitudes of oscillations of the RR Lyrae and the classical Cepheids are very high, their light curves are not sinusoidal and cannot be reproduced by the linear theory. We will not consider them here and the following discussion applies mainly to δ Scuti stars.

For δ Scuti stars, significant phase differences ψ_T between the effective temperature variation and the displacement are observed and predicted by theoretical non-adiabatic computations (see Section 4.3.6, Figures 4.51, 4.52, 4.53 and 4.54). It is therefore useful to use this phase information when comparing observations and theoretical predictions; mode identification methods using it have been derived by Garrido et al. (1990) and Balona & Evers (1999). The method of Garrido et al. (1990) is based on the use of phase-amplitude diagrams as will be detailed below and the method of Balona & Evers

(1999) is based on a least square minimization, with an appropriate χ^2 goodness-of-fit criterion.

Garrido et al. (1990) derived a method of mode identification using Strömgren photometry and applied it to many δ Scuti stars observed with the 1.5 m telescope of the Sierra Nevada Observatory. In their method, the degree of non-adiabaticity R (see Eq. (3.38)) and the phase-lag ψ_T were considered as free *ad-hoc* parameters such that $0.25 \leq R \leq 1$ and $90° \leq \psi_T \leq 135°$. The principle is to construct phase-amplitude diagrams corresponding to judicious combinations of the Strömgren filters. By using Eq. (3.28) integrated over the passband of the filters (Eq. (3.30)), with R and ψ_T as free parameters, different "regions" corresponding to different degree ℓ can be determined. The identification of the degree ℓ is obtained by seeing in which "region" the observations are situated. Moreover, the method permits to determine the values of R and ψ_T giving the best agreement between theory and observation, which is particularly useful for the confrontation with theoretical non-adiabatic predictions. Garrido et al. (1990) discussed which combinations of the filters are the most appropriate for this purpose and showed that using colour indices (differences of magnitude between 2 filters) give a better discriminant power to the method than using the filters separately. More precisely, it is easy to show that the variation of the colour indice $m_i - m_j$ is:

$$\delta(m_i - m_j)(t) \;=\; -\,\frac{2.5}{\ln 10}\int_{\lambda_{\min}}^{\lambda_{\max}} \frac{\delta E(\lambda,t)}{E(\lambda)}\,(w_i(\lambda) - w_j(\lambda))\,\mathrm{d}\lambda\,, \tag{3.47}$$

where $w_i(\lambda)$ and $w_j(\lambda)$ are the normalized response curves of the filters i and j

$$\int_{\lambda_{\min}}^{\lambda_{\max}} w_i(\lambda)\,\mathrm{d}\lambda \;=\; \int_{\lambda_{\min}}^{\lambda_{\max}} w_j(\lambda)\,\mathrm{d}\lambda \;=\; 1$$

and $E(\lambda)$ and $\delta E(\lambda, t)$ are defined in Eqs. (3.15) and (3.16).

We see immediately that the terms of $\delta E(\lambda,t)/E(\lambda)$ which do not depend on λ vanish in Eq. (3.47). Garrido et al. (1990) showed that the coefficient $b_{\ell\lambda}$ (see Eq. (3.29)) is very little dependent on λ for $\ell \leq 2$. Therefore, the geometrical distorsion term of Eq. (3.28) proportional to $(1-\ell)(\ell+2)$ vanishes in good approximation in Eq. (3.47).

In what follows, we use the following notations for the magnitude variations:

$$\delta m_i(t) \;=\; \delta m_i\, e^{i\,\sigma\,t} \;=\; |\delta m_i|\, e^{i\,\sigma\,t + \phi(\delta m_i)}\,. \tag{3.48}$$

By appropriate combinations of filters, the contribution of the different terms of Eq. (3.28) can thus be separated, which improves the discriminant power of the method. Since the absolute amplitudes can not be determined in the linear approximation, and the inclination angle i is extremely difficult to determine from the observations, we have to divide Eq. (3.47) by the magnitude variation in a given filter. Garrido et al. (1990) showed that, for Strömgren filters, the combinations $\delta(m_b - m_y)/\delta m_y$ and $\delta(m_v - m_y)/\delta m_y$ give very good results. In an amplitude versus phase diagram and for the first combination, we have thus in abscissa the phase difference: $\phi(\delta(m_b - m_y)) - \phi(\delta m_y)$ and in ordinate the amplitude ratio: $|\delta(m_b - m_y)|\,/\,|\delta m_y|$.

The illustrations of such phase-amplitude diagrams are given in Section 4.3.6, Figures 4.55 and 4.56. In these diagrams, the different "regions" correspond to the theoretical predictions for different degrees ℓ, with the degree of non-adiabaticity R and the phase-lag ψ_T as free parameters, the circles correspond to our non-adiabatic predictions for modes with frequency close to the one of the fundamental radial mode, where f_T and ψ_T are rigorously computed by our non-adiabatic code, and the crosses correspond to the observations of δ Scuti stars by Garrido et al. (1990), all identified as radial pulsators.

We note that the non-adiabatic predictions depend on some dominant parameters of the theoretical models (e.g. the metallicity for β Cephei stars and SPBs, the mixing length parameter α for δ Scuti and γ Doradus stars). Therefore, these parameters can be constrained by a feed-back process after a unique mode identification is achieved. We call this feed-back process *non-adiabatic asteroseismology*, in which we iterate the procedures as above by adjusting the stellar parameters for the identified mode, until we find the best fit between the theoretical non-adiabatic predictions and the observations. More precisely, for β Cephei stars and SPBs, the non-adiabatic predictions are very sensitive to the metallicity, so that this parameter can be constrained for these stars once definite mode identification is achieved. We will illustrate this procedure in Section 4.1.6, for the estimate of the metallicity of the β Cephei star EN Lac. For δ Scuti and γ Doradus stars, the non-adiabatic predictions are very sensitive to the characteristics of the superficial convection zone (see Section 4.3.6 and Balona & Evers 1999). Therefore, the confrontation between our non-adiabatic theoretical predictions and photometric observations can significantly improve our understanding of this convection zone. However, this procedure will be more difficult in this case, because of the lack of knowledge of the convection-pulsation interaction, particularly in the very thin superficial convection zone of δ Scuti and γ Doradus stars. Finally, the theoretical predictions are also very dependent on the atmosphere models and limb-darkening law, throughout the derivatives of the monochromatic flux: $\alpha_{T\lambda}$ and $\alpha_{g\lambda}$ and the coefficients derived from the limb-darkening law and its derivatives: $b_{\ell\lambda}$, $\beta_{T\lambda}$ and $\beta_{g\lambda}$, as they appear in Eq. (3.28). Therefore, these parameters could also be constrained, if the observations are sufficiently precise.

3.3 Non-adiabatic observables in Line Profile Variations (LPVs)

This section is mainly based on the article written by Dr. J. De Ridder and us (De Ridder, Dupret et al. 2002), on the PhD thesis of De Ridder (2001) and on the works made in the frame of a very fruitful collaboration with him and the team of Professor C. Aerts of the Katholieke Universiteit Leuven.

Thirty years ago, Osaki (1971) successfully modeled the basic properties of line profiles of β Cephei stars. He showed that assuming only a non-radial velocity field could mimic rather well the variations in position and width of the spectral lines. Proceeding so, he confirmed that variable stars such as β Cephei are not only radial pulsators but also non-radial pulsators as proposed by P. Ledoux twenty years earlier. Later it was discovered that β Cephei stars are not the only stars which show line profile variations (LPVs) due to non-radial pulsations. The Slowly Pulsating B stars (SPBs), the γ Doradus stars and the δ Scuti stars exhibit similar LPVs.

Since the beginning of the 1980s, the spectroscopic resolution greatly improved so that line profile variations can be studied in great detail. As a consequence of the Doppler effect, precise information about the velocity field at the surface of pulsating stars can be obtained from line-profile time series. LPVs have been used, for example, to study the influence of rotation on pulsation (e.g. Lee & Saio 1990, Townsend 1997), to distinguish between non-radial pulsation and spots (Hatzes 1998, Balona et al. 1999, Briquet et al. 2001) or to perform mode identifications, as explained in more details in Sect. 3.3.3.

3.3.1 Simulation of line profile time series

In this subsection, we show briefly how simulations of line profile variations due to radial and non-radial oscillations can be performed. We recall that other sources of line profile variations such as spots exist; they are not taken into account here. The method presented in Sections 3.3.1 and 3.3.2 was implemented in the code PULSTAR by Dr. J. De Ridder in the frame of his PhD thesis (2001) and is summarized in De Ridder et al. (2002).

We denote by $I(\lambda, \vec{r}, \vec{d}, t)\ d\lambda\ d\omega\ dt$ the amount of energy that is radiated, at the position $\vec{r}$, through a unit surface, in the direction of the vector $\vec{d}$ within the solid angle $d\omega$, in the time interval $[t, t+dt]$ and in the wavelength interval $[\lambda, \lambda + d\lambda]$. The quantity $I(\lambda, \vec{r}, \vec{d}, t)$, called the specific intensity, is often abbreviated with I_λ. Except for the Sun, it is not possible to resolve the disks of stars. All what we see is the flux, which is the integral of the intensity over the stellar disk. The flux of a normalized absorption line profile, which we will denote with $p(\lambda, t)$, can generally be written as

$$p(\lambda, t) = \frac{\displaystyle\iint (d\vec{A}(\theta', \phi', t) \cdot \vec{k}')\ I\left(\frac{\lambda}{1 - \frac{v_{\text{tot}}(\theta',\phi',t)}{c}}, (\theta', \phi'), \vec{k}', t\right)}{\displaystyle\iint (d\vec{A}(\theta', \phi', t) \cdot \vec{k}')\ I_c\left(\frac{\lambda}{1 - \frac{v_{\text{tot}}(\theta',\phi',t)}{c}}, (\theta', \phi'), \vec{k}', t\right)}. \tag{3.49}$$

Here $I_c(\lambda)$ is the continuous intensity (i.e. the intensity that would be observed if the line was absent). $d\vec{A}$ is the local surface normal ($||d\vec{A}||$ is the area of an infinitesimal element of this stellar surface). $v_{\text{tot}}(\theta', \phi', t)$ is the total velocity with respect to the observer (pulsation + rotation + global velocity of the star) of the material element at coordinates (θ', ϕ'), projected on the line of sight. $\vec{k}'$ is the unit vector pointing from the star towards the observer. We omitted the r-coordinate since we assume that it is fixed on the radial coordinate of the line formation layer. We note however that the accurate determination of the line formation layer is an important point, as will be discussed later. The integration domain is the visible disk, and the integration variables used are the angular coordinates in the $\mathcal{O}$ reference frame. The division of the wavelength λ by $(1 - v_{\text{tot}}(\theta', \phi', t)/c)$ in Eq. (3.49) corresponds to the classical Doppler effect and is the main cause of the line profile variations of non-radial pulsators. Intuitively, during the non-radial pulsation, some parts of the star are moving towards the observer (which results in a blue-shift of the line) and at the same time, other parts of the star are moving in the opposite direction (which results in a red-shift of the line); by integrating all these local effects over the entire stellar disk, we obtain a complex variation of the line profile containing direct information about the velocity field at the stellar surface.

The surface on which the integrations of Eq. (3.49) are performed has to be chosen with care. As in Section 3.2.2, we work in the one-layer approximation, but we have to determine precisely the distance of this layer to the center of the star. It appears that the layer which contributes most to the flux depression of a spectral line is generally situated in much outer layers than the photosphere. In our simulations of line-profile variations, we have chosen the Si^{2+} triplet (456.784 nm) for β Cephei stars and the Si^{+} doublet (412.81 nm) for Slowly Pulsating B stars. These two lines are very popular for such simulations. On the basis of a method firstly derived by Magain (1986), De Ridder et al. (2002) showed that the layer which contributes most to the flux line depression of the Si^{2+} triplet is situated at $\log \tau = -1.625$ for a typical β Cephei atmosphere; and the layer which contributes most to the flux line depression of the Si^{+} doublet is situated at $\log \tau = -2$ for a typical SPB atmosphere. We chose these layers as integration domain of Eq. (3.49). We denote by R_l the the distance from the center of the star to the line formation layer, and we note that $R_l > R$.

Once the depth of this layer is determined, we can derive its distorsion due to non-radial oscillations. We assume here that this layer follows the movement of the matter. For a discussion about the validity of this approximation, we refer to Section 3.2.4. The variation of the surface elements $d\vec{A}(\theta', \phi', t)$ can be derived, using the full Lagrangian formalism of Heynderickx et al. (1994) (we refer to De Ridder 2001, §2.8 for more details), or by using a radial Lagrangian formalism, as we do in Section 3.2.2.

The local velocity of a stellar surface element projected on the line of sight (v_{tot}) is the sum of three terms: the pulsation velocity, the rotation velocity and the global velocity of the star which respect to the observer.

The pulsation velocity

By taking the time derivative of Eq. (1.45) and using the definition of the spherical harmonics in term of the associated Legendre functions, it is easy to show that for a spheroidal mode of degree ℓ and azimuthal order m, the velocity field at the line formation layer can be written in the $\mathcal{R}$ reference frame:

$$\left\{\begin{array}{lcl} \delta v_r(\theta,\phi,t) & = & -v_p\ N_\ell^m\ P_\ell^{|m|}(\cos\theta)\ \sin(\sigma t+m\phi), \\ \delta v_\theta(\theta,\phi,t) & = & -v_p\ \dfrac{\xi_h(R_l)}{\xi_r(R_l)}\ N_\ell^m\ \dfrac{\partial P_\ell^{|m|}(\cos\theta)}{\partial\theta}\ \sin(\sigma t+m\phi), \\ \delta v_\phi(\theta,\phi,t) & = & -\dfrac{v_p\ m}{\sin\theta}\ \dfrac{\xi_h(R_l)}{\xi_r(R_l)}\ N_\ell^m\ P_\ell^{|m|}(\cos\theta)\ \cos(\sigma t+m\phi), \end{array}\right. \qquad (3.50)$$

In order to get the contribution of the pulsation velocity on $v_{\rm tot}$, we just have to project Eq. (3.50) on the line of sight. For this purpose, it is appropriate to rewrite Eq. (3.50) in the $\mathcal{O}$ reference frame (we refer to De Ridder 2001, §2.7.2 for more details).

The rotation velocity

Assuming a uniform rotation, the rotation velocity projected on the line of sight is simply given by:

$$v_{\rm rot}(\theta,\phi)\ =\ v_e\ \sin i\ \sin\theta\ \sin\phi\ =\ v_e\ \sin i\ \sin\theta'\ \sin\phi'\ . \qquad (3.51)$$

The way to determine the other elements of Eq. (3.49) will be discussed in the next section.

3.3.2 Influence of non-adiabatic temperature variations on LPVs

Our main contribution in the interpretation of LPVs has been to determine the influence of non-adiabatic temperature variations, as will be discussed in this section.

Our main assumption in our non-adiabatic treatment of the stellar atmosphere is, as detailed in Section 2.3, to assume that the local atmosphere remains in radiative equilibrium during the pulsation. This assumption is justified by the fact that the thermal relaxation time of the atmosphere ($\approx 1s$) is much smaller than the typical periods of pulsation. We can therefore expect that, during the pulsation, the local intensity field of a spectral line will remain the same as the intensity field given by equilibrium atmosphere models. More precisely, we make in this section the same assumptions as in Section 3.2.2 (assumptions (a1) to (a9)), but with the following differrences. Firstly, our assumptions concern now the intensity field I_λ of a spectral line instead of the monochromatic outwards flux of the continuum (F_λ^+). Secondly, the distorded stellar surface used in the frame of our one-layer approximation is now the line formation layer, which is situated in the very outer atmosphere and not at the photosphere (see above).

Plane parallel equilibrium atmosphere models give the intensity $I_{\rm Kur}$ as function of the wavelength λ, the cosine of the angle between the line of sight and the stellar surface normal $\mu = \cos\theta'$, the effective temperature $T_{\rm eff}$, the logarithm of gravity $\log g$ and the chemical composition. In our applications, we computed and tabulated an LTE Kurucz intensity grid $I_{\rm Kur}(\lambda,\mu,T_{\rm eff},\log g)$ with the Kurucz (1993) spectrum synthesis software, with solar chemical composition and microturbulent velocity fixed at a value of 2 km/s. Under the above assumptions, we can derive the intensity field as function of θ, ϕ and t from the Kurucz grids, which gives:

$$(I_0+\delta I)(\lambda,\theta,\phi,t) \;=\; \tag{3.52}$$
$$I_{\rm Kur}\left[\frac{\lambda}{1-\frac{v_{\rm tot}(\theta,\phi,t)}{c}}\,,\;\mu+\delta\mu(\theta,\phi,t)\,,\;T_{\rm eff}+\delta T_{\rm eff}(\theta,\phi,t)\,,\;\log(g+\delta g_e(\theta,\phi,t))\right]\,.$$

The influence of the non-adiabatic effective temperature appears in the term $\delta T_{\rm eff}$ of this equation. This term can be directly computed by our non-adiabatic code, if the amplitude of the radial displacement $a = v_p/\sigma$ is fixed at the line formation layer. More precisely, we have:

$$\frac{\delta T_{\rm eff}}{T_{\rm eff}}(\theta,\phi,t) \;=\; f_{T\,l}\;a\;N_\ell^m\;P_\ell^{|m|}(\cos\theta)\;\;\cos(\sigma t+m\,\phi+\psi_{\rm T})\,, \tag{3.53}$$

where $f_{T\,l}$ (amplitude of local effetive temperature variation for a normalized radial displacement at the line formation layer) and ψ_T (phase-lag) are computed by our non-adiabatic code. We note that the convention of normalization in the determination of $f_{T\,l}$ is not the same as for f_T (Eq. (3.13)), because the line formation layer is not the photosphere.

Similarly, we have for the effective gravity variation:

$$\frac{\delta g_e}{g_e}(\theta,\phi,t) \;=\; -\,f_{g\,l}\;a\;N_\ell^m\;P_\ell^{|m|}(\cos\theta)\;\;\cos(\sigma t+m\,\phi)\,, \tag{3.54}$$

where $f_{g\,l}$ (amplitude of local effetive gravity variation for a normalized radial displacement at the line formation layer) is also computed by our non-adiabatic code (see Eq. (2.44)). We note that, for this coefficient, the difference between the adiabatic and non-adiabatic values is negligible.

We simplified the dependence of $I_{\rm Kur}$ with respect to μ by a least square fit to a limb-darkening law of the form:

$$I_\lambda(\mu) = a_0+\sum_{k=1}^{3} a_k\;(1-\mu^{\frac{k}{2}})\,, \tag{3.55}$$

which is a simplification of the non-linear limb-darkening law proposed by Claret (2000):

$$\frac{I_\lambda(\mu)}{I_\lambda(\mu=1)} = 1-\sum_{k=1}^{4} a_k\;(1-\mu^{\frac{k}{2}})\,. \tag{3.56}$$

And finally, $\delta\mu(\theta,\phi,t)$ was determined with the full Lagrangian formalism of Heynderickx et al. (1994) (see De Ridder 2001, §2.8). We note that we could also use the Eulerian formalism of Buta & Smith (1979) or our radial Lagrangian formalism (see Eqs. (3.19) and (3.20)).

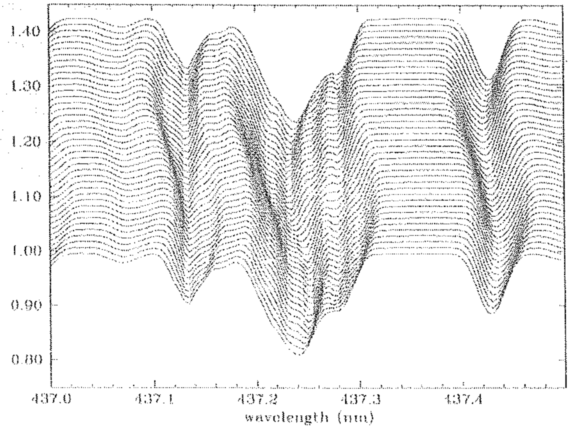

Figure 3.4: Time series of part of the normalized spectrum of a β Cephei star pulsating in the mode $(\ell, m) = (2, 1)$ and viewed under an inclination angle of 45°. To obtain a better visual effect, the successive normalised spectra are shifted with 0.011 continuum units. The visible lines are mainly from Fe^{2+} and C^{+}. Figure taken from De Ridder (2001).

So, we have described how all the ingredients of Eqs. (3.49) and (3.52) can be determined. As usually, for practical numerical simulations the integrals of Eq. (3.49) have to be approximated by a discrete sum, subdividing the integration domain in finite elements. In this case, the visible part of the star is subdivided in many cells (typically, $(\Delta\theta, \Delta\phi) = (2^\circ, 2^\circ)$ for each cells). This method of simulation of line profile time series, taking the non-adiabatic effects into account, was implemented in the computer code "PULSTAR" by Dr. J. De Ridder. In Figure 3.4, we illustrate the time series of part of the spectrum of a β Cephei star pulsating in the mode $(\ell, m) = (2, 1)$. We refer to Sections 4.1.7 and 4.2.7 for the application of this method to β Cephei and Slowly Pulsating B stars respectively.

3.3.3 Mode identification based on LPVs

Essentially three techniques of mode identification based on line profile variations are currently used: line profile fitting, the moment method and Doppler imaging. We will speak only about the first two methods and refer to Gies & Kullavanijaya (1988) and Telting & Schrijvers (1997) for more details about the Doppler imaging method.

Line profile fitting

The basic principle of line profile fitting is quite simple: compare time series of theoretically computed line profiles with time series of the observed line profiles using a goodness of fit measure (e.g. based on least squares) to obtain a set of "best fitting parameters". In practice, this can be done as follows. For many couples (ℓ, m), a grid of all other (continuous) parameters (e.g. v_p, v_e and i) is set up. For each of these grid points a time series of line profiles is computed and compared with the observational data. An iterative convergence algorithm like the Levenberg-Marquardt method of optimisation by non-linear least squares can be implemented in order to find the best solution. A nice feature of this technique is that it is not only able to deliver the numbers (ℓ, m) but also other parameters such as the inclination angle and the rotational equatorial velocity. The main default of this method is that it is extremely CPU-time consuming.

The moment method

In the moment method, the pulsation parameters are estimated by fitting only the first few moments of a line profile instead of fitting the entire line profile (see e.g. Aerts et al. 1992). Using a basic line profile model (Gaussian profiles with variations only due to the Doppler shift), Aerts (1993) derived the following expressions for the first three normalized moments:

$$\begin{aligned} \langle v \rangle &= a_1 \sin(\sigma t + \alpha_1) , \qquad (3.57) \\ \langle v^2 \rangle &= b_0 + b_1 \sin(\sigma t + \beta_1) + b_2 \sin(2\sigma t + \beta_2) , \qquad (3.58) \\ \langle v^3 \rangle &= c_1 \sin(\sigma t + \gamma_1) + c_2 \sin(2\sigma t + \gamma_2) + c_3 \sin(3\sigma t + \gamma_3) , \qquad (3.59) \end{aligned}$$

The amplitudes a_1, b_i and c_i depend on the pulsation and rotation parameters ℓ, m, v_p, v_e and i (and on the shape of the local line profile). The principle of the method is to fit the observed variations of the first three moments with functions of the form Eqs. (3.57), (3.58) and (3.59). In this procedure, the choice of an accurate discriminant is very important (Aerts 1996). Briquet et al. (2003a and 2003b) included the effect of rotation in the moment method and optimized it for multi-periodic stars.

Chapter 4

Applications

4.1 β Cephei stars

4.1.1 β Cephei stars from an observational point of view

We begin by giving a very short summary of what are β Cephei stars from an observational point of view. β Cephei stars are population I main-sequence stars (close to the turn-off) with spectral types between B0 and B2.5. They are pulsating stars with periods going from 3 to 8 hours. Most of the β Cephei are multiperiodic and, for many of them, there is a strong evidence that some of their pulsation modes are non-radial. Their masses range from 7 $M_\odot$ to 20 $M_\odot$. β Cephei stars show generally photometric as well as spectroscopic variations. However, more and more β Cephei stars are now being discovered which show line profile variations, without detectable corresponding photometric variations, e.g. ω^1 Sco (Schrijvers 1999). By now, more than 100 stars are confirmed or suspected β Cephei stars. Among them, slow rotators as well as rapid rotators have been observed. Up to now, no magnetic fields have been detected, with the exception of the prototype star β Cephei itself (Henrichs et al. 2000). The pulsation periods are stable, although variations of the order of a second or smaller per century have been observed in some β Cephei stars (e.g. Cuypers 1986). Except for the star BW Vulpeculae, the pulsation of β Cephei stars is well described by the linear theory (the light curves are sinusoidal). The amplitude in the V filter is usually smaller than 0.1 mag.

4.1.2 β Cephei stars from a theoretical point of view

From a stellar evolution point of view, β Cephei stars are close the end of the core hydrogen-burning stage in the main sequence. Due to the high temperature sensitivity of the dominant CNO cycle, they have a large convection core, but no superficial convection zone is present. The periods of the β Cephei stars point towards low order p-modes and/or low order g-modes. For such modes, the transversal compression of

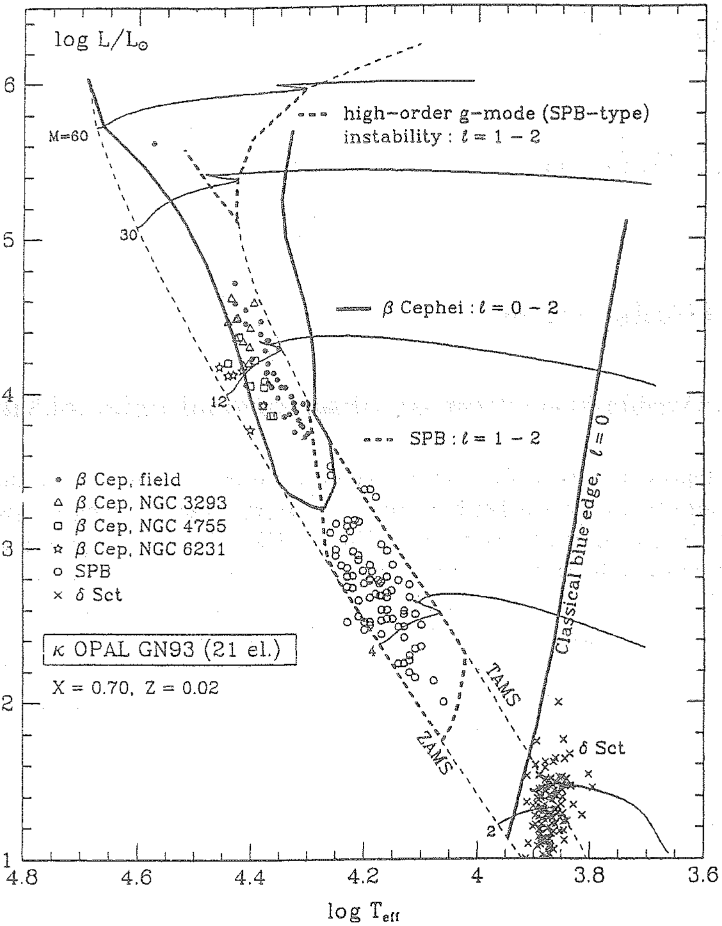

Figure 4.1: Situation of the β Cephei (●, △, □ and ⋆), SPB (○) and δ scuti stars (×) in a HR diagram and theoretical instability strips as computed by Pamyatnykh (1999).

1.0

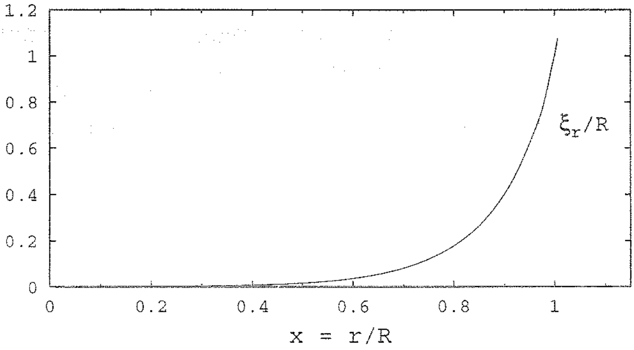

Figure 4.2: Real part of the radial displacement: $\Re\{\xi_r/R\}$ as function of $x = r/R$ for the fundamental radial mode of a $9.5\,M_\odot$ β Cephei model.

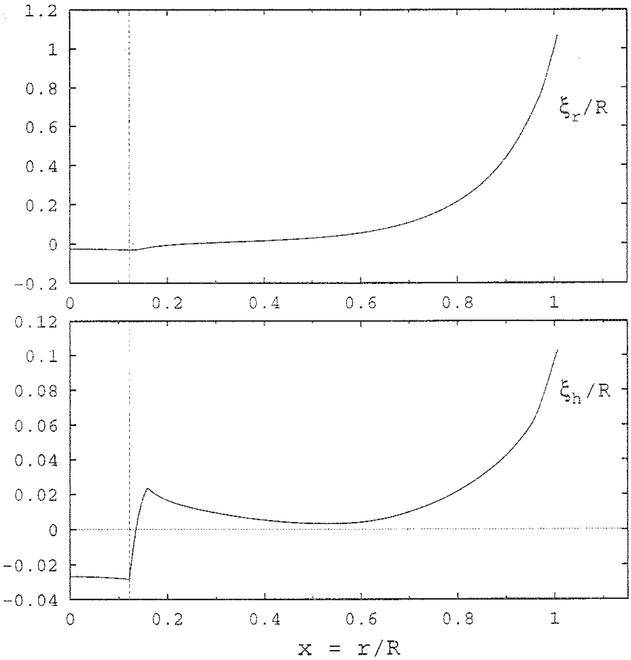

Figure 4.3: Real part of the radial displacement: $\Re\{\xi_r/R\}$ (top) and of the transversal displacement: $\Re\{\xi_h/R\}$ (bottom) as function of $x = r/R$ for the mode $\ell = 1$, g_1 of a $9.5\,M_\odot$ β Cephei model. The vertical line corresponds to the frontier between the central convection zone and the radiative envelope.

the matter is much smaller than the radial compression: more precisely, the term proportional to $\ell(\ell+1)$ is very small in the equation of mass conservation (Eqs. (1.47) and (2.3)). Because of the dominating radial compression, we deduce also that in the superficial layers and under the adiabatic approximation, $\delta\rho/\rho$ and $\delta P/P$ are in antiphase with the radial displacement (contrary to high order g-modes for which they have the same phase). Our non-adiabatic computations predict a very small extra phase-lag between the superficial temperature variation and the radial displacement, as will be shown in Section 4.1.6. Avoided crossings and mixing between g-modes and p-modes are frequent phenomenons in β Cephei stars; a typical illustration of the avoided crossings can be seen in Figures 4.8, 4.9 and 4.10 where the behaviour of the frequencies of different modes as function of the age of the model are given along some β Cephei evolution tracks.

We can see in Figure 4.1 the situation of some β Cephei stars in a HR diagram (represented with $\bullet$, $\triangle$, $\square$ and $\star$). On the same figure, the theoretical instability strip derived by Pamyatnykh (1999) is given. In Figure 4.2, we give the real part of the radial displacement $\Re\{\xi_r/R\}$ for the fundamental radial mode of a 9.5 $M_\odot$ β Cephei model (the global characteristics of this model are given in Table 4.2, model 2a). In Figure 4.3, we give the real part of the displacement in the radial direction ($\Re\{\xi_r/R\}$, top) and in the transversal direction ($\Re\{\xi_h/R\}$, bottom) for the mode $\ell=1$, g_1 of the same model. In these figures, the abscissa corresponds to $x=r/R$ (from left to right, we go from the center to the surface of the star). These eigenfunctions are normalized in such a way that $\xi_r/R=1$ at the photosphere ($x=1$). The mode $\ell=1$, g_1 illustrates the typical case of a mixed mode, with a g-mode behaviour (significant transversal displacement) in the central layers and a p-mode behaviour (dominating radial displacement) in the superficial layers.

4.1.3 Driving mechanism of the β Cephei stars

An important capacity of our non-adiabatic code is that it permits to study with high precision the driving mechanisms occuring in β Cephei stars. As proposed by Cox et al. (1992), Moskalik & Dziembowski (1992), Kiriakidis et al. (1992), Dziembowski & Pamyatnykh (1993a) and Pamyatnykh (1999), the driving mechanism at the basis of the excitation of the β Cephei low order p-modes and g-modes is a κ-mechanism associated to the metal opacity bump, at temperatures around 200.000 K ($\log T \simeq 5.3$). In order to illustrate this phenomenon, we give the results we obtained for a β Cephei model whose the global characteristics are given in Table 4.2 (model 2a). It is a good model of the star EN(16) Lac: the global characteristics (effective temperature and luminosity) and the theoretical periods are very close to the observations.

In Figure 4.4, we give at the the top the opacity in cm^2/g as function of the logarithm of temperature (from left to right, we go from the stellar center to the surface). We can see 2 bumps of opacity. The first bump at $\log T \simeq 5.3$ is due to the tremendous number of iron lines in this region (Cox et al. 1992). This opacity bump is very important since it is at the origin of the driving of β Cephei stars. And a second bump at $\log T \simeq 4.6$

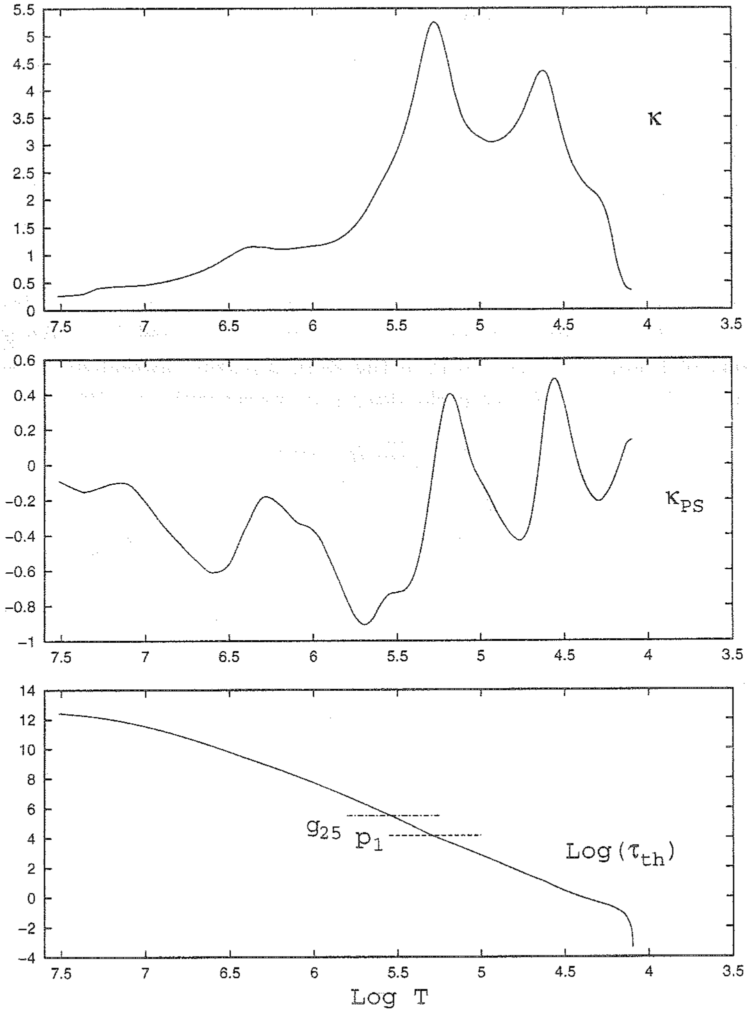

Figure 4.4: Opacity in cm^2/g (top), $\kappa_{PS} = \left.\frac{\partial \ln \kappa}{\partial \ln P}\right|_S$ (middle) and logarithm of the thermal relaxation time in seconds: $\log(\tau_{th})$ (bottom), as function of the logarithm of temperature, for a $9.5\,M_\odot$ model of the β Cephei star EN Lac.

corresponds to the second partial ionization zone of Helium. At the middle of Figure 4.4, we give the graph of the logarithmic derivative of the opacity with respect to the pressure at constant entropy:

$$\kappa_{PS} = \left.\frac{\partial \ln \kappa}{\partial \ln P}\right|_S = \frac{\Gamma_3 - 1}{\Gamma_1}\,\kappa_T + \frac{\kappa_\rho}{\Gamma_1}\,. \tag{4.1}$$

This graph will help us in the qualitative explanation of the κ mechanism. The important point is that κ_{PS} increases outwards in the driving region. Finally, we give at the bottom the graph of the logarithm of the thermal relaxation time in seconds: $\log(\tau_{th})$, as function of the logarithm of temperature. The horizontal dashed line with the label p_1 gives the logarithm of the period of pulsation of the fundamental radial mode and the horizontal dot-dashed line with the label g_{25} gives the logarithm of the period of pulsation of the mode $\ell = 1$, g_{25}.

In Figure 4.5, we illustrate some non-adiabatic results obtained for the fundamental radial mode of the β Cephei model given in Table 4.2 (model 2a). We give in the middle panel of Figure 4.5, the graph of the work integral, normalized in such a way that the final value at the surface is the dimensionless growth rate ($W(1) = -\Im\{\omega\}$):

$$\mathrm{W}(x) = \frac{-1}{2\,\Re\{\omega\}}\;\frac{\displaystyle\int_0^x \Im\left\{\frac{\overline{\delta\rho}}{\rho}\,\frac{RT\,\delta S}{GM}\right\}(\Gamma_3 - 1)\,x^2\,\rho_{\mathrm{m}}\,\mathrm{d}x}{\displaystyle\int_0^1 \left(|\xi_r/R|^2 + \ell(\ell+1)\,|\xi_h/R|^2\right)\,x^2\,\rho_{\mathrm{m}}\,\mathrm{d}x}\,. \tag{4.2}$$

The abscissa corresponds to the logaritm of temperature. The regions where W has a positive derivative are driving the mode and the regions where W has a negative derivative are damping the mode. A negative value of W at a given layer means that the work achieved during one cycle by the part of the star below this layer is negative. Therefore, this part of the star is damping the pulsation. A positive value of W at a given layer means that the work achieved during one cycle by the part of the star below this layer is positive. Therefore, this part of the star is driving the pulsation. In the top panel of the same figure, we give the derivative of $-W$ with respect to the logarithm of temperature: $-\mathrm{d}W/\mathrm{d}\log T$. The regions where $-\mathrm{d}W/\mathrm{d}\log T$ is positive are driving the mode and the regions where $-\mathrm{d}W/\mathrm{d}\log T$ is negative are damping the mode. Finally, we give in the bottom panel of Figure 4.5, the graph of the relative amplitude of variation of the luminosity.

On the basis of Figures 4.4 and 4.5, we can now explain in details the driving mechanism occuring in β Cephei stars. As usually in stellar stability, we can divide the star in three parts (see the graph of the thermal relaxation time, bottom of Figure 4.4). Firstly, there is the quasi-adiabatic region where the thermal relaxation time is much larger than the period of pulsation. Secondly, there is the transition region where the thermal relaxation time is of the same order as the period of pulsation. The middle of the transition region is given by the intersection between the horizontal dashed line with the label p_1 (logarithm of the theoretical period of the fundamental radial mode) and the logarithm of the thermal relaxation time in the bottom panel of Figure 4.4. And thirdly, there is the highly non-adiabatic region where the thermal relaxation time

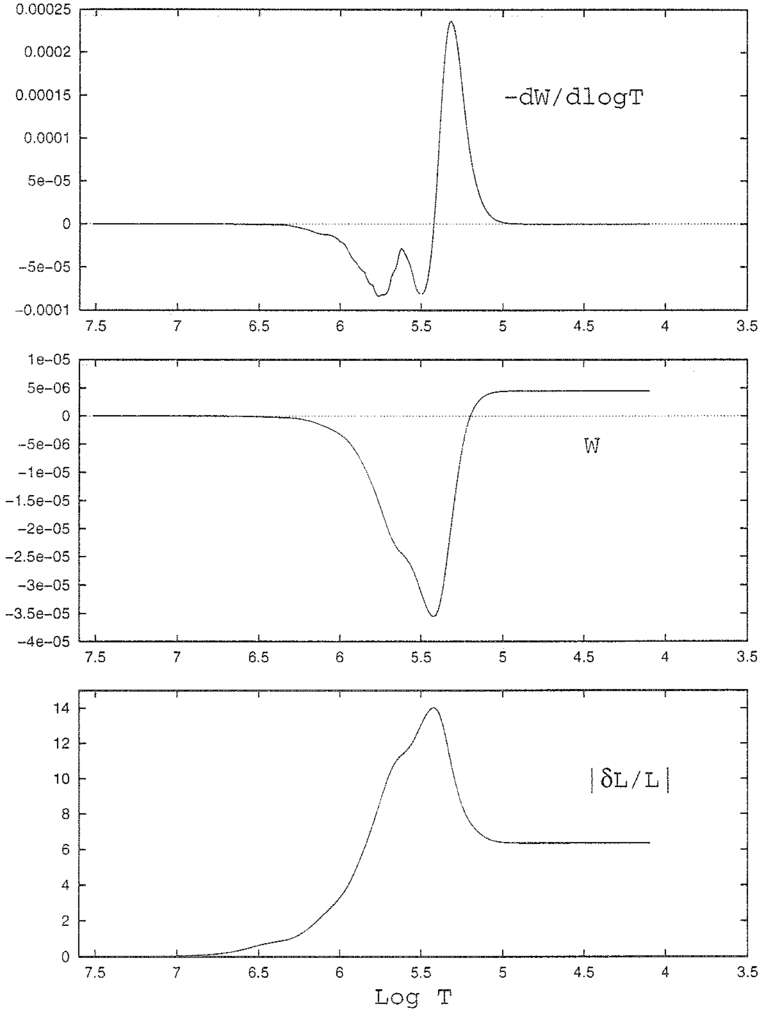

Figure 4.5: $-\mathrm{d}W/\mathrm{d}\log T$ (top), dimensionless work integral W (middle) and amplitude of luminosity variation: $|\delta L/L|$ (bottom), as function of the logarithm of temperature, for the fundamental radial mode of a $9.5\,M_\odot$ model of the β Cephei star EN Lac.

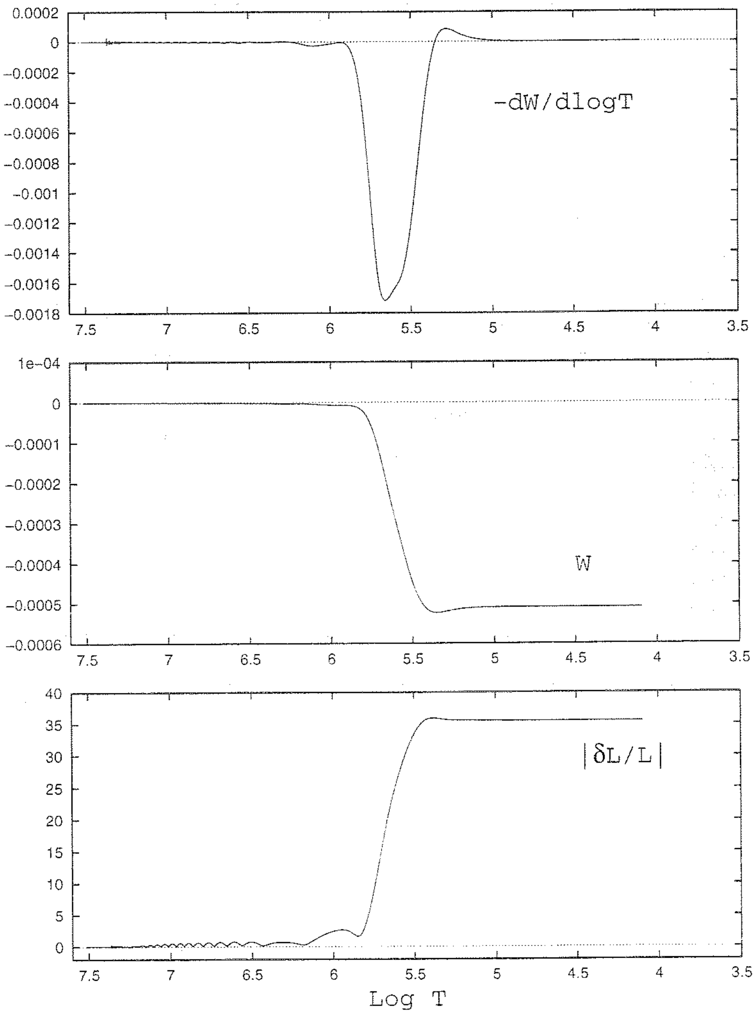

Figure 4.6: $-\mathrm{d}W/\mathrm{d}\log T$ (top), dimensionless work integral W (middle) and amplitude of luminosity variation: $|\delta L/L|$ (bottom), as function of the logarithm of temperature, for the mode $\ell = 1$, g_{25} of a $9.5\,M_\odot$ model of the β Cephei star EN Lac.

is much smaller than the period of pulsation. The region of a star where the driving or damping mechanisms are the most efficient is always the transition region. In our case, the transition region is situated at $\log T \simeq 5.3$, which is exactly the place of the metal opacity bump (see Figure 4.4). For the physical interpretation of the driving, we refer firstly to Eq. (1.78). This equation corresponds to the quasi-adiabatic approximation and to a radial mode, but it is sufficient for the present discussion. We deduce from Eq. (1.78) that the driving regions are the regions where δL is decreasing outwards at the hot phase (motor thermodynamical cycle). And we see that it is exactly what we obtain for our model in Figure 4.5 (bottom): $|\delta L/L|$ is decreasing outwards in the transition region. The cause of this luminosity decrease is the metal opacity bump. More precisely, κ_{PS} is increasing outwards in the transition region (Figure 4.4, middle). Therefore, $\delta\kappa/\kappa$ is increasing outwards at the hot phase. And finally, from Eq. (2.6) or Eq. (2.7), this implies that $\delta L/L$ is decreasing outwards at the hot phase. As a simple summary, at the transition region and during the hot phase, the luminosity variation is blocked by the opacity barrier, which is driving the oscillation.

In order to show that this driving mechanism affects low order p-modes and g-modes but not high order g-modes (for β Cephei stars), we give in Figure 4.6 the results obtained for the mode $\ell = 1$, g_{25} of our 9.5 $M_\odot$ model. The explanation of the stability of the high order g-modes of β Cephei stars is the following. For high order g-modes (greater periods), the transition region where the period is of the same order as the thermal relaxation time is situated in more inside layers (Figure 4.4, bottom). In this region, κ_{PS} (Figure 4.4, middle) and thus $\delta\kappa/\kappa$ has not a steep gradient outwards (contrary to the more outside layers). And therefore $\delta L/L$ is increasing outwards at the hot phase (around $\log T = 5.6$ in Figure 4.6, bottom), which has a damping effect on the pulsation (Figure 4.6, top and middle). In the exciting regions situated more outside, the thermal relaxation time is much smaller than the period of pulsation, so that the driving is inefficient and cannot counterbalance the damping of the more inside layers.

In Figure 4.7, we give HR diagrams with evolution tracks of models with different masses and metallicities. The blue edges of the instability strips obtained with our non-adiabatic code for the fundamental radial mode are also given. We show in more details the unstable modes of these models in Figures 4.8, 4.9, 4.10 and 4.11. The first three figures correspond to sequences with different metallicities: $Z = 0.02$ in Figure 4.8, $Z = 0.025$ in Figure 4.9 and $Z = 0.015$ in Figure 4.10. The masses of the stars corresponding to these 3 sequences are slightly different and where chosen in such a way that the evolution tracks are very close in the HR diagram. In Figure 4.11, we show the unstable modes obtained along a more massive 12 $M_\odot$ sequence with solar metallicity. In each figure, we give four graphs corresponding to the spherical degrees $\ell = 0$, $\ell = 1$, $\ell = 2$ and $\ell = 3$. In each graph, we give the frequencies in cycles/day of modes of different radial order n, as function of the age of the models in Myears, and a scale with the logarithm of the effective temperature is given at the top. The empty circles correspond to stable modes and the full circles to unstable modes.

We see that only modes with frequencies close to the frequency of the fundamental radial mode are predicted to be unstable. Except for the $Z = 0.025$ models, we predict no unstable modes for the young models close to the ZAMS. By comparing the 3 figures, we see that the number of unstable modes increases quickly with the metallicity of the model. The physical explanation is simple. The larger is the metallicity, the larger is the metal opacity bump, and therefore the more efficient is the κ-mechanism driving the modes. These theoretical results are in good agreement with the typical observed frequencies of β Cephei stars. In particular, for the β Cephei star EN Lac, well represented by the models with an age of approximately 16 Myears, all the modes in the observed range of frequency are predicted to be unstables, even for the model with the small metallicity $Z = 0.015$. By comparing the results obtained for the 9.5 $M_\odot$ and 12 $M_\odot$ sequences of evolution with solar metallicity (Figures 4.7 (left), 4.8 and 4.11), we see that the blue edge of the instability strip is closer to the turn-off for the more massive 12 $M_\odot$ models than for the 9.5 $M_\odot$ models, in agreement with Pamyatnykh (1999). We see that the radial orders of the unstable modes are little dependent on the mass, for a given metallicity; we only note that the first radial overtone is unstable for the evolved 12 $M_\odot$ models but it is always stable for the 9.5 $M_\odot$ models with solar metallicity.

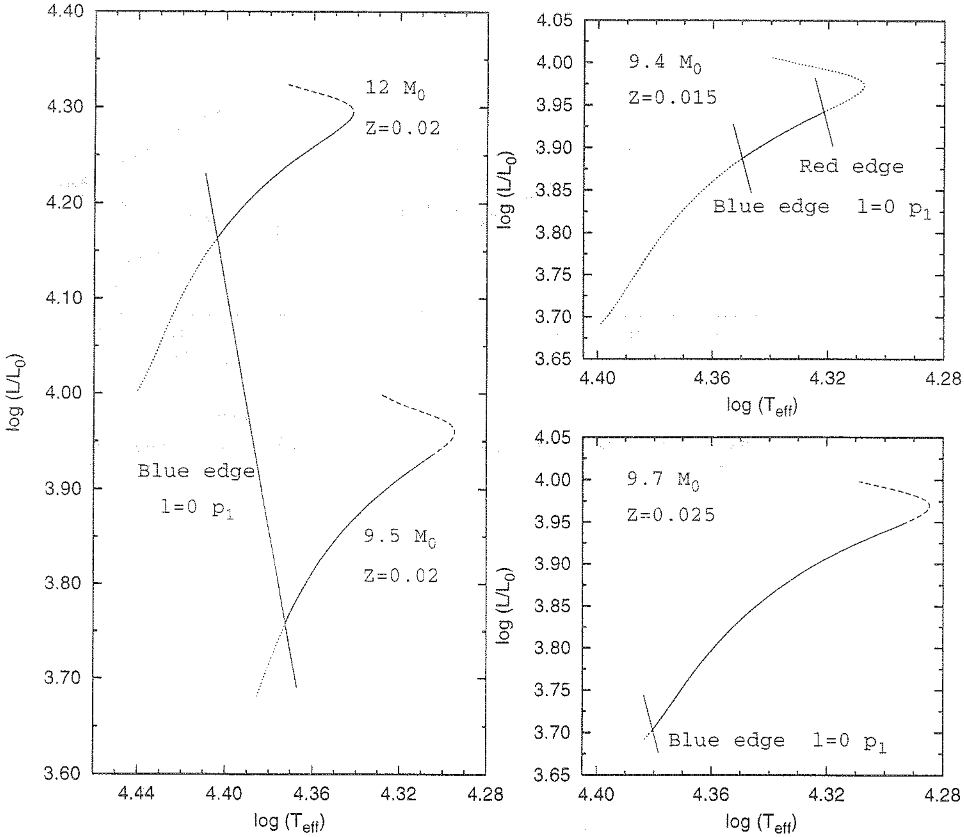

Figure 4.7: HR diagram with the blue edge of the instability strip for the fundamental radial mode and for models with different metallicities and masses.

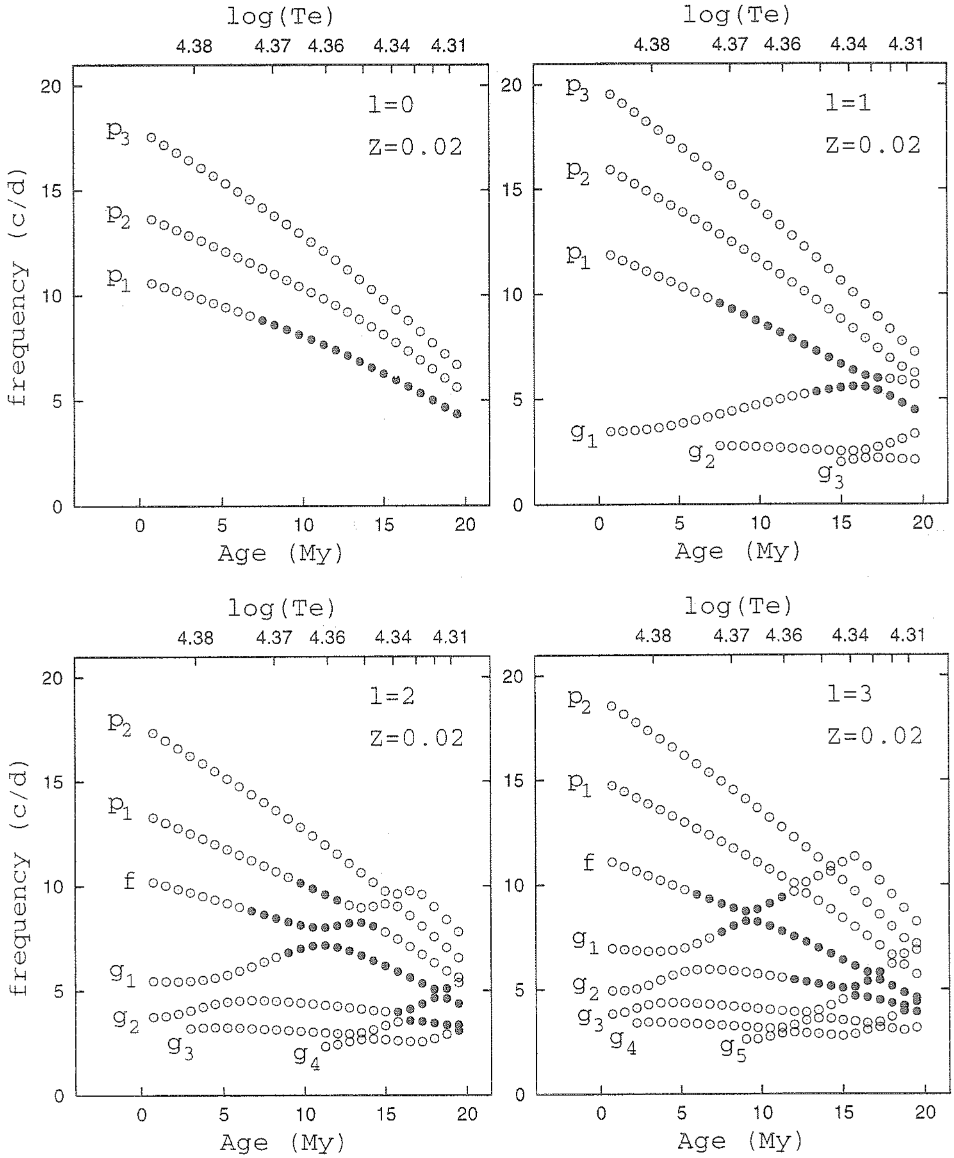

Figure 4.8: Stable and unstable modes of degree $\ell = 0$ (left, top), $\ell = 1$ (right, top), $\ell = 2$ (left, bottom) and $\ell = 3$ (right, bottom) along a $9.5\,M_\odot$ sequence of evolution with solar metallicity ($Z = 0.02$). We give the frequencies of the modes in cycles/day as function of the age in Myears and of $\log(T_{\rm eff})$. The full circles correspond to the unstable modes and the empty circles to the stable modes.

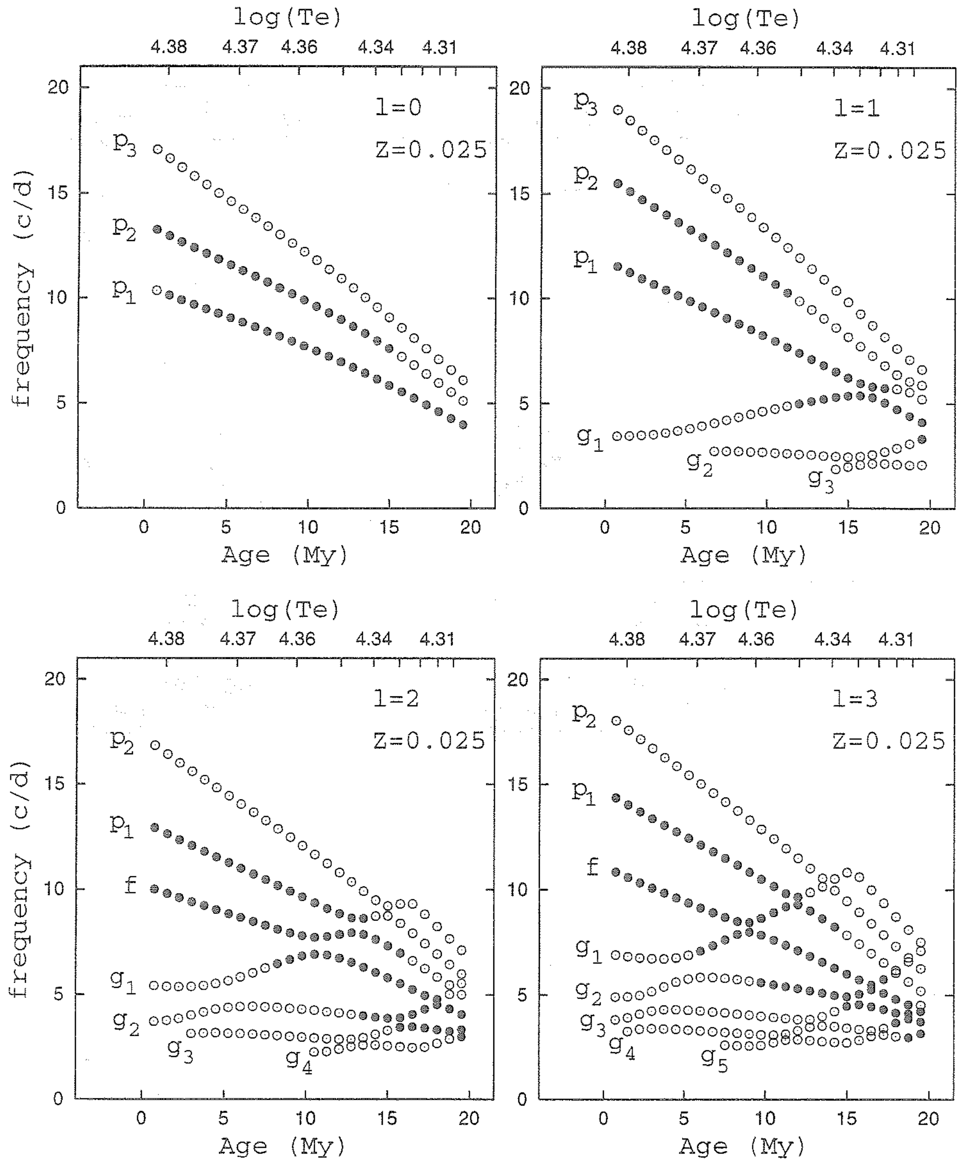

Figure 4.9: Stable and unstable modes of degree $\ell = 0$ (left, top), $\ell = 1$ (right, top), $\ell = 2$ (left, bottom) and $\ell = 3$ (right, bottom) along a $9.7\,M_\odot$ sequence of evolution with $Z = 0.025$. We give the frequencies of the modes in cycles/day as function of the age in Myears and of $\log(T_{\rm eff})$. The full circles correspond to the unstable modes and the empty circles to the stable modes.

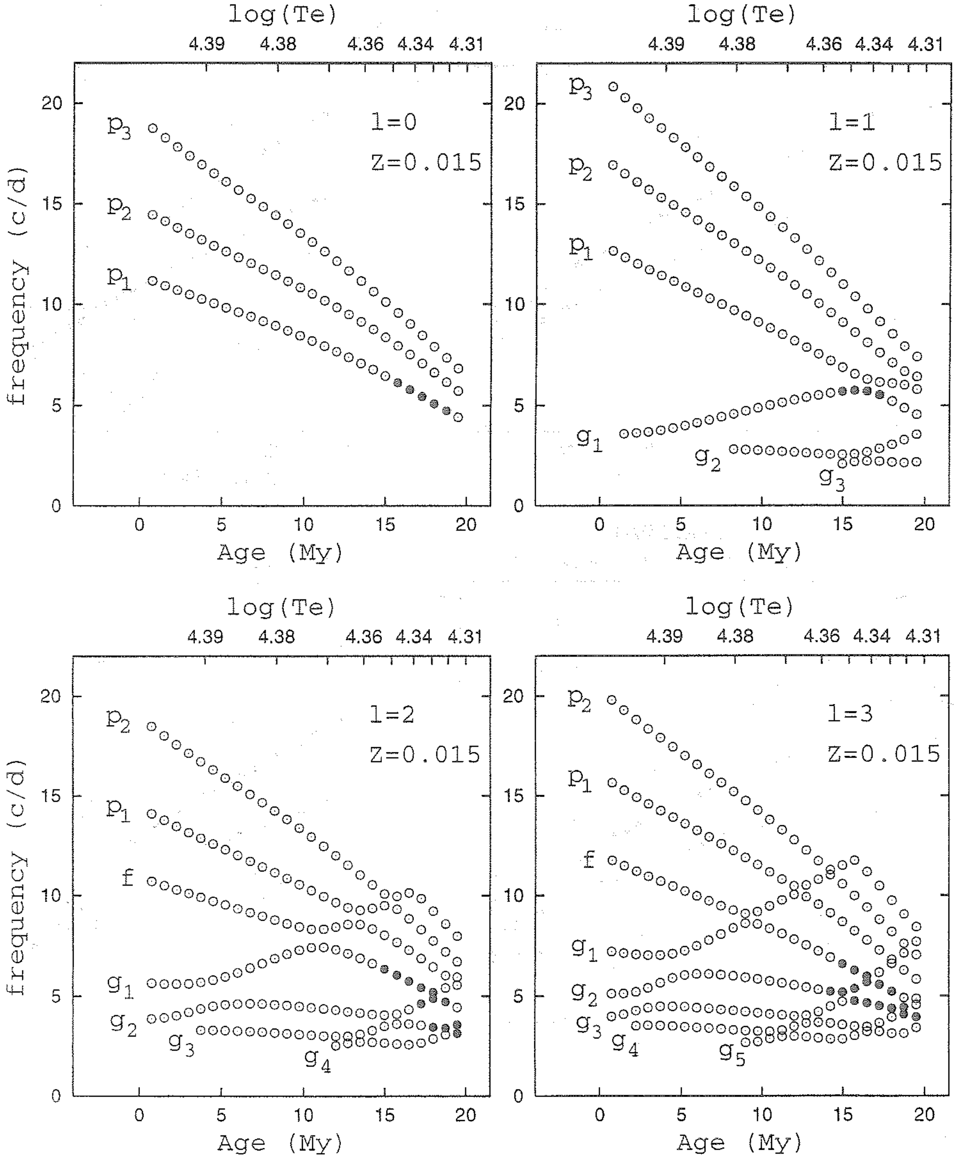

Figure 4.10: Stable and unstable modes of degree $\ell = 0$ (left, top), $\ell = 1$ (right, top), $\ell = 2$ (left, bottom) and $\ell = 3$ (right, bottom) along a $9.4\,M_{\odot}$ sequence of evolution with $Z = 0.015$. We give the frequencies of the modes in cycles/day as function of the age in Myears and of $\log(T_{\text{eff}})$. The full circles correspond to the unstable modes and the empty circles to the stable modes.

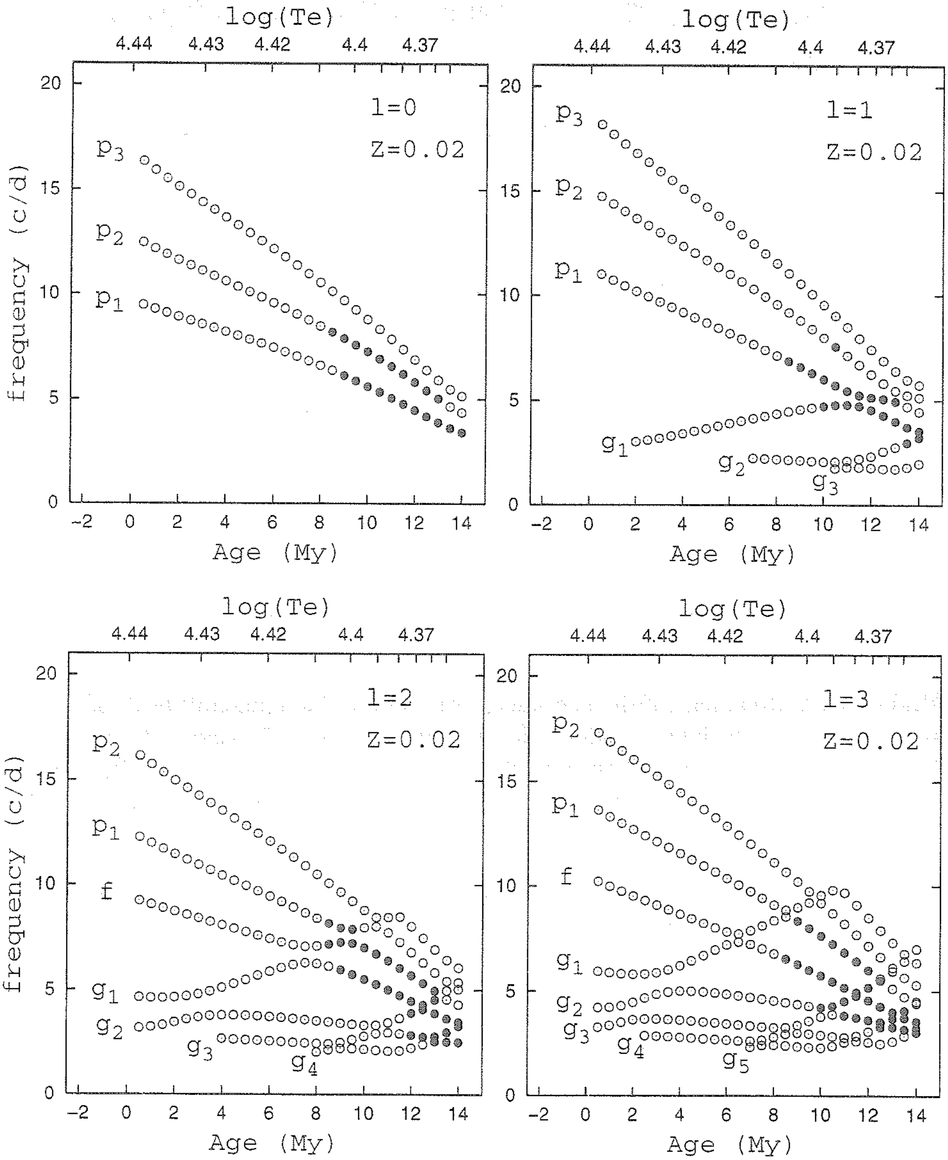

Figure 4.11: Stable and unstable modes of degree $\ell = 0$ (left, top), $\ell = 1$ (right, top), $\ell = 2$ (left, bottom) and $\ell = 3$ (right, bottom) along a $12\,M_\odot$ sequence of evolution with solar metallicity ($X = 0.7$ and $Z = 0.02$). We give the frequencies of the modes in cycles/day as function of the age in Myears and of $\log(T_{\rm eff})$. The full circles correspond to the unstable modes and the empty circles to the stable modes.

4.1.4 Comparison between adiabatic and non-adiabatic eigenfunctions

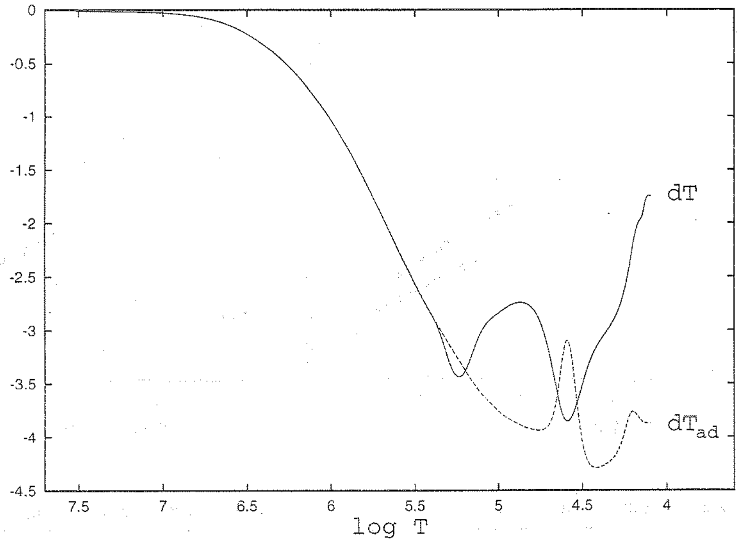

Figure 4.12: Real part of the Lagrangian variation of the temperature $\delta T/T$ as computed by our non-adiabatic code (solid line with the label dT) compared to the adiabatic Lagrangian variation of the temperature $\delta T/T|_{\rm ad} = (\Gamma_3 - 1)/\Gamma_1\, \delta P/P|_{\rm ad}$ (dashed line with the label dT$_{\rm ad}$), as function of the logarithm of temperature, from the center to the surface of the star.

It is useful to show how different are the adiabatic and non-adiabatic eigenfunctions in the interior of β Cephei stars. As in Section 4.1.3, we illustrate the results obtained for a typical 9.5 $M_\odot$ β Cephei model whose global characteristics are given in Table 4.2 (model 2a), and for the fundamental radial mode. In Figure 4.12, we compare the real part of the Lagrangian variation of the temperature $\delta T/T$ as computed by our non-adiabatic code (solid line with the label dT) to the adiabatic Lagrangian variation of the temperature (dashed line with the label dT$_{\rm ad}$) defined by:

$$\left.\frac{\delta T}{T}\right|_{\rm ad} = \frac{\Gamma_3 - 1}{\Gamma_1} \left.\frac{\delta P}{P}\right|_{\rm ad} . \tag{4.3}$$

The eigenfunctions are normalized in such a way that the relative radial displacement is equal to 1 at the photosphere. We see that in the quasi-adiabatic region (from the center to $\log T \simeq 5.4$), the non-adiabatic and the adiabatic temperature variations are the same. On the contrary, from the driving region to the superficial layers, the two become totally different. The high non-adiabaticity of the superficial layers is explained by the small thermal relaxation time compared to the period of pulsation in this region (Figure 4.4, bottom). The qualitative behaviour of the eigenfunctions of Figure 4.12 has a simple physical explanation.

Firstly, concerning the non-adiabatic temperature variation (solid line), the two bumps correspond exactly to the two bumps of opacity (Figure 4.4, top). The reason is the following. In the superficial layers, the luminosity variation $\delta L/L$ is approximately constant because of the small thermal relaxation time (Figure 4.5, bottom). From the perturbed diffusion equation (Eq. (2.6)), changes of the opacity variation $(\delta\kappa/\kappa)$ are thus counterbalanced by changes of $(\partial\,\delta T/\partial r)/(\mathrm{d}T/\mathrm{d}r)$. In other words, changes in the derivatives of the opacity are counterbalanced by changes of the derivative of $\delta T/T$. And therefore, the qualitative behaviour of $\delta T/T$ is scaled on the qualitative behaviour of the equilibrium opacity.

Secondly, concerning the adiabatic temperature variation (dashed line), the bumps correspond exactly to the bumps of the adiabatic gradient $(\Gamma_3 - 1)/\Gamma_1$ due to the partial ionization zones. The reason is that the Lagrangian variation of the pressure has a smooth behaviour because of the control by the equation of momentum conservation (Eq. (2.1)). Therefore, from Eq. (4.3), the qualitative behaviour of the adiabatic temperature variation is scaled on the adiabatic gradient.

4.1.5 Non-adiabatic eigenfunctions in the atmosphere of β Cephei stars

The main specificity of our non-adiabatic code is the special care given to the treatment of the pulsation in the atmosphere, we illustrate in this section some of the results obtained in the atmosphere of a typical β Cephei star (same model and same mode as in Section 4.1.4). For all our applications to β Cephei stars, the connecting layer between the interior and atmosphere specific treatments (Chapter 2) was chosen at $\tau = 10$. This layer is sufficiently deep, so that the diffusion approximation is valid beneath it.

In Figure 4.13, the solid line (label "dT") is the graph of $|\delta T/T|$ in the atmosphere. The abscissa corresponds to the logarithm of the Rosseland optical depth. The vertical line corresponds to the photosphere where $T = T_{\mathrm{eff}}$. The smoothness of the graph at $\log\tau = 1$ confirms that our two specific treatments in the interior and in the atmosphere match very well at the connecting layer. On the same figure, we give the moduli of the different terms of Eq. (2.32), which is the base of our non-adiabatic treatment in the atmosphere. We see that $|\partial\ln T/\partial\ln g_{\mathrm{e}}\;\delta g_{\mathrm{e}}/g_{\mathrm{e}}|$ (label (2)) is very small compared to the other terms. It is important to note that the term $|\partial\ln T/\partial\ln\tau\;(\delta\tau/\tau)|$ (label (3)) is large. Physically, it means that the Lagrangian variation of the temperature $|\delta T/T|$ and the variation of the temperature at constant optical depth $|\Delta_\tau T/T| \simeq |\partial\ln T/\partial\ln T_{\mathrm{eff}}\;(\delta T_{\mathrm{eff}}/T_{\mathrm{eff}})|$ (label (1)) are two totally different quantities for β cephei stars. It could seem surprising that $|\partial\ln T/\partial\ln\tau\;(\delta\tau/\tau)|$ does not go to zero at the outermost layer. This comes from the significant values of $\partial\ln T/\partial\ln\tau$ in the Kurucz atmosphere models, even at very small optical depths (see Figure 2.2). In order to examine if this "surprising" phenomenon has a significant impact on the results, we examined the results obtained by putting artificially $\partial\ln T/\partial\ln\tau\;(\delta\tau/\tau)$ to zero at the outermost layer (last term of Eq. (2.48)). Only the values of $\delta T/T$ in the outermost

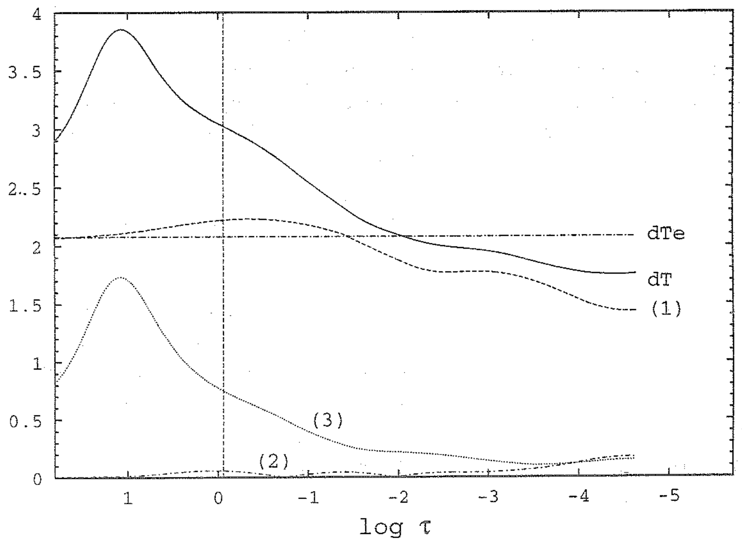

Figure 4.13: Amplitude of Lagrangian temperature variation $|\delta T/T|$ (solid line with the label "dT"), amplitude of local effective temperature variation $|\delta T_{\rm eff}/T_{\rm eff}|$ (dot-dashed line with the label "dTe") and moduli of the different contributing terms of the right-hand side of Eq. (2.32). The dashed line with the label (1) is the modulus of the first term ($\propto \delta T_{\rm eff}/T_{\rm eff}$), the dot-dashed line with the label (2) is the modulus of the second term ($\propto \delta g_{\rm e}/g_{\rm e}$) and the dotted line with the label (3) is the modulus of the third term ($\propto \delta\tau/\tau$), the vertical line corresponds to the photosphere where $T = T_{\rm eff}$. The functions were computed for the fundamental radial mode, in the atmosphere of a 9.5 $M_\odot$ β Cephei model (Table 4.2, model 2a).

layers (from $\log\tau = -2$ to the last layer) are significantly affected by this artificial change. The impact on the other results, such as $\delta T_{\rm eff}/T_{\rm eff}$ is found to be very small.

Comparing the value of $|\delta T/T|$ at the photosphere to the value of $|\delta T_{\rm eff}/T_{\rm eff}|$ shows that they are very different. This leads us to compare the boundary condition we impose on the flux – Eqs. (2.37) and (2.42) – to the thermal boundary condition adopted by Dziembowski (1977a) and Pesnell (1990), which reads: $\delta L_{\rm r}/L = 2\,\xi_r/r + 4\,\delta T/T$. For the latter, it is assumed implicitly that $\delta T/T = \delta T_{\rm eff}/T_{\rm eff}$ (Eq. (3.36)) at the outermost layer of the model. Eq. (3.36) is also assumed in the photometric mode identification method of Cugier et al. (1994) and Balona & Evers (1999). Since we found that these two quantities are very different, our treatment appears as a significant improvement.

4.1.6 Non-adiabatic photometric observables in β Cephei stars

As presented in Section 3.2, multi-colour photometric observations can be confronted to the theoretical predictions of our non-adiabatic code. We have shown that this confrontation can be used as a tool for mode identification. In this Section, we present the application of our method of photometric mode identification to β Cephei stars. A part of the results presented in this Section are given in Dupret et al. (2003a and 2003b) and Aerts et al. (2003b).

We will concentrate on the case of the star EN(16) Lac. This star has been studied by many authors. We refer to Chapellier et al. (1995) and Lehmann et al. (2001) for a summary of the observational studies and to Dziembowski & Jerzykiewicz (1996) for the first seismic study of this β Cephei star. This star is a very good target for asteroseismology for the following reasons: it is a single-lined spectroscopic and an eclipsing binary with well-known orbital elements, which helps to constrain the physical parameters of the β Cep-type primary. Moreover, the primary exhibits multiperiodic pulsations: 3 periods are observed with an extremely high precision. These periods have been studied in quite some detail in the literature. However, general agreement on the mode identification was never reached, so that the seismic application remained limited.

We discuss now the observed characteristics of EN Lac. Concerning the effective temperature, different values based on the same observations (Strömgren indices) but with different calibrations were proposed in the literature. Jerzykiewicz & Sterken (1980) derived the value $\log T_{\rm eff} = 4.357$, while Shobbrook (1985) derived the value $\log T_{\rm eff} = 4.333$. With the same photometric data, Dziembowski & Jerzykiewicz (1996) used more recent calibrations of Napiwotzski et al. (1993) and Balona (1994) and derived the values $\log T_{\rm eff} = 4.358$ and 4.351, respectively. The three observed frequencies used in our study were taken from Lehmann et al. (2001) and the photometric amplitudes obtained with Johnson filters were derived by Jerzykiewicz (1993), a summary of these observations is given in Table 4.1.

Table 4.1: Observed frequencies and photometric amplitudes of EN Lac

Frequency in	Photometric amplitudes in Johnson filters		
cycles / day	A_U	A_B	A_V
$\nu_1 = 5.9112$	33.6 ± 0.5	20.0 ± 0.17	17.9 ± 0.17
$\nu_2 = 5.8551$	12.9 ± 0.5	10.1 ± 0.17	9.7 ± 0.17
$\nu_3 = 5.5033$	14.9 ± 0.5	11.2 ± 0.16	10.5 ± 0.17

Table 4.2: Global characteristics of the theoretical models of EN Lac

Model 1a		
$M/M_\odot = 9.4$	$T_{\rm eff} = 22105\,{\rm K}$	$\log(L/L_\odot) = 3.8992$
$\log g = 3.8429$	$R/R_\odot = 6.0813$	age (My) $= 16.2$
X $= 0.7$	Z $= 0.015$	no overshooting
Model 1b		
$M/M_\odot = 9.7$	$T_{\rm eff} = 22545\,{\rm K}$	$\log(L/L_\odot) = 3.9405$
$\log g = 3.8494$	$R/R_\odot = 6.1313$	age (My) $= 15.15$
X $= 0.7$	Z $= 0.015$	no overshooting
Model 2a		
$M/M_\odot = 9.5$	$T_{\rm eff} = 21756\,{\rm K}$	$\log(L/L_\odot) = 3.8769$
$\log g = 3.8421$	$R/R_\odot = 6.1186$	age (My) $= 15.9$
X $= 0.7$	Z $= 0.02$	no overshooting
Model 2b		
$M/M_\odot = 10$	$T_{\rm eff} = 22491\,{\rm K}$	$\log(L/L_\odot) = 3.9442$
$\log g = 3.8548$	$R/R_\odot = 6.1865$	age (My) $= 13.95$
X $= 0.7$	Z $= 0.02$	no overshooting
Model 3a		
$M/M_\odot = 9.7$	$T_{\rm eff} = 21646\,{\rm K}$	$\log(L/L_\odot) = 3.8739$
$\log g = 3.8454$	$R/R_\odot = 6.1597$	age (My) $= 14.85$
X $= 0.7$	Z $= 0.025$	no overshooting
Model 3b		
$M/M_\odot = 10.3$	$T_{\rm eff} = 22481\,{\rm K}$	$\log(L/L_\odot) = 3.9532$
$\log g = 3.8579$	$R/R_\odot = 6.2561$	age (My) $= 12.9$
X $= 0.7$	Z $= 0.025$	no overshooting

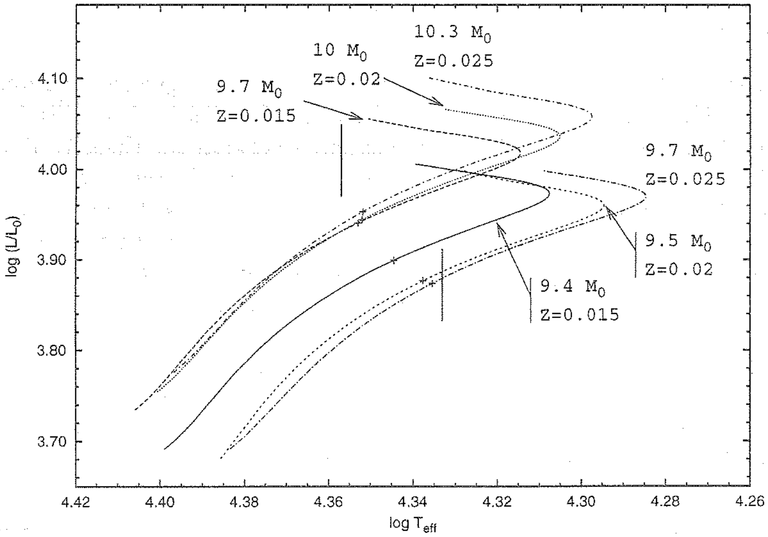

Figure 4.14: HR diagram with evolution tracks corresponding to the different β Cephei models used in Section 4.1.6. The labels "+" give the position of the 6 models of Table 4.2. The left (resp. right) vertical line corresponds to the effective temperature determination by Jerzykiewicz & Sterken (1980) (resp. Shobbrook (1985)).

Mode identification

We present firstly the results obtained for a model with solar metallicity and 9.5 $M_\odot$. The global characteristics of this theoretical model are given in Table 4.2 (model 2a) and are inside the observational error bars. The age of this model was chosen such that the theoretical frequency of the fundamental radial mode is the closest to the main observed frequency $\nu_1 = 5.9112$ c/d. We are going to confirm below this mode identification.

The non-adiabatic effective temperature variations and phase-lags we obtained for different modes (ℓ =0, 1, 2, 3, 4) of this model are given in Figure 4.15 (the vertical lines correspond to the 3 observed frequencies). The non-adiabatic results for the modes with theoretical frequencies closest to the observed ones are given in Table 4.3. Using these non-adiabatic results, we can compute the theoretical photometric amplitude ratios and compare them to the observations, as illustrated in Figure 4.16 (top for the first frequency, middle for the second frequency and bottom for the third frequency). We give in Table 4.4, the discriminants defined by:

$$H_\ell = \sqrt{\frac{1}{2}\sum_{j=2}^{3}\left[\frac{A_{j\,\ell,\mathrm{th}}}{A_{1\,\ell,\mathrm{th}}} - \frac{A_{j,\mathrm{obs}}}{A_{1,\mathrm{obs}}}\right]^2}\,, \tag{4.4}$$

where $A_{j\ell,\mathrm{th}}$ is the theoretical amplitude in the filter j ($j = 1, 2, 3$ for the Johnson filters U, B and V, respectively) with the spherical degree ℓ and $A_{j,\mathrm{obs}}$ is the observed amplitude in the filter j.

We see that, for the first frequency $\nu_1 = 5.9112$ c/d, the best agreement between theory and observations corresponds to the radial mode. The observed amplitude ratios of the second frequency $\nu_2 = 5.8551$ c/d are situated between the theoretical amplitude ratios of an $\ell = 1$ mode and an $\ell = 2$ mode, with a small preference for the $\ell = 2$ mode (see the discriminants in Table 4.4). And finally, the last frequency $\nu_3 = 5.5033$ c/d is identified as an $\ell = 1$ mode. Our photometric mode identifications are in very good agreement with the spectroscopic mode identifications performed by Aerts et al. (2003b and 2003c). By comparing the theoretical frequencies to the observations, no doubt is left about the identification of the second frequency ν_2: it is the $\ell = 2$, g_1 mode. Moreover, the frequencies of the fundamental radial mode and of the $\ell = 2$, g_1 mode follow a close parallel track when the star evolves (see Figure 4.8) and the difference between them is not much affected by changes of the model, so that the mode identification of ν_2 is not model dependent.

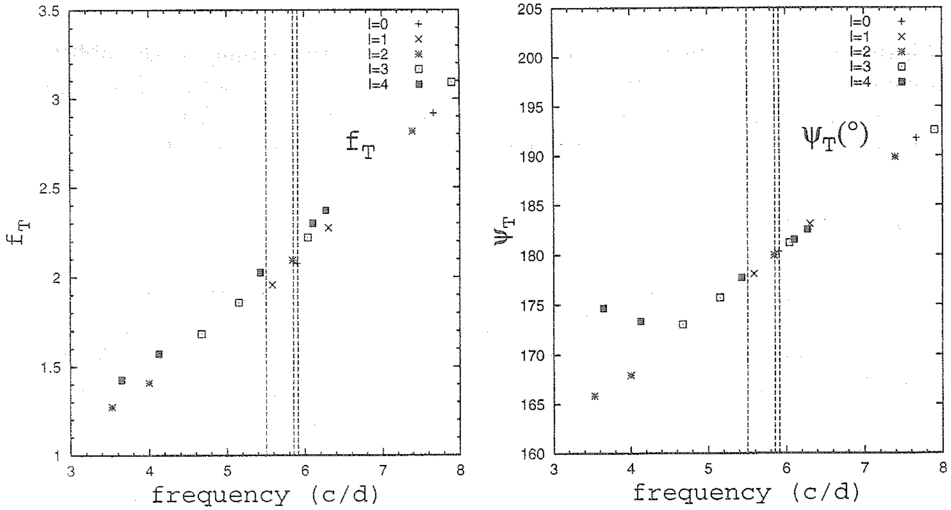

Figure 4.15: Non-adiabatic effective temperature variations and phase-lags for different modes of a 9.5 $M_\odot$ model with solar metallicity (Table 4.2, model 2a). At the left: Amplitude of local effective temperature variations $f_T = |\delta T_{\mathrm{eff}}/T_{\mathrm{eff}}|$ ($\xi_r/R = 1$ at the photosphere), as function of the frequency in cycles/day. At the right: Phase-lag $\psi_T = \psi(\delta T_{\mathrm{eff}}/T_{\mathrm{eff}}) - \psi(\xi_r/R)$ in degrees. The "+" correspond to $\ell = 0$ modes, the "×" correspond to $\ell = 1$ modes, the "$*$" correspond to $\ell = 2$ modes, the "□" to $\ell = 3$ modes and the "▨" to $\ell = 4$ modes.

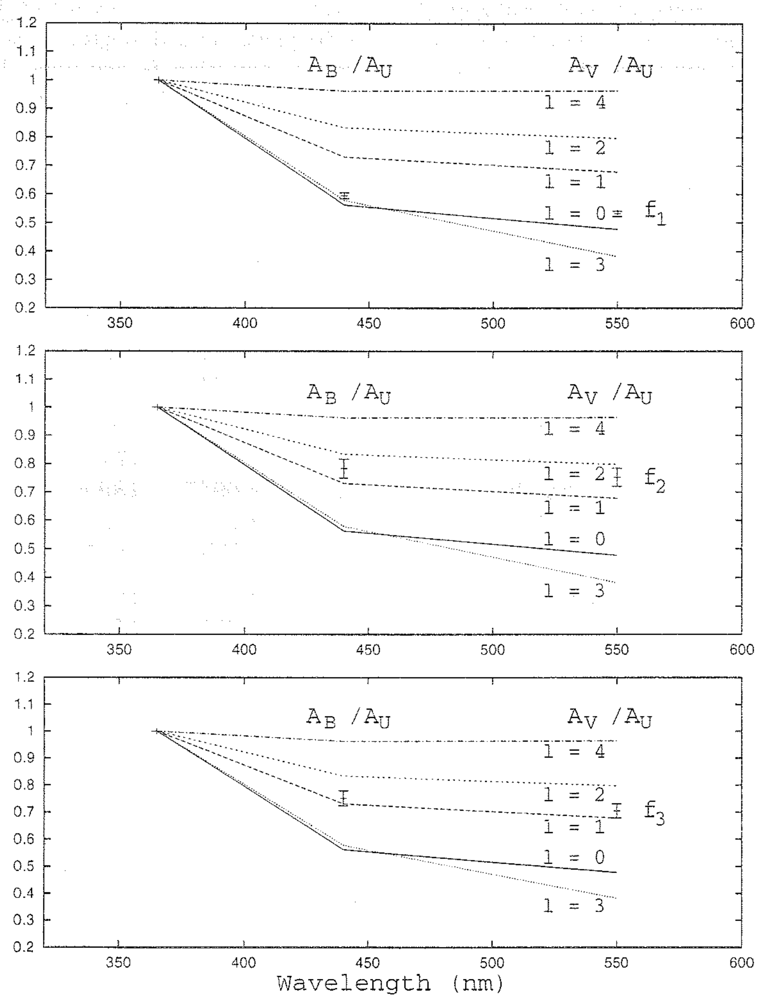

Figure 4.16: Theoretical and observed amplitude ratios obtained with Johnson photometry for the β Cephei star EN Lac (9.5 $M_\odot$ model with solar metallicity). The top, middle and bottom graphs correspond to the first, the second and the third frequency. The error bars with labels f_i correspond to the observed amplitude ratios. The lines correspond to our theoretical predictions for different degrees ℓ.

Table 4.3: Non-adiabatic results for the star EN Lac (9.5 $M_\odot$ model with solar metallicity). Observed frequency in c/d, theoretical frequency in c/d, degree ℓ, radial order, theoretical amplitude of local effective temperature variation f_T and phase-lag ψ_T for the modes with theoretical frequencies closest to the observed frequency. The identified modes are given in bold.

ν_{obs}	ν_{th}	ℓ	n	f_T	ψ_T (°)
5.9112	**5.90252**	**0**	p_1	**2.0754**	**180.3**
	5.58425	1	g_1	1.9551	178.1
	5.84626	2	g_1	2.0937	180.0
	6.04394	3	g_1	2.2193	181.2
	6.10774	4	g_2	2.2986	181.5
5.8551	5.90252	0	p_1	2.0754	180.3
	5.58425	1	g_1	1.9551	178.1
	5.84626	**2**	g_1	**2.0937**	**180.0**
	6.04394	3	g_1	2.2193	181.2
	6.10774	4	g_2	2.2986	181.5
5.5033	5.90252	0	p_1	2.0754	180.3
	5.58425	**1**	g_1	**1.9551**	**178.1**
	5.84626	2	g_1	2.0937	180.0
	5.15273	3	g_2	1.8571	175.7
	5.43116	4	g_3	2.0249	177.7

Table 4.4: Least square discriminants H_ℓ (see Eq. (4.4)) for the different observed frequencies and the different degrees ℓ. In the first column: frequency in cycles/day. In the other columns: H_ℓ for the different degrees ℓ. The identified degrees are given in bold.

ν_{obs}	$\ell = 0$	$\ell = 1$	$\ell = 2$	$\ell = 3$	$\ell = 4$
5.9112	**0.0454**	0.1405	0.2519	0.1072	0.4004
5.8551	0.2489	0.0640	**0.0482**	0.2988	0.1963
5.5033	0.2090	**0.0240**	0.0875	0.2589	0.2361

Constraints on the metallicity

We can see in Figure 4.16 (top) that the theoretical amplitude ratios of the fundamental radial mode are outside the error bars of the observations. We examined if the agreement could be improved by changing slightly the metallicity of the models. For this purpose, we computed six stellar models with different metallicities (their global characteristics are given in Table 4.2). The choice of the models has been made with the following procedure. We computed models with 3 different metallicities: Z = 0.015, Z = 0.02 and Z = 0.025. Because of the uncertainties in the calibration of the effective temperature of EN Lac (see Jerzykiewicz & Sterken 1980, Shobbrook 1985 and Dziembowski & Jerzykiewicz 1996), we computed for each metallicities two evolution tracks corresponding to two different masses (in what follows, the label *a* will denote the less massive models and the label *b* the more massive models). And for each evolution tracks, we selected the model giving the best agreement between the two first theoretical and observed frequencies, relying on the unambiguous mode identification presented in the previous paragraph. We note that for each evolution track, we were able to find a model giving a good agreement between theory and observation for the first two frequencies (radial mode and $\ell = 2$ mode), because these frequencies follow parallel tracks when the star evolves. We note also that the line-profile variations show clearly that the azimuthal order $m = 0$ for the $\ell = 2$ mode (Aerts et al. 2003b and 2003c), so that the rotational splitting has not to be taken into account for this mode. The third frequency ($\ell = 1$ mode) is undergoing an avoided crossing, and we did not use it for the selection of the model (we note that the azimuthal order m is not known for this frequency).

In Figure 4.17, we present the values of f_T (local effective temperature variation for a normalized radial displacement at the photosphere) as a function of the pulsation frequency in $\mathrm{c\,d^{-1}}$, for different modes and for the six models of EN Lac given in Table 4.2. The three vertical lines correspond to the three observed frequencies. We see that, the higher the metallicity, the lower the amplitude of the local effective temperature variation for a normalized radial displacement. The physical origin of this phenomenon is explained in Figure 4.18, where we show the amplitudes of the luminosity variation $|\delta L/L|$ as a function of the logarithm of temperature, from the center to the surface of the star, for the radial fundamental mode and for the models 1a, 2a and 3a of Table 4.2. The higher the metallicity, the more efficient the κ-mechanism in the metal opacity bump, which implies a more important decrease of the luminosity variation in the driving region. Therefore, the amplitude of the luminosity variation and of the local effective temperature variation at the photoshere are smaller for a normalized displacement. By comparing in Figure 4.17 the results obtained for the slightly colder models (models 1a, 2a and 3a) and the slightly hotter models (models 1b, 2b and 3b), we see that changing the values of T_{eff} within the observational error bars for EN Lac (keeping the metallicity constant) has only a very small effect on the non-adiabatic results.

We present in Figure 4.19 the theoretical amplitude ratios obtained for the models 1a, 2a and 3a (Table 4.2) of EN Lac with different metallicities and for the radial mode. We see that the model with $Z = 0.015$ gives the best agreement between the theoretical and observed amplitude ratios. As can be seen in Figure 4.10, all the modes in the observed range of frequencies remain unstable for this low metallicity; lower values are not compatible with mode excitation.

Our non-adiabatic functions can thus be used as a constraint on the metallicity of stars driven by the metal opacity bump (β Cephei and Slowly Pulsating B stars), once we know the identification of the mode. We have seen in Figure 4.17 that the non-adiabatic predictions and thus the theoretical amplitude ratios are little affected by the uncertainties on $T_{\rm eff}$ for a given metallicity, so that the constraints we derived on the metallicity are reliable. This way of determining the metallicity may even turn out to be more precise than the classical method based on the analysis of the spectrum (the number of spectral lines is small in hot stars). We plan to validate our method to derive the metallicity by this feed-back process by confronting our predictions to those of β Cephei stars for which the metallicity is known with high accuracy.

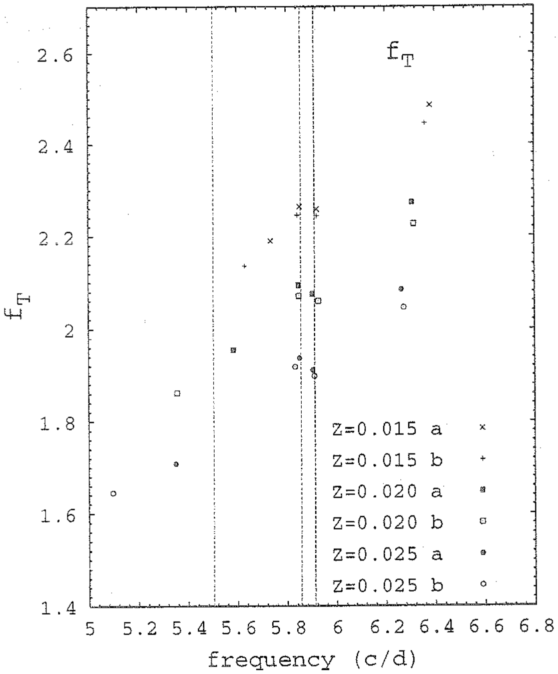

Figure 4.17: f_T (local effective temperature variation for a normalized radial displacement at the photosphere) as function of the pulsation frequency in $\mathrm{c\,d^{-1}}$, for different modes ($0 \leq \ell \leq 2$) and for the six different models of the star EN Lac given in Table 4.2. Each "×" correspond to a mode of the model 1a, the "+" correspond to the model 1b, the full and empty squares correspond to the models 2a and 2b respectively, the full and empty circles correspond to the models 3a and 3b respectively. The three vertical lines correspond to the three observed frequencies: $\nu_1 = 5.9112\ \mathrm{c\,d^{-1}}$, $\nu_2 = 5.8551\ \mathrm{c\,d^{-1}}$ and $\nu_3 = 5.5033\ \mathrm{c\,d^{-1}}$.

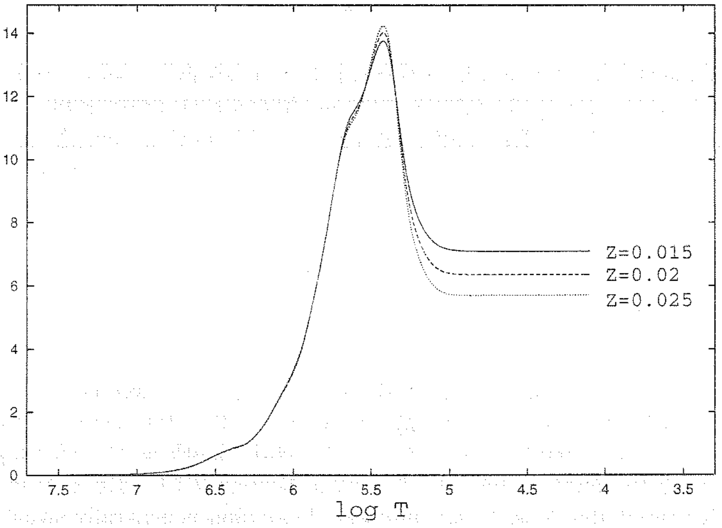

Figure 4.18: Amplitude of luminosity variation $|\delta L/L|$ as function of the logarithm of temperature for the fundamental radial mode, for models of EN Lac with different metallicities (models 1a, 2a and 3a of Table 4.2). The solid line corresponds to the model with $Z = 0.015$, the dashed line to the model with $Z = 0.02$ and the dotted line to the model with $Z = 0.025$.

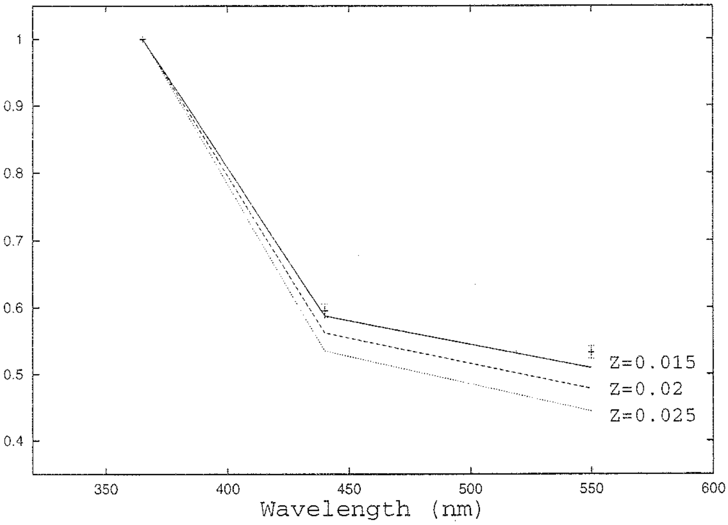

Figure 4.19: Observed and theoretical amplitude ratios (Johnson photometry) for the radial fundamental mode obtained for the three models of EN Lac with different metallicities (models 1a, 2a and 3a of Table 4.2). The solid line corresponds to the model with $Z = 0.015$, the dashed line to the model with $Z = 0.02$ and the dotted line to the model with $Z = 0.025$.

4.1.7 Non-adiabatic spectroscopic observables in β Cephei stars

As presented in Section 3.3, another utility of our non-adiabatic code is that it gives the ingredients for determining the influence of the photospheric temperature variations on the line-profile variations. The results presented in this section were the fruit of a close collaboration with Joris De Ridder of the K-U Leuven and have been published in De Ridder, Dupret et al. (2002).

Si^{2+} line formation layer

We said in Section 3.3.1 that we adopt also the one-layer approximation in our simulations of line-profile time series. It is important to note that the *single surface* we adopt for our spectroscopic simulations is not at the same depth as the *single photosphere* we adopted for the photometric simulations in Section 4.1.6. The reason is that the layer which contributes most to the flux line depression is generally situated in much outer layers than the photosphere. In the case of β Cephei stars, the line we chose for our simulations is the Si^{2+} triplet (456.784 nm). On the basis of a method proposed by Magain (1986), De Ridder et al. (2002) showed that the layer which contributes most to the flux line depression of the Si^{2+} triplet is situated at $\log\tau = -1.625$ for a typical β Cephei atmosphere. In order to avoid confusion, we use here the following notations for the non-adiabatic amplitudes at the Si^{2+} line formation layer: $f_{T\,\mathrm{Si}^{2+}}$ is the amplitude of local effective temperature variation and $f_{g\,\mathrm{Si}^{2+}}$ is the amplitude of local effective gravity variation for a normalized radial displacement at the Si^{2+} line formation layer ($\log\tau = -1.625$).

Model and non-adiabatic quantities

The global characteristics of the β Cephei model we used for our line-profile simulations are given in table 4.5. On the basis of this model, we performed non-adiabatic simulations for different low-order p-modes. The non-adiabatic results are given in Table 4.6.

Table 4.5: Global characteristics of the β Cephei model used for the simulations of line-profile variations

$M/M_\odot = 10$	$T_{\mathrm{eff}} = 22643\,\mathrm{K}$	$\log(L/L_\odot) = 4.05$
$\log g = 3.76$	$R/R_\odot = 6.93$	age (My) = 18.58
X = 0.7	Z = 0.02	no overshooting

mode		K	$f_{T\,\mathrm{Si}^{2+}}$	ψ_T	$f_{g\,\mathrm{Si}^{2+}}$	ψ_g	P (h)
$\ell = 1$	p_1	0.05	2.93	179°	21.0	180°	3.56
$\ell = 1$	p_2	0.04	3.26	187°	26.7	180°	3.09
$\ell = 1$	p_3	0.03	3.54	195°	33.3	180°	2.71
$\ell = 2$	f	0.04	3.27	186°	26.4	180°	3.11
$\ell = 2$	p_1	0.03	3.43	191°	30.2	180°	2.87
$\ell = 2$	p_2	0.02	3.62	199°	36.7	180°	2.55
$\ell = 2$	p_3	0.02	3.66	212°	47.5	180°	2.17
$\ell = 3$	f	0.03	3.43	190°	29.4	180°	2.92
$\ell = 3$	p_1	0.02	3.69	203°	39.8	180°	2.43
$\ell = 3$	p_2	0.02	3.71	209°	45.0	180°	2.24
$\ell = 3$	p_3	0.02	3.59	216°	51.1	180°	2.06
$\ell = 4$	f	0.03	3.59	195°	33.3	180°	2.71
$\ell = 4$	p_1	0.02	3.72	205°	42.4	180°	2.33
$\ell = 4$	p_2	0.01	3.50	219°	53.8	180°	1.99

Table 4.6: $K = |\xi_h/\xi_r|$, $f_{T\,\mathrm{Si}^{2+}}$, ψ_T, $f_{g\,\mathrm{Si}^{2+}}$ and ψ_g, as computed by our non-adiabatic code, for different modes of the 10 $M_\odot$ β Cephei model of Table 4.5. The non-adiabatic amplitudes are determined at the line-formation layer of the Si^{2+} spectral line (456.78 nm) situated at $\log\tau = -1.625$, with a relative radial displacement $\xi_r/r = 1$ at this layer. The last column contains the pulsation periods in hours.

Simulations of line-profile variations

The simulations of line-profile variations presented in this section have been performed with the code PULSTAR written by Dr. J. De Ridder, for the modes given in Table 4.6 and for all the values of m between 0 and ℓ, which means 49 different modes. The rotation was neglected in these simulations.

In our simulations of line-profile variations, we have imposed that the maximum over the entire stellar surface of the amplitude of the local velocity variation $((|\vec{v}|)_{\max})$ is 20 km/s for every mode. The amplitudes of the observed radial velocity variations $\langle v \rangle$ (first moment of the line profile variation integrated over the entire stellar disk) of the modes with degrees $\ell = 1$, 2, 3, and 4 are then respectively about 11 km/s, 7 km/s, 3 km/s and 0.5 km/s. This decrease of $\langle v \rangle$ with increasing ℓ comes from the cancellations occuring for large ℓ when we integrate over the entire stellar disk. With these values, the maximum amplitude of the local relative displacement $(|\vec{\xi}|)_{\max}/R$ was always smaller than 1%. Most of the spectroscopically observed *non-radially* pulsating β Cephei stars have an amplitude of $\langle v \rangle$ smaller than 11 km/s, so that our choice for $(|\vec{v}|)_{\max}$ was appropriate.

A first result of the simulations is that — with the realistic amplitudes given above — the non-adiabatic temperature and gravity variations have very small effect on the line profiles. The relative difference in residual intensity between a line profile computed with and without effective temperature and gravity variations is always about 1% or less. An illustration of this is given in Figure 4.20. It shows line profiles without and with effective temperature and gravity variations for the p_1-mode of the β Cephei star model, with (ℓ, m) = (1,0) and an inclination angle of least cancellation (these inclination angles are such that the amplitude of the observed radial velocity variation $\langle v \rangle$ integrated over the visible disk is the largest for a given value of the equatorial velocity, see De Ridder 2001, Sect. 3.4 for more details). The differences between the two sets of line profiles for this mode are larger than for a typical mode, but they are still very small. In Figure 4.21 we show greyscale diagrams of the difference in residual intensity between the spectra computed with and without temperature, gravity, and surface normal variations, for the p_1-modes $(\ell, m) = (1, 0)$ and $(\ell, m) = (1, 1)$. The abscissa corresponds to the wavelength in nanometer, and the ordinate corresponds to the pulsation phase. The input parameters are the same as mentioned above, with an inclination angle of least cancellation. The greyscale plots can be understood as follows. For the (ℓ, m) = (1,0) mode (upper panel), we look pole-on so that we only see the northern hemisphere. We recall that, for $\ell = 1$ modes, there is no geometrical distorsion of the stellar surface (it remains spherical with a constant radius). In this case $(m = 0)$, the stellar surface follows, in appearance, a simple oscillating movement along the direction of the observer. At phase zero, the northern hemisphere is maximally expanded, the velocity is everywhere equal to zero and there is no Doppler shift due to the pulsation. At the same time the local $T_{\rm eff}$, and therefore also the local EW, is everywhere lower than the equilibrium value. This results in a spectral line with at each wavelength a higher residual intensity than its counterpart computed without temperature effects. At phase 0.5, the situation is reversed. The northern hemisphere is now maximally compressed so that the local EW is everywhere higher than the equilibrium value which results in a spectral line with a lower residual intensity. For the $(\ell, m) = (1,1)$ mode (lower panel), we look equator-on. Now the stellar surface follows, in appearance, a revolution round the polar axis perpendicular to the direction of the observer. At phase zero, the visible part of the star is the closest to the observer, the nodal line of the radial displacement, and therefore also of δT_{eff}, coincides with the edge of the disk. The nodal line of the radial component of the pulsational velocity, however, coincides then with the meridian. Half of the disk is receding from us, half of the disk is approaching towards us. This averages out so that the observed spectral line is centered around its laboratory wavelength. The entire visible disk is in expanded state, so that the local T_{eff}, and therefore also the local EW, is everywhere lower than the equilibrium value. As for the $(\ell, m) = (1,0)$ mode, this results in a spectral line with a higher residual intensity for each wavelength. At phase 0.5, the situation is exactly the reverse one.

By fitting, for each mode, the EW curve with a sine function in order to obtain its amplitude and its phase difference with the velocity curve, we found that, in general, a larger degree ℓ corresponds to a smaller amplitude of the EW variation, which can be explained from surface cancellation effects. The largest EW variations are found for the $\ell = 1$ modes (we recall that we did not consider here $\ell = 0$ modes), with $|\delta\,\mathrm{EW}/\mathrm{EW}|$ of the order of maximum 2%, and secondly for $\ell = 2$ modes with $|\delta\,\mathrm{EW}/\mathrm{EW}|$ of the order of maximum 1%. The other modes show an EW variability below the current detection level.

The causes of the global EW variations are in the first place the local T_{eff} variations and in the second place the local effective gravity variations. It was found that including both T_{eff} and $\log g$ variations results in a lower amplitude of the EW variation than including only T_{eff} variations. The reason is that the EW of the Si^{2+} (456.78 nm) line at $(T_{\mathrm{eff}}, \log g) \approx (22000\ \mathrm{K}, 4.0)$ increases with increasing T_{eff} but decreases with increasing g. We also recall that the importance of the effective gravity variation increases with increasing radial order, as a simple consequence of the increasing acceleration.

We explicitly verified that the variation of the moments of the line profile are very little affected by the T_{eff} and $\log g$ variations. This means that line profile fitting, as well as the moment method could not be confused by temperature and gravity variations as far as mode identification is concerned (at least for slow rotators). Although the moment method assumes a constant equivalent width, Aerts et al. (1992) showed that the method is sufficiently robust to handle EW variations of a few percent.

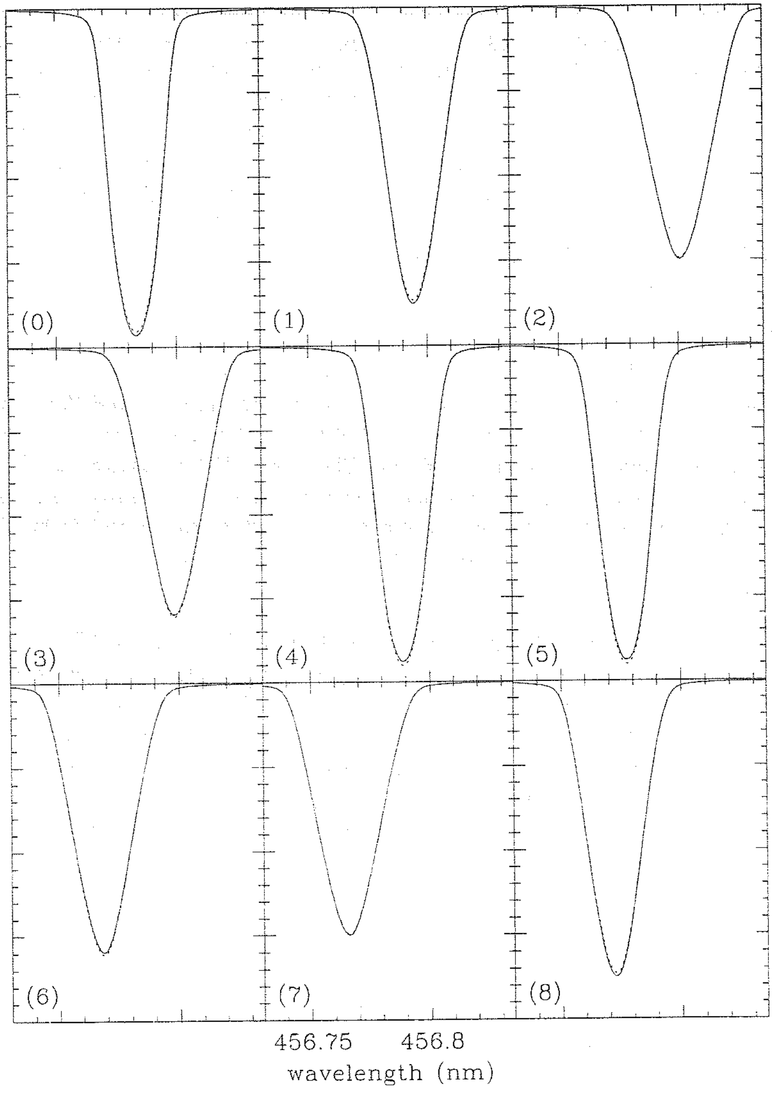

Figure 4.20: Comparison between line profiles without (solid lines) and with (dotted lines) T_{eff} and g variation, for the mode p_1 of a 10 $M_\odot$ β Cephei model (Table 4.5), with $(\ell, m) = (1,0)$. The phase of each line profile is $n/9$ where (n) is given in the lower left corner of each box. Figure taken from De Ridder (2001).

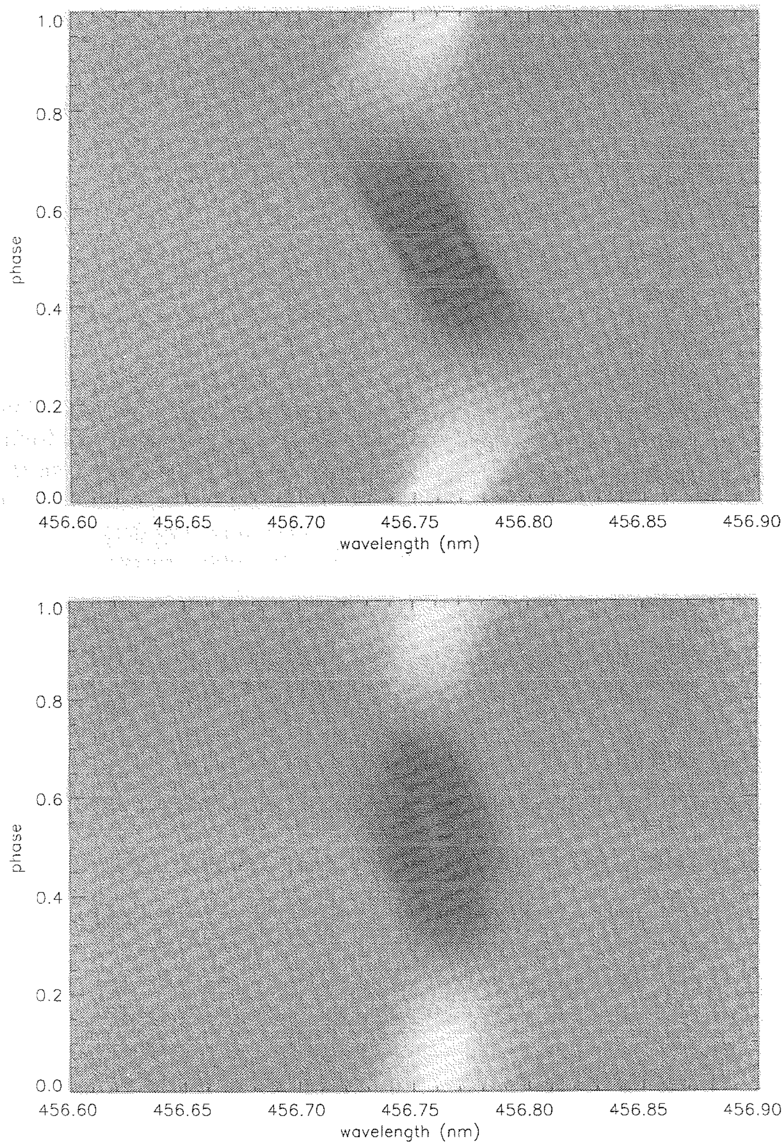

Figure 4.21: Greyscale plots of the difference in residual intensity between the spectra computed with and without temperature, gravity, and surface normal variations. White indicates a positive difference, black a negative difference. Both panels are for the Si^{2+} (456.784 nm) line and for the mode p_1 of a 10 $M_\odot$ β Cephei model (Table 4.5). The upper panel is for the $(\ell, m) = (1,0)$ mode, the lower panel is for the $(\ell, m) = (1,1)$ mode. In both cases, the maximum relative difference in residual intensity is about 0.8%. Figure taken from De Ridder (2001).

4.2 Slowly Pulsating B stars

4.2.1 SPBs from an observational point of view

The slowly pulsating B stars (SPBs) are multiperiodic population I main sequence stars with periods typically between 1 and 4 days. Their spectral types range from B3 to B8, their masses from about 3 $M_\odot$ to about 8 $M_\odot$. The SPBs have been very recently discovered and were introduced as a new class of pulsating stars by Waelkens (1991). Very few SPB stars were actually known until very recent times. The satellite HIPPARCOS, however, spectacularly increased the number of known SPB stars by almost an order of magnitude (Waelkens et al. 1998). By now, a little more than 100 stars are confirmed or suspected SPB stars. The most important reason for this huge increase in number is the long pulsation period together with the even longer beat periods, which makes it quite challenging to discover and study them from ground-based datasets. Moreover, periods around 1 day are difficult to find from the ground because of the daily aliasing effect. Slowly as well as rapidly rotating SPB stars have been observed, but none with a magnetic field. A deep and very detailed observational study of SPBs was achieved recently by Peter De Cat (2001) in the frame of his PhD thesis.

4.2.2 SPBs from a theoretical point of view

From a stellar evolution point of view, the SPBs are at the core hydrogen-burning stage, between the Zero Age Main Sequence (ZAMS) and the Terminal Age Main Sequence (TAMS). They have a large convection core, but no superficial convection zone is present. The long periods of the SPBs correspond to high order g-mode pulsations. As a consequence of these large periods, the transversal compression of the matter is larger than the radial compression in high order g-modes: more precisely, the term proportional to $\ell(\ell+1)$ is dominating in the equation of mass conservation (Eqs. (1.47) and (2.3)). Because of this dominating transversal compression, we deduce also that in the superficial layers and under the adiabatic approximation, $\delta\rho/\rho$ and $\delta P/P$ have the same phase as the radial displacement (contrary to p-modes for which we have an opposition of phase). Our non-adiabatic computations predict a small phase-lag between the superficial temperature variation and the radial displacement, as will be shown in Section 4.2.6.

We can see in Figure 4.1 the situation of SPB stars in a HR diagram (represented with $\circ$). On the same figure, the theoretical instability strip derived by Pamyatnykh (1999) is given. In Figure 4.22, we give the real part of the displacement in the radial direction ($\Re\{\xi_r/R\}$) and in the transversal direction ($\Re\{\xi_h/R\}$) (the definition of ξ_r and ξ_h are given in Eq. (1.45)), for the mode $\ell = 1$ g_{22} of a typical $4\,M_\odot$ SPB model (the global characteristics of this model are given in Table 4.12). These eigenfunctions are normalized in such a way that $\xi_r/R = 1$ at the photosphere ($x = 1$). The vertical line corresponds to the frontier between the central convection zone and the radiative

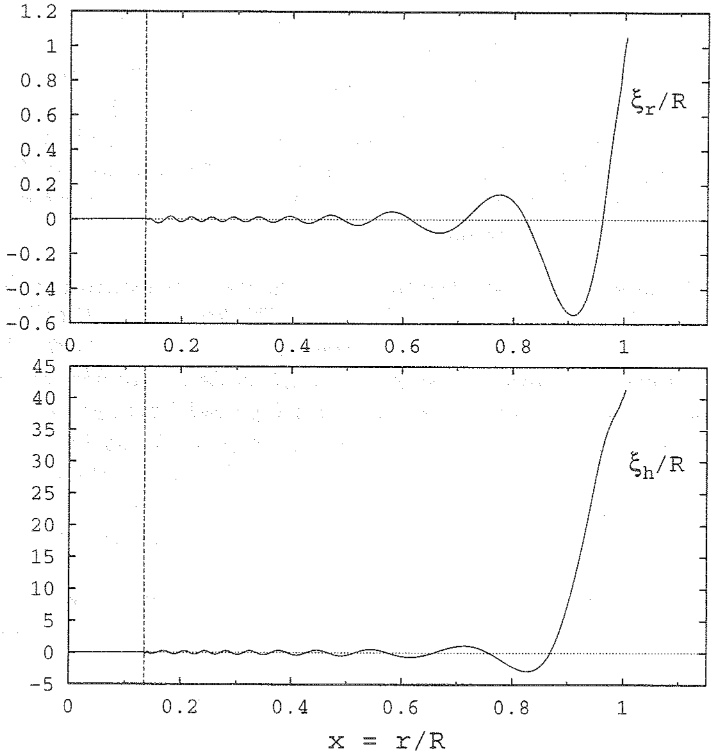

Figure 4.22: Real part of the radial displacement: $\Re\{\xi_r/R\}$ (top) and of the transversal displacement: $\Re\{\xi_h/R\}$ (bottom) as function of $x = r/R$ for the mode $\ell = 1$ g_{22} of a typical $4\,M_\odot$ SPB model. The vertical line is the frontier between the core convection zone and the radiative envelope.

envelope. We can see the large number of nodes and the oscillatory behaviour of these eigenfunctions beginning at the frontier between the central convection zone and the radiative envelope. We see also that the transversal displacement is much larger than the radial displacement. Because of the significant amplitudes obtained in the internal layers, the SPBs are very promising targets for asteroseismology.

4.2.3 Driving mechanism of the SPBs

As proposed by Dziembowski et al. (1993b) and Pamyatnykh (1999), the driving mechanism at the base of the excitation of high order g-modes of SPBs is a κ-mechanism associated to the metal opacity bump, at temperatures around 200.000 K ($\log T \simeq 5.3$). In order to illustrate this phenomenon, we give the results obtained for a typical SPB model whose global characteristics are given in Table 4.12. This model has the effective temperature and luminosity of the SPB star HD 215573 observed by Peter De Cat (2001). We have chosen the mode $\ell = 1$ g_{22} whose theoretical period is close to the observed period ($P_{\mathrm{th}} = 1.76188$ days).

In Figure 4.23, we give at the the top the opacity in cm^2/g as function of the logarithm of temperature. We can see 3 bumps of opacity. The first bump at $\log T \simeq 5.3$ is due to the tremendous number of iron lines in this region (Cox et al. 1992). This opacity bump is very important since it is at the origin of the driving of SPB stars. A second bump at $\log T \simeq 4.6$ corresponds to the second partial ionization zone of Helium. And a third small bump at $\log T \simeq 4.15$ corresponds to the partial ionization zone of Hydrogen and the first partial ionization zone of Helium. At the middle of Figure 4.23, we give the graph of the logarithmic derivative of the opacity with respect to the pressure at constant entropy (Eq. (4.1)). As for β Cephei stars, the important point is that κ_{PS} increases outwards in the driving region. Finally, we give at the bottom the graph of the logarithm of the thermal relaxation time in seconds: $\log(\tau_{th})$, as function of the logarithm of temperature. The horizontal dashed line with the label g_{22} gives the logarithm of the period of pulsation of the mode $\ell = 1$ g_{22} and the horizontal dot-dashed line with the label p_1 gives the logarithm of the period of pulsation of the mode $\ell = 1$ p_1.

In Figure 4.24, we illustrate some results obtained for the mode $\ell = 1$ g_{22} of the SPB model given in Table 4.12. We give in the middle panel of this figure the graph of the work integral, as defined in Eq. (4.2). The regions where W has a positive derivative are driving the mode and the regions where W has a negative derivative are damping the mode. In the top panel of Figure 4.24, we give $-\mathrm{d}W/\mathrm{d}\log T$. The regions where $-\mathrm{d}W/\mathrm{d}\log T$ is positive are driving the mode and the regions where $-\mathrm{d}W/\mathrm{d}\log T$ is negative are damping the mode. Finally, we give at the bottom of Figure 4.24, the graph of the relative amplitude of variation of the "local" luminosity defined by:

$$\left|\frac{\delta L}{L}\right| = \left|\frac{\delta(4\pi r^2 F_r)}{L}\right| , \tag{4.5}$$

where F_r is the local radial flux.

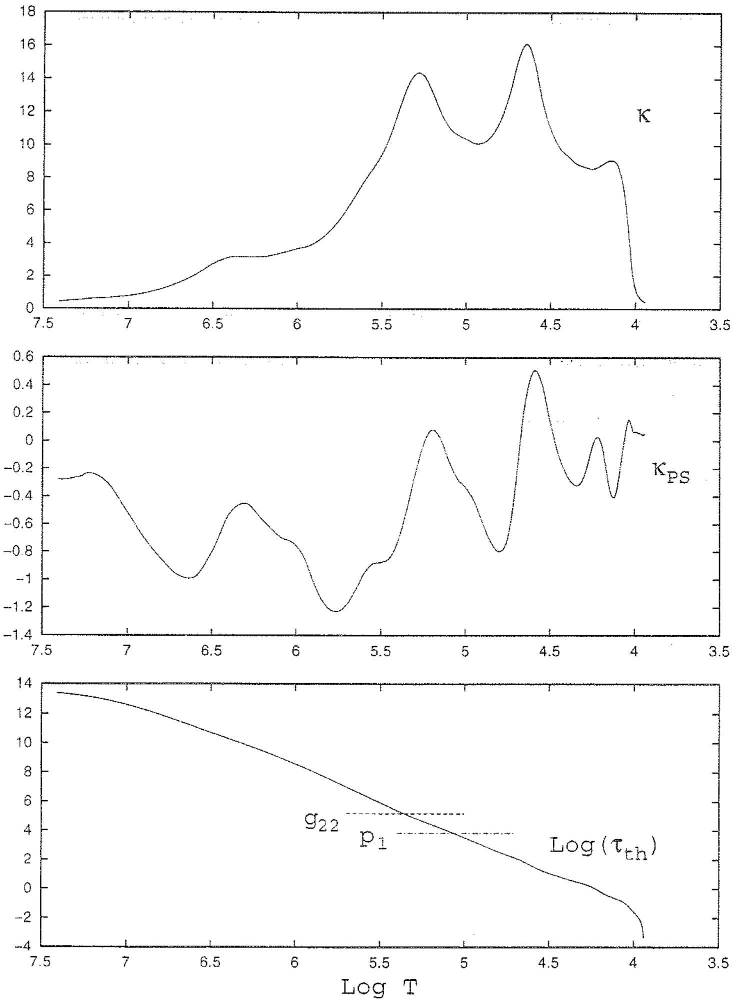

Figure 4.23: Opacity in cm^2/g (top), $\kappa_{PS} = \left.\frac{\partial \ln \kappa}{\partial \ln P}\right|_S$ (middle) and logarithm of the thermal relaxation time in seconds: $\log(\tau_{th})$ (bottom), as function of the logarithm of temperature. for a typical $4\,M_\odot$ SPB model.

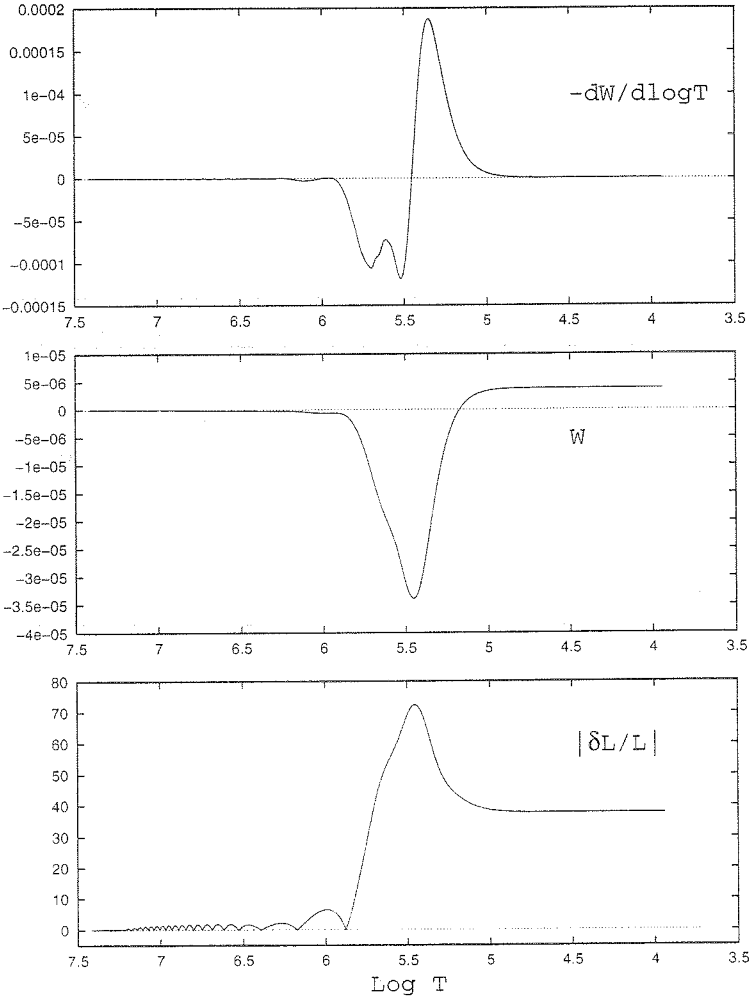

Figure 4.24: $-\mathrm{d}W/\mathrm{d}\log T$ (top), dimensionless work integral W (middle) and amplitude of luminosity variation: $|\delta L/L|$ (bottom), as function of the logarithm of temperature. for the mode $\ell = 1$ g_{22} of a typical $4\,M_\odot$ SPB model.

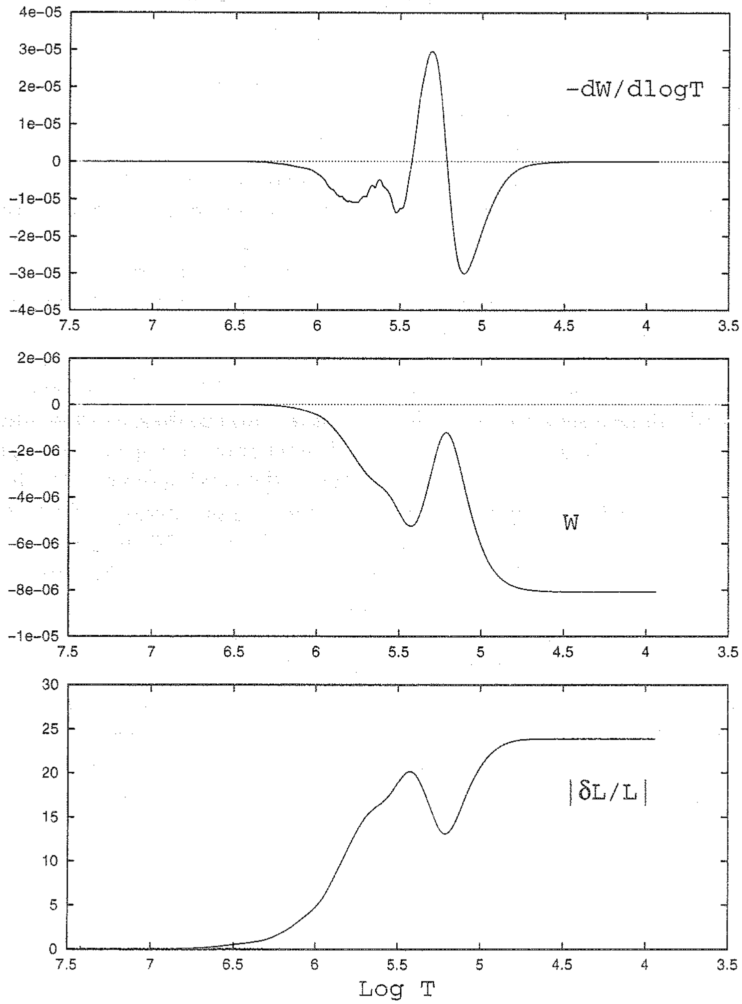

Figure 4.25: $-\mathrm{d}W/\mathrm{d}\log T$ (top), dimensionless work integral W (middle) and amplitude of luminosity variation: $|\delta L/L|$ (bottom), as function of the logarithm of temperature, for the mode $\ell = 1$ p_1 of a typical $4\,M_\odot$ SPB model.

The driving mechanism of SPBs is very similar to the one of β Cephei stars. The transition region where the thermal relaxation time is of the same order as the period of pulsation (bottom of Figure 4.23, intersection with the horizontal dashed line with label g_{22}) is exactly situated at the metal opacity bump where κ_{PS} is increasing outwards. This opacity barrier is blocking the luminosity variation at the hot phase, which is driving the mode. Since the explanation of this process is exactly the same as for β Cephei stars, we refer to Section 4.1.3 for more details.

In order to show that this driving mechanism affects high order g-modes but not p-modes (for SPBs), we give in Figure 4.25 the results obtained for the mode $\ell = 1$ p_1 of our $4M_\odot$ SPB model. The explanation of the stability of the SPB's p-modes is the following. For p-modes (smaller periods), the transition region where the period is of the same order as the thermal relaxation time is situated in more outside layers (Figure 4.23, bottom). In a non negligible part of this region, κ_{PS} (Figure 4.23, middle) and thus $\delta\kappa/\kappa$ is decreasing outwards at the hot phase. And therefore $\delta L/L$ is increasing outwards at the hot phase (around $\log T = 5.1$ in Figure 4.25, bottom), which has a damping effect on the pulsation (Figure 4.25, top and middle).

In Figures 4.26, 4.27 and 4.28, we give all the unstable modes found by our non-adiabatic code along a sequence of evolution of $4M_\odot$ (an HR diagram with this evolution track and other ones is given in Figure 4.31). Each figure corresponds to a given degree ℓ. The abscissa corresponds to the age of the models and a scale with the logarithm of effective temperature is given at the top. Each cross corresponds to an unstable mode. The upper figures give the radial orders of the unstable g-modes and the lower figures give the periods of the unstable modes in days. These theoretical results are in good agreement with the typical observed periods of SPBs (De Cat 2001). On one hand, by comparing the results obtained for different degrees ℓ, we see that the periods and the interval of periods of the set of unstable modes decrease with increasing ℓ. On the other hand, by comparing the results obtained for different ages (same ℓ), we see that the periods and the interval of periods of the set of unstable modes increase with increasing age. Finally we remark that, for all the models between the ZAMS and the TAMS, unstable high-order g-modes are predicted by our non-adiabatic code, in agreement with Pamyatnykh (1999).

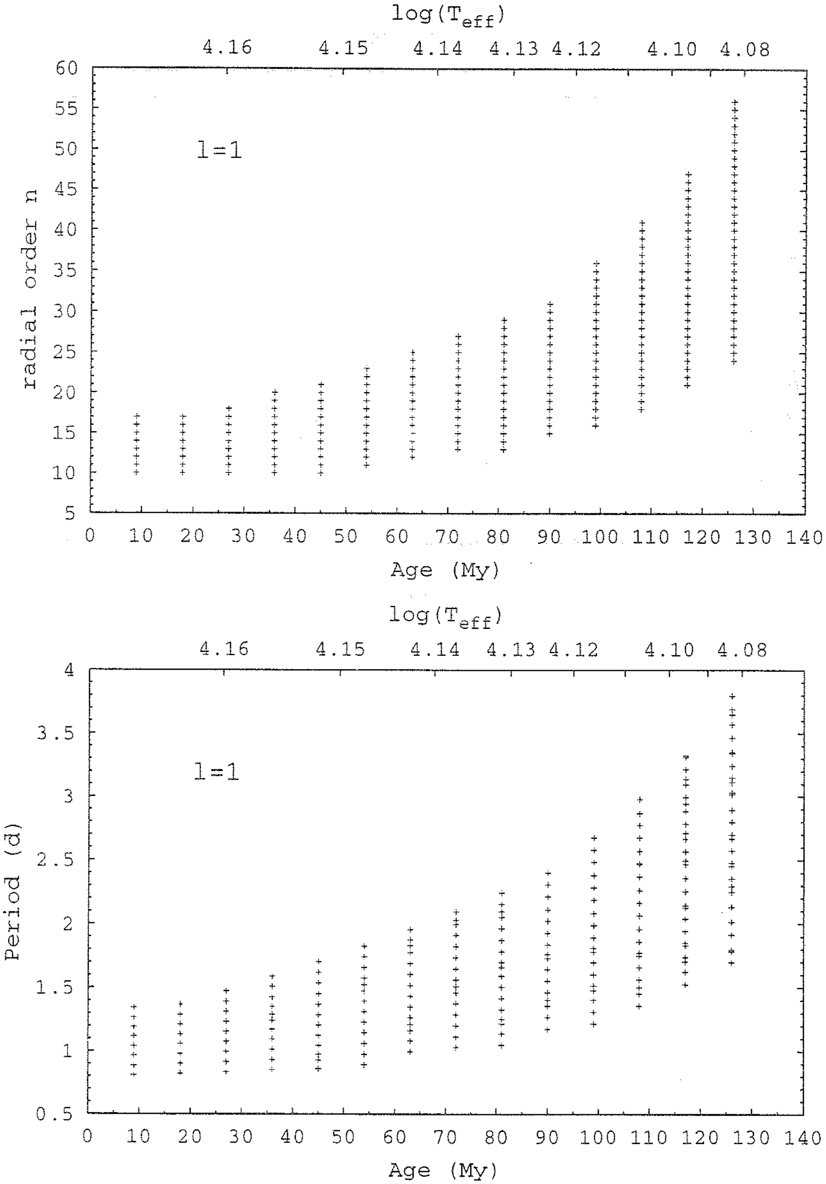

Figure 4.26: Unstable modes of degree $\ell = 1$ along a $4M_\odot$ sequence of evolution. The upper graph gives the radial order of the unstable g-modes as function of the age in Myears and of $\log(T_{\rm eff})$. The lower graph gives the period of the unstable modes in days.

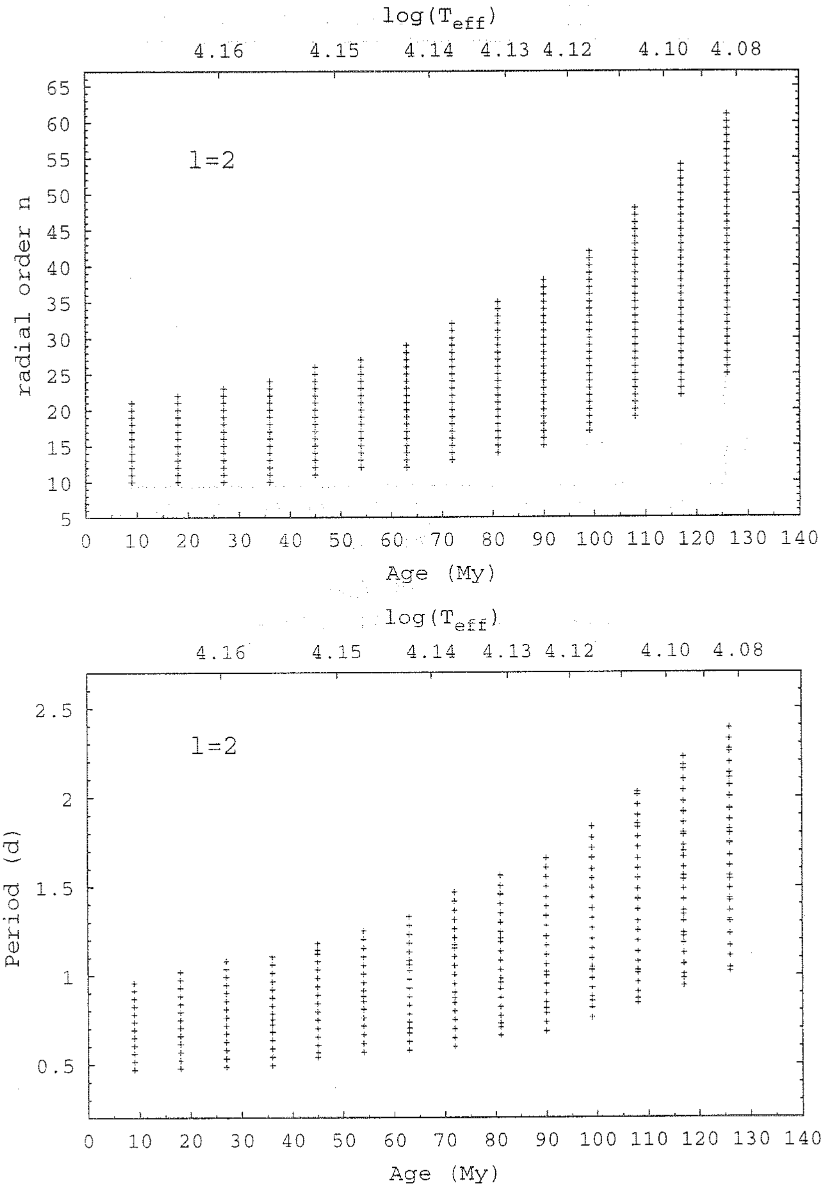

Figure 4.27: Unstable modes of degree $\ell = 2$ along a $4M_{\odot}$ sequence of evolution. The upper graph gives the radial order of the unstable g-modes as function of the age in Myears and of $\log(T_{\rm eff})$. The lower graph gives the period of the unstable modes in days.

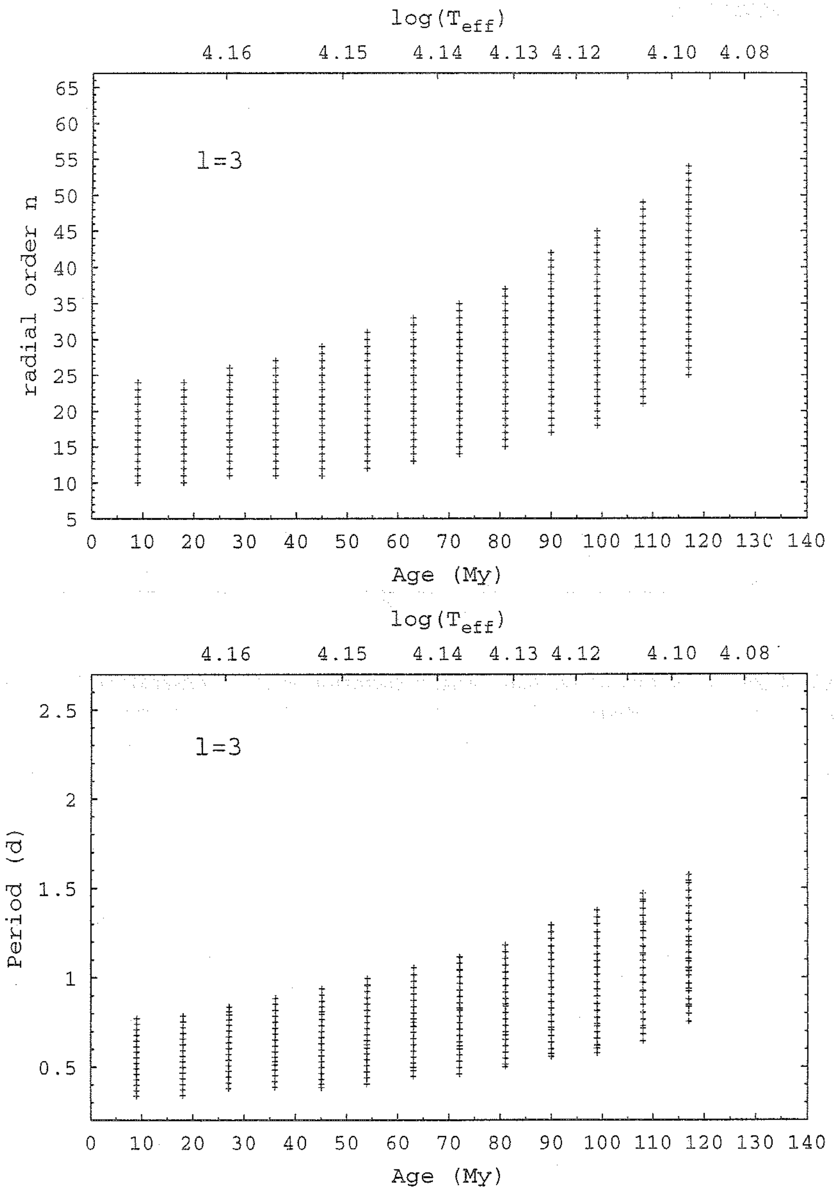

Figure 4.28: Unstable modes of degree $\ell = 3$ along a $4M_\odot$ sequence of evolution. The upper graph gives the radial order of the unstable g-modes as function of the age in Myears and of $\log(T_{\mathrm{eff}})$. The lower graph gives the period of the unstable modes in days.

4.2.4 Comparison between adiabatic and non-adiabatic eigenfunctions

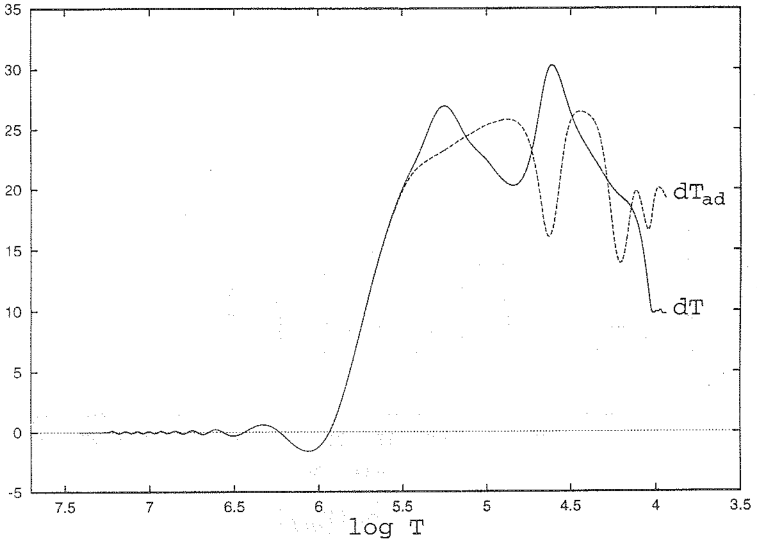

Figure 4.29: Real part of the Lagrangian variation of the temperature $\delta T/T$ as computed by our non-adiabatic code (solid line with the label dT) compared to the adiabatic Lagrangian variation of the temperature $\delta T/T|_{\rm ad} = (\Gamma_3-1)/\Gamma_1\,\delta P/P|_{\rm ad}$ (dashed line with the label $\mathrm{dT_{ad}}$), as function of the logarithm of temperature, from the center to the surface of the star.

We compare now the adiabatic and non-adiabatic eigenfunctions obtained for a typical 4 $M_\odot$ SPB model whose global characteristics are given in Table 4.12, and for the mode $\ell = 1$, g_{22}. In Figure 4.29, we compare the real part of the Lagrangian variation of the temperature $\delta T/T$ as computed by our non-adiabatic code (solid line) to the adiabatic Lagrangian variation of the temperature (dashed line) defined by Eq. (4.3). We recall that $\xi_r/R = 1$ at the photosphere.

We see that in the quasi-adiabatic region (from the center to $\log T \simeq 5.5$), the non-adiabatic and the adiabatic temperature variations are the same. On the contrary, from the driving region to the superficial layers, the pulsation becomes highly non-adiabatic and the non-adiabatic and adiabatic temperature variations are totally different. The qualitative behaviour of the eigenfunctions of Figure 4.29 has the same physical explanation as for β Cephei stars (see Section 4.1.4): the two bumps of the non-adiabatic temperature variation correspond exactly to the two bumps of opacity (Figure 4.23, top) and the the adiabatic temperature variation is scaled on the adiabatic gradient $(\Gamma_3 - 1)/\Gamma_1$ in the superficial layers.

4.2.5 Non-adiabatic eigenfunctions in the atmosphere of SPBs

Similarly to Section 4.1.5, we illustrate now in Figure 4.30 some of the results obtained in the atmosphere of a typical SPB star (same model and same mode as in Section 4.2.4). For all our applications to SPBs, the connecting layer between the interior and atmosphere specific treatments (Chapter 2) was chosen at $\tau = 10$. We note the smoothness of $|\delta T/T|$ (label "dT") at $\log \tau = 1$, confirming the validity of our treatment. We do not give $|\partial \ln T/\partial \ln g_e \; \delta g_e/g_e|$, because it turns out to be totally negligible. As for β Cephei stars (Figure 4.13), the term $|\partial \ln T/\partial \ln \tau \; (\delta\tau/\tau)|$ (label (3)) is large, so that the Lagrangian variation of the temperature $|\delta T/T|$ and the variation of the temperature at constant optical depth $|\Delta_\tau T/T| \simeq |\partial \ln T/\partial \ln T_{\text{eff}} \; (\delta T_{\text{eff}}/T_{\text{eff}})|$ (label (1)) are two totally different quantities. We note that, because of the significant values of $\partial \ln T/\partial \ln \tau$ in the outermost layers of the Kurucz atmosphere models, $|\partial \ln T/\partial \ln \tau \; (\delta\tau/\tau)|$ does not go to zero at the outermost layer. Finally, we see that $|\delta T/T|$ and $|\delta T_{\text{eff}}/T_{\text{eff}}|$ (label "dTe") are very different at the photosphere. So that it is inappropriate to replace $|\delta T_{\text{eff}}/T_{\text{eff}}|$ by $|\delta T/T|$ in the flux boundary condition. We recall that $\xi_r/R = 1$ at the photosphere.

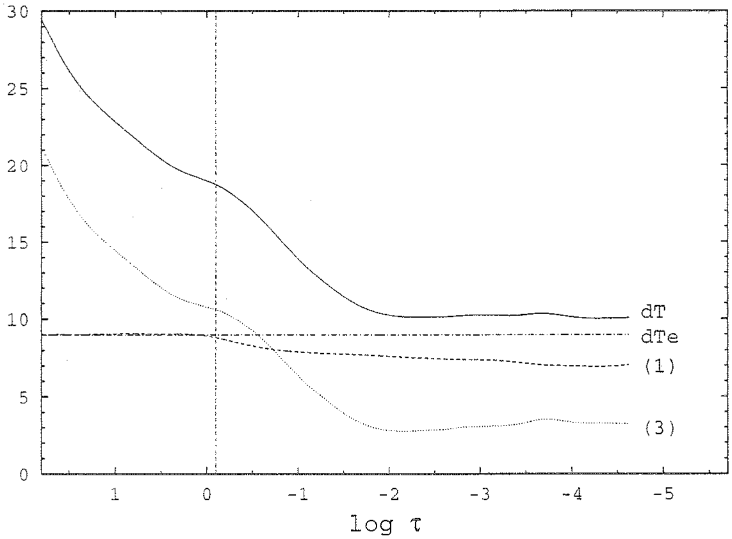

Figure 4.30: Amplitude of Lagrangian temperature variation $|\delta T/T|$ (solid line with the label "dT"), amplitude of local effective temperature variation $|\delta T_{\text{eff}}/T_{\text{eff}}|$ (dot-dashed line with the label "dTe") and moduli of the first and last terms of the right-hand side of Eq. (2.32). The dashed line with the label "(1)" is the modulus of the first term ($\propto \delta T_{\text{eff}}/T_{\text{eff}}$), the dotted line with the label "(3)" is the modulus of the third term ($\propto \delta\tau/\tau$), the vertical line corresponds to the photosphere where $T = T_{\text{eff}}$. The functions were computed for the mode $\ell = 1$, g_{22}, in the atmosphere of a 4 $M_\odot$ SPB model (see Table 4.12).

4.2.6 Non-adiabatic photometric observables in SPBs

As presented in Section 3.2, multi-colour photometric observations can be confronted to the theoretical predictions of our non-adiabatic code. We have shown that this confrontation can be used as a tool for mode identification. In this Section, we present the results obtained for 3 Slowly Pulsating B stars observed by Peter De Cat with Geneva photometry (De Cat 2001). In the original version of this text, the applications to 8 additional SPBs are also presented (HD 74195, HD 123515, HD 53921, HD 140873, HD 74560, HD 24587, HD 177863 and HD 181558), see the prefatory note at the beginning of this thesis. Using the calibrations of Künzli et al. (1997), De Cat (2001) determined the effective temperature and gravity of these SPBs. Even for the binary stars of this sample, there are no reliable observational constraints on their mass. For the chemical composition also, there are no precise observational constraints. We determined thus the theoretical stellar models as follows. We adopted a solar chemical composition for each models, with $X = 0.7$ and $Z = 0.02$, and we put no overshooting. For each star, we chose then appropriately the mass so that the evolution track goes the closest to the observed effective temperature and gravity and we selected the model closest to these values. And finally, for each models, we have performed non-adiabatic computations and photometric mode identifications of the dominant pulsation modes.

We give in Figure 4.31, HR diagrams with the evolution tracks computed with the Code Liégeois d'Évolution Stellaire (CLÉS). Observational error boxes corresponding to each stars are also given in this figure. In Table 4.7, we give in the first column the names of the stars. In the second column, we give the observed effective temperatures with error bars; in the third column, we give the observed gravities with error bars and in the last column, we give the masses we have adopted for each of the 3 SPBs.

Since the phase-lags are close to zero, a mode identification method based on amplitude ratios is adapted. Dr. De Ridder improved the initial code of Heynderickx et al. (1994) in order to take our non-adiabatic predictions into account. We present now star by star our non-adiabatic results and the photometric mode identification.

Table 4.7: Names, observed effective temperatures, observed gravities, and adopted masses of the 3 SPBs studied in Section 4.2.6

Name	$T_{\rm eff}$	$\log g$	$M/M_\odot$
HD 26326	15210 ± 110 K	4.14 ± 0.14	4.5
HD 138764	14050 ± 80 K	4.20 ± 0.12	3.9
HD 215573	13960 ± 80 K	4.09 ± 0.13	4

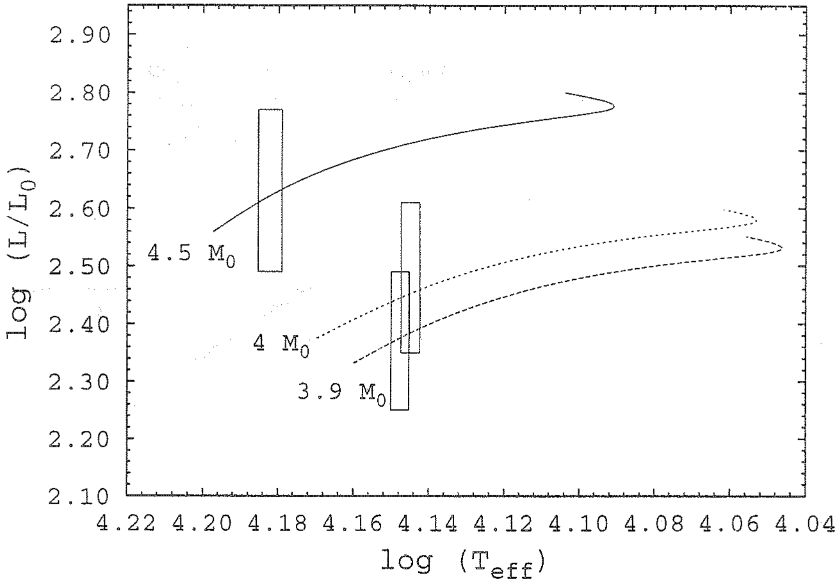

Figure 4.31: HR diagrams with the evolution tracks and the observational error boxes for the 3 SPBs studied in Section 4.2.6. The lower diagram is a zoom of the upper diagram

HD 26326

HD 26326 (GU Eridani) is a B5 IV star without known companion for which no Hα emission is observed. Photometric variations were reported by Savage et. al (1985). Using the photometric observations of the Hipparcos space mission, De Cat (2001) detected two intrinsic frequencies: $\nu_1 = 0.5338$ c/d and $\nu_2 = 0.1723$ c/d. In spectroscopy, these two frequencies were also detected. In the Geneva photometry, no evidence for ν_2 is found, and the best candidate for a second intrinsic frequency is $\nu_3 = 0.7629$ c/d. We consider here the results obtained for ν_1 and ν_3.

Table 4.8: Global characteristics of the theoretical model of HD 26326

$M/M_\odot = 4.5$	$T_{\rm eff} = 15203\,$K	$\log(L/L_\odot) = 2.6218$
$\log g = 4.1501$	$R/R_\odot = 2.9540$	age (My) = 35.1
X = 0.7	Z = 0.02	no overshooting

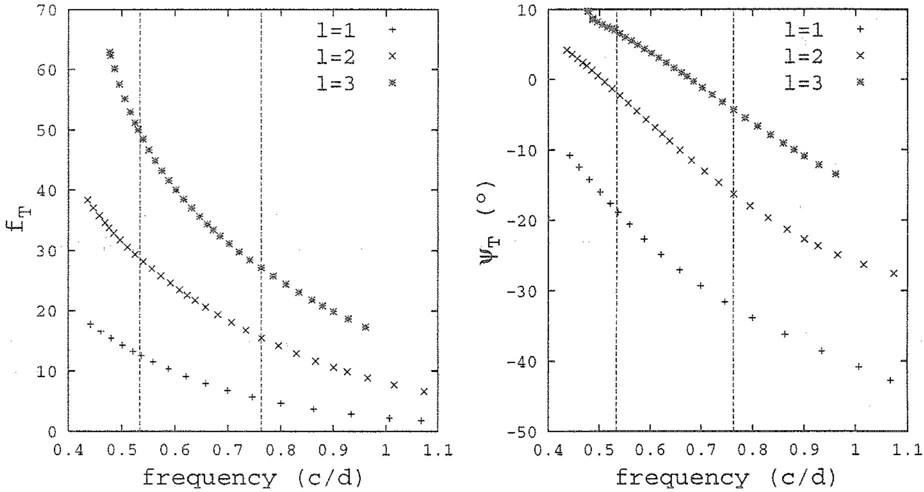

Figure 4.32: Non-adiabatic amplitudes and phase-lags for the star HD 26326. At the left: Amplitude of local effective temperature variations $f_T = |\delta T_{\rm eff}/T_{\rm eff}|$ ($\xi_r/R = 1$ at the photosphere), as function of the frequency in cycles/day. At the right: Phase-lag $\psi_T = \psi(\delta T_{\rm eff}/T_{\rm eff}) - \psi(\xi_r/R)$ in degrees. The "+" correspond to $\ell = 1$ modes, the "×" correspond to $\ell = 2$ modes and the asterisks correspond to $\ell = 3$ modes.

In Figure 4.32, we give some of the results obtained with our non-adiabatic code for different modes of HD 26326.

In Figures 4.33 and 4.34, we give the amplitude ratios obtained with Geneva photometry for the frequencies $\nu_1 = 0.5338$ c/d and $\nu_3 = 0.7629$ c/d. The black points with error bars correspond to the observations. The lines correspond to the theoretical predictions for different degrees ℓ: solid line for $\ell = 1$, dashed line for $\ell = 2$ and dot-dashed line for $\ell = 3$.

In table 4.9, the modes identified by the method of photometric amplitudes are given in bold.

Table 4.9: Non-adiabatic results and mode identification for the star HD 26326. Observed frequency, degree ℓ, radial order, theoretical amplitude of local effective temperature variation f_T and phase-lag ψ_T for the modes with theoretical frequencies closest to the observed frequency. The identified modes are given in bold.

$\nu_{\rm obs}$	ℓ	g_n	f_T	ψ_T (°)
0.5338	**1**	g_{21}	**12.56**	**−18.9**
	2	g_{37}	28.16	−2.3
	3	g_{53}	50.05	7.0
0.7629	**1**	g_{15}	**5.71**	**−31.6**
	2	g_{26}	15.52	−16.3
	3	g_{37}	27.11	−4.3

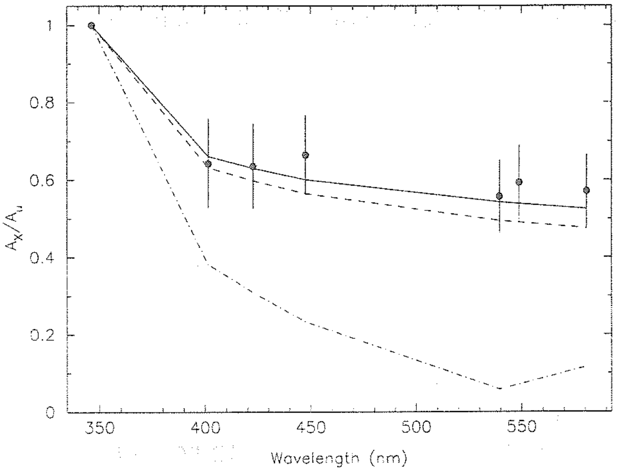

Figure 4.33: Amplitude ratios obtained with Geneva photometry for the first frequency $\nu_1 = 0.5338$ c/d of the SPB star HD 26326. The black points with error bars correspond to the observations. The lines correspond to the theoretical predictions for different degrees ℓ: solid line for $\ell = 1$, dashed line for $\ell = 2$ and dot-dashed line for $\ell = 3$.

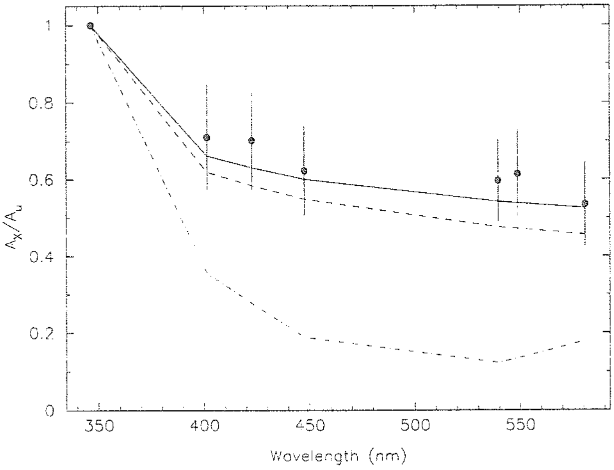

Figure 4.34: Amplitude ratios obtained with Geneva photometry for the third frequency $\nu_3 = 0.7629$ c/d of the SPB star HD 26326. The black points with error bars correspond to the observations. The lines correspond to the theoretical predictions for different degrees ℓ: solid line for $\ell = 1$, dashed line for $\ell = 2$ and dot-dashed line for $\ell = 3$.

HD 138764

HD 138764 is a bright member of the Upper Scorpius subgroup of the Scorpio-Centaurus OB-association (Sco OB2). It is listed in the "General Catalogue of Ap and Am stars" (Renson et al. 1991) as a suspected Si star. De Cat (2001) was the first to report light variations in optical photometry of this star. More precisely, he detected one frequency $\nu_1 = 0.7944$ c/d with Geneva photometry. The global characteristics of the model we have used for our non-adiabatic computations are given in table 4.10.

Table 4.10: Global characteristics of the theoretical model of HD 138764

$M/M_\odot = 3.9$	$T_{\rm eff} = 14047\,{\rm K}$	$\log(L/L_\odot) = 2.3760$
$\log g = 4.1964$	$R/R_\odot = 2.6073$	age (My) = 38
X = 0.7	Z = 0.02	no overshooting

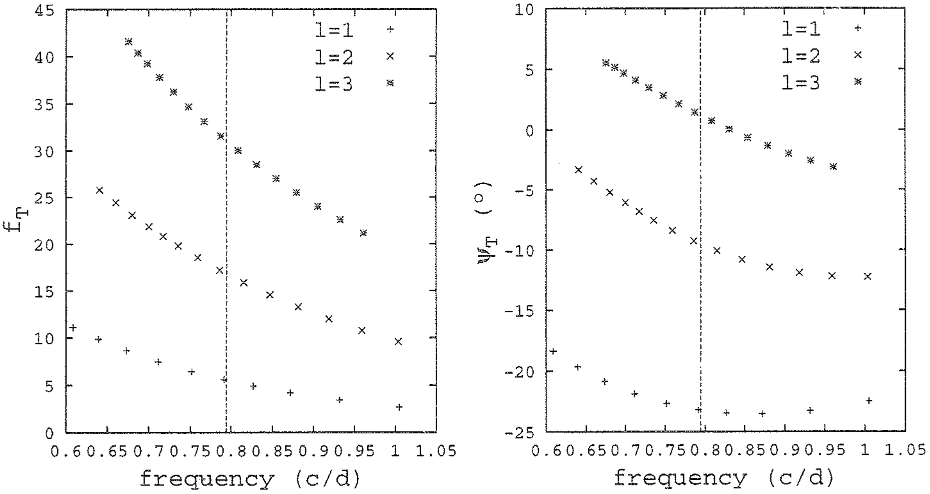

Figure 4.35: Non-adiabatic amplitudes and phase-lags for the star HD 138764. At the left: Amplitude of local effective temperature variations $f_T = |\delta T_{\rm eff}/T_{\rm eff}|$ ($\xi_r/R = 1$ at the photosphere), as function of the frequency in cycles/day. At the right: Phase-lag $\psi_T = \psi(\delta T_{\rm eff}/T_{\rm eff}) - \psi(\xi_r/R)$ in degrees. The "+" correspond to $\ell = 1$ modes, the "×" correspond to $\ell = 2$ modes and the asterisks correspond to $\ell = 3$ modes.

In Figure 4.35, we give some of the results obtained with our non-adiabatic code for different modes of HD 138764.

In Figure 4.36, we give the amplitude ratios obtained with Geneva photometry for the frequency $\nu_1 = 0.7944$ c/d. The black points with error bars correspond to the observations. The lines correspond to the theoretical predictions for different degrees ℓ: solid line for $\ell = 1$, dashed line for $\ell = 2$ and dot-dashed line for $\ell = 3$.

In table 4.11, the mode identified by the method of photometric amplitudes is given in bold.

Table 4.11: Non-adiabatic results and mode identification for the star HD 138764. Observed frequency, degree ℓ, radial order, theoretical amplitude of local effective temperature variation f_T and phase-lag ψ_T for the modes with theoretical frequencies closest to the observed frequency. The identified modes are given in bold.

ν_{obs}	ℓ	g_n	f_T	ψ_T (°)
0.7944	**1**	$\mathbf{g_{16}}$	**5.59**	**−23.2**
	2	g_{28}	17.23	-9.3
	3	g_{40}	31.57	1.4

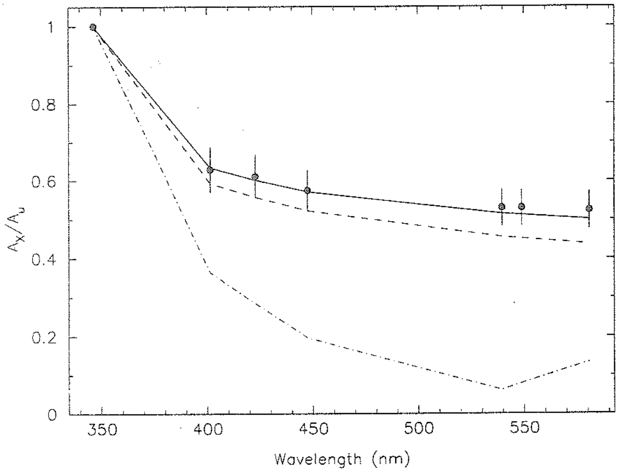

Figure 4.36: Amplitude ratios obtained with Geneva photometry for the first frequency $\nu_1 = 0.7944$ c/d of the SPB star HD 138764. The black points with error bars correspond to the observations. The lines correspond to the theoretical predictions for different degrees ℓ: solid line for $\ell = 1$, dashed line for $\ell = 2$ and dot-dashed line for $\ell = 3$.

HD 215573

Many abundance analyses of HD 215573 have been performed. Eggen (1977) was the first to report upon the variability of this star, and De Cat (2001) was the first to classify it as an SPB. One frequency has been detected by De Cat (2001) with Geneva photometry: $\nu_1 = 0.5654$ c/d. The global characteristics of the model we have used for our non-adiabatic computations are given in table 4.12.

Table 4.12: Global characteristics of the theoretical model of HD 215573

$M/M_{\odot} = 4$	$T_{\rm eff} = 13955K$	$\log(L/L_{\odot}) = 2.4532$
$\log g = 4.1187$	$R/R_{\odot} = 2.8876$	age (My) $= 59.4$
X = 0.7	Z = 0.02	no overshooting

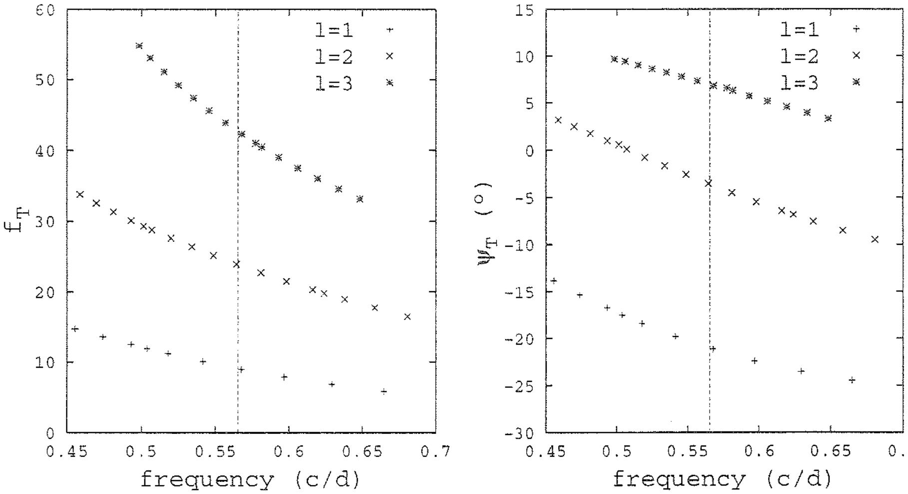

Figure 4.37: Non-adiabatic amplitudes and phase-lags for the star HD 215573. At the left: Amplitude of local effective temperature variations $f_T = |\delta T_{\rm eff}/T_{\rm eff}|$ ($\xi_r/R = 1$ at the photosphere), as function of the frequency in cycles/day. At the right: Phase-lag $\psi_T = \psi(\delta T_{\rm eff}/T_{\rm eff}) - \psi(\xi_r/R)$ in degrees. The "+" correspond to $\ell = 1$ modes, the "×" correspond to $\ell = 2$ modes and the asterisks correspond to $\ell = 3$ modes.

In Figure 4.37, we give some of the results obtained with our non-adiabatic code for different modes of HD 215573.

In Figure 4.38, we give the amplitude ratios obtained with Geneva photometry for the frequency $\nu_1 = 0.5654$ c/d. The black points with error bars correspond to the observations. The lines correspond to the theoretical predictions for different degrees ℓ: solid line for $\ell = 1$, dashed line for $\ell = 2$ and dot-dashed line for $\ell = 3$.

In table 4.13, the mode identified by the method of photometric amplitudes is given in bold.

Table 4.13: Non-adiabatic results and mode identification for the star HD 215573. Observed frequency, degree ℓ, radial order, theoretical amplitude of local effective temperature variation f_T and phase-lag ψ_T for the modes with theoretical frequencies closest to the observed frequency. The identified modes are given in bold.

$\nu_{\rm obs}$	ℓ	g_n	f_T	ψ_T (°)
0.5654	**1**	$\boldsymbol{g_{22}}$	**8.97**	**−21.2**
	2	g_{39}	23.94	-3.5
	3	g_{55}	42.26	6.8

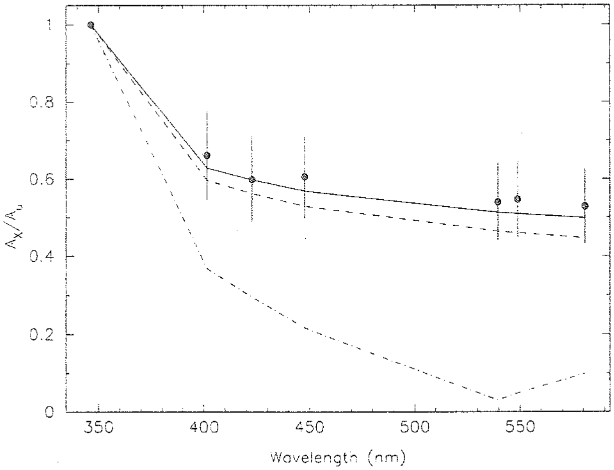

Figure 4.38: Amplitude ratios obtained with Geneva photometry for the first frequency $\nu_1 = 0.5654$ c/d of the SPB star HD 215573. The black points with error bars correspond to the observations. The lines correspond to the theoretical predictions for different degrees ℓ: solid line for $\ell = 1$, dashed line for $\ell = 2$ and dot-dashed line for $\ell = 3$.

4.2.7 Non-adiabatic spectroscopic observables in SPBs

As presented in Section 3.3, our non-adiabatic code permits to determine the influence of the effective temperature variations on the line-profile variations. The results presented in this section were the fruit of a close collaboration with Joris De Ridder of the K-U Leuven.

Si^+ line formation layer

We adopt the one-layer approximation in our simulations of line-profile time series of SPBs. We recall that the *single layer* we adopt for our spectroscopic simulations is not at the same depth as the *single photosphere* we adopted for the photometric simulations in Section 4.2.6. In the case of SPBs, the line we chose for our simulations is the Si^+ doublet (412.81 nm). De Ridder et al. (2002) showed that the layer which contributes most to the flux line depression of the Si^+ doublet is situated at $\log\tau = -2$ for a typical SPB atmosphere. In order to avoid confusion, we use here the following notations for the non-adiabatic amplitudes at the Si^+ line formation layer: $f_{T\,\mathrm{Si}^+}$ is the amplitude of local effective temperature variation and $f_{g\,\mathrm{Si}^+}$ is the amplitude of local effective gravity variation for a normalized radial displacement at the Si^+ line formation layer ($\log\tau = -2$).

Model and non-adiabatic quantities

The global characteristics of the SPB model we used for our line-profile simulations are given in table 4.14. On the basis of this model, we performed non-adiabatic simulations for different high-order g-modes. The non-adiabatic results are given in Table 4.15.

Table 4.14: Global characteristics of the SPB model used for the simulations of line-profile variations

$M/M_\odot = 5$	$T_{\rm eff} = 15190\,$K	$\log(L/L_\odot) = 2.88$
$\log g = 3.93$	$R/R_\odot = 4.00$	age (My) = 59.07
X = 0.7	Z = 0.02	no overshooting

Simulations of line-profile variations

The simulations of line-profile variations have been performed with the code PULSTAR written by Dr. De Ridder, for the modes given in Table 4.15 and for all the values of m between 0 and ℓ, which means 59 different modes. The rotation was neglected in these

mode		K	$f_{T\,\mathrm{Si}^+}$	ψ_T	$f_{g\,\mathrm{Si}^+}$	ψ_g	P (h)
$\ell = 1$	g_{20}	17.5	3.62	319°	2.00	180°	41.36
$\ell = 1$	g_{25}	24.6	5.68	327°	1.95	180°	48.82
$\ell = 1$	g_{30}	36.1	8.54	336°	1.89	180°	58.73
$\ell = 1$	g_{35}	50.0	11.2	343°	1.86	180°	68.31
$\ell = 1$	g_{40}	66.7	13.6	349°	1.79	180°	78.38
$\ell = 1$	g_{45}	86.1	15.4	354°	1.73	180°	88.11
$\ell = 1$	g_{50}	108	16.9	357°	1.66	180°	97.85
$\ell = 2$	g_{30}	12.9	6.94	329°	1.95	180°	35.03
$\ell = 2$	g_{35}	17.9	9.89	337°	1.88	180°	40.86
$\ell = 2$	g_{40}	23.2	12.4	343°	1.81	180°	46.18
$\ell = 2$	g_{45}	30.3	14.8	349°	1.74	180°	52.11
$\ell = 2$	g_{50}	38.3	16.8	353°	1.68	180°	57.86
$\ell = 2$	g_{55}	47.0	18.4	357°	1.61	180°	63.23
$\ell = 2$	g_{60}	58.3	19.9	0°	1.53	180°	69.24
$\ell = 3$	g_{40}	11.6	10.7	339°	1.87	180°	32.71
$\ell = 3$	g_{45}	15.2	13.5	345°	1.79	180°	36.88
$\ell = 3$	g_{50}	19.2	15.8	350°	1.71	180°	40.96
$\ell = 3$	g_{55}	23.6	17.8	354°	1.63	180°	44.75
$\ell = 3$	g_{60}	29.2	19.6	358°	1.55	180°	48.98
$\ell = 3$	g_{65}	35.7	21.2	0°	1.45	180°	53.15

Table 4.15: $K = |\xi_h/\xi_r|$, $f_{T\,\mathrm{Si}^+}$, ψ_T, $f_{g\,\mathrm{Si}^+}$ and ψ_g, as computed by our non-adiabatic code, for different modes of the SPB stellar model of Table 4.14. The non-adiabatic amplitudes are determined at the line-formation layer of the Si^+ spectral line (412.81 nm) situated at $\log\tau = -2.0$, with a relative radial displacement $\xi_r/r = 1$ at this layer. The last column contains the pulsation periods in hours.

simulations. The inclination angle was always chosen as an angle of least cancellation for the results presented in this Section.

In our simulations of line-profile variations, we have imposed that the maximum over the entire stellar surface of the amplitude of the relative displacement $(|\vec{\xi}|)_{\rm max}/R$ is 10% for every mode. This led to amplitudes of $\langle v \rangle$ (first moment of the line profile variation integrated over the entire stellar disk) between 1.5 km/s and 6.5 km/s. This can be compared with the largest amplitude of $\langle v \rangle$ ever observed for an SPB: 6.7 km/s for HD 181558 (De Cat 2001). With these values, the maximum amplitude of the local pulsation velocity variation $(|\vec{v}|)_{\rm max}$ ranged from 5 km/s to 15 km/s.

With the amplitudes given above, the non-adiabatic temperature and gravity variations deduced from Table 4.15 have a very small effect on the line profiles. The relative difference between the line profiles computed with and without non-adiabatic effects are about 1% or lower. In Figure 4.39, we show greyscale diagrams of the difference in residual intensity between the spectra computed with and without temperature, gravity, and surface normal variations. These diagrams were computed for the Si^+ (412.8054 nm) line and for the g_{40}-mode with $(\ell, m) = (2{,}2)$ (upper panel) and $(\ell, m) = (2{,}1)$ (lower panel). The interplay between the different sectors and zones now causes a more complex pattern. Parts of the spectral line have a higher residual intensity while other parts have a lower residual intensity than the corresponding spectral line computed without temperature effects.

For all our simulations, the largest EW variations were found for the $\ell = 1$ modes, with $|\delta\,\mathrm{EW}/\mathrm{EW}|$ of the order of maximum 2% (even for the modes of highest radial order n, which have a rather large $f_{T\,\mathrm{Si}^+}$ value). The cancellation effects are thus as important for the EW variation as for the $\langle v \rangle$ variation. For SPB high-order g-modes, the gravity variation is very small and does not play a significant role in the EW variation, so that the latter is mainly caused by the $T_{\rm eff}$ variation. As a consequence, the predicted non-adiabatic phase difference between the EW and the $\langle v \rangle$ curve is very close to the non-adiabatic phase difference between the local effective temperature variation and the local pulsation velocity variation.

Neither the line profile variations nor the moments of the lines are significantly affected by the inclusion of non-adiabatic temperature variations. Modelling the line profile variations of the silicon lines with the velocity field only, is therefore a good approximation for the SPB stars.

The surface normal variation played only a minor role compared to the velocity and temperature variations. The deviation of the surface normal from the local radial vector was never much more than a few degrees.

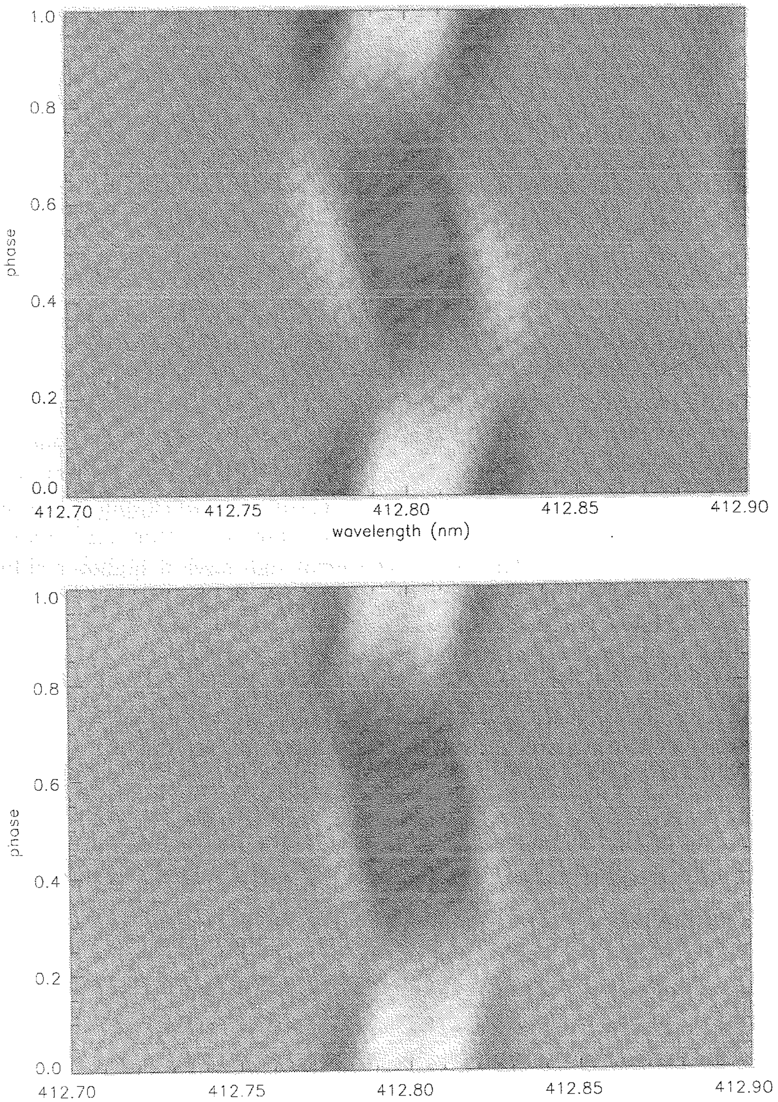

Figure 4.39: Greyscale plots of the difference in residual intensity between the spectra computed with and without temperature, gravity, and surface normal variations. White indicates a positive difference, black a negative difference. Both panels are for the Si$^+$ (412.8054 nm) line, for the mode g_{40} of the 5 $M_\odot$ SPB model of Table 4.14. The upper panel is for the $(\ell, m) = (2,2)$ mode, the lower panel is for the $(\ell, m) = (2,1)$ mode. In both cases, the maximum relative difference in residual intensity is about 0.6%. Figure taken from De Ridder (2001).

4.3 δ Scuti stars

4.3.1 δ Scuti stars from an observational point of view

δ Scuti stars are pulsating stars with masses between 1.5 $M_\odot$ and 2.5 $M_\odot$. Their pulsation periods go from 0.5 to 6 hours. Their spectral types range from A2 to F0 on the main sequence and from A3 to F5 at luminosity class III (Kurtz 2000). Most of the δ Scuti stars are moderate to fast rotators with $v \sin i$ up to 200, even 250 km s^{-1}. In their catalogue of δ Scuti and related stars, Rodríguez et al. (2000) list more than 600 stars with amplitudes up to a few hundreds of a milli-magnitude. Only about 50% of the stars in the δ Scuti instability strip are found to be photometrically variable (Breger 2000), but since the number of confirmed pulsators increases steeply towards low amplitudes (Gautschy & Saio 1996), one can expect many variables to pulsate with an amplitude below the current detection level. For some δ Scuti stars, more than 20 oscillation modes have been detected; typical examples are FG Vir with 24 frequencies (Breger, Zima et al. 1998), 4 Canum Venaticorum with more than 30 frequencies (Breger, Handler et al. 1999) and BI CMi with 29 frequencies (Breger, Garrido et al. 2002). δ Scuti stars with slowly changing pulsation periods have been observed, but cannot always be explained by invoking evolutionary effects (Breger & Pamyatnykh 1998). The latter authors discuss non-linear mode interaction as the possible main cause of non-evolutionary period changes.

4.3.2 δ Scuti stars from a theoretical point of view

The δ Scuti stars are near main sequence variable stars either core hydrogen-burning or shell hydrogen-burning. During their evolution on the main sequence, a large convective core develops, which later shrinks leaving behind a gradient in mean molecular weight. Overshooting is expected at the end of the convective core, constraints imposed by 2 $M_\odot$ eclipsing binaries yield a value of $\alpha_{\rm ov} = \Delta r_{\rm ov}/H_p = 0.17 \pm 0.05$ (Ribas et al. 2000). Two very thin superficial convection zones are present, they are due to the opacity bumps in the He^+, He and H partial ionization zones (see Figures 4.54 (top) and 4.58). The rotation can induce mixing of chemicals and affects the evolution (Maeder 1999). The typical periods of pulsation of the δ Scuti point towards low order p and g-modes. The oscillations are driven by the κ-γ-mechanism acting in the $\mathrm{He}^+ \rightleftarrows \mathrm{He}^{++}$ (HeII) partial ionization zone, as will be explained in Section 4.3.3. We note that, compared to the observations, an order of magnitude more unstable modes are predicted by the linear theory (e.g. Bradley & Guzik 2000). It is not yet clear what mechanisms explain the observed amplitude distributions and the modal selections, but non-linear mode interaction has been suggested as a possible candidate. The effect of rotation on pulsation can be important for fast rotators, treatments up to the cubic order have been proposed by Soufi et al. (1998). Mixing between p and g-modes and avoided crossings are frequent in δ Scuti stars (see Figures 4.46, 4.47 and 4.48).

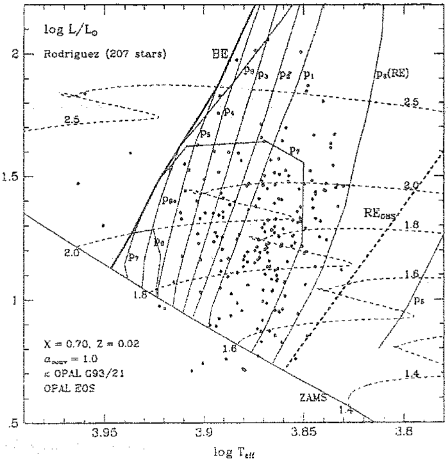

Figure 4.40: Position of the δ scuti stars in a HR diagram and theoretical blue edges of the instability domain of the δ Scuti stars for radial oscillations, as computed by Pamyatnykh (2000). The ZAMS and some evolution tracks are shown. Figure taken from Pamyatnykh (2000).

4.3.3 Driving mechanism of the δ Scuti stars

The driving mechanism of the δ Scuti is the classical κ-γ-mechanism acting in the HeII partial ionization zone. The same mechanism explains the variability of the RR Lyrae and δ Cephei stars in the "classical" instability strip (see Figure 1).

In order to illustrate this mechanism, we begin by giving some equilibrium characteristics of a typical δ Scuti model in Figure 4.41. The global characteristics of this model are given in Table 4.16 (model 2). The shape of the different physical quantities given in Figure 4.41 is modeled by the different partial ionization zones. The partial ionization zone of metals is at the origin of the small bump of opacity at $\log T \simeq 5.3$ (top of Figure 4.41). The HeII partial ionization zone is at the origin of the second bump of opacity at $\log T \simeq 4.6$. This partial ionization zone affects also the adiabatic gradient $(\Gamma_3 - 1)/\Gamma_1$ (graph with the label T_{PS}). Finally, the He $\rightleftarrows$ He$^+$ (HeI) and H $\rightleftarrows$ H$^+$ (H) partial ionization zones are at the origin of the big bump of opacity around $\log T \simeq 4.1$ and affect also strongly the adiabatic gradient $(\Gamma_3 - 1)/\Gamma_1$. Finally, we give at the bottom, the graph of the logarithm of the thermal relaxation time in seconds $\log(\tau_{th})$, as a function of the logarithm of temperature. The horizontal dashed line gives the logarithm of the period of pulsation of the fundamental radial mode. The intersection between this horizontal line and the thermal relaxation time gives the position of the transition region, we see that it is situated exactly in the HeII partial ionization zone.

In Figures 4.43, 4.44 and 4.45, we give the results obtained for the models 2, 3 and 4 of Table 4.16. We refer to Eq. (4.2) for the definition of W. The physical explanation

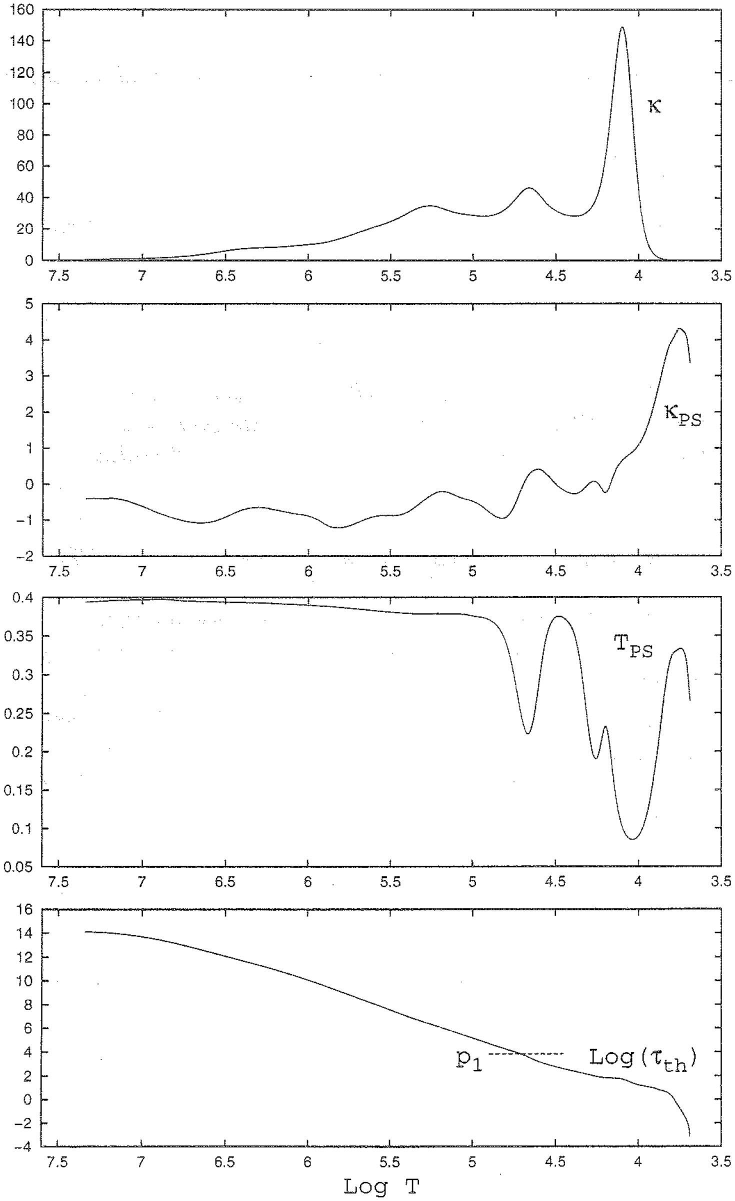

Figure 4.41: From top to bottom: Opacity in cm^2/g, $\kappa_{PS} = \left.\frac{\partial \ln \kappa}{\partial \ln P}\right|_S$, $T_{PS} = \left.\frac{\partial \ln T}{\partial \ln P}\right|_S = \frac{\Gamma_3 - 1}{\Gamma_1}$ and logarithm of the thermal relaxation time in seconds: $\log(\tau_{th})$, as function of the logarithm of temperature, for a 1.8 $M_\odot$ δ Scuti model in the middle of the instability strip (Table 4.16, model 2).

Table 4.16: Global characteristics of some δ Scuti models used in Sections 4.3.3 to 4.3.6.

model 1		
$M/M_\odot = 1.8$	$T_{\text{eff}} = 7473\,\text{K}$	$\log(L/L_\odot) = 1.1218$
$\log g = 4.0183$	$R/R_\odot = 2.1743$	age (Gy) = 1.02
$(X, Z) = (0.7, 0.02)$	$\alpha = 0.7$	no overshooting
model 2		
$M/M_\odot = 1.8$	$T_{\text{eff}} = 7479\,\text{K}$	$\log(L/L_\odot) = 1.1225$
$\log g = 4.0192$	$R/R_\odot = 2.1721$	age (Gy) = 1.02
$(X, Z) = (0.7, 0.02)$	$\alpha = 1$	no overshooting
model 3		
$M/M_\odot = 1.8$	$T_{\text{eff}} = 7493\,\text{K}$	$\log(L/L_\odot) = 1.1294$
$\log g = 4.0154$	$R/R_\odot = 2.1816$	age (Gy) = 1.1
$(X, Z) = (0.7, 0.02)$	$\alpha = 1.5$	no overshooting
model 4		
$M/M_\odot = 2$	$T_{\text{eff}} = 8816\,\text{K}$	$\log(L/L_\odot) = 1.2200$
$\log g = 4.2531$	$R/R_\odot = 1.7491$	age (Gy) = 0.2
$(X, Z) = (0.7, 0.02)$	$\alpha = 1$	overshooting = $0.2\,H_p$
model 5		
$M/M_\odot = 2$	$T_{\text{eff}} = 7552\,\text{K}$	$\log(L/L_\odot) = 1.3530$
$\log g = 3.8514$	$R/R_\odot = 2.7778$	age (Gy) = 1.1
$(X, Z) = (0.7, 0.02)$	$\alpha = 0.5$	overshooting = $0.2\,H_p$
model 6		
$M/M_\odot = 2$	$T_{\text{eff}} = 7590\,\text{K}$	$\log(L/L_\odot) = 1.3529$
$\log g = 3.8600$	$R/R_\odot = 2.7503$	age (Gy) = 1.08
$(X, Z) = (0.7, 0.02)$	$\alpha = 1$	overshooting = $0.2\,H_p$
model 7		
$M/M_\odot = 2$	$T_{\text{eff}} = 7624\,\text{K}$	$\log(L/L_\odot) = 1.3519$
$\log g = 3.8688$	$R/R_\odot = 2.7224$	age (Gy) = 1.08
$(X, Z) = (0.7, 0.02)$	$\alpha = 1.5$	overshooting = $0.2\,H_p$

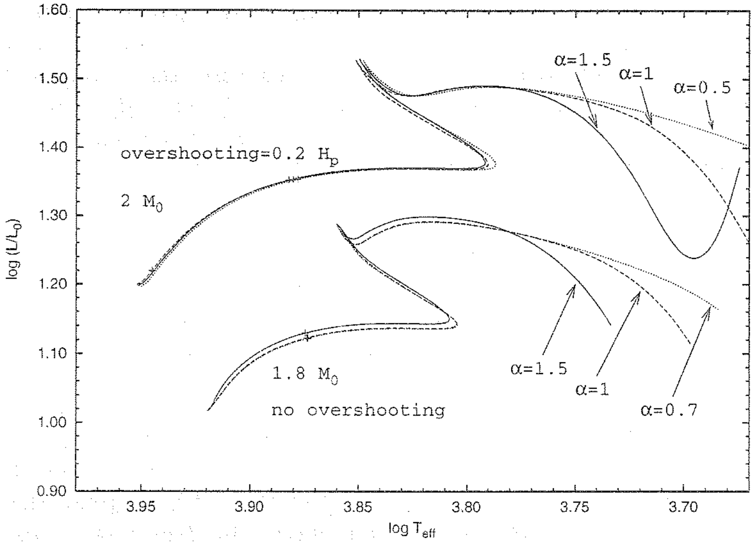

Figure 4.42: HR diagram with evolution tracks corresponding to the different δ Scuti models used in Section 4.3. The labels "+" give the position of the 7 models of Table 4.16. The 1.8 $M_\odot$ models are without overshooting but the 2 $M_\odot$ models are with an overshooting of 0.2 H_p. We see that, between the ZAMS and the TAMS, the value of the mixing length parameter α has a negligible impact on the evolution tracks.

of the κ-γ mechanism driving the δ Scuti stars is much the same as the κ mechanism driving the β Cephei stars, and we refer to Section 4.1.3 for more details. The difference is that the driving region is now situated exactly in the HeII partial ionization zone where κ_{PS} is increasing outwards (Figure 4.41). The significant decrease of the adiabatic exponents Γ_1, Γ_2 and Γ_3 in this region (graph of $(\Gamma_3-1)/\Gamma_1$ with the label $\mathrm{T_{PS}}$ in Figure 4.41) affects strongly the opacity and temperature variations, and plays thus also a significant role in the driving process. This mechanism has been initially proposed by Cox (1967) and is usually called the κ-γ mechanism.

Figures 4.43 and 4.44 give the typical case of a 1.8 $M_\odot$ δ Scuti with an unstable fundamental radial mode. The model of Figure 4.43 has a mixing length parameter $\alpha = 1$ (model 2 of Table 4.16) and in the model of Figure 4.44, $\alpha = 1.5$ (model 3 of Table 4.16). We see in these figures that the main driving region is, as expected, the HeII partial ionization zone. But a small driving is also induced by the HeI and H partial ionization zones. By comparing the two figures, we see that the larger is α, the more efficient is the driving in this small region. We propose the following explanation. We see in Figure 4.57 that the higher is α, the lower is the gradient of temperature in the thin convection zone of this region. Because the interval of temperature between the base and the top of the H partial ionization zone is approximately constant, the mass and the heat capacity of this zone is thus increasing with α, so that the driving is more efficient for larger α.

In order to understand the origin of the blue edge of the instability strip, we give in Figure 4.45 the results obtained for a young $2\,M_\odot$ model (model 4 of Table 4.16), just out of the instability strip. We see that, in this case, the driving of the HeII partial ionization zone is not enough efficient to counterbalance the damping of the more internal layers. The physical explanation is that, for hotter models, the partial ionization zone is closer to the surface, where the heat capacity is too small to drive efficiently the mode.

In Figures 4.46, 4.47 and 4.48, we show the unstable modes determined by our non-adiabatic code along 3 sequences of evolution. In each figure, we give four graphs corresponding to the spherical degrees $\ell = 0$, $\ell = 1$, $\ell = 2$ and $\ell = 3$. In each graph, we give the frequencies in cycles/day of modes of different radial order n, as function of the age of the models in Gyears, a scale with the logarithm of the effective temperature is given at the top. The empty circles correspond to stable modes and the full circles to unstable modes. Figures 4.46 and 4.47 are for two $1.8\,M_\odot$ evolution track with two different values of the mixing-length parameter α: 1 and 1.5 respectively. Since the superficial convection zone is very thin in this part of the HR diagram, the internal structure and the evolution tracks are very little affected by changes of α. But it is not the case of the non-adiabatic results. By comparing Figures 4.46 and 4.47, we see that more unstable modes are predicted for larger α. This comes from the small driving of the H partial ionization zone very sensitive to α (compare Figures 4.43 and 4.44). For the $1.8\,M_\odot$ evolution tracks, p-modes from typically p_4 to p_7 are unstable for the young models close to the ZAMS, and low-order p-modes and g-modes are unstable for older models close to the TAMS. The numerous avoided crossings occuring in the evolved models and resulting from the mixing between p and g-modes can also be seen in these figures. In Figure 4.48, we give the results obtained for a 2 $M_\odot$ evolution track. The young 2 $M_\odot$ models are beyond the blue edge of the instability strip and no unstable modes are predicted (see also Figure 4.45). As the star evolves, the HeII partial ionization zone goes deeper, where the heat capacity is sufficient to drive efficiently the star, and more unstable modes are predicted and observed.

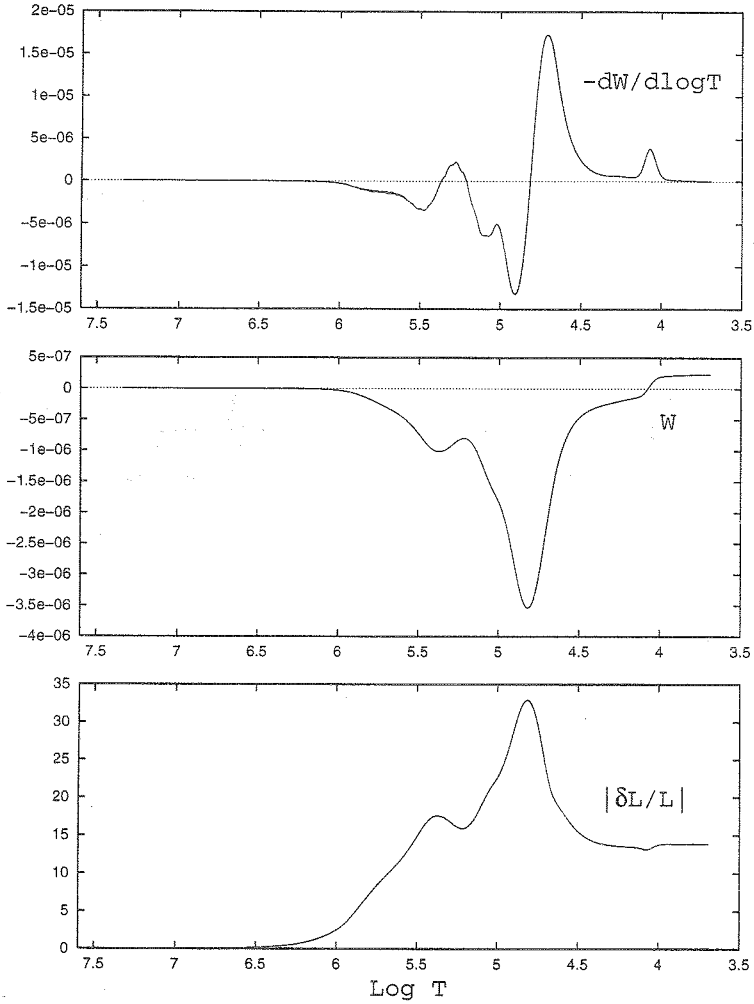

Figure 4.43: $-\mathrm{d}W/\mathrm{d}\log T$ (top), dimensionless work integral W (middle) and amplitude of luminosity variation: $|\delta L/L|$ (bottom), as function of the logarithm of temperature, for the fundamental radial mode of a $1.8\,M_\odot$ δ Scuti model with $\alpha = 1$ (Table 4.16, model 2).

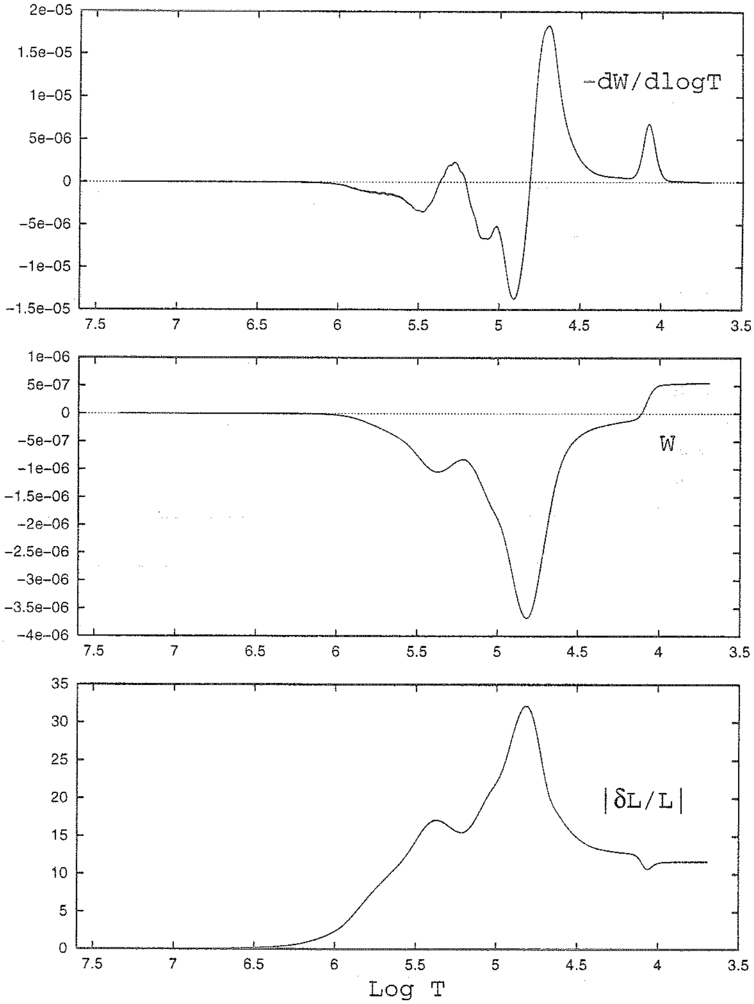

Figure 4.44: $-\mathrm{d}W/\mathrm{d}\log T$ (top), dimensionless work integral W (middle) and amplitude of luminosity variation: $|\delta L/L|$ (bottom), as function of the logarithm of temperature, for the fundamental radial mode of a $1.8\,M_\odot$ δ Scuti model with $\alpha = 1.5$ (Table 4.16, model 3).

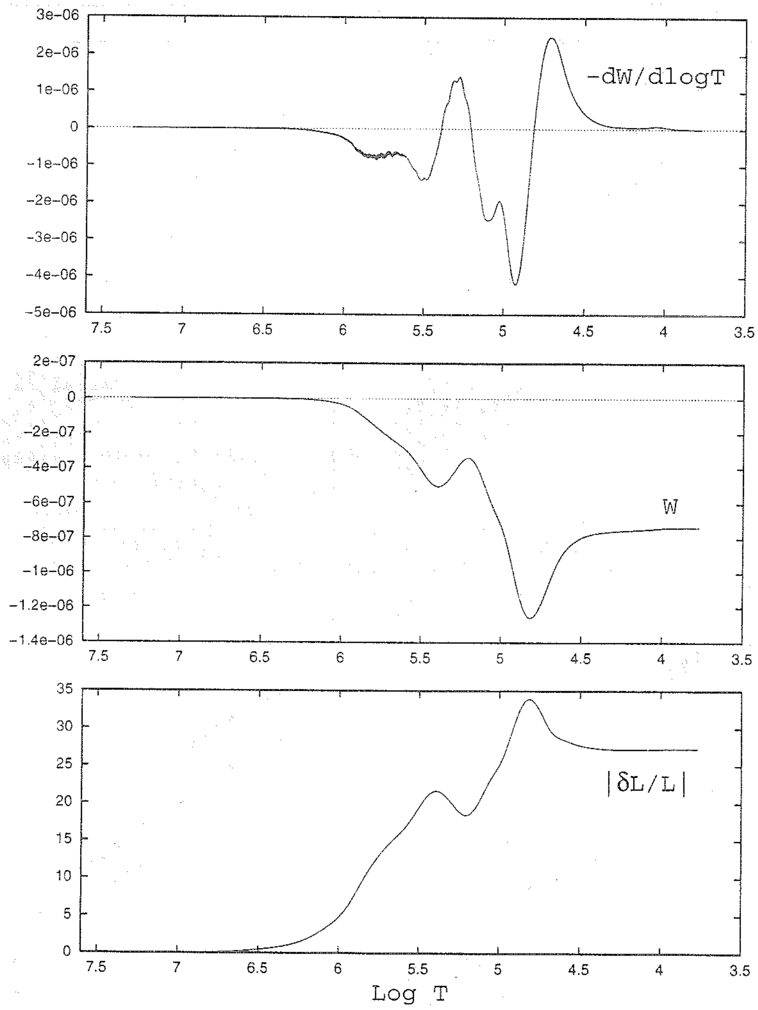

Figure 4.45: $-\mathrm{d}W/\mathrm{d}\log T$ (top), dimensionless work integral W (middle) and amplitude of luminosity variation: $|\delta L/L|$ (bottom), as function of the logarithm of temperature, for the fundamental radial mode of a young $2\,M_\odot$ model with $\alpha = 1$ (Table 4.16, model 4).

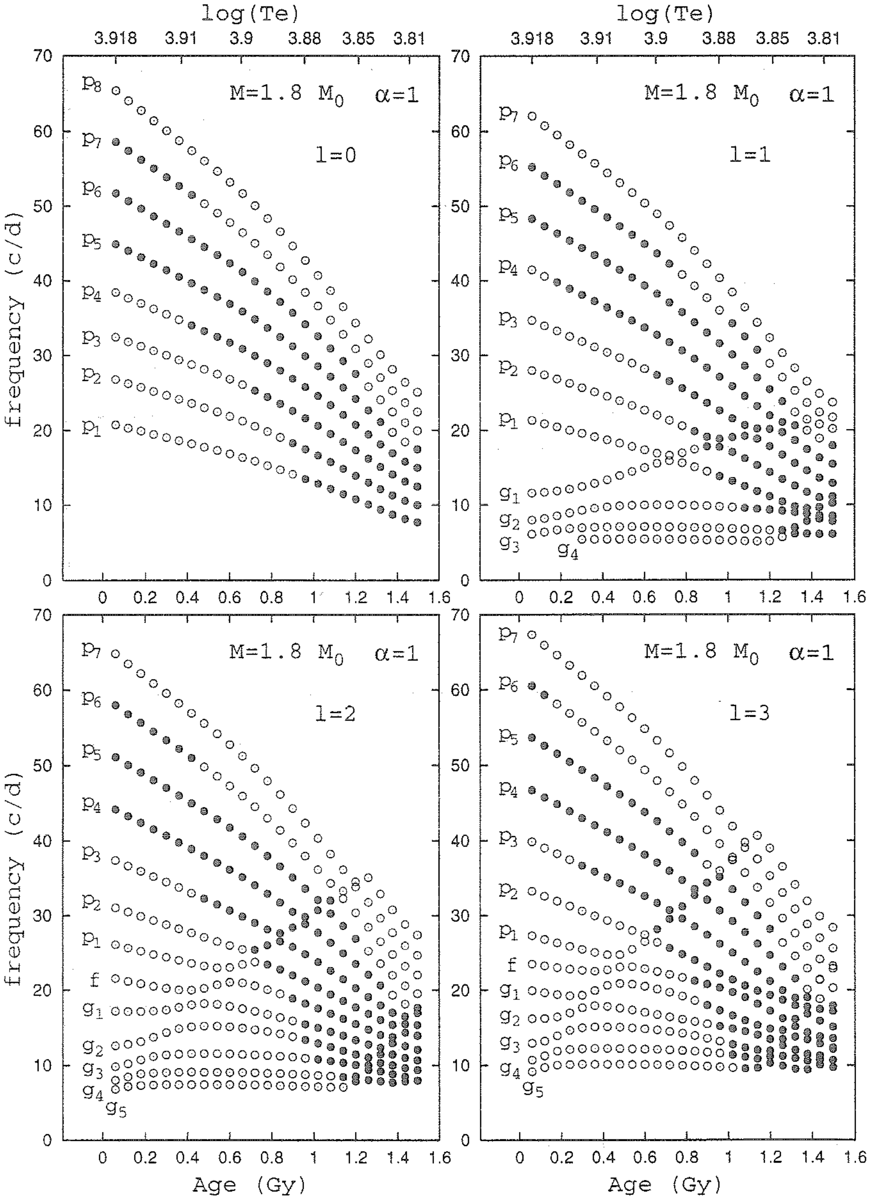

Figure 4.46: Stable and unstable modes of degree $\ell = 0$ (left, top), $\ell = 1$ (right, top), $\ell = 2$ (left, bottom) and $\ell = 3$ (right, bottom) along a $1.8\,M_{\odot}$ sequence of evolution with $\alpha = 1$. We give the frequencies of the modes in cycles/day as function of the age in Gyears and of $\log(T_{\rm eff})$. The full circles correspond to the unstable modes and the empty circles to the stable modes.

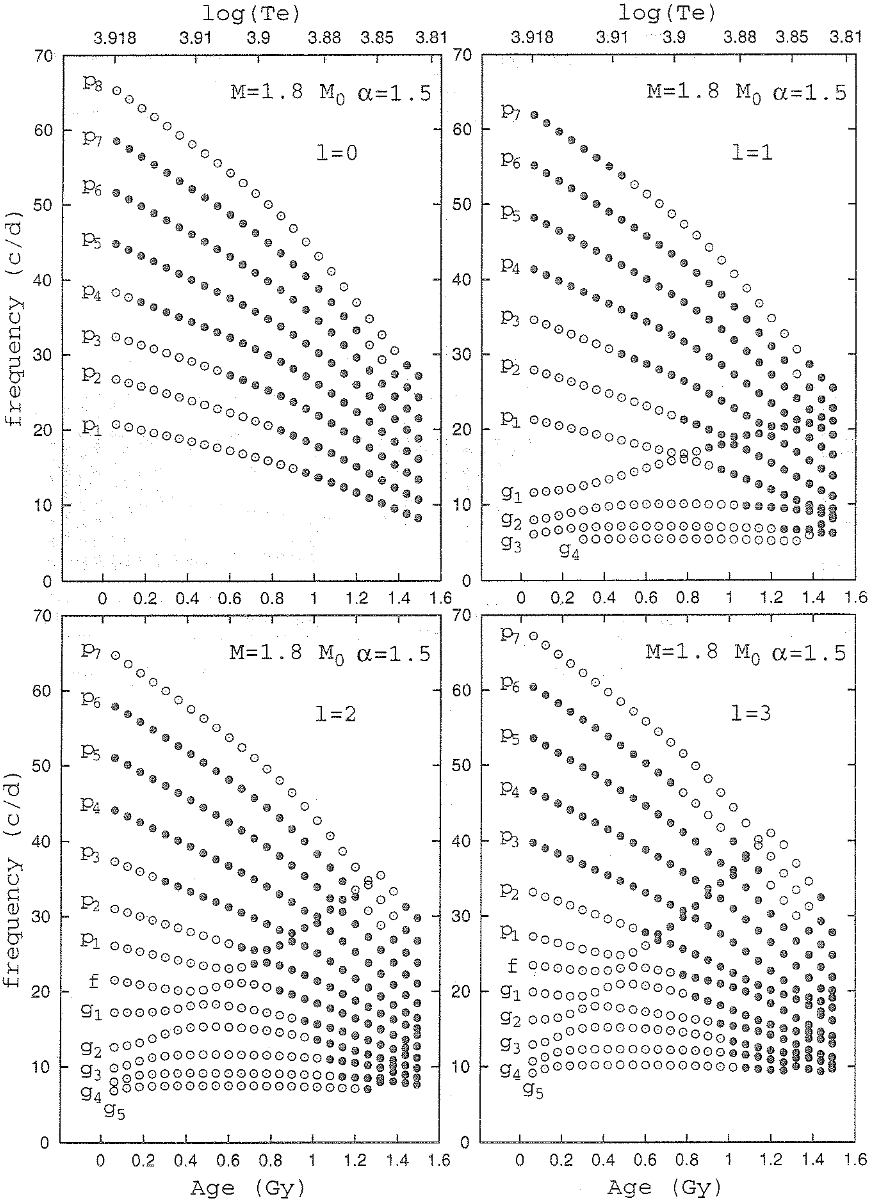

Figure 4.47: Stable and unstable modes of degree $\ell = 0$ (left, top), $\ell = 1$ (right, top), $\ell = 2$ (left, bottom) and $\ell = 3$ (right, bottom) along a $1.8\,M_\odot$ sequence of evolution with $\alpha = 1.5$. We give the frequencies of the modes in cycles/day as function of the age in Gyears and of $\log(T_{\rm eff})$. The full circles correspond to the unstable modes and the empty circles to the stable modes.

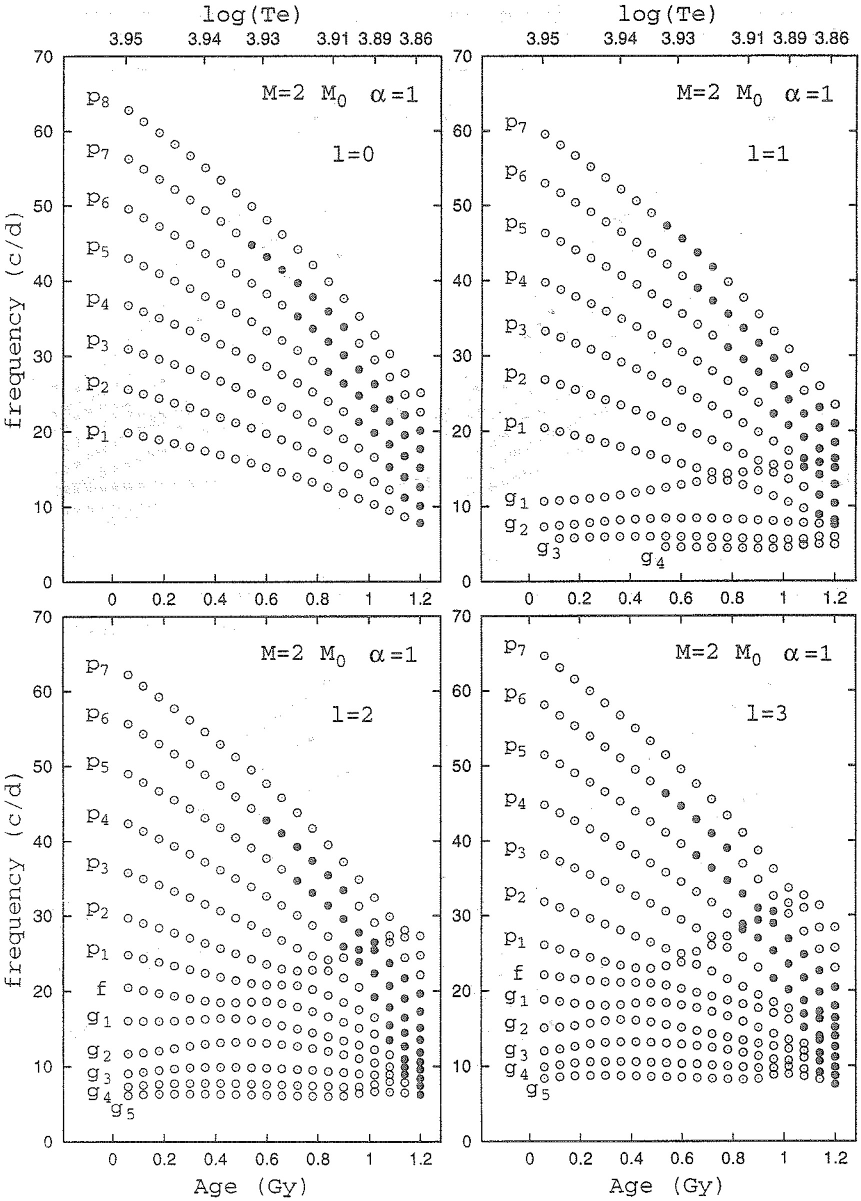

Figure 4.48: Stable and unstable modes of degree $\ell = 0$ (left, top), $\ell = 1$ (right, top), $\ell = 2$ (left, bottom) and $\ell = 3$ (right, bottom) along a $2\,M_\odot$ sequence of evolution with $\alpha = 1$. We give the frequencies of the modes in cycles/day as function of the age in Gyears and of $\log(T_{\rm eff})$. The full circles correspond to the unstable modes and the empty circles to the stable modes.

4.3.4 Comparison between adiabatic and non-adiabatic eigenfunctions

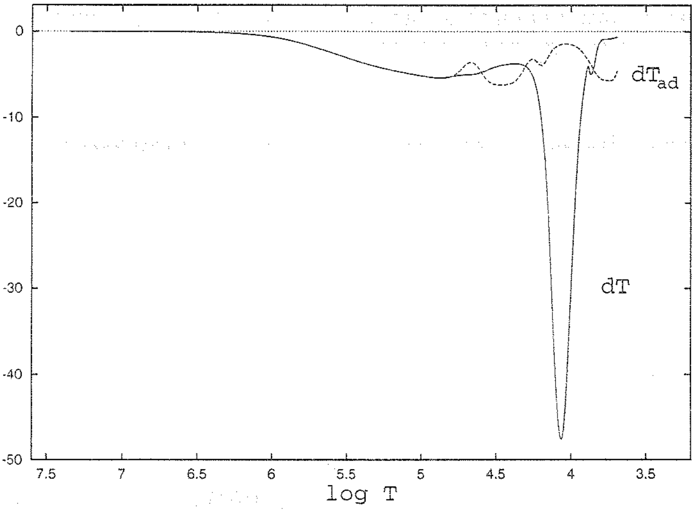

Figure 4.49: Real part of the Lagrangian variation of the temperature $\Re\{\delta T/T\}$ as computed by our non-adiabatic code (solid line with the label dT) compared to the adiabatic Lagrangian variation of the temperature $\delta T/T|_{\mathrm{ad}} = (\Gamma_3 - 1)/\Gamma_1\, \delta P/P|_{\mathrm{ad}}$ (dashed line with the label dT$_{\mathrm{ad}}$), as function of the logarithm of temperature, from the center to the surface of the star, for the fundamental radial mode of a $1.8\, M_\odot$ δ Scuti model.

For δ Scuti stars, the adiabatic and non-adiabatic eigenfunctions are extremely different in the superficial layers. We illustrate the results obtained for a 1.8 $M_\odot$ δ scuti model whose global characteristics are given in Table 4.16 (model 2), for the fundamental radial mode. In Figure 4.49, we compare the real part of the Lagrangian variation of the temperature $\delta T/T$ as computed by our non-adiabatic code (solid line with the label dT) to the adiabatic Lagrangian variation of the temperature (dashed line with the label dT$_{\mathrm{ad}}$) defined by Eq. (4.3).

The eigenfunctions are normalized in such a way that the relative radial displacement is equal to 1 at the photosphere. As usually, the adiabatic and non-adiabatic results are the same in the quasi-adiabatic region (from the center to $\log T \simeq 4.8$). On the contrary, from the driving region to the superficial layers, the two become totally different. The non-adiabatic computations give a very big bump of $\delta T/T$ in the H partial ionization zone (around $\log T \simeq 4.1$). The explanation of this phenomenon is the following. On one hand, we have a big bump of opacity in this region (Figure 4.41, top). On the other hand, the luminosity variation is controled by the equation of energy conservation and the small thermal relaxation time (Figure 4.41, bottom), imposing a flat behaviour of δL in this region (Figure 4.43, bottom). The balance between the the opacity variation $\delta\kappa/\kappa$ and the gradient of temperature variation $(\partial\, \delta T/\partial r)/(\mathrm{d}T/\mathrm{d}r)$

in the perturbed diffusion equation (Eq. (2.6)) leads to the δT bump of Figure 4.49. A more intuitive explanation is that the movement of the matter is very different from the movement of constant optical depth layers (significant Lagrangian variation of the optical depth), because of the significant opacity variations. Therefore, the huge temperature variation of these layers comes from the significant movement of the matter throughout the approximately constant $T(\tau)$ distribution.

4.3.5 Non-adiabatic eigenfunctions in the atmosphere of δ Scuti stars

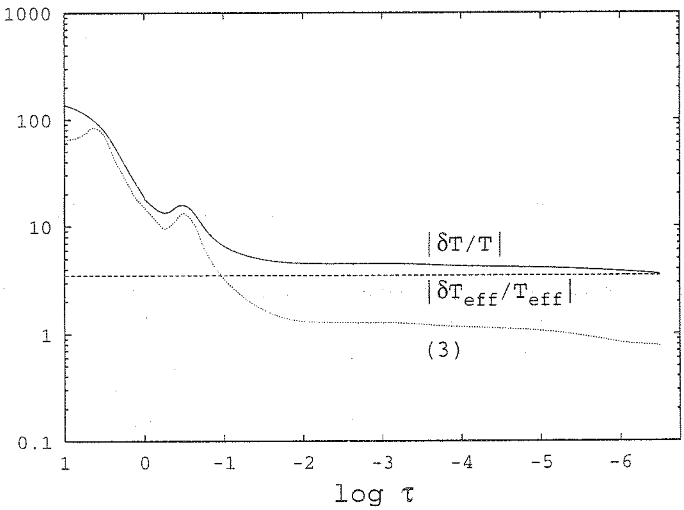

Figure 4.50: Amplitude of Lagrangian temperature variation $|\delta T/T|$ (solid line), amplitude of local effective temperature variation $f_T = |\delta T_{\rm eff}/T_{\rm eff}|$ (dashed line) and $|\partial \ln T/\partial \ln \tau \ (\delta\tau/\tau)|$ (dotted line with the label "(3)"), in the atmosphere of a 1.8 $M_\odot$ δ Scuti model. The y-axis is in a logarithmic scale.

Similarly to Sections 4.1.5 and 4.2.5, we illustrate now in Figure 4.50 some of the results obtained in the atmosphere of a typical δ Scuti star (same model and same mode as in Section 4.3.4). For δ Scuti stars, the presence of a thin superficial convection zone up to the photosphere does not give much latitude for the choice of the connecting layer between the interior and atmosphere specific treatments (Chapter 2). It has to be at the same time sufficiently deep, so that the diffusion approximation is valid beneath it, and it has to be out of the superficial convection zone, because our treatment of the transfer in the atmosphere is not adapted to the presence of a convection zone. The best compromise we found for δ Scuti stars was to put the connecting layer at $\log\tau = 0$. In Figure 4.50, the solid line is the graph of $|\delta T/T|$ in the atmosphere, we note that the y-scale is logarithmic. The smoothness of $|\delta T/T|$ at $\log\tau = 0$ confirms that our two specific treatments in the interior and in the atmosphere match well at the connecting layer. The dotted line with the label "(3)" is $|\partial \ln T/\partial \ln \tau \; (\delta\tau/\tau)|$ (third term of Eq. (2.32)). As for β cephei and SPB stars, this term is large, so that the Lagrangian variation of the temperature $\delta T/T$ and the variation of the temperature at constant optical depth are very different in the atmosphere. We see also that this term does not go to zero at the last layer, because of the significant values of $\partial \ln T/\partial \ln \tau$ in the outermost layers of the Kurucz atmosphere models. We note that the small bump of $|\delta T/T|$ around $\log \tau = -0.6$ comes from a similar bump of $\partial \ln T/\partial \ln \tau$ in the non-grey Kurucz atmosphere. In the same figure, the horizontal line is the amplitude of local effective temperature variation $f_T = |\delta T_{\rm eff}/T_{\rm eff}|$ (for a normalized relative radial displacement at the photosphere). $\delta T/T$ and $\delta T_{\rm eff}/T_{\rm eff}$ are very different at the photosphere. It is important to take this difference into account in the flux boundary conditions and in the photometric mode identification methods. For the sake of clarity, the terms $|\partial \ln T/\partial \ln g_{\rm e} \; \delta g_{\rm e}/g_{\rm e}|$ and $|\partial \ln T/\partial \ln T_{\rm eff} \; (\delta T_{\rm eff}/T_{\rm eff})|$ are not given in Figure 4.50, the first is close to zero and the second is close to $f_T = |\delta T_{\rm eff}/T_{\rm eff}|$.

4.3.6 Non-adiabatic photometric observables in δ scuti stars

As presented in Section 3.2, multi-colour photometric observations can be confronted to the theoretical predictions of our non-adiabatic code. We have shown that this confrontation can be used as a tool for mode identification. In this Section, we present the application of our method of photometric mode identification to δ Scuti stars.

An important specificity of δ Scuti stars, compared to β Cephei stars and SPBs is that, for the first, the observations show significant phase differences between the magnitude variations in different filters, as well as a phase-lag between the light-curve and the velocity-curve very different from the adiabatic 90°. As we will show, these phase-lags are also predicted by our non-adiabatic computations. They are very useful observables for the photometric mode identification methods and have to be taken into account (Garrido et al. 1990). They can also be used as a constraint on the models. We will see that the non-adiabatic phase-lags and amplitude ratios predicted by our non-adiabatic code are very sensitive to the characteristics of the thin superficial convection zone, so that a confrontation with the observations can constrain it and test the different theories of convection (mixing-length, FST, 3-D hydrodynamic simulations). So strong constraints could not be derived from the study of the pulsation frequencies alone. More precisely, the pulsation kinetic energy of the thin superficial convection zone is negligible compared to the total kinetic energy of the star. Therefore, the pulsation frequencies are very little affected by the physical characteristics of this zone. We term *non-adiabatic asteroseismology* the process of constraining the superficial regions of a star by confronting the predictions of a non-adiabatic code to the photometric observables (amplitude ratios and phases in different filters).

In Figure 4.51, we give the non-adiabatic effective temperature variations f_T (left) and phase-lags ψ_T (right) obtained for different modes of a $1.8\,M_\odot$ δ Scuti model with $\alpha = 1$ (Table 4.16, model 2), as function of the constant of pulsation Q in days. We refer to Eq. (1.2), for the definition of Q. Here, $Q = 0.0326$ days for the fundamental radial mode

(p_1) and $Q = 0.0103$ days for the mode ($\ell = 0$, p_8). The different symbols correspond to modes of different degrees ℓ ($0 \leq \ell \leq 4$). We see that, in good approximation, the amplitudes and phase-lags are independent of ℓ, for a given pulsation period. This is a usual result for p-modes pulsations, with dominating radial compression. We see also that the phase-lags ψ_T are very different from the adiabatic 180°. In Figure 4.52, we compare the values of f_T and ψ_T obtained for $1.8\,M_\odot$ models with different values of the mixing-length parameter α: $\alpha = 0.7$ (Table 4.16, model 1), $\alpha = 1$ (Table 4.16, model 2) and $\alpha = 1.5$ (Table 4.16, model 3). And in Figure 4.53, we make a similar comparison for $2\,M_\odot$ models with $\alpha = 0.5$ (Table 4.16, model 5), $\alpha = 1$ (Table 4.16, model 6) and $\alpha = 1.5$ (Table 4.16, model 7). We see that the non-adiabatic results (mainly the phase-lags) are very dependent on this parameter.

The origin of the strong dependence of the non-adiabatic results with respect to the mixing-length parameter α can be seen in Figure 4.54. In this figure, we give at the bottom the phase difference between the luminosity variation and the radial displacement $\psi_L = \psi(\delta L/L) - \psi(\xi_r/R)$, as function of the logarithm of temperature, for the fundamental radial mode of $1.8\,M_\odot$ models with three different values of α (same models as for Figure 4.52). At the top of Figure 4.54, we give the ratio between the radiative luminosity and the total luminosity L_{R}/L of the star for the same three models. We see that a first phase-lag between the luminosity variation and the displacement appears in the driving region (HeII partial ionization), at $\log T \simeq 4.6$. This phase-lag is independent of α, since no significant convection zone is present in this region. But a second phase-lag appears in the thin superficial convection zone (H partial ionization), which depends strongly on α. The larger is α, the larger is the size of this thin convection zone (Figure 4.54, top), which implies a more important phase-lag in this region. The significant change of phase of δL in this convection zone means that large transfers of energy and entropy variations are occuring, even in this region of very small thermal relaxation time (Figure 4.41), with a driving effect on the star depending on α (Figures 4.43 and 4.44). It is important to note that, contrary to the non-adiabatic amplitudes and phases, the evolution tracks (see Figure 4.42) as well as the pulsation frequencies are very little affected by the value of α. Therefore, it is only on the basis of non-adiabatic computations that precise constraints on the superficial convection zone of δ Scuti stars can be obtained.

δ Scuti stars with high amplitudes and a dominant radial mode are mainly observed in the upper part of the δ Scuti instability strip, corresponding to evolved stars with higher masses and lower gravities. For such stars, the multi-colour photometric observations are sufficiently precise, so that we adopted them for the confrontation between theory and observations. The observations we used here are from Garrido et al. (1990). We take two theoretical models of $2\,M_\odot$ with $\alpha = 0.5$ and $\alpha = 1.5$ as representative of these stars (Table 4.16, model 5 and model 7). In Figures 4.55 and 4.56, we give phase-amplitude diagrams for Strömgren filters, for the $2\,M_\odot$ δ Scuti models with $\alpha = 0.5$ and $\alpha = 1.5$ respectively. The top figures give violet versus yellow amplitude ratios (y-axis) and phase differences (x-axis). The bottom figures give temperature indicators: $b - y$ versus y amplitude ratios (y-axis) and phase differences (x-axis). In these figures, the different regions are for different degrees ℓ (solid line for $\ell = 0$, dashed line for $\ell = 1$, dotted line for $\ell = 2$ and dot-dashed line for $\ell = 3$). These regions correspond to the method of Garrido et al. (1990), where the degree of non-adiabaticity R and the phase-lag ψ_T are free parameters such that $0.25 \leq R \leq 1$ and $90^\circ \leq \psi_T \leq 135^\circ$. The circles correspond to our non-adiabatic theoretical predictions for modes of different degrees ℓ with periods close to the one of the fundamental radial mode. In order to obtain these results, the mode identification code of Garrido was improved, so that it can now take our non-adiabatic computations into account, following Eq. (3.28). The crosses correspond to observations of δ Scuti stars (Garrido et al. 1990). All these stars are identified as radial pulsators.

The difference between theory and observations (mainly for violet versus yellow indicators) can have many origins. A first source of uncertainty comes from the atmosphere models used by our non-adiabatic code and for the determination of the monochromatic flux and limb darkening derivatives used in Eq. (3.28). For the present simulations, we used the atmosphere models of Kurucz (1993). Two weak points of the Kurucz (1993) models are, on one hand, the treatment of the convection (mixing-length theory with a fixed value $\alpha \doteq 1.25$), and on the other hand, the small number of points of the mesh. These two weak points were recently improved by Heiter et al. (2002) and we intend to include these new atmosphere models in our non-adiabatic code, as well as in the photometric mode identification codes of Garrido and Heynderickx. A second source of uncertainty comes from the assumptions made in the derivation of the monochromatic magnitude variation (Eq. (3.28)). Two weak points are typically that we make the one-layer approximation (see Section 3.2.1) and that we neglect the rotation-pulsation interaction (see Daszyńska-Daszkiewicz et al. 2002). Finally, we recall that the convection-pulsation interaction is not taken into account in our present non-adiabatic code (frozen convection).

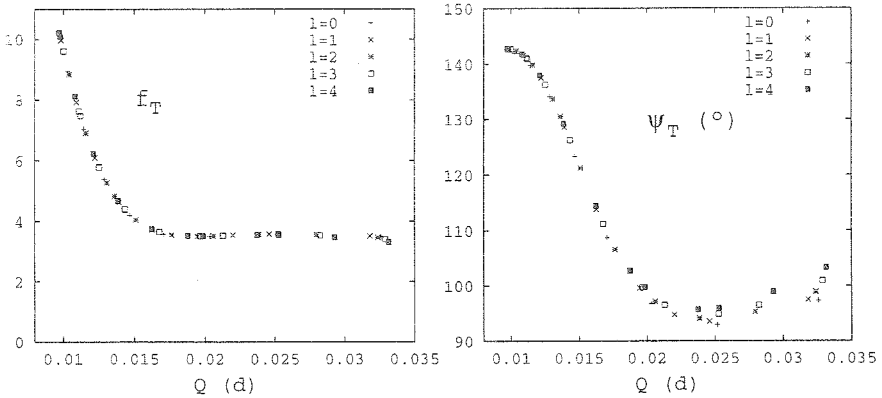

Figure 4.51: Non-adiabatic effective temperature variations and phase-lags for different modes of a $1.8\,M_\odot$ δ Scuti model with $\alpha = 1$ (Table 4.16, model 2). At the left: amplitude of local effective temperature variations $f_T = |\delta T_{\rm eff}/T_{\rm eff}|$, as function of the constant of pulsation Q in days. At the right: phase-lag ψ_T in degrees. The "+" are for $\ell = 0$ modes, the "×" for $\ell = 1$ modes, the asterisks for $\ell = 2$ modes, the "□" for $\ell = 3$ modes and the "■" for $\ell = 4$ modes.

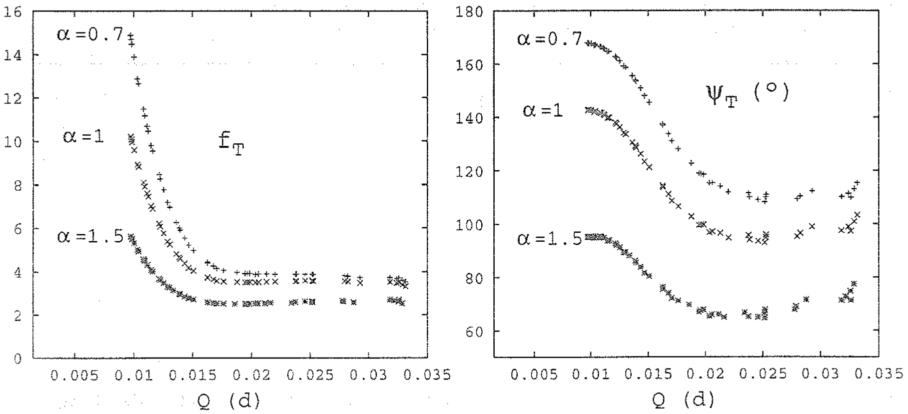

Figure 4.52: Non-adiabatic effective temperature variations f_T (left) and phase-lags ψ_T (right) for different modes ($0 \leq \ell \leq 4$) of $1.8\,M_\odot$ δ Scuti models with different values of α (0.7, 1 and 1.5). The "+" are for the model with $\alpha = 0.7$ (Table 4.16, model 1), the "×" for the model with $\alpha = 1$ (Table 4.16, model 2) and the asterisks for the model with $\alpha = 1.5$ (Table 4.16, model 3).

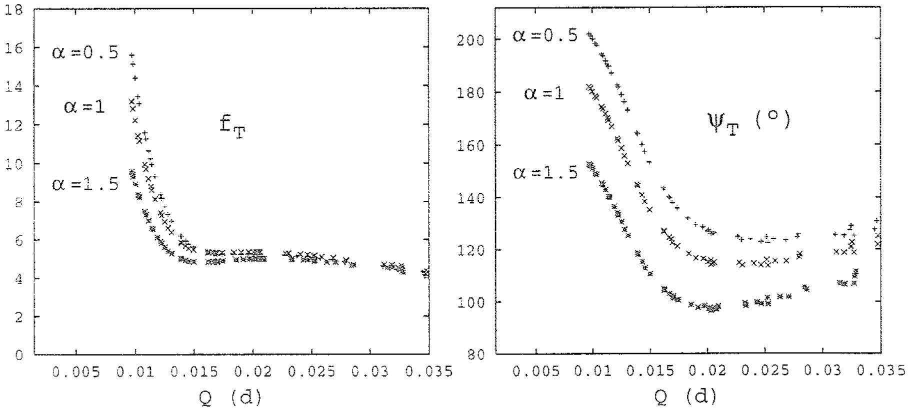

Figure 4.53: Non-adiabatic effective temperature variations f_T (left) and phase-lags ψ_T (right) for different modes of $2\,M_\odot$ δ Scuti models with different values of α (0.5, 1 and 1.5). The "+" are for the model with $\alpha = 0.5$ (Table 4.16, model 5), the "×" for the model with $\alpha = 1$ (Table 4.16, model 6) and the asterisks for the model with $\alpha = 1.5$ (Table 4.16, model 7).

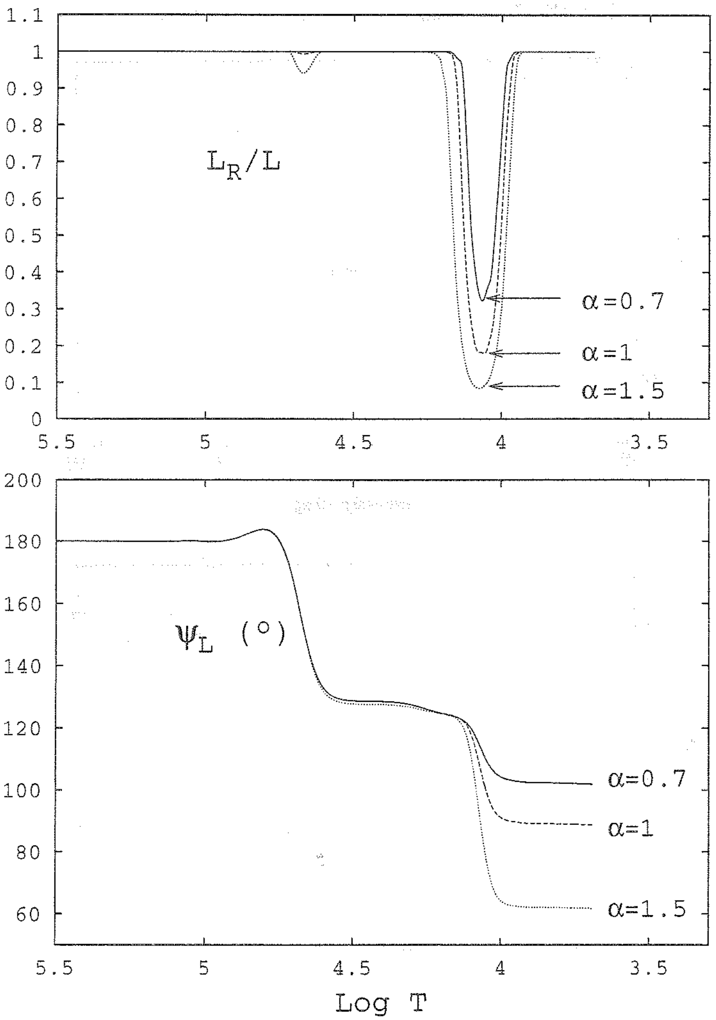

Figure 4.54: At the bottom: phase difference between the luminosity variation and the radial displacement $\psi_L = \psi(\delta L/L) - \psi(\xi_r/R)$, as function of the logarithm of temperature, for the fundamental radial mode of $1.8\,M_\odot$ models with three different values of α (solid line for $\alpha = 0.7$, dashed line for $\alpha = 1$ and dotted line for $\alpha = 1.5$). At the top: ratio between the radiative luminosity and the total luminosity of the star for the same three models.

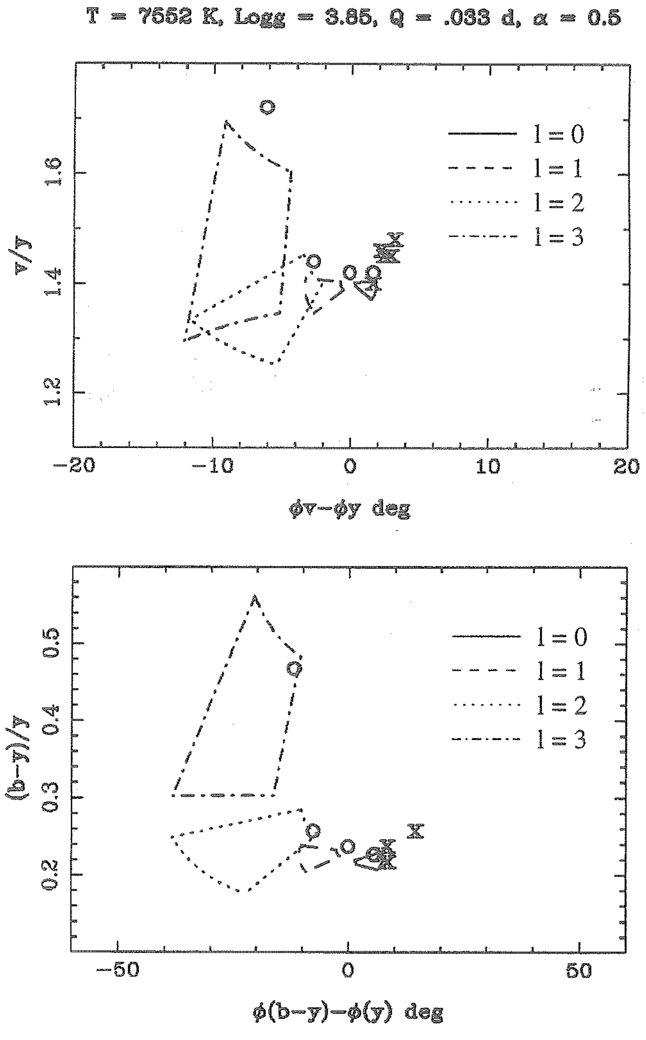

Figure 4.55: Phase-amplitude diagrams for Strömgren filters and for a $2\,M_\odot$ δ Scuti model with $\alpha = 0.5$ (Table 4.16, model 5). At the top: violet versus yellow amplitude ratios (y-axis) and phase differences (x-axis). At the bottom: temperature indicators, $b - y$ versus y amplitude ratios (y-axis) and phase differences (x-axis). The different regions are for different degrees ℓ, with R and ψ_T as free parameters (Garrido et al. 1990), the circles are our non-adiabatic predictions for a period close to the one of the fundamental radial mode and the crosses are the observations of δ Scuti stars identified as radial pulsators.

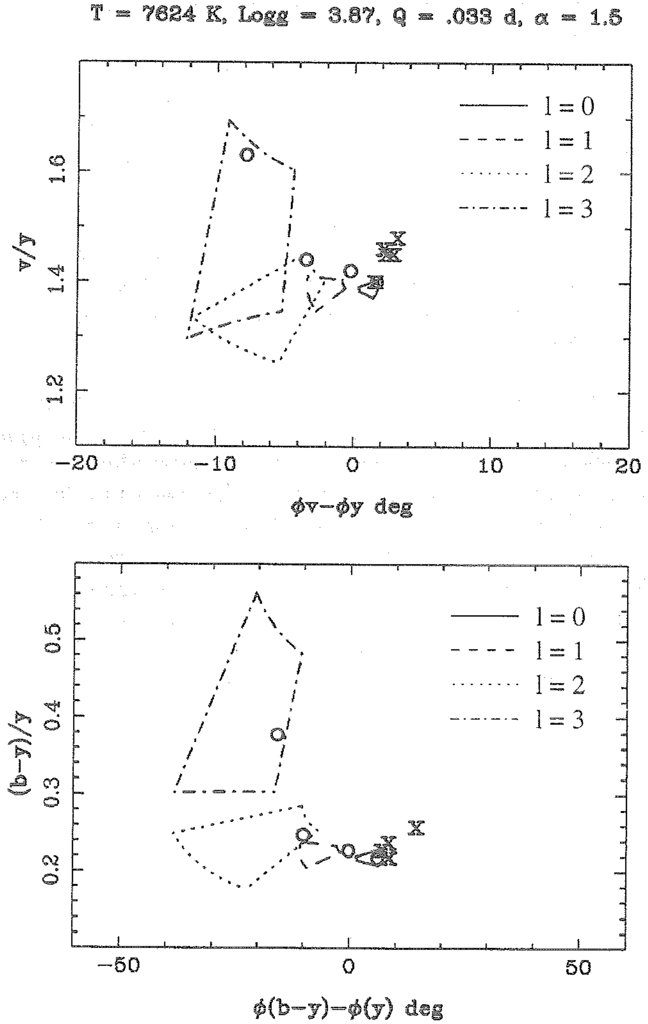

Figure 4.56: Same caption as in Figure 4.55, but for a $2\,M_{\odot}$ δ Scuti model with $\alpha = 1.5$ (Table 4.16, model 7).

4.3.7 The thin superficial convective zone

The real characteristics of the thin superficial convection zone of δ Scuti stars are badly known. The main problem is that this zone is so thin that the usual mixing-length theory (MLT) does not give an appropriate description of it. The basic assumption of the MLT is to assume that the mean free path of a convective element (MPCE) is $l = \alpha H_p$. However, in the very thin superficial convection zones of the δ Scuti stars, this hypothesis becomes questionable. This is evident at the view of Figure 4.58. At the top of this figure, we give the ratio between the radiative luminosity and the total luminosity as function of $x = r/R$, for the three $1.8\,M_\odot$ models with $\alpha = 0.7$, 1 and 1.5. As expected, the larger is α, the larger is the size of the thin superficial convection zone. But in the same figure, we give the intervals dx corresponding to the MPCE: $\mathrm{dx} = l/R = \alpha H_p/R$. It is striking to see that, in the three cases, the size of the convection zone is smaller than the MPCE ! The origin of this paradox is that the MLT is local and does not take the convection zone boundaries into account in the determination of the MPCE.

Another problem is the pulsation-convection interaction. As said before, we adopt a frozen convection approximation in our non-adiabatic treatment. This approximation is reasonably good when the mean life time of the convective elements τ_{conv} is longer than the period of pulsation, so that the dynamic of the convection has not the time to adapt to the physical changes due to the pulsation. Unfortunately, this is not the case in the thin superficial convection zone of δ Scuti stars, as illustrated at the bottom of Figure 4.58 where we give the values of τ_{conv} (in seconds) obtained for models with different α (the horizontal line is the period of the fundamental radial mode). Therefore, we can expect that the pulsation-convection interaction is not negligible in δ Scuti stars and could affect significantly the photometric amplitudes and phase-lags.

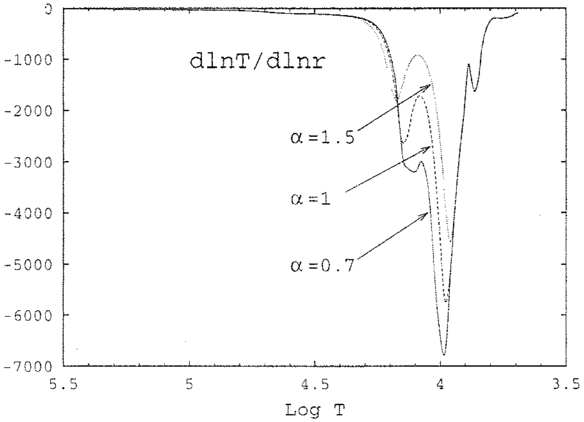

Figure 4.57: $\mathrm{d}\ln T/\mathrm{d}\ln r$ as function of the logarithm of temperature for $1.8\,M_\odot$ δ Scuti models with three different values of α (solid line for $\alpha = 0.7$, dashed line for $\alpha = 1$ and dotted line for $\alpha = 1.5$).

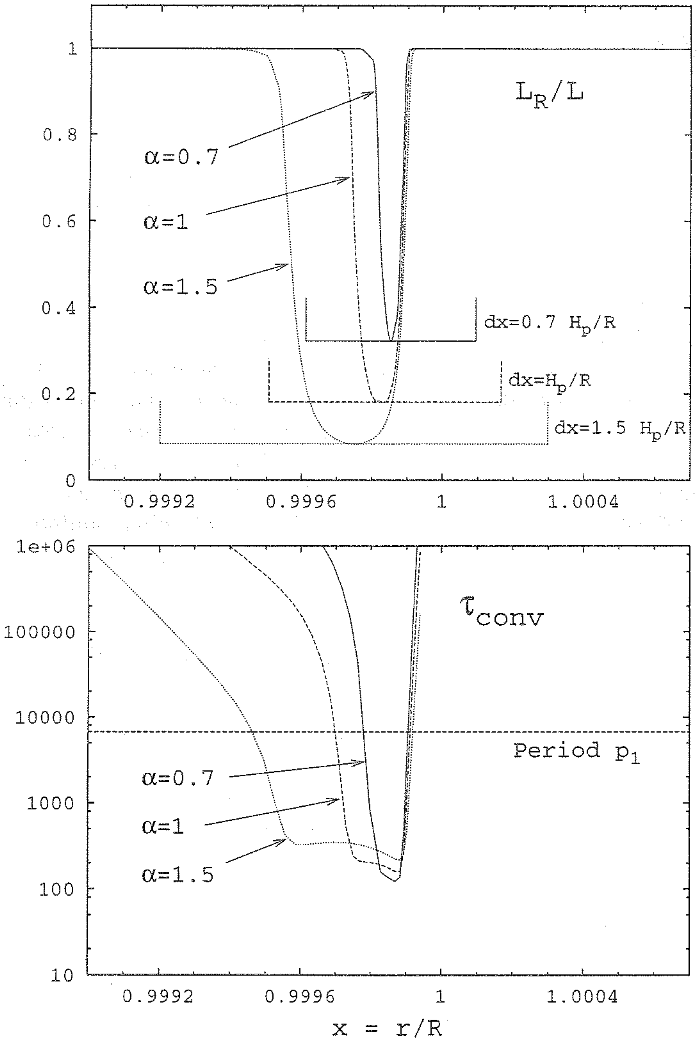

Figure 4.58: In the top panel, we give the ratio between the radiative luminosity and the total luminosity as function of $x = r/R$ for $1.8\,M_\odot$ δ Scuti models with three different values of α (solid line for $\alpha = 0.7$, dashed line for $\alpha = 1$ and dotted line for $\alpha = 1.5$). We give also the intervals $\mathrm{d}x = \alpha\, H_p/R$ corresponding to the mean free path of the convective elements in the MLT. In the bottom panel, we give the mean life time of the convective elements (in seconds) as predicted by the MLT for the same three models with different values of α. The horizontal line corresponds to the period of the fundamental radial mode.

4.4 γ Doradus stars

4.4.1 γ Doradus stars from an observational point of view

Just at the right and partially inside the instability strip of δ Scuti stars, a new class of variable stars has recently been discovered: the γ Doradus stars. The periods of the γ Dor stars are between 8 hours and 3 days, many of them are multiperiodic. The observed periods are not always stable (Kaye et al. 2000). They show periodic photometric variability as well as line profile variability. A typical amplitude in the Johnson V filter stays below 0.05 mag, and a typical amplitude of radial velocity is a few km/s. Long term campaigns have been carried out for the search of new γ Dor stars, such as the FlanSA γ Dor campaign (Eyer et al. 2002), moreover the use of the Hipparcos data base permitted to find numerous new candidates (Aerts et al. 1998, Handler 1999, Koen & Eyer 2002). The current number of *bona fide* γ Doradus stars is 30. Since the δ Scuti and γ Doradus instability strips overlap, searches of objects showing both δ Scuti short periods and γ Doradus long periods have been carried out. (Handler & Shobbrook 2002). The star HD 209295 shows clearly such an "hybrid" γ Dor / δ Scut behaviour (Handler, Balona et al. 2002), and other candidates for which the long periods are not observational artifacts have been found (Breger 2003).

4.4.2 γ Doradus stars from a theoretical point of view

γ Doradus stars remain a mystery, from the point of view of a theoretician. The position of these stars in the HR diagram points towards main sequence stars of typically 1.5 $M_\odot$ and $T_{\rm eff} \simeq 7000$ K. As for the δ Scuti stars, the γ Doradus stars have one central convection and one (or two) envelope convection zones, all the discussions in the next sections will concern the envelope convection zone. No doubt is left that, at least for some of them, the variability comes from real pulsation and not from travelling spots or binarity, for example the prototype star γ Doradus itself (Balona et al. 1996). The typical periods of the γ Doradus point towards high order gravity modes, as for the SPBs. Up to now, no generally accepted theoretical mechanism has been found, which explains the instability of the γ Doradus stars; Guzik et al. (2000) proposed a driving mechanism due to convective blocking (see Section 4.4.4).

4.4.3 Some observations and theoretical models

We chose the two γ Doradus stars HD 12901 and HD 48501 as reference for the applications presented in the next sections. Observations of these star with Geneva photometry were carried out by the team of C. Aerts with the old Swiss 0.7 m telescope at La Silla (Eyer & Aerts 2000). The analysis of 174 and 184 measurements for respectively HD 12901 and HD 48501, spread over 6566 and 7245 days was done by Aerts et al. (2003a). We present in Table 4.17 a summary of the observational results for these two stars. The calibrations by Künzli et al. (1997) were used for the estimation of $\log T_{\text{eff}}$ and $\log g$.

Table 4.17: $\log T_{\text{eff}}$, $\log g$, frequencies and Geneva photometric magnitude variations for the two γ Doradus stars HD 12901 and HD 48501 (Aerts et al. 2003a).

Frequency in cycles / day	Photometric magnitude variation in Geneva filters						
	δm_U	δm_{B_1}	δm_B	δm_{B_2}	δm_{V_1}	δm_V	δm_G
HD 12901	$\log T_{\text{eff}} = 3.85$		$\log g = 4.47$		$[M/H] = -0.4$		
$f_1 = 1.21562$	0.0140	0.0218	0.0204	0.0197	0.0150	0.0148	0.0135
$f_2 = 1.39594$	0.0062	0.0106	0.0106	0.0101	0.0078	0.0074	0.0066
$f_3 = 2.18637$	0.0058	0.0106	0.0106	0.0094	0.0080	0.0079	0.0074
HD 48501	$\log T_{\text{eff}} = 3.85$		$\log g = 4.49$		$[M/H] = -0.1$		
$f_1 = 1.09401$	0.0129	0.0186	0.0180	0.0167	0.0138	0.0134	0.0121
$f_2 = 1.29050$	0.0132	0.0192	0.0187	0.0183	0.0139	0.0135	0.0124
$f_3 = 1.19927$	0.0065	0.0093	0.0086	0.0082	0.0059	0.0065	0.0057

Table 4.18: Global characteristics of some γ Doradus models used in Section 4.4

Model 1		
$M/M_{\odot} = 1.5$	$T_{\text{eff}} = 7084\,\text{K}$	$\log(L/L_{\odot}) = 0.918$
$\log g = 4.05$	$R/R_{\odot} = 1.914$	age (Gy) = 1.74
$(X, Z) = (0.7, 0.013)$	$\alpha = 2$	no overshooting
Model 2		
$M/M_{\odot} = 1.5$	$T_{\text{eff}} = 7091\,\text{K}$	$\log(L/L_{\odot}) = 0.916$
$\log g = 4.05$	$R/R_{\odot} = 1.905$	age (Gy) = 1.71
$(X, Z) = (0.7, 0.013)$	$\alpha = 1.5$	no overshooting
Model 3		
$M/M_{\odot} = 1.5$	$T_{\text{eff}} = 7090\,\text{K}$	$\log(L/L_{\odot}) = 0.916$
$\log g = 4.05$	$R/R_{\odot} = 1.905$	age (Gy) = 1.71
$(X, Z) = (0.7, 0.013)$	$\alpha = 1$	no overshooting
Model 4		
$M/M_{\odot} = 1.5$	$T_{\text{eff}} = 7085\,\text{K}$	$\log(L/L_{\odot}) = 0.918$
$\log g = 4.05$	$R/R_{\odot} = 1.914$	age (Gy) = 1.74
$(X, Z) = (0.7, 0.013)$	$\alpha = 0.5$	no overshooting

We computed theoretical stellar models with different values of the mixing-length parameter α, close to the effective temperature and metallicity of HD 48501, with a mass of $1.5\,M_{\odot}$. We did not take the gravity measurement of this star into account because it is too high and corresponds to models below the ZAMS (see the discussion in Eyer et al. (2002)). The global characteristics of these models are given in Table 4.18.

4.4.4 Driving the gravity modes of γ Doradus stars

Contrary to the other stars of our study, the driving of γ Doradus high-order g-modes cannot be explained by a classical $\kappa - \gamma$ mechanism. More precisely, for these longer periods, the transition region where the thermal relaxation time is of the same order as the period of pulsation is situated deeper, between the HeII partial ionization zone and the very small metal opacity bump, where the κ mechanism is inefficient. Therefore, another driving mechanism has to be found. Guzik et al. (2000) explained the driving of γ Doradus stars as a convective blocking mechanism, where the luminosity is periodically blocked at the base of the envelope convection zone. For their computations, Guzik et al. used the non-adiabatic code of Pesnell (1990), in which the Lagrangian variation of the convective luminosity is set to zero during the pulsation cycle (frozen-in convection, see Eq. (2.7)). We confirm this result with our non-adiabatic computations and with the same way to freeze the convection. In Figure 4.59, we give the results obtained for the mode ($\ell = 1$, g_{26}) of a $1.5\,M_\odot$ model with $\alpha = 2$ (Table 4.18, model 1). The frequency of this mode is close to the observed main frequency of HD 48501. We see that, at the base of the convection zone, $-\mathrm{d}W/\mathrm{d}\log T$ is positive and W has a positive derivative, so that this region has a driving effect on the star. A significant decrease of the luminosity variation $|\delta L/L|$ at the base of the convection zone can be seen at the bottom of Figure 4.59 and is at the origin of this driving. This decrease of $|\delta L/L|$ comes from the quick decrease of L_R/L at the base of the convection zone (see Eq. (2.7) and the top of Figure 4.59). We note that our models have smaller metallicities than the models of Guzik et al. (2000). Therefore, this driving mechanism is not much dependent on the metallicity.

The driving is efficient when the envelope convection zone goes sufficiently deep, so that its base is close to the transition region. On the contrary, when the the convection zone is very small, it is no longer efficient. In order to illustrate this, we give in Figure 4.60 the results obtained for a model with $\alpha = 0.5$ (Table 4.18, model 4). For this model, the convective blocking is inefficient because the convection zone is situated in a region of too small heat capacity (see the flat behaviour of W and $|\delta L/L|$ in the outer layers). The convection can be frozen in different ways (freezing the variation of the convective flux, of the convective luminosity, of the divergence of the convective flux, ...) and Löffler (2003) showed that the convective blocking mechanism is not efficient for any kind of frozen convection approximation. More precisely, he showed that by neglecting the Lagrangian variation of the divergence of the convective flux instead of freezing the convective luminosity (as we and Guzik et al. (2002) do), the high-order g-modes of typical γ Doradus models are no longer unstable.

As conclusions, for models with a sufficiently deep envelope convection zone and by freezing the Lagrangian variation of the convective luminosity, we can explain the driving of the high-order g-modes of γ Doradus stars (see Figure 4.59 and Guzik et

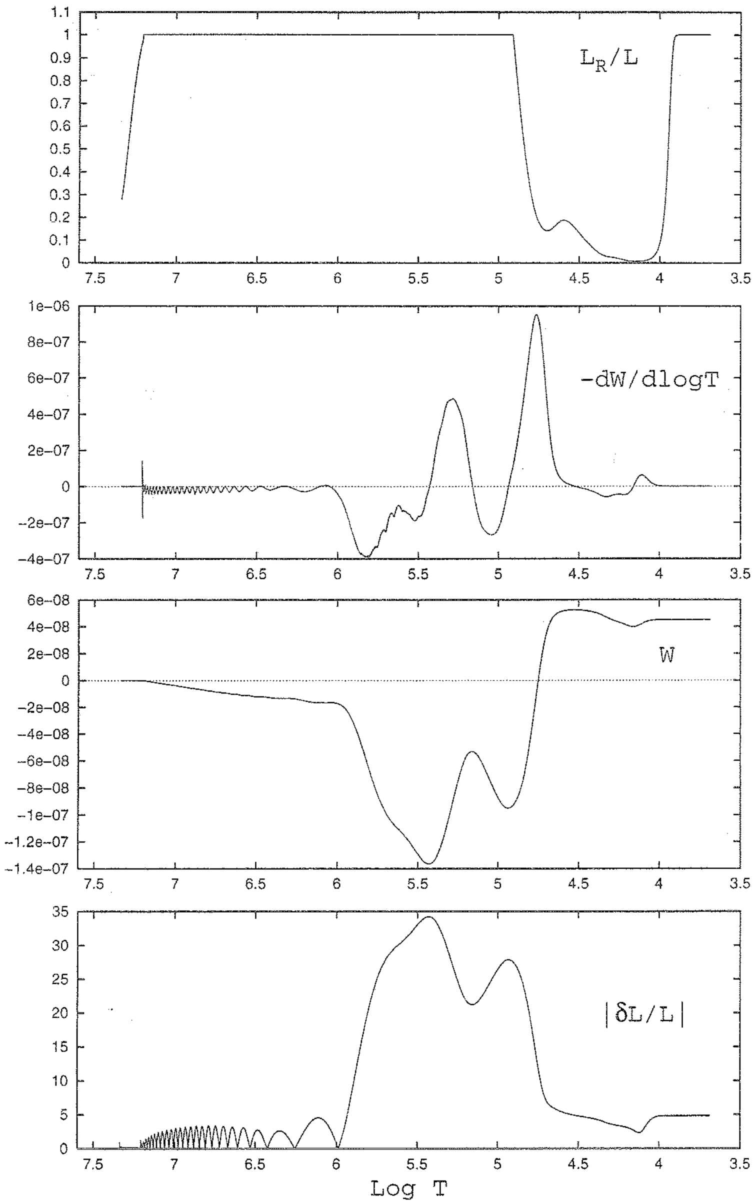

Figure 4.59: From top to bottom: ratio between the radiative luminosity and the total luminosity L_R/L (top), $-\mathrm{d}W/\mathrm{d}\log T$, dimensionless work integral W and amplitude of luminosity variation $|\delta L/L|$ (bottom), as function of the logarithm of temperature, for the mode ($\ell = 1$, g_{26}) of a $1.5\,M_\odot$ model with $\alpha = 2$ (Table 4.18, model 1).

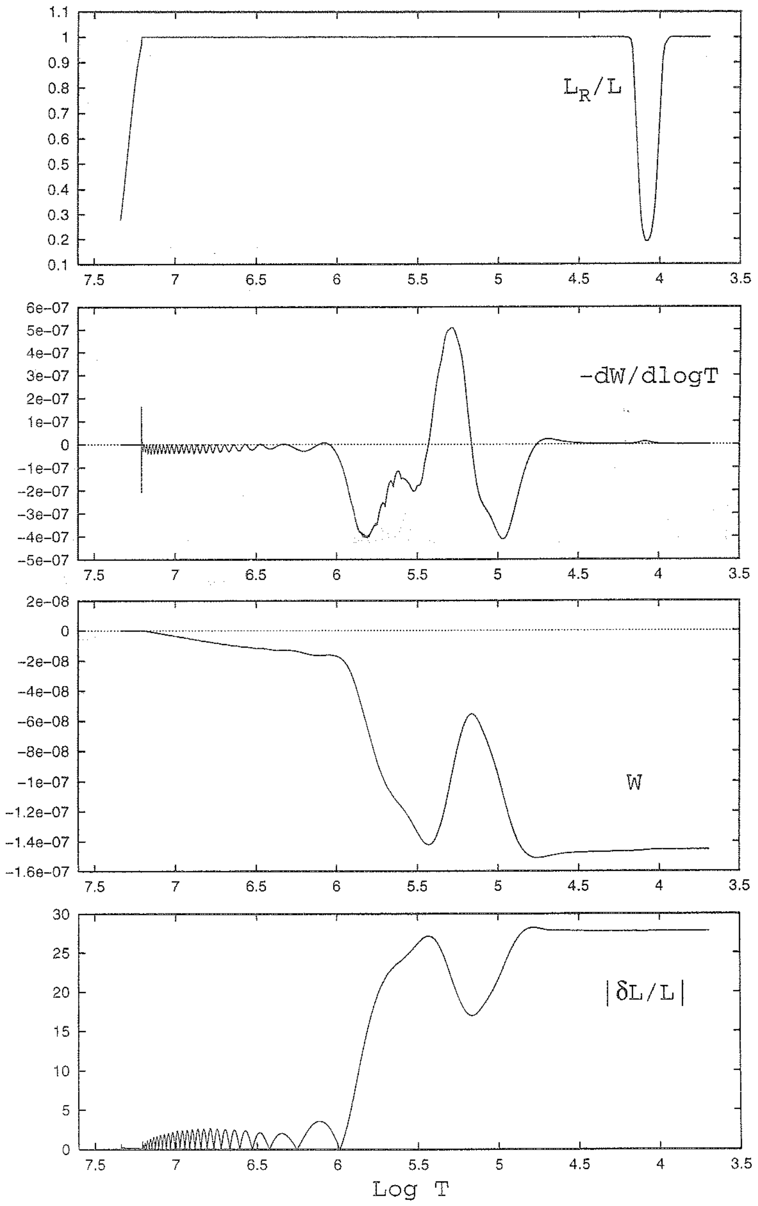

Figure 4.60: Same caption as Figure 4.59, for the mode ($\ell = 1$, g_{26}) of a 1.5 $M_\odot$ model with $\alpha = 0.5$ (Table 4.18, model 4).

al. (2000)). However, this driving mechanism is not efficient when the envelope convection zone is thin (Figure 4.60) and it depends on the adopted frozen convection approximation (Löffler 2003).

4.4.5 Non-adiabatic photometric observables in γ Doradus stars

We have presented in Table 4.17 the Geneva photometric amplitudes observed for the two γ Doradus stars HD 12901 and HD 48501 (Aerts et al. 2003a). These observations can be confronted to our theoretical predictions. We will concentrate on theoretical models of HD 48501 (Table 4.18). In Figures 4.61, 4.62, 4.63 and 4.64, we present the non-adiabatic effective temperature variations and phase-lags obtained for different models of HD 48501 with $\alpha = 2$, 1.5, 1 and 0.5 respectively (Table 4.18, models 1, 2, 3 and 4). We see that changing α gives totally different non-adiabatic results. The amplitudes of local effective temperature variations and the phase-lags are thus extremely dependent on the size of the envelope convection zone. This sensitivity is particularly dramatic for the phase-lags ψ_T: high values of α corresponding to a large envelope convection zone give phase-lags close to $-180°$ (Figure 4.61, right) and low values of α corresponding to a small envelope convection zone give phase-lags close to 0° (Figure 4.64, right) !

The very strong dependence of the non-adiabatic results on the size of the envelope convection zone is explained in Figure 4.65. In this figure, we give the ratio between the radiative luminosity and the total luminosity L_R/L (top), the real part of the luminosity variation $\Re\{\delta L/L\}$ (middle) and the phase difference between the luminosity variation and the radial displacement $\psi_L = \psi(\delta L/L) - \psi(\xi_r/R)$ (bottom) as function of the logarithm of temperature for the same γ Doradus models as previously (Table 4.18, models 1, 2, 3 and 4), and for the mode ($\ell = 1$, g_{26}) with theoretical frequency closest to the dominant frequency of HD 48501. For the real part of the luminosity variation, we did not use the usual normalization, but the radial displacement was normalized to -1 at $\log T = 5.7$, so that the results are identical in the quasi-adiabatic region (from the center to $\log T \simeq 5$). We see that, for high values of α and thus for a deeper convection zone, the luminosity variation is blocked at the base of the convection zone. This blocking is so efficient for the model with $\alpha = 2$ that a node is present in the real part of the luminosity variation, at $\log T \simeq 4.7$ (Figure 4.65, middle), which explains the phase ψ_L close to $-180°$ (Figure 4.65, bottom). On the contrary, for low values of α, the envelope convection zone is very thin, the heat capacity of this region is very small and the luminosity variation is not much affected by the convection, so that the phase ψ_L remains close to the adiabatic 0°.

In Figures 4.59 to 4.65, we have illustrated the influence of the size of the envelope convection zone on the non-adiabatic results by changing the mixing length parameter α; we note that we found exactly the same sensitivity to the size of the convection zone by comparing the results obtained for models with different effective temperatures. In Figure 4.66, we compare the theoretical and observed amplitude ratios obtained with Geneva photometry for HD 48501. The four figures correspond to the four models with $\alpha = 2$ (top, left), $\alpha = 1.5$ (top, right), $\alpha = 1$ (bottom, left) and $\alpha = 0.5$ (bottom, right). The "+", "×" and "⊡" correspond to the observed amplitude ratios of the 3 frequencies f_1, f_2 and f_3. The lines correspond to our non-adiabatic theoretical predictions for modes of different degrees ℓ with theoretical frequency closest to the observed frequency f_1 (solid line for $\ell = 1$, dashed line for $\ell = 2$ and dotted line for $\ell = 3$). We see in Figure 4.66 that none of the theoretical models can reproduce the observations. We see also in this figure that the theoretical amplitude ratios (mainly for $\ell = 1$) are very little affected by changes of α, although the non-adiabatic quantities f_T and ψ_T are extremely dependent on it (Figures 4.61, 4.62, 4.63 and 4.64). The explanation is that the geometrical distorsion term is zero for $\ell = 1$ modes and the gravity term is very small for high-order g-modes, so that the term associated to the effective temperature variation is dominating in Eq. (3.28). Therefore, the f_T and ψ_T dependences vanish in the amplitude ratios which reflect essentially ratios of the monochromatic flux derivatives $\alpha_{T\lambda}$ (Eq. (3.10)).

Because none of our theoretical models could reproduce the observations (Figure 4.66), we decided to let f_T as a free parameter and searched for the values leading to the best agreement with the observations. For the other parameters, we took $\psi_T = 0°$ (no phase differences are observed between different filters) and $f_g = 2 + K^{-1}$ (Eq. (3.40)). The results obtained are presented in Figure 4.67 and they are very surprising. In this figure, the "+", "×" and "⊡" correspond to the observed amplitude ratios of the 3 frequencies and the lines are the theoretical predictions for the values of ℓ (1) and f_T which best fit the observations. On one hand, the degree is identified without any doubt as $\ell = 1$ (the other values of ℓ cannot fit the observations, whatever the value of f_T). On the other hand, the values of f_T which fit the observations are extremely low: $f_T = 0.14$ (solid line), $f_T = 0.17$ (dashed line) and $f_T = 0.22$ (dotted line) ! So low values of f_T are very hardly explained by classical g-mode pulsation. More precisely, for high-order g-modes, high density variations and thus high temperature variations are expected for a normalized radial displacement at the photosphere, because of the dominating transversal compression; and low gravity variations are expected because of the low radial displacement and acceleration of the matter. On the contrary, the low values of f_T given above would correspond to a physical phenomenon where the gravity variations are dominating. Significant gravity darkenings are typically encountered in close binary systems where the two components affect each other by tidal effects (Willems & Aerts 2002, Claret & Willems 2002). Unfortunately, these stars are not close binaries (Aerts, private communication). Further investigations would be necessary in order to determine what is really happening in HD 48501. We did not present here the results obtained for HD 12901. They are very similar to the ones obtained for HD 48501: our theoretical models do not succeed to reproduce the observed amplitude ratios, the values found for f_T when it is let as a free parameter are also very low and all the frequencies are identified as $\ell = 1$ modes. Therefore, our conclusions are the same for this star.

We note finally that multi-colour photometric observations can be used as a test of the driving mechanism of γ Doradus stars. More precisely, both the theoretical photometric magnitude variations and the driving mechanism can be determined by non-adiabatic computations. For a simple reason of consistency, the same non-adiabatic computations would have thus to explain at the same time the photometric amplitude ratios and the driving of the modes. For the stars HD 48501 and HD 12901, the confrontation between the theoretical and observed amplitude ratios was not successful, so that we could hardly consider these observations as high-order g-modes driven by the convective blocking at the base of the envelope convection zone.

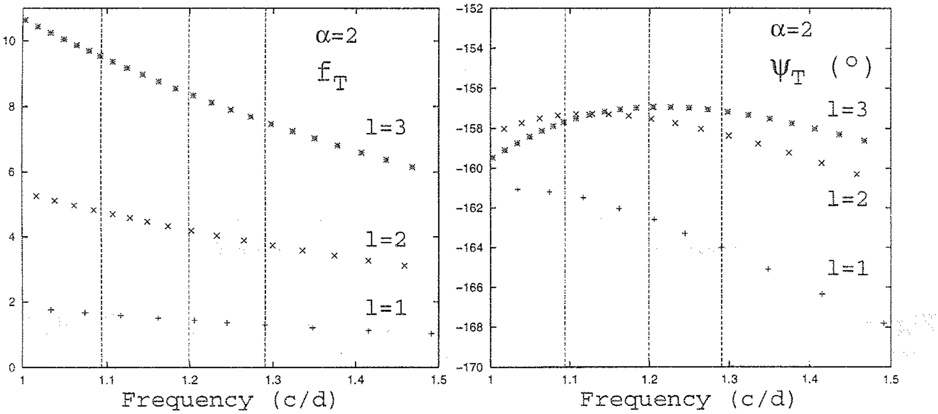

Figure 4.61: Same caption as in Figure 4.62, but for a model with $\alpha = 2$ (Table 4.18, model 1).

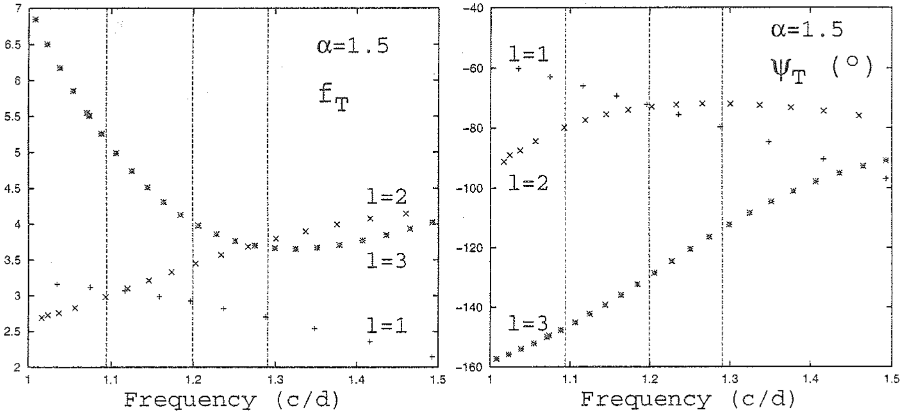

Figure 4.62: Non-adiabatic effective temperature variations and phase-lags for different modes of a $1.5\,M_\odot$ model with $\alpha = 1.5$ (Table 4.18, model 2). At the left: amplitude of local effective temperature variations $f_T = |\delta T_{\rm eff}/T_{\rm eff}|$ (normalized radial displacement at the photosphere), as function of the pulsation frequency in cycles/day. At the right: phase-lag ψ_T in degrees. The "+" are for $\ell = 1$ modes, the "×" for $\ell = 2$ modes and the asterisks for $\ell = 3$ modes. The three vertical lines correspond to the three observed frequencies of the γ Doradus star HD 48501.

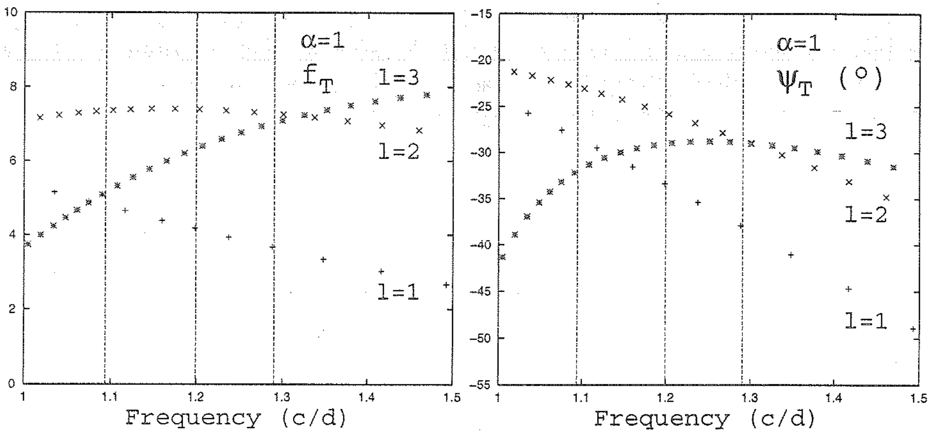

Figure 4.63: Same caption as in Figure 4.64, but for a model with $\alpha = 1$ (Table 4.18, model 3).

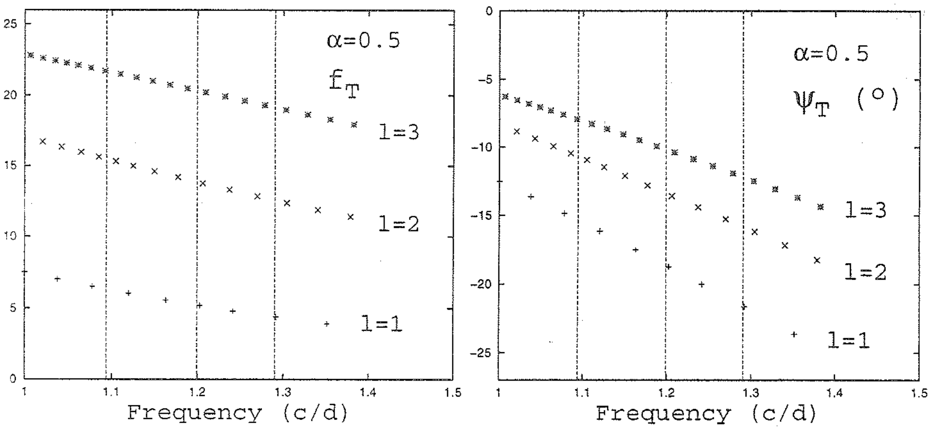

Figure 4.64: Non-adiabatic effective temperature variations and phase-lags for different modes of a $1.5\,M_\odot$ model with $\alpha = 0.5$ (Table 4.18, model 4). At the left: amplitude of local effective temperature variations $f_T = |\delta T_{\rm eff}/T_{\rm eff}|$ (normalized radial displacement at the photosphere), as function of the pulsation frequency in cycles/day. At the right: phase-lag ψ_T in degrees. The "+" are for $\ell = 1$ modes, the "×" for $\ell = 2$ modes and the asterisks for $\ell = 3$ modes. The three vertical lines correspond to the three observed frequencies of the γ Doradus star HD 48501.

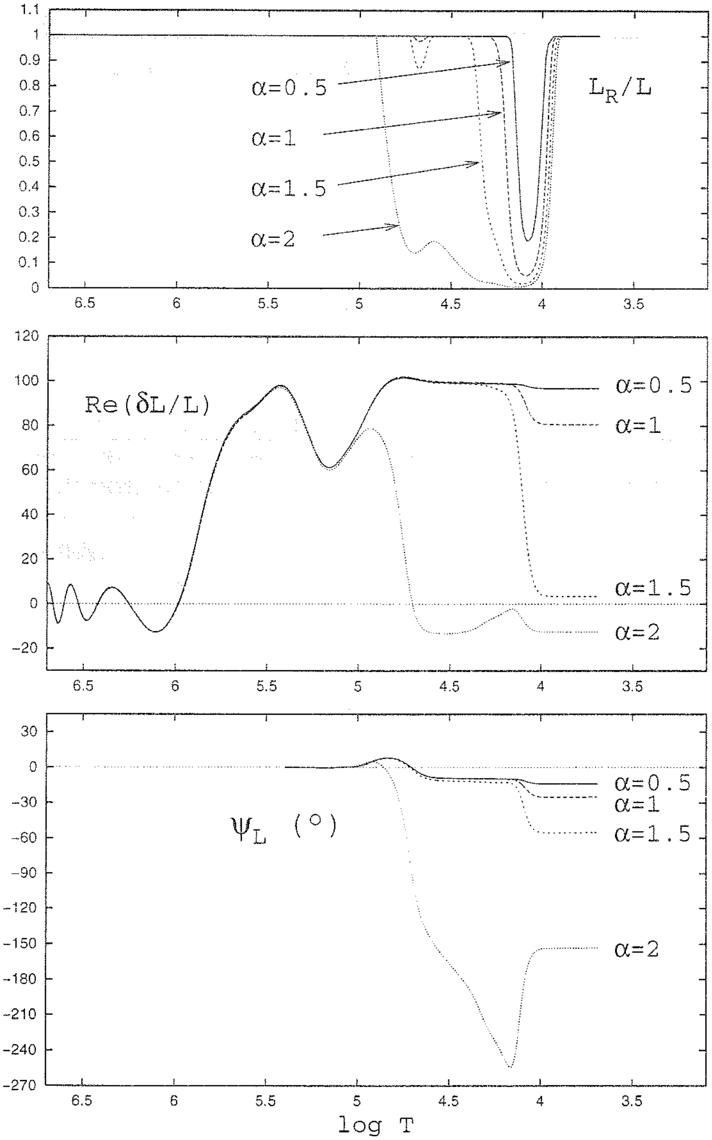

Figure 4.65: Ratio between the radiative luminosity and the total luminosity L_R/L (top), real part of the luminosity variation $\Re\{\delta L/L\}$ (middle) and phase difference between the luminosity variation and the radial displacement $\psi_L = \psi(\delta L/L) - \psi(\xi_r/R)$ (bottom) as function of the logarithm of temperature for γ Doradus models with 4 different values of α (Table 4.18, models 1, 2, 3 and 4), and for the mode ($\ell = 1$, g_{26}) with theoretical frequency closest to the dominant frequency of HD 48501.

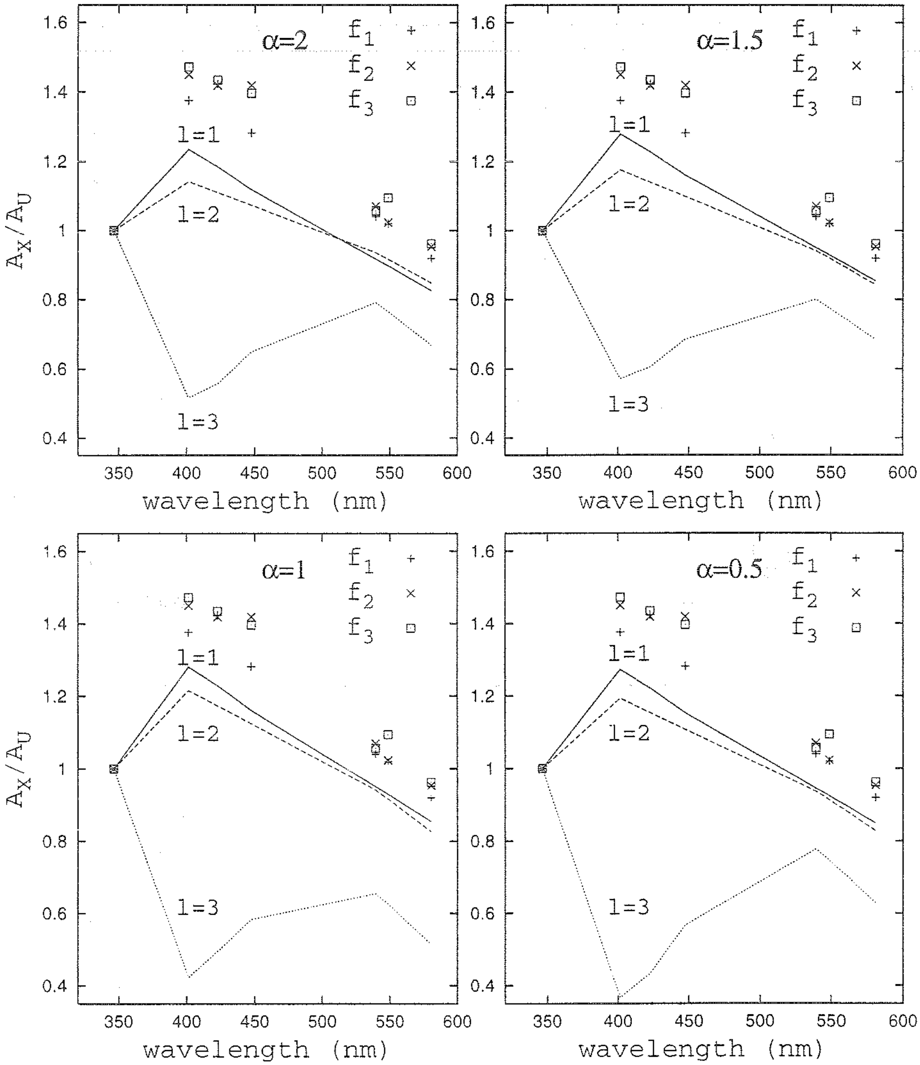

Figure 4.66: Theoretical and observed amplitude ratios obtained with Geneva photometry for the γ Doradus star HD 48501. The four figures correspond to the four models with $\alpha = 2$ (top, left), $\alpha = 1.5$ (top, right), $\alpha = 1$ (bottom, left) and $\alpha = 0.5$ (bottom, right). The "+", "×" and "□" correspond to the observed amplitude ratios of the 3 frequencies $f_1 = 1.09401\,\mathrm{c\,d^{-1}}$, $f_2 = 1.29050\,\mathrm{c\,d^{-1}}$ and $f_3 = 1.19927\,\mathrm{c\,d^{-1}}$, respectively. The lines correspond to our non-adiabatic theoretical predictions for modes of different degrees ℓ with theoretical frequency closest to the observed frequency f_1 (solid line for $\ell = 1$, dashed line for $\ell = 2$ and dotted line for $\ell = 3$).

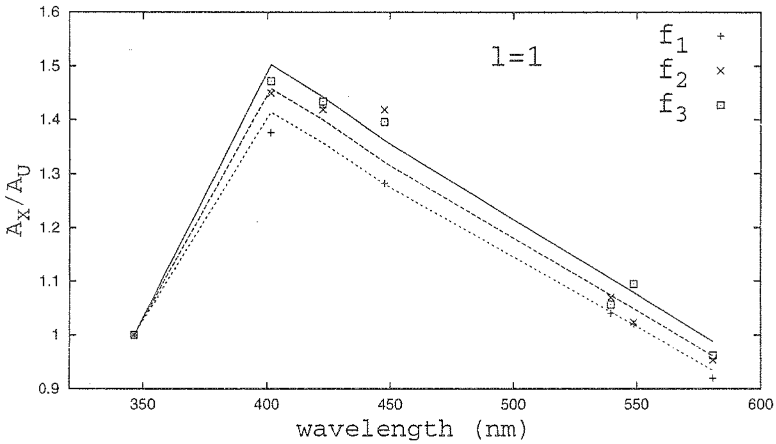

Figure 4.67: Observed Geneva photometric amplitude ratios for the 3 frequencies of the γ Doradus star HD 48501 ("+", "×" and "⊡"). The lines are the theoretical amplitude ratios for a mode of degree $\ell = 1$, with 3 values of f_T considered as a free parameter: $f_T = 0.14$ (solid line), $f_T = 0.17$ (dashed line) and $f_T = 0.22$ (dotted line).

Chapter 5

Conclusions and future prospects

5.1 Conclusions

In the frame of our thesis, we have written a code which computes the non-radial non-adiabatic oscillations of stellar models. This code is very useful in the frame of asteroseismology (see Chapter 3):

- It is able to determine very precisely the driving mechanisms at the origin of stellar pulsations.
- It can be used as a tool for photometric mode identification. Moreover, it can be used to constrain stellar interiors and atmospheres, by searching for the best fit between the theoretical and observed photometric amplitude ratios and phase-lags, a procedure we term *non-adiabatic asteroseismology.*
- Finally, it can be used to determine the influence of temperature variations on the line-profile variations due to stellar pulsations.

The main specificity of our non-adiabatic code is the special care given to the treatment of the pulsation in the stellar atmosphere (see Section 2.3). In comparison with non-adiabatic codes without such atmospheric treatment, its theoretical predictions are thus more precise in the superficial layers, opening the way to a better confrontation with photospheric observables (photometric amplitude ratios and phases) and spectroscopic observables (line-profile variations).

The numerical method of solution has not been presented here and we refer to the original text for more details (see the prefatory note at the beginning of this book). As a summary, for the resolution of the problem, we have adopted a finite difference method. We took a two grids interlaced mesh and the discretization was chosen such that the system of difference equations is intrinsically compatible with the integral expressions for the eigenvalues, which improves significantly the precision and the stability of our numerical method. A generalized inverse iteration algorithm permits then to converge very quickly towards the solution (eigenfunctions and eigenvalues).

We have applied our non-adiabatic code to the study of four types of near-main sequence variable stars.

β Cephei stars

The application of our non-adiabatic code to β Cephei stars shows firstly the mechanism at the origin of their pulsation: it is a κ-mechanism associated to the opacity bump in the partial ionization zone of iron, at temperatures around 200 000 K. The periods of the unstable modes predicted by our non-adiabatic code are in agreement with the typical observed periods of β Cephei stars. Secondly, we have performed a deep theoretical study of the photometric variations of the star 16 Lacertae. On one hand, we could identify the degrees ℓ of the three observed modes. On the other hand, by searching for the model which best fits the observations, we could constrain the metallicity of this star, finding that it is slightly smaller than the solar metallicity ($Z \simeq 0.015$). Thirdly, we have studied the influence of non-adiabatic temperature variations on the line-profile variations of the Si^{2+} triplet (456.784 nm) for different modes of a typical β Cephei model. Our conclusion is that the the non-adiabatic temperature and gravity variations have very small effect on the line-profile variations compared to the influence of the velocity field, so that spectroscopic mode identification methods which do not take these non-adiabatic effects into account (e.g. the moment method) can be used for β Cephei stars.

Slowly Pulsating B stars

Similarly to the β Cephei stars, our non-adiabatic code shows that the mechanism at the origin of the pulsations of Slowly Pulsating B stars (SPBs) is a κ-mechanism associated to the opacity bump in the partial ionization zone of iron. The periods of the unstable high-order g-modes predicted by our non-adiabatic code are in agreement with the typical observed periods of SPBs. Secondly, we have applied our non-adiabatic code to the study of 11 SPBs observed by De Cat (2001). More precisely, we computed specific theoretical models, we performed non-adiabatic computations and we have identified the degree ℓ of the dominant modes, for each of these stars. Thirdly, we have studied the influence of non-adiabatic temperature variations on the line-profile variations of the Si^{+} doublet (412.81 nm) for different high-order g-modes of a typical SPB model. Our conclusion is the same as for β Cephei stars: the non-adiabatic temperature and gravity variations have very small effect on the line-profile variations compared to the influence of the velocity field, so that spectroscopic mode identification methods which do not take these non-adiabatic effects into account can be used for SPBs.

δ Scuti stars

Firstly, our non-adiabatic code shows clearly the mechanism at the origin of the pulsations of δ Scuti stars. It is the well known κ-γ mechanism associated to the opacity bump and the depletion of Γ_1 and Γ_3 in the second partial ionization zone of helium. The same mechanism explains the instability of all the variable stars of the classical instability strip (classical Cepheids, RR Lyrae, ...). Secondly, we have applied our non-adiabatic code to the study of the multi-colour photometric variations of δ Scuti stars. Our non-adiabatic results, and thus the photometric amplitude ratios and phases, are very sensitive to the characteristics of the very thin superficial convection zone. Therefore, this not well known zone can be constrained by an adequate confrontation between theory and observations.

γ Doradus stars

We have applied also our non-adiabatic code to the study of γ Doradus stars. We have found (in agreement with Guzik et al. 2000) that, if the superficial convection zone goes sufficiently deep, the driving of high-order g-modes can be explained by the convective blocking at the base of this zone. However, the validity of the frozen convection approximation is not evident for these stars, and we are not sure that the "real" convective envelope has the required size. We performed non-adiabatic computations for models with different sizes of the convective envelope and it appears that the growth or damping rates, the amplitudes and the phases of effective temperature variations are extremely dependent on the characteristics of this convection zone. However, none of our theoretical results could reproduce accurately the photometric amplitude ratios observed for the γ Doradus stars HD 48501 and HD 12901 by the team of Prof. Aerts. We conclude that the variability of γ Doradus stars remains a mystery for the theoreticians.

5.2 Future prospects

Our main future prospects are to include a better treatment of the interaction of stellar pulsation with rotation and with convection in our non-adiabatic code, and to include better atmosphere models in our non-adiabatic code, in the Code Liégeois d'Évolution Stellaire (CLÉS) and in the photometric mode identification code.

5.2.1 Influence of rotation

Our treatment is admissible for slow or moderate rotators. However, in fast rotators, the effect of rotation on the dynamic of stellar pulsation appears throughout the two well known fictive forces: the centrifugal force which affects the equilibrium configuration as well as the pulsation, and the Coriolis force which can play a significant role in the equation of momentum conservation. There are two different approaches for the treatment of the pulsation-rotation interaction.

Firstly, we can treat it in a perturbative way based on Taylor developments in (Ω/σ), where Ω is the angular frequency of rotation and σ is the angular frequency of pulsation. This approach was initially derived by Cowling (1949) and Ledoux (1951), by keeping only the first order terms in (Ω/σ). This theory predicts the well know equidistant rotational splitting of frequencies, which gives for a uniform rotation:

$$\sigma_{n\ell m} = \sigma_{n\ell 0} - m\,(1 - C_{n\ell})\,\Omega\,, \tag{5.1}$$

where $C_{n\ell}$ is called the Ledoux's constant. The perturbative approach has been developed up to the second order (Lee & Baraffe 1995) and to the third order (Soufi et al. 1998). In these cases, the rotation induces a coupling between the spheroidal modes. Daszyńska et al. (2002) showed recently that this coupling can affect significantly the photometric observables for fast rotators. Therefore, it is necessary to take it into account in the photometric mode identification for fast rotators.

Secondly, non-perturbative theories of the rotation-pulsation interaction have been developed. In Unno et al. (1989 §34), Lee & Saio derived a method based on the "traditional approximation", where the Coriolis force associated with radial motion and the radial component of the Coriolis force associated with horizontal motion are neglected. Under the adiabatic approximation, the Cowling approximation and the traditional approximation, the problem is much simplified and all the derivatives with respect to the angular coordinates appear under one single operator. By computing the eigenfunctions $(\tilde{Y}_{\ell_j}^m(\theta,\phi))$ and eigenvalues $(\lambda_{\ell_j}^m)$ of this operator, we obtain an infinite family of functions for which the problem is uncoupled (in the absence of rotation this operator is the Legendre operator $\mathcal{L}^2$, its eigenfunctions are the spherical harmonics and its eigenvalues are $\ell(\ell+1)$). With this procedure, the final system of differential equations is very similar to the problem without rotation (we just have to replace $\ell(\ell+1)$ by $\lambda_{\ell_j}^m$ in the equation of mass conservation). The problem is that this procedure is no longer valid if we do not make the adiabatic, Cowling or traditional approximations, because the derivatives with respect to the angular coordinates no longer appear under one single operator. Townsend (1997) used this treatment for the determination of the velocity field and the line-profile variations of fast rotators and implemented it in the codes BRUCE and KYLIE. Another non-perturbative treatment has been proposed by Dintrans & Rieutord (2000). This treatment is based on the anelastic approximation and the integration of the characteristics of the mixed-type operator.

We conclude that the problem of the rotation-pulsation interaction is far from being completely solved. Since the spectroscopic and photometric observables can be significantly affected by fast rotation, it is useful to study this problem in more details and include it in our treatment, which is one of our main prospects for the future.

5.2.2 Influence of the convection envelope

Another difficult problem is the interaction between convection and pulsation. For hot stars such as β Cephei stars and SPBs, there is no convective envelope, so that we do not have to care about this problem. For colder stars with a convective envelope, the complexity of the convection-pulsation interaction is often avoided by freezing the convection (as we did until now in our non-adiabatic treatment). This approximation is admissible only if the mean life time of the convective elements is much longer than the pulsation periods. We remark however that there are different ways to freeze the convection, which can lead to different results. In solar-type stars, a large convective envelope is present and the convection-pulsation interaction plays a major role in their excitation. This mechanism is called the stochastic excitation, where the oscillations are forced stochastically by the acoustical energy generation coming from the turbulent convection (Houdek et al. 1999). Even for pulsating stars with a very thin superficial convection zone (δ Scuti and γ Doradus stars), we showed that the characteristics of this zone have a significant influence on the non-adiabatic photometric observables. As shown in the bottom of Figure 4.58, the validity of the frozen convection approximation is questionable in the thin superficial convection zone of δ Scuti stars, because the mean life time of the convective elements predicted by the mixing-length theory (MLT) is smaller than the period of the fundamental radial mode. Moreover, the validity of the MLT itself is questionable for δ Scuti stars because, as illustrated in the top of Figure 4.58, the size of the thin superficial convection zone is smaller than the mean free path of the convective elements predicted by the MLT. Therefore, progress has to be done in the modelling of this zone and in the treatment of its interaction with pulsation. In this frame, the confrontation with photometric observables (amplitude ratios and phase-lags) would permit to discriminate between different theories of convection (MLT, FST (Canuto & Mazzitelli), 3D hydrodynamic simulations) and different treatments of the convection-pulsation interaction. We intend also to work on this difficult field in the future.

5.2.3 Atmosphere models

Finally, constraints on the atmosphere models can also be derived from the study of the photometric amplitudes and phase-lags due to stellar pulsation. As can be seen in Eq. (3.28), the photometric amplitudes and phase-lags depend on the atmosphere models throughout the derivatives of the monochromatic flux ($\alpha_{T\lambda}$ and $\alpha_{g\lambda}$) and throughout the integrals of the monochromatic limb-darkening law (times the Legendre polynomials) and its derivatives ($b_{\ell\lambda}$, $\beta_{T\lambda}$ and $\beta_{g\lambda}$). Firstly concerning the limb-darkening law, we note that an improved non-linear limb darkening law has been recently proposed by Claret (2000). Secondly, new atmosphere models have been recently computed by Heiter et al. (2002), including different treatments of the convection and increasing significantly the number of points of the grids. We intend to include these atmosphere models in our non-adiabatic code, in the Code Liégeois d'Évolution Stellaire (CLÉS) and in the photometric mode identification code of Garrido. By confronting the results obtained to observed photometric amplitude ratios and phase-lags, we could determine the models (and thus the treatment of the convection) which best fit the observations. Since these atmosphere models are already computed, their inclusion in the different codes would be the easiest step of our future prospects.

References

Achmad, L., de Jager, C., Nieuwenhuijzen, H., 1991, A&A 250, 445, *The contribution function for the depth of formation of lines in a stellar atmosphere*

Aerts, C., 1993, PhD thesis, Katholieke Universiteit Leuven, *Line-profile variations in B stars. Mode identification with the moment method*

Aerts, C., 1996, A&A 314, 115, *Mode identification of pulsating stars from line-profile variations with the moment method: a more accurate discriminant*

Aerts, C., De Pauw, M., Waelkens, C., 1992, A&A 266, 294, *Mode identification of pulsating stars from line profile variations with the moment method. an example - The β Cephei star δ Ceti*

Aerts, C., Waelkens, C., De Pauw, M., 1994, A&A 286, 136, *Mode identification with the moment method in four multiperiodic β Cephei stars: KK Velorum, ν Eri, β CMa, and V348 Normae*

Aerts, C., Eyer, L., Kestens, E., 1998, A&A 337, 790, *The discovery of new γ Doradus stars from the HIPPARCOS mission*

Aerts, C., De Cat P., et al., 1999a, A&A 343, 872, *Selection of a sample of bright southern Slowly Pulsating B Stars for long-term photometric and spectroscopic monitoring*

Aerts, C., De Boeck I., Malfait, K., De Cat, P., 1999b, A&A 347, 524, *HD 42927 and HD 126341: two pulsating B stars surrounded by circumstellar dust*

Aerts, C., Cuypers, J., Dupret, M.-A., De Ridder, J., Scuflaire, R., Eyer, L., 2003a, In: Asteroseismology Across the HR Diagram, Ap&SS, in press, *Photometric Mode Identification in the two γ Doradus Stars HD 12901 and HD 48501*

Aerts, C., Lehmann, H., Scuflaire R., Dupret, M.-A., Briquet, M., De Ridder, J., Thoul A., 2003b, In: Asteroseismology Across the HR Diagram, Ap&SS, in press, *Mode identification and Seismic Modelling in the β Cep Star EN (16) Lac*

Aerts, C., Lehmann, H., Briquet, M., Scuflaire R., Dupret, M.-A., De Ridder, J., Thoul A., 2003c, *Spectroscopic mode identification for the β Cephei star EN (16) Lacertae*, submitted to A&A

Albrow, M.D., Cottrell, P.L., 1996, MNRAS 278, 337, *Contribution functions and the depths of formation of spectral lines in Cepheids*

Alexander, D.R., Ferguson, J.W., 1994, ApJ 437, 879, *Low-temperature Rosseland opacities*

Ando, H., Osaki, Y., 1975, PASJ 27, 581, *Nonadiabatic nonradial oscillations - an application to the five-minute oscillation of the sun*

Balmforth, N.J., 1992, MNRAS 255, 603, *Solar pulsational stability. I - Pulsation-mode thermodynamics*

Balona, L.A., 1987, MNRAS 224, 41, *Mode identification from line profile variations. III - Temperature variation and toroidal modes*

Balona, L.A., 1994, MNRAS 268, 119, *Effective Temperature Bolometric Correction and Mass Calibration of O-F*

Balona, L.A., Evers, E.A., 1999, MNRAS 302, 349, *Mode identification and asteroseismology of δ Scuti stars*

Balona, L.A., Stobie, R.S., 1979, MNRAS 187, 217, *Application of the Wesselink method to a non-radially oscillating star*

Balona, L.A., Böhm, T., Foing, B.H., Ghosh, K.K., et al., 1996, MNRAS 281, 1315, *Line profile variations in gamma Doradus*

Bouchy, F., Carrier, F., 2001, A&A 374, L5, *P-mode observations on α Cen A*

Bouchy, F., Carrier, F., 2002, A&A 390, 205, *The acoustic spectrum of alpha Cen A*

Bradley, P.A., Guzik, J.A., 2000, In: The Impact of Large-Scale Surveys on Pulsating Star Research, Ed.: Szabados L. & Kurtz D.W., ASP Conference Series, Vol. 203, *Suppressing g Modes in Shell Hydrogen-Burning δ Scuti Stars*

Breger. M., 2000, In: The 6th Vienna Workshop on "δ Scuti and related stars", Ed. M. Breger and M.H. Montgommery, ASP Conference Series, Vol. 210, *δ Scuti Stars (Review)*

Breger, M., 2003, In: Asteroseismology Across the HR Diagram, Ap&SS, in press, *Are gravity modes found in δ Scuti stars ?*

Breger, M., Garrido, R., Handler, G., et al., 2002, MNRAS 329, 531, *29 frequencies for the delta Scuti variable BI CMi: the 1997-2000 multisite campaigns*

Breger, M., Handler, G., Garrido, R., et al., 1999, A&A 349, 225, *30+ frequencies for the delta Scuti variable 4 Canum Venaticorum: results of the 1996 multisite campaign*

Breger, M., Zima, W., Handler, G., Poretti, E., Shobbrook, R.R., et al., 1998, A&A 331, 271, *The delta Scuti star FG Vir. III. The 1995 multisite campaign and the detection of 24 pulsation frequencies*

Briquet, M., Aerts, C., De Cat, P., 2001, A&A 366, 121, *Optical variability of the B-type star HD 105382: Pulsation or rotation?*

Briquet, M., Aerts, C., 2003a, In: Asteroseismology Across the HR Diagram, Ap&SS, *A new version of the moment method, optimized for mode identification in multiperiodic stars*, in press

Briquet, M., Aerts, C., 2003b, *A new version of the moment method, optimized for mode identification in multiperiodic stars*, submitted to A&A

Buta, R., Smith, M.A., 1979, ApJ 232, 213, *The light variations of nonradial pulsators - Theory and application to the line profile variable 53 Persei*

Castor, J.I., 1971, ApJ 166, 109, *On the Calculation of Linear, Nonadiabatic Pulsations of Stellar Models*

Chapellier, E., Le Contel, J.M., Le Contel, D., Sareyan, J.P., Valtier, J.C., 1995, A&A 304, 406, *Pulsation and binarity in β Cephei stars. II. 16 Lacertae*

Christensen-Dalsgaard, J., Däppen, W., 1992, A&ARv 4, 267, *Solar oscillations and the equation of state*

Christensen-Dalsgaard, J., Dziembowski, W.A., 1998, Variable Stars as Essential Astrophysical Tools, Proc. NATO Advanced Study Institute, ed. C. Ibanoglu, Kluwer Academic Publishers, p. 1-57, *I. Basic aspects of stellar structure and pulsation*

Claret, A., 2000, A&A 363, 1081, *A new non-linear limb-darkening law for LTE stellar atmosphere models. Calculations for* $-5.0 \leq \log[M/H] \leq +1$, $2000K \leq T_{\rm eff} \leq 50000K$ *at several surface gravities*

Claret, A., Willems, B., 2002, A&A 388, 518, *New results on the apsidal-motion test to stellar structure and evolution including the effects of dynamic tides*

Cowling, T.G., 1941, MNRAS 101, 367, *The non-radial oscillations of polytropic stars*

Cowling, T.G., Newing, R.A., 1949, ApJ 109, 149, *The Oscillations of a Rotating Star*

Cox, A.N., Morgan, S.M., Rogers, F.J., Iglesias, C.A., 1992, ApJ 393, 272, *An opacity mechanism for the pulsations of OB stars*

Cox, J.P., 1967, In: Aerodynamic Phenomena in Stellar Atmospheres, IAU Symposium no. 28, Ed. R. N. Thomas, Academic Press, London, p.3, *The linear theory: initiation of pulsational instability in stars*

Cox, J.P., 1980, Theory of Stellar Pulsation, Princeton Univ. Press, Princeton

Cugier, H., 1993, AcA 43, 27, *Modeling line profiles in β Cephei stars including temperature and pressure effects*

Cugier, H., Daszyńska-Daszkiewicz, J., 2001, A&A 377, 113, *Spectroscopic nonadiabatic observables in β Cephei models*

Cugier, H., Dziembowski, W., Pamyatnykh A., 1994, A&A 291, 143, *Nonadiabatic observables in beta Cephei models*

Curtis, H.D., 1909, ApJ 29, 229, *Five stars having variable radial velocities*

Cuypers J., 1986, A&A 167, 282, *A new method of detecting frequency variations in variable stars applied to the β Cephei star δ Ceti*

Daszyńska-Daszkiewicz, J., Dziembowski, W.A., Pamyatnykh, A.A., Goupil, M.-J., 2002, A&A 392, 151, *Photometric amplitudes and phases of nonradial oscillations in rotating stars*

Daszyńska-Daszkiewicz, J., Dziembowski, W., Pamyatnykh A., 2003, In: Asteroseismology Across the HR Diagram, Ap&SS, in press, *Photometric nonadiabatic observables in rotating β Cephei models*

De Cat, P., 2001, PhD thesis, Katholieke Universiteit Leuven, *An observational study of bright southern slowly pulsating B stars*

De Ridder, J., 2001, PhD thesis, Katholieke Universiteit Leuven, *Contributions to the Interpretation of Line-Profile Variations of Pulsating B Stars*

De Ridder, J., Dupret, M.-A., Neuforge C., and Aerts C., 2002, A&A 385, 572, *Influence of non-adiabatic temperature variations on line profile variations of slowly rotating β Cephei stars and SPBs. II. Simulations of line profile time series*

Dintrans, B., Rieutord, M., 2000, A&A 354, 86, *Oscillations of a rotating star: a non-perturbative theory*

Dupret, M.-A., 2001, A&A 366, 166, *Nonradial nonadiabatic stellar pulsations: A numerical method and its application to a β Cephei model*

Dupret, M.-A., De Ridder, J., Neuforge C., Aerts C., and Scuflaire R., 2002, A&A 385, 563, *Influence of non-adiabatic temperature variations on line profile variations of slowly rotating β Cephei stars and SPBs. I. Non-adiabatic eigenfunctions in the atmosphere of a pulsating star*

Dupret, M.-A., De Ridder, J., De Cat, P., Aerts, C., Scuflaire, R., Noels, A., Thoul, A., 2003a, A&A 398, 677, *A photometric mode identification method, including an improved non-adiabatic treatment of the atmosphere*

Dupret, M.-A., Garrido, R., De Ridder, J., Scuflaire, R., De Cat, P., Aerts, C., Moya, A., Noels, A., Thoul, A., 2003b, In: Asteroseismology Across the HR Diagram, Ap&SS, *An improved photometric mode identification method : applications to Slowly Pulsating B stars, β Cephei, δ Scuti and γ Doradus stars*, in press

Dziembowski, W., 1977a, Acta Astron. 27, 95, *Oscillations of giants and supergiants*

Dziembowski, W., 1977b, Acta Astron. 27, 203, *Light and radial velocity variations in a nonradially oscillating star*

Dziembowski, W., Jerzykiewicz, M., 1996, A&A 306, 436, *Asteroseismology of the β Cephei stars. I. 16 (EN) Lacertae*

Dziembowski, W.A., Pamyatnykh, A.A., 1993a, MNRAS 262, 204, *The opacity mechanism in B-type stars. I - Unstable modes in β Cephei star models*

Dziembowski, W.A., Moskalik, P., Pamyatnykh, A.A., 1993b, MNRAS 265, 588, *The opacity mechanism in B-Type stars - II. Excitation of high-order g-modes in main-sequence stars*

Eggen, O.J., 1977, PASP 89, 187, *Is star formation bimodal ? II. The nearest early-type stars.*

Eyer, L., Aerts, C., van Loon, M., Bouckaert, F., Cuypers, J., In: Observational Aspects of Pulsating B- and A Stars, Ed. C. Sterken and D.W. Kurtz, ASP Conference Proceedings, Vol. 256, 203, *The gamma Doradus stars campaign*

Gabriel, M., 1989, A&A 208, 122, *The thermal surface boundary condition for stellar pulsations*

Gabriel, M., Scuflaire, R., 1979, Acta Astron. 29, 135, *Properties of Non-radial Stellar Oscillations*

Garrido, R., 2000, In: The 6th Vienna Workshop on "δ Scuti and related stars", Ed. M. Breger and M.H. Montgommery, ASP Conference Series, Vol. 210, Invited talk, 67-98

Garrido, R., Garcia-Lobo, E., & Rodriguez, E., 1990, A&A 234, 262, *Modal discrimination of pulsating stars by using Strömgren photometry*

Gautschy, A., Saio, H., 1996, AR A&A 34, 551, *Stellar Pulsations across the HR Diagram: Part 2*

Gies, D.R., Kullavanijaya, A., 1988, ApJ 326, 813, *The line profile variations of Epsilon Persei. I - Evidence for multimode nonradial pulsations*

Gray, D.F., 1992, The observation and analysis of stellar photospheres, 2nd edition, Cambridge University Press

Guzik, J.A., Kaye, A.B., Bradley, P.A., Cox, A.N., Neuforge, C., 2000, ApJ 542, L57, *Driving the Gravity-Mode Pulsations in γ Doradus Variables*

Handler, G., 1999, MNRAS 309, L19, *The domain of γ Doradus variables in the Hertzsprung-Russell diagram*

Handler, G., Shobbrook, R.R., In: Observational Aspects of Pulsating B- and A Stars, Ed. C. Sterken and D.W. Kurtz, ASP Conference Proceedings, Vol. 256, 117, *A progress report on the search for delta Scuti pulsations of gamma Doradus candidates in the classical instability strip*

Handler, G., Balona, L.A., Shobbrook, R.R., Koen,C., Bruch, A., Romero-Colmenero, E., Pamyatnykh, A.A., Willems, B., Eyer, L., James, D.J., Maas, T., 2002, MNRAS 333, 262, *Discovery and analysis of p-mode and g-mode oscillations in the A-type primary of the eccentric binary HD 209295*

Heiter, U., Kupka, F., van 't Veer-Menneret, C., Barban, C., Weiss, W.W., Goupil, M.-J., Schmidt, W., Katz, D., Garrido, R., 2002, A&A, in press, *New grids of ATLAS9 atmospheres I: Influence of convection treatments on model structure and on observable quantities*

Henrichs H.F. et al., 2000, The Be Phenomenon in Early-Type Stars, ASP Conference Series, Vol. 214, eds.: Smith M.A., Henrichs H.F., *The magnetic field of β Cep and the Be phenomenon*

Heynderickx, D., Waelkens, C., Smeyers, P., 1994, A&AS 105, 447, *A photometric study of β Cephei stars. II. Determination of the degrees ℓ of pulsation modes*

Houdek, G., Balmforth, N.J., Christensen-Dalsgaard, J., Gough, D.O., A&A 351, 582, *Amplitudes of stochastically excited oscillations in main-sequence stars*

Iglesias, C.A., Rogers, F.J., 1996, ApJ 464, 943,I *Updated Opal Opacities*

Jerzykiewicz, M., 1993, Acta Astron. 43, 13, *UBV photometry of the β Cephei type variable stars. V - 16 (EN) Lacertae*

Jerzykiewicz, M., Sterken, C., 1980, In: Variability in stars and galaxies, Fifth European Regional meeting in Astronomy, Institut d'Astrophysique de Liège, *β Cephei stars - A review of recent observational data*

Kaye, A.B., Handler, G., Krisciunas, K., et al., 2000, In: The Impact of Large-Scale Surveys on Pulsating Star Research, Eds.: Szabados L. & Kurtz D.W., ASP Conference Series, Vol. 203, *The newly-discovered γ Doradus variables*

Keeley, D.A., 1977, ApJ 211, 926, *Linear stability analysis of stellar models by the inverse iteration method*

Kippenhahn, R., Weigert A., 1990, Astronomy and astrophysics library, Springer Berlin, *Stellar structure and evolution*

Kiriakidis, M., El Eid, M.F., Glatzel, W., 1992, MNRAS 255, 1P, *Heavy element opacities and the pulsations of β Cepheid stars*

Koen, C., Eyer, L., 2002, MNRAS 331, 45, *New periodic variables from the Hipparcos epoch photometry*

Künzli, M., North, P., Kurucz, R.L., Nicolet, B., 1997, A&AS 122, 51, *A calibration of Geneva photometry for B to G stars in terms of* T_{eff}, $\log g$ *and [M/H]*

Kurtz D.W., 2000, In: The 6th Vienna Workshop on "δ Scuti and related stars", Ed. M. Breger and M.H. Montgommery, ASP Conference Series, Vol. 210, *Pulsation of Chemically Peculiar and Pre-Main Sequence Stars in the δ Scuti Instability Strip*

Kurucz, R.L., 1970, ATLAS: A computer program for calculating model stellar atmospheres, Smithsonian Astrophysical Observatory, special report 309

Kurucz, R.L., 1993, ATLAS9 Stellar Atmosphere programs and 2 km/s grids. Kurucz CDROM No 13

Ledoux, P., 1951, ApJ 114, 373, *The Nonradial Oscillations of Gaseous Stars and the Problem of Beta Canis Majoris*

Ledoux, P., 1958, Handbuch der Physik, ed. S. Flügge 51, 605, *Stellar stability*

Ledoux, P., Walraven, Th., 1958, Handbuch der Physik, ed. S. Flügge 51, 353, *Variable stars*

Lee, U., Baraffe, I., 1995, A&A 301, 419, *Pulsational stability of rotating main sequence stars: the second order effects of rotation on the nonadiabatic oscillations*

Lee, U., Saio, H., 1990, ApJ 349, 570, *Line profile variations caused by low-frequency nonradial pulsations of rapidly rotating stars*

Lee, U., Jeffery, C.S., Saio, H., 1992, MNRAS 254, 185, *Line profile variations caused by low-frequency non-radial pulsations of rapidly rotating stars. II*

Lehmann, H., Harmanec, P., Aerts, C., Bozic, H., Eenens, P., Hildebrandt, G., Holmgren, D., Mathias, P., Scholz, G., Slechta, M., Yang, S., 2001, A&A 367, 236, *A new analysis of the radial velocity variations of the eclipsing and spectroscopic binary EN Lacertae*

Maeder, A., 1999, A&A 347, 185, *Stellar evolution with rotation IV: von Zeipel's theorem and anisotropic losses of mass and angular momentum*

Magain, P., 1986, A&A 163, 135, *Contribution functions and the depths of formation of spectral lines*

Mihalas, D., 1978, Stellar Atmospheres, (2nd ed.), W. H. Freeman and company, San Francisco

Mihalas, D., Weibel-Mihalas, B., 1999, Foundations of Radiation Hydrodynamics, Dover Publications, Inc. Mineola, New York

Moskalik, P., Dziembowski, W.A., 1992, A&A 256, L5, *New opacities and the origin of the β Cephei pulsation*

Napiwotzki, R., Schoenberner, D., Wenske, V., 1993, A&A 268, 653, *On the determination of effective temperature and surface gravity of B, A, and F stars using Strömgren UVBY beta photometry*

Noels, A., 1998, In: A Half Century of Stellar Pulsation Interpretation: A Tribute to Arthur N. Cox, Ed. P. Bradley and J. Guzik, ASP Conference Series, Vol. 135, p. 400, Invited talk, *Stability Problems and Linear Driving*

Osaki, Y., 1971, PASJ 23, 485, *Non-Radial Oscillations and the β Canis Majoris phenomenon*

Pamyatnykh, A.A., 1999, Acta Astron. 49, 119, *Pulsational Instability Domains in the Upper Main Sequence*

Pesnell, W.D., 1990, ApJ 363, 227, *Nonradial, nonadiabatic stellar pulsations*

Renson, P., 1991, A&AS 89, 429, *General catalogue of Ap and Am stars*

Ribas, I., Jordi, C., Giménez, Á., 2000, MNRAS 318, L55, *The mass dependence of the overshooting parameter determined from eclipsing binary data*

Rodríguez, E., López-González, M.J., López de Coca, P., 2000, A&AS 144, 469. *A revised catalogue of delta Sct stars*

Saio, H., Cox, J.P., 1980, ApJ 236, 549, *Linear, nonadiabatic analysis of nonradial oscillations of massive near main sequence stars*

Savage, B.D., Massa, D., Meade, M., Wesselius, P.R., 1985, ApJS 59, 397, *A catalog of ultraviolet interstellar extinction excesses for 1415 stars*

Schrijver, H., 1997, "The Hipparcos and Tycho Catalogues (Volume 10) : Hipparcos Double and Multiple Systems Annex, Solar System Objects", SAS Publications Division, c/o ESTEC, Noordwijk, The Netherlands

Schrijvers, C., 1999, PhD thesis, University of Amsterdam, *Spectroscopic diagnostics of pulsation in rotating stars*

Scuflaire, R., 1974a, A&A 34, 449, *Space Oscillations of Stellar Non Radial Eigenfuncions*

Scuflaire, R., 1974b, A&A 36, 107, *The Non Radial Oscillations of Condensed Polytropes*

Scuflaire, R., 1975, PhD thesis, Université de Liège, *Traitement des perturbations stellaires non adiabatiques et applications aux étoiles supermassives*

Scuflaire, R., 2000, Cours de *Stabilité Stellaire*, DEA en Astrophysique et Géophysique, Université de Liège

Shibahashi, H., Aerts, C., 2000, ApJL 531, L143, *Asteroseismology and Oblique Pulsator Model of β Cephei*

Shobbrook, R.R., 1985, MNRAS 214, 33, *New radial pulsation constants for the β Cephei variables*

Smith, M.A., Buta, R.J., 1979, ApJ 232L, 193, *The nonradial mode identification of 53 Persei during late 1977 and 1978*

Soufi, F., Goupil, M.J., Dziembowski, W.A., 1998, A&A 334, 911, *Effects of moderate rotation on stellar pulsation. I. Third order perturbation formalism*

Stamford, P.A., Watson, R.D., 1981, Ap&SS 77, 131, *Baade-Wesselink and related techniques for mode discrimination in nonradial stellar pulsations*

Telting, J.H., Schrijvers, C., 1997, A&A 317, 723, *Line-profile variations of non-radial adiabatic pulsations of rotating stars. II. The diagnostic value of amplitude and phase diagrams derived from time series of spectra*

Telting, J.H., Schrijvers, C., 1999, A&A 342, 453, *Line-profile variations due to adiabatic non-radial pulsations in rotating stars. IV. The effects of intrinsic profile variations on the IPS diagnostics*

Toutain, T., Berthomieu, G., Provost, J., 1999, A&A 344, 188, *Light perturbation from stellar nonradial oscillations: an application to solar oscillations*

Townsend, R., 1997, MNRAS 284, 839, *Spectroscopic modelling of non-radial pulsation in rotating early-type stars*

Unno, W., Osaki, Y., Ando, H., Saio, H., Shibahashi, H., 1989, Nonradial oscillations of stars, 2$^{\rm nd}$ edition, Univ. Tokyo Press, Tokyo

van Hoof, A., 1972, A&A 18, 51, *Omicron velorum a new β CMa star*

Wade, R.A, Rucinski, S.M., 1985, A&AS 60, 471, *Linear and quadratic limb-darkening coefficients for a large grid of LTE model atmospheres*

Waelkens C., 1991, A&A 246, 453, *Slowly pulsating B stars*

Waelkens C., Aerts C., Kestens E., et al., 1998, A&A 330, 215, *Study of an unbiased sample of B stars observed with Hipparcos: the discovery of a large amount of new slowly pulsating B stars*

Watson, R.D., 1988, Ap&SS 140, 255, *Contributing factors to flux changes in nonradial stellar pulsations*

Wilkinson, J.H., 1965, The Algebraic Eigenvalue Problem, Oxford Univ. Press, Oxford

Willems, B., Aerts, C., 2002, A&A 384, 441, *Tidally induced radial-velocity variations in close binaries*